Atomic physics with vapor-cell clocks

Bart Hunter McGuyer

A Dissertation

Presented to the Faculty

of Princeton University

in Candidacy for the Degree

of Doctor of Philosophy

Recommended for Acceptance

by the Department of

Physics

Adviser: William Happer

June 2012

Abstract

The most widely used atomic frequency standards (or clocks) are based on the microwave resonant frequencies of optically pumped vapors of alkali-metal atoms in glass cells filled with buffer gas. These vapor-cell clocks are secondary, not primary frequency standards mainly because of the light and pressure shifts, which alter the resonant frequencies of the alkali-metal atoms. This dissertation presents studies of atomic physics important to vapor-cell clocks and, in particular, their accuracy.

First, we report a simple method to suppress the light shift in optical pumping systems. This method uses only frequency modulation of a radio frequency or microwave source, which excites an atomic resonance, to simultaneously lock the source frequency to the atomic resonance and lock the pumping light frequency to suppress the light shift. This technique can be applied to many optical pumping systems that experience light shifts. It is especially useful for atomic clocks because it improves the long-term performance, reduces the influence of a pumping laser, and requires less equipment than previous methods.

Next, we present three studies of the pressure shift, starting with an estimation of the hyperfine-shift potential that is responsible for most of the pressure shift. We then show that the microwave resonant frequencies of ground-state Rb and Cs atoms in Xe buffer gas have a relatively large nonlinear dependence on the Xe pressure, presumably because of short-lived RbXe and CsXe van der Waals molecules. The Xe data show striking discrepancies with the previous theory for nonlinear shifts, most of which is eliminated by accounting for the spin-rotation interaction in addition to the hyperfine-shift interaction in the molecules. To the limit of our experimental accuracy, the shifts of Rb and Cs in He, Ne, and N_2 were linear with pressure. We then consider the prospects for suppressing the pressure shift with buffer-gas mixtures and feedback.

Finally, we report an investigation of the potential for integrating spheres to enhance absorption in optically thin alkali-metal vapor cells. We demonstrate a roughly ten-fold increase of the optical absorption that seems to be limited by the glass cell required to contain the alkali-metal vapor.

Acknowledgements

This dissertation would not have been possible without the support of many people. First, I must thank my adviser, Professor William Happer, who is truly a world-class scientist and a first-rate mentor. I am honored to have been one of his students, and to be a part of his scientific legacy.

I am also very grateful for the excellent support of Professor Michael Romalis, and for the close relationship between the Happer and Romalis research groups.

Also to my collaborators, whose work contributed to this dissertation: to Yuan-Yu Jau for his guidance, insights, and contributions on many of my projects; to Tian Xia for the Cs measurements in Chapter 4; to Steven Morgan for collaborating on the measurements in Chapter 5; to Alan Braun and Timothy Davis at Sarnoff Corporation for loaning the vacuum bellows in Chapter 5; to Amit Ben-Kish for collaborating on Chapter 6; and, of course, to Michael Souza for expert glassblowing.

There are many colleagues and friends who enriched my time at Princeton, more than I can mention here, but I'd like to thank Ben Olsen, for being a great labmate and expert figure critiquer; Justin Brown, for asking questions that helped me think outside the box; Fei Gong and Brian Patton for helping me get started in the Happer group; and Michael Schroer and Joe Checkelsky for good times on the B-level.

I am indebted to the wonderful staff of the Physics Department, in particular, Regina Savadge, Barbara Grunwerg, Laurel Lerner, and Omelan Stryzak, who let me build a Tesla coil for Princeton.

To my family for taking me to construction sites as a kid, finding things for me to disassemble, tolerating questionable garage experiments, and always encouraging my curiosity.

Finally, to my wife, Melissa Miller, for being my best friend and smiling whenever I say, "Stand back! I'm going to try science!"

Contents

List of Tables

List of Figures

Chapter 1

Introduction

To measure the passage of time, a clock counts the cycles of an oscillator. In a perfect clock the cycles of this oscillator would repeat with a temporal frequency that never changes. In practice, the quality of a clock depends on the ability of its oscillator to provide a stable, known frequency. Thus, the art and science of making clocks is that of making stable oscillators, or frequency standards. Over time, clocks have evolved to use many different types of frequency standards, for example, astronomical cycles in sundials, pendulums in mechanical clocks, and quartz crystals in electrical clocks [1, 2]. This ongoing development of frequency standards continues to improve the stability, accuracy, and reliability of clocks, and to expand their range of applications.

During the 1870's, James Clerk Maxwell and Lord Kelvin (William Thomson) suggested that the natural oscillations of atoms could make excellent frequency standards [3, 4]. The properties of atoms, as far as we know, are constant. An unperturbed cesium atom (^{133}Cs), for example, is identical to any other cesium atom, and its unperturbed natural oscillations are the same as those of any other past, present, or future cesium atom, no matter where it is in the universe. In contrast, even the best quartz oscillators cannot be manufactured identically, and their properties change with age. It took until the early 20th century for Isaac Isidor Rabi to suggest a practical means

to implement an atomic frequency standard (or atomic clock), and until 1948 for the first working prototype, which used Rabi's magnetic-resonance technique with ammonia molecules, to be built by Harold Lyons at the National Bureau of Standards (now the National Institute of Standards and Technology, or NIST) in the United States (US) [5, 6, 7]. Ever since, the development of atomic clocks has progressed rapidly [8]. By 1968, the International System of Units (SI) second was redefined to be exactly 9,192,631,770 cycles of oscillation corresponding to a transition between the two hyperfine sublevels of a ground-state ^{133}Cs atom [9, 10]. Today, atomic clocks provide the most precise and accurate measurements of time and frequency. Besides scientific research, these clocks are crucial to much of modern technology, for example, the Global Positioning System (GPS), the high-speed networks behind cellular phones, and even long-distance electrical power transmission [7].

Most modern atomic clocks are based on the ground-state properties of either H or an alkali-metal atom, typically Cs or Rb [11]. In these atoms, the hyperfine coupling between the spins of the single valence electron and of the nucleus leads to convenient resonant frequencies in the microwave (GHz) range. Different clocks use different techniques to access these atomic resonant frequencies as standards. For example, active atomic masers usually inject a beam of H atoms into a tuned microwave cavity in such a way that the atoms excite a detectable electrical resonance of the cavity. Atomic beam clocks usually send a stream of Cs atoms through a vacuum chamber with varying magnetic fields and two microwave cavities. Microwaves applied to the cavities are tuned to an atomic resonance by optimizing the number of atoms transmitted. The current primary standard of time and frequency for the US is an atomic fountain clock that launches clouds of Cs atoms upward into a vacuum chamber, to pass up and down through the same microwave cavity, eliminating the errors in beam clocks from differences between cavities [7]. However, the development of new and improved atomic clocks is ongoing, and clocks that use other atoms and

techniques, for example, trapped-ion clocks and optical lattice clocks, continue to play an increasing role [12, 13].

Of the many types of modern atomic clocks, the most widespread is the vapor-cell (or gas-cell) clock, which uses a glass cell to contain a dilute vapor of alkali-metal atoms and an inert buffer gas [11, 14]. These clocks are robust enough for use onboard GPS satellites, and simple enough to mass produce inexpensively, for example, as compact laboratory frequency standards (e.g., Stanford Research Systems FS725). Though vapor-cell clocks originated in the late 1950's, they have enjoyed a recent resurgence of interest [14, 15, 16]. Much of the current focus has been on either improving these clocks by incorporating lasers, which allow for new techniques, or miniaturizing them towards the level of integrated circuits for use in even more diverse applications. The first miniaturized, chip-scale atomic clock was, in fact, a laser-based vapor-cell clock built by Svenja Knappe and her collaborators at NIST in 2004 [17].

In conventional vapor-cell clocks, the alkali-metal vapor is optically pumped by light and probed by microwaves in a technique known as microwave-optical double resonance. First proposed by Alfred Kastler in 1950, optical pumping is the process where resonant light polarizes atoms through absorption and scattering, by redistributing the population of atoms between different sublevels of the atomic ground and excited states [18, 19, 20, 21]. The pumping light creates an imbalance between the atomic populations of the different ground-state hyperfine sublevels in the vapor. This imbalance allows the vapor to absorb resonant microwaves that transfer population back between the sublevels, which in turn alters how the vapor absorbs the light. By measuring the transmission of the pumping light through the cell, the microwaves may be tuned to a particular hyperfine resonant frequency, and output as a clock signal. Buffer gas is required to increase the optical pumping efficiency, in particular, by slowing the diffusion of the alkali-metal atoms to the cell walls, where collisions destroy polarization. As discovered by Robert Dicke, the tight con-

finement of the alkali-metal atoms by the cell (and in some situations, by collisions with the buffer gas) leads to narrow hyperfine resonance lines that are nearly free of Doppler broadening, enhancing the clock precision [22]. Because of the relative ease to produce pumping light for ^{87}Rb atoms with discharge lamps, vapor-cell clocks have traditionally used ^{87}Rb atoms, and so are often referred to as rubidium standards [23].

Despite their maturity and renewed interest, some elements of the physics important to vapor-cell clocks and, in particular, their accuracy are not yet fully understood. This dissertation presents studies of atomic physics important to vapor-cell clocks, and is organized as follows:

Chapter 2 addresses the light shift, or the frequency shift of an atomic resonance due to the dynamic (or AC) Stark effect of optical pumping light [24]. The light shift is an important source of error in many optical pumping systems, and is one of the main reasons for the difficulty in implementing vapor-cell clocks with lasers. We report a simple method to suppress the light shift [25, 26, 27, 28]. This method uses only frequency modulation of a radio frequency or microwave source, which is used to excite an atomic resonance, to simultaneously lock the source frequency to the atomic resonance and lock the pumping light to suppress the light shift. This method can be applied to many optical pumping systems that experience light shifts. It is especially useful for atomic clocks because it improves the long-term performance, reduces the influence of a pumping laser, and requires less equipment than previous methods.

Chapters 3–5 address the pressure shift, or the frequency shift of an atomic resonance due to collisions with a chemically inert buffer gas [29, 30]. The pressure shift is the main reason why vapor-cell clocks are secondary, not primary standards, since the atomic resonant frequencies are not the same as free-atom frequencies, but instead depend on the pressure, temperature, and composition of the buffer gas [11]. Most of the pressure shift is due to the hyperfine-shift interaction $\delta A\, \mathbf{I} \cdot \mathbf{S}$ between the electronic spin $\mathbf{S}$ and nuclear spin $\mathbf{I}$ of an alkali-metal atom during binary colli-

sions with the buffer gas. Despite much theoretical and experimental attention, not much is known yet about the potential $\delta A = \delta A(R)$ as a function of the internuclear separation R of a colliding pair, especially at small R. Chapter 3 demonstrates how to use experimental data for the pressure shift to estimate simple trials forms of the potentials $\delta A(R)$ for Na, K, and Rb in He, Ne, or Ar gas. Though these trial forms are not unique, they still yield a surprising amount of information about the shapes of the $\delta A(R)$ about a potential well in an interaction potential $V(R)$ for the colliding pair, which agree well with theoretical and experimental results in the few cases where they are available. Additionally, to aid these estimates, we provide an improved estimate of the large-R asymptote of the ratio $\delta A(R)/V(R)$.

Chapter 4 reports on precision measurements of the dependence of the microwave resonant frequencies of ground-state ^{87}Rb, ^{85}Rb, and ^{133}Cs atoms on the pressure of the buffer gases He, Ne, N_2, Ar, Kr, and Xe [31, 32, 33, 34, 35, 36]. Recent work has shown that short-lived van der Waals molecules, which are known to form between certain pairs of alkali-metal and buffer-gas atoms in three-body collisions [37, 38], may lead to a nonlinear dependence of the pressure shift on the buffer-gas pressure for certain gases [39, 40]. We show that the nonlinear shifts for Xe are opposite in sign to the shifts for Ar and Kr, even though all three have negative linear shifts. The Xe data show striking discrepancies with the previous theory for nonlinear shifts [39], most of which is eliminated by accounting for the spin-rotation interaction, $\gamma\,\mathbf{N}\cdot\mathbf{S}$, between the rotational angular momentum $\mathbf{N}$ of the molecules and $\mathbf{S}$ [41, 42], in addition to the hyperfine-shift interaction $\delta A\,\mathbf{I}\cdot\mathbf{S}$. To the limit of our experimental accuracy, the shifts of Rb and Cs in He, Ne, and N_2 were linear with pressure.

Chapter 5 considers the prospects for suppressing the pressure shift in vapor-cell clocks. We demonstrate the properties of buffer-gas mixtures that are adjusted to give no pressure shift at a particular temperature, and propose some possible implementations of feedback to suppress the pressure shift using these mixtures. We

examine how the nonlinear pressure shifts from van der Waals molecules may limit the accuracy of these implementations. With suppression of the pressure shift, it might be possible to significantly reduce the long-term drift of vapor-cell clocks and the need for calibration.

Finally, Chapter 6 reports an investigation of the potential for integrating spheres, or diffuse-reflectance optical cavities, to enhance the absorption of light in optically thin alkali-metal vapor cells [43]. Miniaturized vapor cells for atomic clocks and magnetometers have shortened optical path lengths. To compensate, miniature cells usually operate at higher temperatures to increase the density of alkali-metal atoms, which leads to reduced performance from spin-exchange broadening of the microwave resonance lines [44] and to an increased power demand from heating the cell. Another way to enhance absorption is to pass light through the cell multiple times with a cavity, without increasing the temperature or alkali-metal density. Integrating spheres are simple and robust optical cavities, since they do not require the precise alignment of specular-reflectance cavities with mirrors, which can misalign over time. We demonstrate a roughly ten-fold enhancement of optical absorption, which seems to be limited by the glass cell required to contain the alkali-metal vapor.

Chapter 2

Simple method of light-shift suppression

2.1 Introduction

The light shift normally refers to the frequency shift of an atomic resonance due to the dynamic (or AC) Stark effect from optical pumping light [24]. The shift depends on both the frequency and intensity of the light. The light shift is an important source of error in many optical pumping systems. In particular, it is one of the main performance limitations in atomic frequency standards (or clocks), since it turns the fluctuations of the pumping light frequency and intensity into drift and noise in the clock output. This is one reason it is difficult to implement atomic clocks with diode lasers. Accordingly, understanding and reducing the light shift in optical pumping systems remains an active area of research [14, 15, 16].

There are various ways to suppress light shifts. One simple technique for monochromatic pumping sources, such as diode lasers, is to tune them to a zero-shift optical frequency or "magic wavelength" that produces no light shift [24]. The zero-shift frequencies are very close to the peaks of the optical absorption lines. The

conventional method to suppress light shifts in laser-pumped atomic clocks uses an additional feedback loop to lock the laser to a zero-shift frequency [39, 45, 46]. Other methods are even more complicated [15, 16, 47, 48, 49, 50, 51]. In the method we describe here, we use the same feedback loop that locks the local oscillator to the microwave resonant frequency of the atoms to simultaneously adjust the laser frequency to suppress the light shift [25, 26, 27, 28].

Before we begin, we first provide some background on the structure of alkali-metal atoms, on the microwave-optical double resonance technique, and on the light shift relevant to vapor-cell clocks.

2.1.1 Alkali-metal atomic structure

Most atomic clocks are based on the hyperfine resonances of ground-state alkali-metal atoms, so we review the atomic structure relevant to this and later chapters here. Fig. 2.1 is a sketch of this atomic structure for ^{87}Rb, the most commonly used isotope of Rb in clocks, which we describe below. For additional information about alkali-metal atoms, we recommend the book *Optically Pumped Atoms* by Happer, Jau, and Walker [21] and the reference compilations of Steck [52].

The common alkali-metal atoms Na, K, Rb, and Cs have ground states with a single valence electron and structures that are similar to H. Their electronic structure [X]ns^1 is the sum of a noble-gas-like core [X] and a valence S-state electron with principle quantum number n: [Ne]3s^1, [Ar]4s^1, [Kr]5s^1, and [Xe]6s^1 for Na, K, Rb, and Cs, respectively. The ground state is designated by the term symbol $^{2S+1}L_J = {}^2\mathrm{S}_{1/2}$. Term symbols are often written as $n\,{}^{2S+1}L_J$, such as in Fig. 2.1. The total atomic angular momentum $\mathbf{F} = \mathbf{I} + \mathbf{J}$ is the sum of the nuclear spin $\mathbf{I}$ and the total electronic angular momentum $\mathbf{J} = \mathbf{L}+\mathbf{S}$. For S-states, the orbital angular momentum $\mathbf{L} = 0$, so the electronic total $\mathbf{J} = \mathbf{S}$, which is the electronic spin with quantum number $S = 1/2$. The nuclear spin $\mathbf{I}$ is non-zero for the naturally occurring isotopes of each

alkali-metal atom; for example, the nuclear spin quantum number I is 3/2 for ^{23}Na, ^{39}K, and ^{87}Rb, 5/2 for ^{85}Rb, and 7/2 for ^{133}Cs.

The strongest optical resonant lines of the alkali-metal atoms lie in the near-infrared or visible range. In particular, the strong optical transitions between the ground and lowest excited states are most often used for optical pumping. The lowest excited state has an electronic structure $[\mathrm{X}]n\mathrm{p}^1$, with a valence P-state electron with orbital quantum number $L = 1$. This state is split by fine structure into a doublet (D) with the two terms $^2\mathrm{P}_{1/2}$ and $^2\mathrm{P}_{3/2}$, which have total electronic spin quantum numbers $J = 1/2$ and 3/2, respectively. The optical transitions $^2\mathrm{S}_{1/2}$–$^2\mathrm{P}_{1/2}$ and $^2\mathrm{S}_{1/2}$–$^2\mathrm{P}_{3/2}$ are known as the D1 and D2 transitions, respectively, and for Rb have wavelengths of roughly 795 and 780 nm. For simplicity, Fig. 2.1 includes only the D1 transition. As sketched in the figure, the lowest excited states of the alkali-metal atoms have similar, though usually more complicated structures than the ground states. The rest of this section will focus on the ground-state structure, and we recommend Refs. [21, 52] for more information about the excited-state structure.

A free alkali-metal atom evolves according to the ground-state spin Hamiltonian

$$H^{\{g\}} = A\,\mathbf{I}\cdot\mathbf{S} - \boldsymbol{\mu}\cdot\mathbf{B}, \tag{2.1}$$

where the first term is the hyperfine coupling of the nuclear spin $\mathbf{I}$ and electronic spin $\mathbf{S}$ of the alkali-metal atom, with the magnetic-dipole coupling coefficient A. For the ground S-states, this coupling is due to a contact magnetic-dipole interaction,

$$H_{\mathrm{hf}} = \frac{8\pi}{3} g_S \mu_B \frac{\mu_I}{I} \delta(\mathbf{r}_{\mathrm{e}})\,\mathbf{I}\cdot\mathbf{S}, \tag{2.2}$$

which leads to the coefficient

$$A = \frac{8\pi}{3} g_S \mu_B \frac{\mu_I}{I} |\psi(0)|^2, \tag{2.3}$$

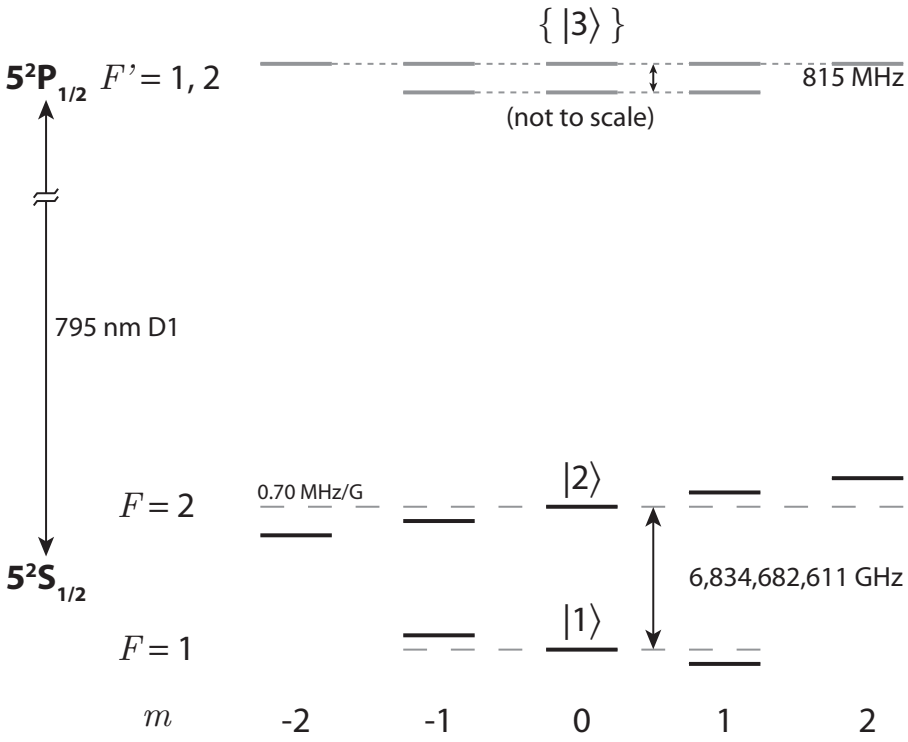

Figure 2.1: Energy levels of ^{87}Rb ($I = 3/2$) important to vapor-cell clocks (not to scale). The ground state is split into upper and lower hyperfine manifolds with $F = a = I + 1/2$ and $F = b = I - 1/2$, respectively. The hyperfine transition between the sublevels $|F\, m\rangle$ with $m = 0$ is the known as the 0–0 or clock transition, and corresponds to a microwave frequency $\nu_{00} \approx 6.834$ GHz for ^{87}Rb. The kets $|1\rangle$, $|2\rangle$, and $|3\rangle$ highlight the sublevels that are often used in approximate two- and three-level models for vapor-cell clocks [11, 15, 16].

where $|\psi(0)|^2$ is the finite probability density for the valence electron to be located at the nucleus. Here, $g_S = 2.0023$ is the electronic g factor, μ_B is the Bohr magneton, and μ_I is the nuclear moment. Additional hyperfine couplings, in particular, electric-quadrupole and non-contact magnetic-dipole interactions, are important for the excited states [53].

The second term in (2.1) is the Zeeman interaction of the total magnetic dipole moment of the atom,

$$\boldsymbol{\mu} = -g_S \mu_B \mathbf{S} + \frac{\mu_I}{I}\mathbf{I}, \tag{2.4}$$

with an externally applied magnetic field $\mathbf{B}$ of amplitude $B = |\mathbf{B}|$. Since the nuclear moment μ_I is of the order of the nuclear magneton $\mu_N \approx \mu_B/1836$, where 1836 is roughly the ratio of the proton to electron mass, the total moment (2.4) is almost entirely due to the electronic contribution. By default, we assume that any external field is static and oriented along the Cartesian unit vector $\mathbf{z}$, such that $\mathbf{B} = B\mathbf{z}$.

The sublevel energies E_μ and spin eigenvectors $|\mu\rangle$ of free, ground-state atoms are given by the time-independent Schrödinger equation,

$$H^{\{g\}}|\mu\rangle = E_\mu|\mu\rangle. \tag{2.5}$$

Here, the energies E_μ are understood to be the shifts of the sublevels $|\mu\rangle$ away from the mean ground-state energy. The eigenvectors are complete, $\sum_\mu |\mu\rangle\langle\mu| = 1$, and orthonormal, $\langle\mu|\nu\rangle = \delta_{\nu\mu}$. The integer index $\mu = 1, 2, \ldots, g^{\{g\}}$, where the total number of ground-state sublevels is $g^{\{g\}} = [I][S]$. Here and subsequently, the notation

$$[I] = 2I + 1 \tag{2.6}$$

denotes the number of sublevels (or degeneracy) for a spin of quantum number I.

For zero applied field, $B = 0$, the Hamiltonian $H^{\{g\}}$ commutes with the angular-momentum operator $\mathbf{F}$ and its square $\mathbf{F}^2 = \mathbf{F} \cdot \mathbf{F}$, as well as $\mathbf{I} \cdot \mathbf{I}$ and $\mathbf{S} \cdot \mathbf{S}$, since we may write the operator $\mathbf{I} \cdot \mathbf{S} = (\mathbf{F} \cdot \mathbf{F} - \mathbf{I} \cdot \mathbf{I} - \mathbf{S} \cdot \mathbf{S})/2$. As a result, we can choose the zero-field sublevels to be the the simultaneous eigenstates of $\mathbf{F} \cdot \mathbf{F}$ and $F_z = \mathbf{F} \cdot \mathbf{z}$. Let $|\mu\rangle = |F\, m\rangle$, where the total spin quantum number $F = I \pm 1/2$ and the azimuthal quantum number $m = m_F$ can take the values $-F, 1-F, \ldots, F-1, F$. The zero-field

eigenvectors then satisfy

$$\mathbf{F}\cdot\mathbf{F}|F\,m\rangle = F(F+1)|F\,m\rangle, \tag{2.7}$$

$$F_z|F\,m\rangle = m|F\,m\rangle, \tag{2.8}$$

$$\mathbf{I}\cdot\mathbf{I}|F\,m\rangle = I(I+1)|F\,m\rangle, \text{ and} \tag{2.9}$$

$$\mathbf{S}\cdot\mathbf{S}|F\,m\rangle = J(J+1)|F\,m\rangle, \tag{2.10}$$

where we use the convention that the angular-momentum operators are dimensionless, and have the zero-field energies

$$E_F^0 = \frac{A}{2}[F(F+1) - I(I+1) - S(S+1)]. \tag{2.11}$$

In terms of the uncoupled spin states $|S\,m_S\rangle$ for the electron and $|I\,m_I\rangle$ for the nucleus, we may expand the zero-field coupled-spin states as

$$|F\,m\rangle = \sum_{m_I m_S} C^{Fm}_{Im_ISm_S}|I\,m_I\rangle\otimes|S\,m_S\rangle, \tag{2.12}$$

where $C^{Fm}_{Im_ISm_S}$ is a Clebsch–Gordon coefficient [54].

The zero-field eigenvectors $|F\,m\rangle$ are still a good approximation for the true eigenectors $|\mu\rangle$ of (2.5) as long as the applied field B is weak enough that $g_S\mu_B B \ll AI$. This is usually satisfied for fields B of several Gauss or less, which are typical for atomic clocks. In this case, the hyperfine coupling is still the dominant interaction in the Hamiltonian $H^{\{g\}}$. To determine the low-field energies $E_\mu \approx E_{Fm}$ we treat the Zeeman interaction as a perturbation. To first order, the low-field energies are

$$\begin{aligned} E_{Fm} &\approx E_F^0 - \langle F\,m|\boldsymbol{\mu}\cdot\mathbf{B}|F\,m\rangle \\ &= E_F^0 + g_S\mu_B B\langle F\,m|S_z|F\,m\rangle - \frac{\mu_I}{I}\langle F\,m|I_z|F\,m\rangle. \end{aligned} \tag{2.13}$$

To evaluate these matrix elements, we may use the Wigner-Eckhart theorem to substitute the operators $\mathbf{S}$ and $\mathbf{I}$ with their projections along $\mathbf{F}$,

$$\mathbf{S} \to \frac{(\mathbf{S}\cdot\mathbf{F})\mathbf{F}}{F(F+1)} \quad \text{and} \quad \mathbf{I} \to \frac{(\mathbf{I}\cdot\mathbf{F})\mathbf{F}}{F(F+1)}. \tag{2.14}$$

As a result, we may write the low-field energies as

$$E_{Fm} \approx E_F^0 + g_F \mu_B B m, \tag{2.15}$$

where the coefficient

$$g_F = g_S \frac{F(F+1)+S(S+1)-I(I+1)}{2F(F+1)} - \left(\frac{\mu_I}{I\mu_B}\right)\frac{F(F+1)-S(S+1)+I(I+1)}{2F(F+1)}. \tag{2.16}$$

As mentioned before, the nuclear contribution to the Zeeman interaction is roughly a part-per-thousand correction, so the second term above can usually be neglected.

In this low-field basis, the ground-state of an alkali-metal atom has a structure like that sketched in Fig. 2.1. The ground-state sublevels $|F\,m\rangle$ split into upper and lower hyperfine manifolds with $F = a = I + 1/2$ and $F = b = I - 1/2$, respectively. For ^{87}Rb, $a = 2$ and $b = 1$. Neglecting the nuclear contribution to the Zeeman interaction, the coefficient (2.16) simplifies to

$$g_F \approx g_S \frac{(-1)^{F-a}}{[I]}, \tag{2.17}$$

and the ground-state sublevel energies (2.15) become

$$E_{Fm} \approx \frac{A}{2}\{(F-a)[b] + (F-b)[a]\} + \frac{g_S \mu_B B}{[I]}(-1)^{F-a} m. \tag{2.18}$$

We see that the Zeeman interaction leads to a first-order dependence of the energy E_{Fm} on the applied field B for all sublevels except those with $m = 0$. Note that the hyperfine and first-order Zeeman interactions lead to no net shift of the ground-state energy, $\sum_\mu E_\mu = 0$.

The transitions between sublevels of different hyperfine manifolds ($\Delta F = 1$ transitions) are known as hyperfine transitions, and correspond to resonant frequencies in the microwave range. These transitions are the atomic resonances used by vapor-cell atomic clocks. Conventionally, vapor-cell clocks use the transition between the two sublevels with $m = 0$, $|a\,0\rangle$ and $|b\,0\rangle$, known as the "0–0" or "clock" transition, since it has no first-order dependence on the applied field B. This is clear if we use (2.18) to write the (angular) Bohr frequency $\omega_{\alpha\beta}$ for the transition between the states $|a\,\alpha\rangle$ and $|b\,\beta\rangle$ as

$$\omega_{\alpha\beta} = \frac{E_{a\alpha} - E_{b\beta}}{\hbar} \approx \frac{A[I]}{2\hbar} + \frac{g_S \mu_B B}{[I]\hbar}(\alpha + \beta), \tag{2.19}$$

where $\hbar = h/(2\pi)$ is the reduced Planck constant. The corresponding temporal frequency, for example, of microwaves resonant with the "α–β" transition, is $\nu_{\alpha\beta} = \omega_{\alpha\beta}/(2\pi)$. For the 0–0 transition, this frequency is

$$\nu_{00} \approx \frac{A[I]}{2h}, \tag{2.20}$$

which is exact in the absence of an applied field B. The unperturbed, free-atom values of ν_{00} are known very precisely for many alkali-metal atoms: 1.7716261288 GHz for ^{23}Na ($I = 3/2$), 461.7197202 MHz for ^{39}K ($I = 3/2$), 3.0357324390 GHz for ^{85}Rb ($I = 5/2$), 6.8346826109 GHz for ^{87}Rb ($I = 3/5$), and 9.192631770 GHz (exact) for ^{133}Cs ($I = 7/2$) [53]. However, the 0–0 transition still has a small second-order dependence on the field B, which in practice is often used to calibrate the clock frequency against drift and other inaccuracies by adjusting the applied amplitude B

[14]. This applied field B is also used to isolate the 0–0 transition from the other, field-sensitive hyperfine transitions. In some cases, there are advantages to using other transitions, for example, in "end-resonance" clocks [44] or "lin‖lin" clocks [55], so vapor-cell clocks are by no means limited to using only the 0–0 transition.

As we discuss in later chapters, collisions with an inert buffer gas effectively lead to small changes in the alkali-metal atomic structure, such as a shift in the value of the magnetic-dipole coupling coefficient A. As a result, it is convenient to think of the mean values of quantities such as optical transition and hyperfine transition wavelengths as "thermodynamic" variables that depend on the buffer-gas pressure, temperature, and composition [21]. While these changes may be small, they are important to such high-precision optical pumping systems as atomic clocks.

2.1.2 Microwave-optical double resonance

Conventional vapor-cell clocks access the 0–0 transition for an ensemble of alkali-metal atoms in a vapor by using both light for optical pumping and microwaves for magnetic resonance, in a technique known as microwave-optical double resonance. This section expands on the description of this technique from Chapter 1.

Optical pumping is used to create a difference between the populations of alkali-metal atoms in the two ground-state sublevels forming the 0–0 transition, highlighted with the kets $|1\rangle$ and $|2\rangle$ in Fig. 2.1. This is usually done with either unpolarized lamp light or linearly polarized laser light, either of which propagate along the quantization axis defined by an applied field $\mathbf{B}$. Without this light, all the ground-state sublevels would have nearly equal populations, since the differences between the energies of these sublevels are much smaller than the mean thermal excitation energy in the vapor: $h\nu_{00} \approx 28$ μeV versus $3kT/2 \approx 40$ meV for ^{87}Rb, where k is the Boltzmann constant and a typical temperature $T \approx 40^\circ$ C. With this light, optical pumping can produce differences between the populations of the ground-state sublevels.

For example, consider linearly (π) polarized D1 light with an optical frequency that is tuned to be resonant, or nearly resonant, with transitions between the ground state and the lowest $P_{1/2}$ excited state, highlighted by the ket $|3\rangle$ in Fig. 2.1. For light propagating along the quantization axis, there are allowed electric-dipole σ-transitions between the ground-state sublevels $|F\,m\rangle$ and excited-state sublevels $|F'\,m'\rangle$ that satisfy the selection rules $m' - m = \pm 1$ and $F' - F = 0, \pm 1$. Absorption of light transfers atoms from the ground to the excited state, which, depending on the tuning of the light, depopulates some ground-state sublevels more than others. For a typical small applied field B in a clock, this depopulation is similar for all sublevels in the same hyperfine manifold, but may be different for the two manifolds. For example, for light tuned near the schematic transition $|1\rangle$–$|3\rangle$, the depopulation would be greater for lower manifold than the higher manifold. Atoms in the excited state quickly decay back to the ground-state, which, for the typical conditions in a clock, repopulates the different ground-state sublevels approximately equally, on average. Overall, this process is known as depopulation pumping. Because of buffer-gas collisions, which tend to depolarize the atoms in the excited state, there is no significant repopulation pumping, or transfer of polarization from the excited state to the ground state by spontaneous decay [19]. In the steady state, the pumping light produces nearly equal populations of sublevels in the same ground-state hyperfine manifold, but possibly different populations between the hyperfine manifolds, depending on the tuning. For example, for light tuned near the schematic transition $|1\rangle$–$|3\rangle$, there will be more population in the sublevel $|2\rangle$ than in $|1\rangle$, and for light tuned near $|2\rangle$–$|3\rangle$, more in $|1\rangle$ than $|2\rangle$. Buffer gas, typically a mixture of Ar and N_2, is used to improve the efficiency of this optical pumping by slowing the diffusion of atoms to the cell walls, where collisions tend to depolarize the atoms. The molecular gas N_2 also reduces (or quenches) the emission of resonant light by atoms decaying from the excited state, which otherwise could cause unwanted pumping.

Microwaves, in turn, are used to reduce the population difference between the states forming the 0–0 transition. This is usually done with standing waves in a resonant cavity or traveling waves from a horn antenna, either of which provide an oscillatory magnetic field along the quantization axis. The microwaves have allowed magnetic-dipole π-transitions between the ground-state sublevels with the same azimuthal quantum numbers m, for example, $|1\rangle$–$|2\rangle$. Absorption of these microwaves transfers atoms between the hyperfine manifolds, with a rate that depends on the field strength and the tuning of the microwave frequency. Without pumping light, the microwaves would not appreciably affect the atomic populations, since any transfer induced from the sublevel $|1\rangle$ to $|2\rangle$ would be counterbalanced by a transfer induced from $|2\rangle$ to $|1\rangle$. With pumping light, the initial population difference from optical pumping would allow an opposing, net transfer from the microwaves. In other words, the pumping light allows the vapor to absorb resonant microwaves. This absorption is strongest when the microwaves are resonant with a hyperfine transition, and in turn allows the vapor to absorb more light. In the steady state, the net effect on the populations is a balance between the effects of the pumping light and the microwaves. A fortunate consequence is that the transmission of the pumping light through the vapor may be used as a signal to determine when the microwaves are tuned to a hyperfine resonance. In practice, feedback may be used to tune the applied microwaves to the 0–0 transition, locking the microwave frequency to the 0–0 frequency, which may then be output as a frequency reference or clock signal. The details of this feedback will be discussed later in this chapter, starting with Section 2.2.

Of course, this qualitative discussion has greatly simplified the physics of actual vapor-cell clocks. It has also neglected other techniques used in vapor-cell clocks besides microwave-optical double resonance, for example, coherent population trapping (CPT). Later, in Section (2.4) we provide a more quantitative, two-level density-matrix model of a conventional vapor-cell clock. For additional information on vapor-

cell clocks, we recommend the book *The Quantum Physics of Atomic Frequency Standards* by Vanier and Audoin [11] and the review articles by Vanier [15] and Vanier and Mandache [16]. For detailed modeling of optical pumping and magnetic resonance, we recommend the book *Optically Pumped Atoms* by Happer, Jau, and Walker [21].

2.1.3 Light shifts

Most atomic clocks suffer light shifts from optical pumping light, so we review the features of the light shift relevant to this and later chapters here. For ground-state alkali-metal atoms, there are many different types of light shifts: scalar light shifts of the net (or center of mass) ground-state energy or the hyperfine structure, vector light shifts of the Zeeman structure, and additional tensor light shifts [24]. In addition to these AC Stark shifts due to the virtual absorption of light, there are also shifts from the real absorption of light, involving the transfer of coherence through the excited state and back, but these shifts are usually negligible for hyperfine transitions.

For conventional vapor-cell clocks, the phrase "light shift" specifically refers to the differential shift of the 0–0 hyperfine transition from pumping light [11, 14, 16]. This light shift is proportional to the intensity of the pumping light, but depends on the optical frequency of the light in a complicated manner. Fig. 2.2 is a sketch of this shift for ^{87}Rb with monochromatic D1 pumping light, as calculated by Mathur *et al.* [24] and discussed below. The most important point to notice is that there are zero crossings at certain optical frequencies that produce no light shift. These zero-shift frequencies or "magic wavelengths" are very close to the peaks of the D1 optical absorption line, and so may still be used for optical pumping. Therefore, a simple technique to suppress the light shift is to tune the pumping light to a zero-shift frequency. However, these zero-shift frequencies depend on the buffer-gas pressure, temperature, and composition, so feedback is required to lock the light to a zero-shift

frequency. The rest of this chapter describes a simple feedback method to implement this technique.

Since discussions of light shifts and the AC Stark effect are less common than those of similar effects from external fields (e.g., Zeeman effects from magnetic fields, or the DC Stark effect from static electric fields), we provide a short, approximate derivation of the light shift in a vapor-cell clock below. This derivation qualitatively explains the curves shown in Fig. 2.2. For additional information about the AC Stark effect, we recommend the book *Atomic Physics: An Exploration through Problems and Solutions* by Budker, Kimball, and DeMille [56], as well as related articles in the *American Journal of Physics* [57, 58, 59].

We may approximately derive the light shift in a conventional vapor-cell clock as follows. Following the discussion in Section 2.1.2, we consider only the two sublevels

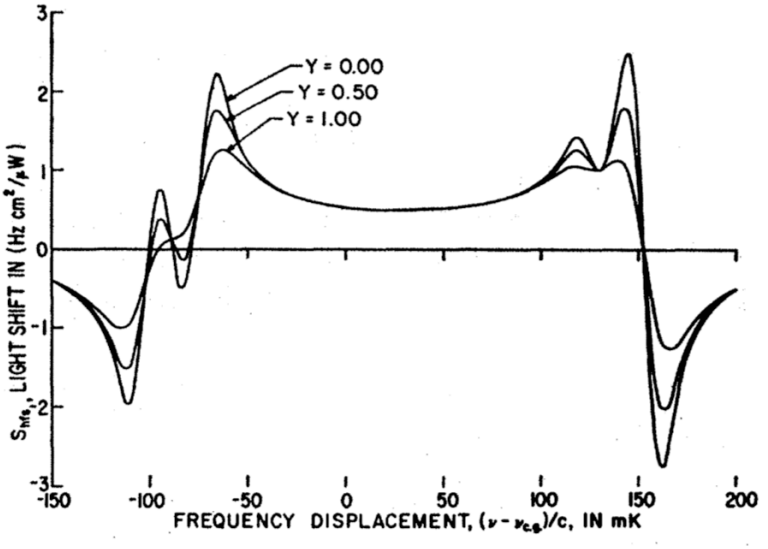

Figure 2.2: Calculated light shift for the 0–0 transition of ^{87}Rb with monochromatic 795 nm D1 pumping light from Mathur, Tang, and Happer [24]. Each curve is the shift divided by the light intensity for a different buffer-gas pressure, as parameterized by Y. The frequency displacement is in units of millikayser (1 mK $= 10^{-3}$ cm^{-1}), and the light frequency increases from left to right. The two zero-crossing regions correspond to pumping light tuned near transitions with the upper and lower hyperfine multiplets, respectively. Reprinted figure with permission from [24]. Copyright 1968 by the American Physical Society.

that form the 0–0 transition as well as the lowest $P_{1/2}$ excited state, highlighted by the kets $|1\rangle$, $|2\rangle$, and $|3\rangle$ in Fig. 2.1. We write a Hamiltonian for these states as

$$H = E_1|1\rangle\langle 1| + E_2|2\rangle\langle 2| + E_3|3\rangle\langle 3| + V(t), \tag{2.21}$$

where the interaction $V(t)$ of the alkali-metal atom with the pumping light will be treated as a perturbation. In the long-wavelength approximation, this interaction is

$$V(t) = -\mathbf{d} \cdot \mathbf{E}(t), \tag{2.22}$$

where $\mathbf{d}$ is the instantaneous dipole moment of the valence electron and $\mathbf{E}(t)$ is the electric field of the light. We consider monochromatic light with an angular frequency ω, such that the oscillating electric field $\mathbf{E}(t) = \mathbf{E}(0)\cos(\omega t)$.

In a vapor-cell clock, the optical pumping light will be in, or near resonance with both of the optical transitions $|1\rangle$–$|3\rangle$ and $|2\rangle$–$|3\rangle$. As a result, the light shift of the 0–0 microwave transition, $|1\rangle$–$|2\rangle$, will be equal to the difference between the shifts of these two optical transitions. To calculate the light shift, we will first calculate the shift of the $|2\rangle$–$|3\rangle$ transition, corresponding to the transition with the lower optical frequency (or the left side of Fig. 2.2). Define the (possibly complex) angular Rabi frequency

$$\Omega_{32} = \langle 3|\mathbf{d}|2\rangle \cdot \mathbf{E}(0)/\hbar, \tag{2.23}$$

which we assume to be non-zero. Ignoring the sublevel $|1\rangle$, we may rewrite the Hamiltonian (2.21) as

$$H_{32} = E_2|2\rangle\langle 2| + E_3|3\rangle\langle 3| - \hbar\cos(\omega t)\{\Omega_{32}|3\rangle\langle 2| + \Omega_{32}^*|2\rangle\langle 3|\}. \tag{2.24}$$

For simplicity, let $E_2 = 0$ and $E_3 = \hbar\omega_{32}$, where the Bohr frequency $\omega_{32} = (E_3 - E_2)/\hbar$. If we write a trial wave function $|\psi\rangle$ as a column vector

$$|\psi\rangle = c_2|2\rangle + c_3|3\rangle = \begin{pmatrix} c_2 \\ c_3 \end{pmatrix}, \tag{2.25}$$

then we may write the Hamiltonian (2.24) as

$$H_{32} = \hbar \begin{pmatrix} 0 & -\Omega_{32}^* \cos(\omega t) \\ -\Omega_{32} \cos(\omega t) & \omega_{32} \end{pmatrix}. \tag{2.26}$$

Since this Hamiltonian depends on time, the wave function evolves according to the time-dependent Schrödinger equation

$$i\hbar \frac{\partial}{\partial t}|\psi\rangle = H_{32}|\psi\rangle, \tag{2.27}$$

which we must solve in order to calculate the shift.

However, we may simplify the calculation by removing the time dependence of the Hamiltonian as follows. First, perform a unitary transformation into a rotating frame with the operator

$$U = \begin{pmatrix} 1 & 0 \\ 0 & e^{-i\omega t} \end{pmatrix}. \tag{2.28}$$

In the rotating frame, the time-dependent Schrödinger equation (2.26) becomes

$$i\hbar \frac{\partial}{\partial t}|\psi'\rangle = H'_{32}|\psi'\rangle, \tag{2.29}$$

where the transformed wave function is $|\psi'\rangle = U^\dagger|\psi\rangle$ and the transformed Hamiltonian is

$$H'_{32} = U^\dagger H_{32} U - i\hbar U^\dagger \frac{\partial U}{\partial t} = \hbar \begin{pmatrix} 0 & -\Omega_{32}^* \cos(\omega t) e^{-i\omega t} \\ -\Omega_{32} \cos(\omega t) e^{i\omega t} & \omega_{32} - \omega \end{pmatrix}. \tag{2.30}$$

Since the light is resonant, $\omega \approx \omega_{32}$, we may use the secular (or rotating-wave) approximation to drop the oscillatory terms with frequencies $\pm 2\omega$,

$$H'_{32} \approx \hbar \begin{pmatrix} 0 & -\Omega_{32}^*/2 \\ -\Omega_{32}/2 & -\delta_{32} \end{pmatrix}, \tag{2.31}$$

where we introduce a frequency detuning $\delta_{32} = \omega - \omega_{32}$ for the light.

Since the Hamiltonian (2.31) is time independent, we may solve for the effect of V as a time-independent perturbation. Up to second-order in $|\Omega_{32}|$, the two energy eigenvalues of H'_{32} are

$$E'_2 = 0 + \delta^2 E', \text{ and } E'_3 = -\hbar\,\delta_{32} - \delta^2 E', \tag{2.32}$$

where the second-order perturbation, or AC Stark shift, is

$$\delta^2 E' = \frac{|\langle 2'|V|3'\rangle|^2}{\hbar\,\delta_{32}} \approx \frac{\hbar|\Omega_{32}|^2}{4\,\delta_{32}}. \tag{2.33}$$

This symmetric shift, or splitting, of the energy eigenvalues by the AC Stark effect is analogous to a DC Stark effect in the rotating frame for the static electric field $\mathbf{E}(0)/2$. Since we neglected the finite linewidth Γ_{32} of the optical transition, the expression (2.33) is not applicable near resonance, $\delta_{32} \approx 0$, where it diverges. However, we may use a trick to include this linewidth [56]. If we substitute $\omega_{32} \to \omega_{32} - i\Gamma_{32}$, or

equivalently $E_3 \to E_3 - i\hbar\Gamma_{32}$, then the expression (2.33) becomes

$$\delta^2 E' = \frac{\hbar|\Omega_{32}|^2}{4}\,\mathrm{Re}\left[\frac{1}{\delta_{32} - i\Gamma_{32}}\right] = \frac{\hbar|\Omega_{32}|^2}{4}\left(\frac{\delta_{32}}{\delta_{32}^2 + \Gamma_{32}^2}\right). \tag{2.34}$$

For a narrow linewidth, this expression is a good approximation of the result of a more detailed calculation (e.g., Problem 2.7(e) in Ref. [56]). This substitution trick to include the linewidth is not rigorous, and makes the Hamiltonian (2.31) non-Hermitian. It only works in some cases, such as this one. In general, relaxation effects should be included using a density-matrix approach.

Finally, we need to connect the rotating-frame shifts (2.34) to the optical transition $|2\rangle$–$|3\rangle$. Without light, $\Omega_{32} = 0$, the two unshifted energies in the rotating frame are $E_2' = 0$ and $E_3' = -\hbar\,\delta_{32}$, which can be though of as dressed-state energies. The constant difference between these unshifted rotating-frame energies and those in the lab frame, E_2 and E_3, is just a result of the unitary transformation, and are not part of the light shift. As a result, the shift of the Bohr frequency in either frame is

$$\delta\omega_{32} = -\frac{|\Omega_{32}|^2}{2}\left(\frac{\delta_{32}}{\delta_{32}^2 + \Gamma_{32}^2}\right), \tag{2.35}$$

which has a dispersive shape about resonance, $\delta_{32} = \omega - \omega_{32} = 0$, similar to the right side of Fig. 2.2. Note that this shift can be of either sign, depending on the detuning δ_{32}. Though a second-order time-independent perturbation of a two-level system always leads to an positive shift of the transition energy, we had a second-order perturbation in a rotating frame. The sign of the detuning δ_{32} controls which of the two unshifted rotating-frame energies E_2' and E_3' is largest, and so allows the shift $\delta\omega_{32}$ to be of either sign in the lab frame.

If we repeated our analysis for the transition $|1\rangle$–$|3\rangle$, we would find a shift analogous to (2.35),

$$\delta\omega_{31} = -\frac{|\Omega_{31}|^2}{2}\left(\frac{\delta_{31}}{\delta_{31}^2+\Gamma_{31}^2}\right), \tag{2.36}$$

with Rabi frequency Ω_{31}, linewidth Γ_{31}, and detuning $\delta_{31} = \omega - \omega_{31}$. Using (2.36) and (2.35), the light shift of the 0–0 transition with Bohr frequency $\omega_{21} = 2\pi\nu_{00}$ is

$$\delta\omega_{21} = \delta\omega_{31} - \delta\omega_{32} = \frac{|\Omega_{32}|^2}{2}\left(\frac{\omega-\omega_{32}}{(\omega-\omega_{32})^2+\Gamma_{32}^2}\right) - \frac{|\Omega_{31}|^2}{2}\left(\frac{\omega-\omega_{31}}{(\omega-\omega_{31})^2+\Gamma_{31}^2}\right). \tag{2.37}$$

Since the quantities $|\Omega_{32}|^2$ and $|\Omega_{31}|^2$ are proportional to the light intensity, the light shift is also. Noting that the two optical transitions are offset by the 0–0 transition, $\omega_{32}-\omega_{31} = \omega_{21}$, we see that the shift (2.37) qualitatively reproduces the curves shown in Fig. 2.2, whose overall shapes are the differences between two offset dispersive curves. The extra features in the figure are due to the hyperfine structure of the excited state, which we neglected. By inspection of (2.37), we see that the light shift is zero for laser frequencies ω that satisfy $\delta\omega_{31} = \delta\omega_{32}$. For the light shift (2.37), there are two zero-shift frequencies, corresponding to ω slightly less than the smaller optical transition ω_{32} or slightly more than the larger ω_{31}. Since collisions with the buffer gas perturb the transition linewidths and Bohr frequencies of each alkali-metal atom, these zero-shift frequencies are not fixed, but depend on the buffer-gas pressure, temperature, and composition.

2.2 Quadrature error signal in vapor-cell clocks

In conventional atomic clocks, the microwave field is frequency modulated (FM) at a relatively low rate, typically less than 1 kHz. If the microwave carrier frequency is

slightly higher than the atomic resonant frequency, the intensity of the pumping light emerging from the vapor will be modulated at the 1st harmonic of the FM rate. If the carrier frequency is slightly lower, the 1st harmonic component will reverse sign. Only if the carrier frequency is at exact resonance (the "zero-crossing frequency") will there be no 1st harmonic modulation in the intensity. The 1st harmonic component (the signal) is normally detected synchronously with a lock-in amplifier and used as an error signal to lock the microwave carrier frequency (the local oscillator) to the center of the atomic resonance line. Fig. 2.3 is a sketch of this feedback loop.

Superficially, it would seem that the phase adjustment of the lock-in amplifier would not be critical. However, we were surprised to find that there were often different zero-crossing frequencies for the in-phase and out-of-phase (quadrature) channels of the lock-in amplifier, as shown in Fig. 2.4. We eventually found that if the laser was tuned to a zero-shift frequency, the microwave zero-crossing frequency was in-

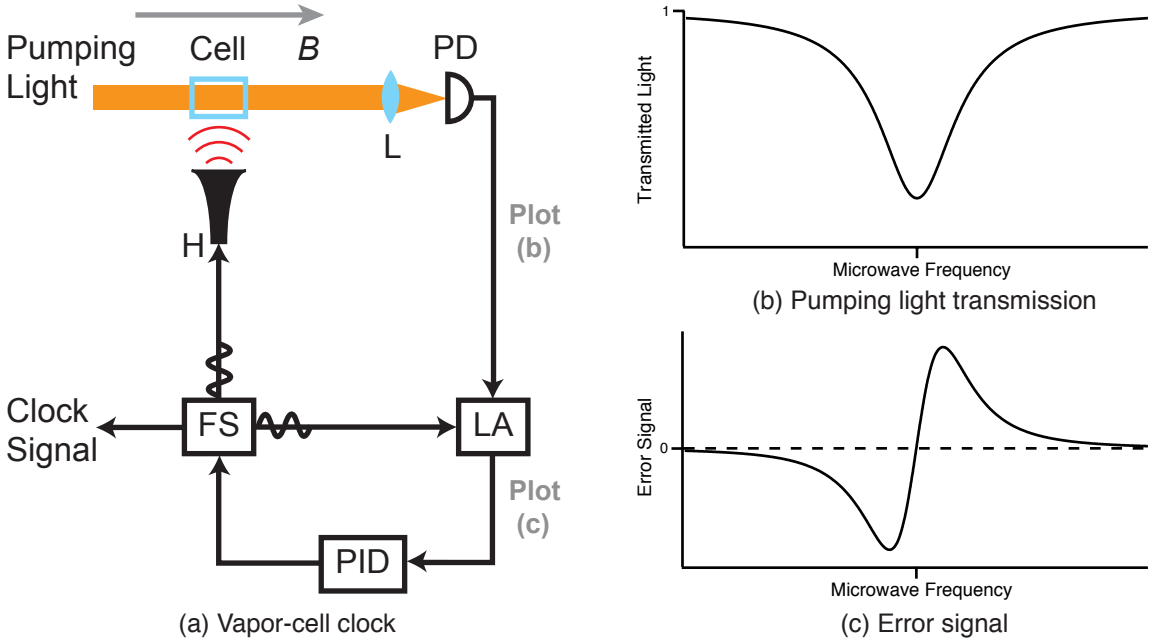

Figure 2.3: Feedback loop in a conventional vapor-cell clock that uses frequency modulation to lock the microwave carrier to an atomic resonance. B, applied magnetic field; L, lens; PD, photodetector; LA, lock-in amplifier; PID, proportional-integral-derivative (PID) controller; FS, frequency synthesizer; H, horn.

dependent of the lock-in amplifier phase. This is the phenomenon that is used for the laser stabilization method described here. We use the in-phase and quadrature channels from the synchronous detector of a single feedback loop as two independent error signals to lock the local oscillator and suppress the light shift.

The density of atomic vapor used in atomic clocks is normally adjusted to attenuate the laser beam by a factor of about $1/e$. This means that any light shift will be greater where the beam enters the cell than where it exits. A spatial beam profile will have a similar effect. Without a light shift, the entire cell will share a zero-crossing frequency. However, with a light shift, such light-intensity gradients will lead to regions in the cell with different light shifts and different homogenous broadening, as depicted in Fig. 2.4. For stronger light intensities than typical in clocks, this leads to the inhomogenous light shift [60].

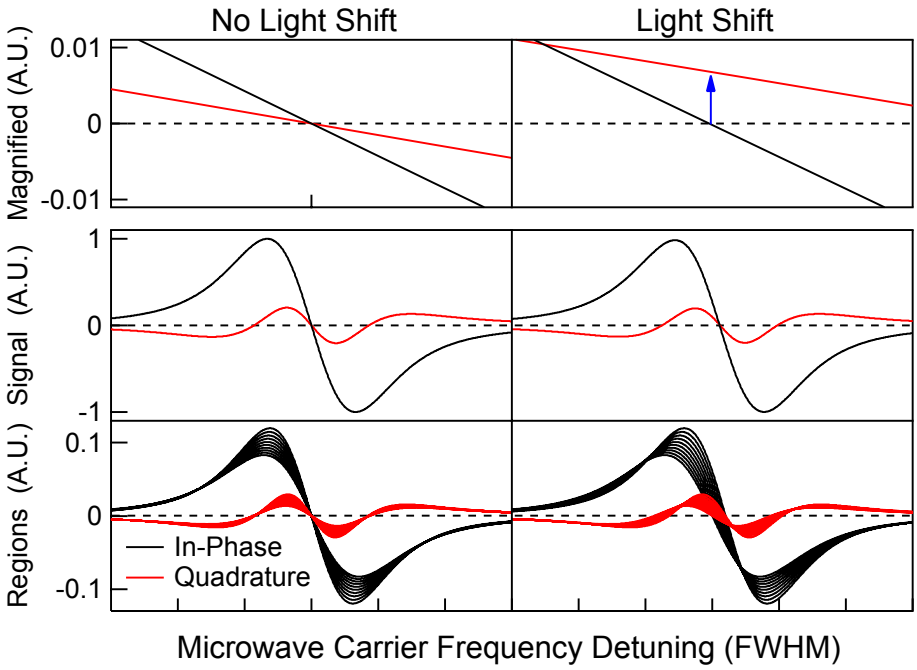

Figure 2.4: Modeling of lock-in channels versus microwave carrier frequency, where the in-phase channel is optimized as the microwave error signal. An array representing the different regions in a cell with a light-intensity gradient is combined to obtain the total signal. The top panel shows the zero-crossing region of the middle panel, with both axes magnified. The arrow indicates the quadrature channel output at the in-phase channel zero-crossing. See Section 2.4 for modeling detail.

The phase response of the signal from each cell region depends on the linewidth (Γ), the carrier detuning, and the FM parameters, such as the modulation rate (ω_{m}) and index. When there is a light shift, the different cell regions will not only have different detunings, but will also experience different effective FM rates ($\omega_{\mathrm{m}}/\Gamma$) due to intensity broadening from the pumping light. Hence, there is significant phase variation in the signals from each region. As a result, when there is a light shift, the total signal amplitude will not vanish for any carrier frequency, or in other words, there will be no choice of carrier for which both lock-in channels vanish. When the in-phase channel is used to lock the local oscillator, the quadrature channel is proportional to the light shift near a zero-shift frequency. Therefore the quadrature channel may be used as an error signal to lock the pumping light to a zero-shift frequency. This is the origin of the phenomenon outlined above, which makes it possible to both lock the local oscillator and suppress the light shift with a single feedback loop. The method is sensitive to the choice of FM parameters and works best if the cell is not optically thin.

2.2.1 Semi-quantitative model

A relatively simple and semi-quantitative way to explain this phenomenon is as follows. Suppose that the signal input to the lock-in amplifier from a particular spatial region of the vapor-cell has the form

$$S_1(\omega) = A(\omega - \omega_1)e^{i(\omega_{\mathrm{m}}t+\phi_1)}, \tag{2.38}$$

where ω is the (angular) microwave carrier frequency, ω_1 is the resonant frequency for the particular region in the cell, ω_{m} is the microwave FM rate, and ϕ_1 is the phase response of the signal with respect to the microwave modulation. Let the amplitude $A(\omega)$ be a real-valued function with the shape of the error signal sketched

in Fig. 2.3(c), and with a zero-crossing at $A(0) = 0$. Lock-in detection of the signal S_1 at the frequency $\omega_{\rm m}$ and phase $\phi_0 = \phi_1$ gives the following X and Y channel outputs:

$$X(\omega) = \mathrm{Re}[S_1(\omega)e^{-i(\omega_{\rm m}t+\phi_0)}] = A(\omega - \omega_1), \tag{2.39}$$

$$Y(\omega) = \mathrm{Im}[S_1(\omega)e^{-i(\omega_{\rm m}t+\phi_0)}] = 0. \tag{2.40}$$

We see that this particular choice of the lock-in phase ϕ_0 produces a quadrature channel Y that is always zero, and an in-phase channel X that is an error signal. Here, the microwave feedback loop would lock the carrier frequency ω to the resonant frequency ω_1, such that both channels are zero, $X(\omega_1) = Y(\omega_1) = 0$.

Now suppose that the lock-in measures a total signal $S = S_1 + S_2$, where the additional signal

$$S_2(\omega) = A(\omega - \omega_2)e^{i(\omega_{\rm m}t+\phi_2)} \tag{2.41}$$

is from a different spatial region of the cell. Let the signal S_2 have a slightly different resonant frequency ω_2 and phase response ϕ_2 than S_1, because of a slight difference in light shift and intensity broadening, respectively, between the two cell regions. Denote these small differences as $\delta\omega = \omega_2 - \omega_1$ and $\delta\phi = \phi_2 - \phi_1$. Then the lock-in signals become

$$X(\omega) = \mathrm{Re}[Se^{-i(\omega_{\rm m}t+\phi_0)}] = A(\omega - \omega_1) + A(\omega - \omega_2)\cos(\delta\phi), \tag{2.42}$$

$$Y(\omega) = \mathrm{Im}[Se^{-i(\omega_{\rm m}t+\phi_0)}] = A(\omega - \omega_2)\sin(\delta\phi). \tag{2.43}$$

Since we assume a small $\delta\phi$, we can approximate $\cos(\delta\phi) \approx 1$ and $\sin(\delta\phi) \approx \delta\phi$. Noting that the error signal amplitude sketched in Fig. 2.3(c) is an odd function, $A(-\omega) = -A(\omega)$, we see that if the in-phase channel X provides the microwave error signal, then the feedback will lock the carrier ω to the weighted average $\overline{\omega} =$

$(\omega_1 + \omega_2)/2$. With ω locked to $\overline{\omega}$ by feedback, the lock-in channels become

$$X(\overline{\omega}) \approx 0, \tag{2.44}$$

$$Y(\overline{\omega}) \approx \delta\phi\, A(\delta\omega/2). \tag{2.45}$$

In contrast to before, the quadrature channel Y is no longer zero when the microwave carrier is locked. Instead, it is proportional to an error signal $A(\delta\omega/2)$ for the light shift, which is responsible for the resonant frequency difference $\delta\omega$ between the different spatial regions. As shown, the microwave feedback loop is unable to make the total error-signal amplitude $R = \sqrt{X^2 + Y^2}$ go to zero, and only suppresses a particular projection, X, while pushing the remaining, non-vanishing amplitude R into the other, quadrature channel Y. Note that the critical factor of $\delta\phi$ in (2.45) is due to the inhomogeneous broadening from the different light intensities in the two spatial regions for S_1 and S_2, and that without this phase-response difference $\delta\phi$, the quadrature error signal (2.45) would be zero, even with a light shift.

2.3 Experiment

A comparison of the "quadrature" method with the conventional, intensity-modulation method to suppress the light shift in a laser-pumped, vapor-cell atomic clock is sketched in Fig. 2.5. Both methods use two different error signals to lock the local oscillator and to tune the laser to the zero-shift frequency. Both measure the light-field-independent, ground-state 0–0 hyperfine resonant frequency of ^{87}Rb atoms to about 1 Hz.

Alternating between the two configurations allowed direct comparison between both methods in the same setup. The experimental setup closely follows the description in Refs. [39] and [40]. For computerized control and measurement with National Instruments NI-DAQ, GPIB, and serial (RS-232) communication, we used IGOR Pro

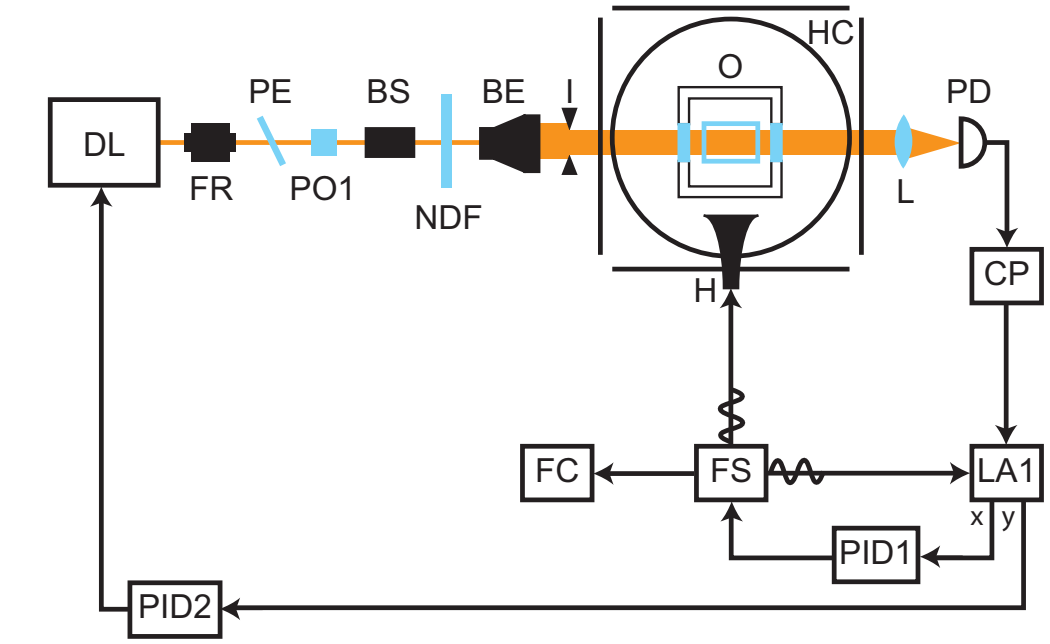

(a) Quadrature method

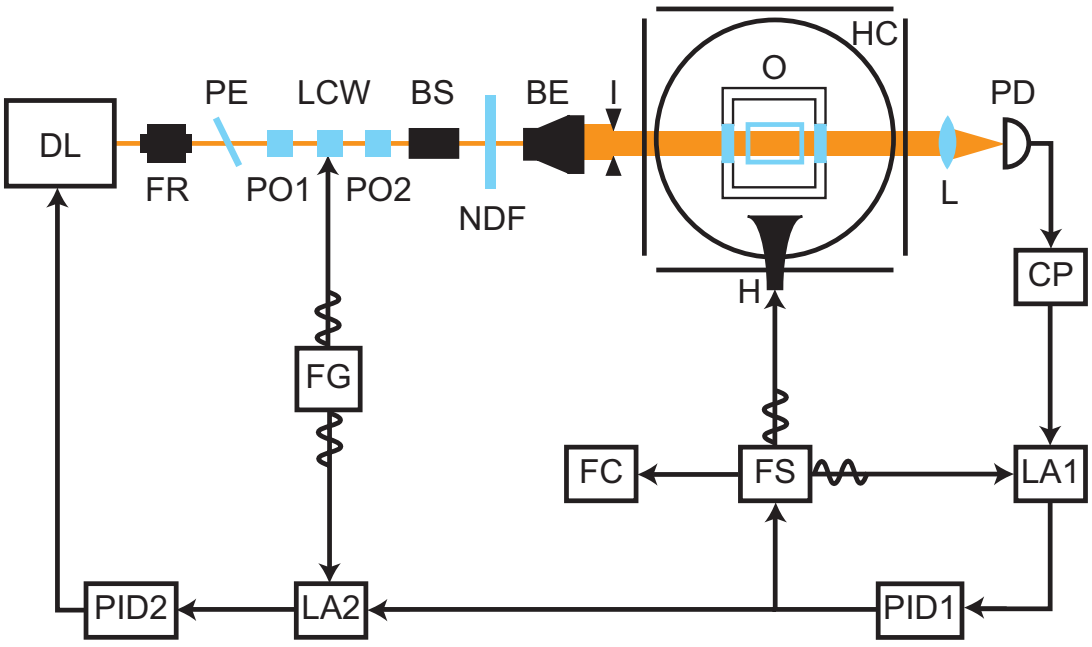

(b) Intensity-modulation method

Figure 2.5: Experimental setups with different light-shift suppression methods. DL, diode laser; FR, Faraday rotator; PE, pellicle; PO, polarizer; LCW, liquid crystal wave plate; BS, beam shaper; NDF, neutral density filter; BE, beam expander; I, iris; O, oven; H, horn; HC, Helmholtz coils; L, lens; PD, photodetector; CP, current preamplifier; LA, lock-in amplifier; PID, PID controller; FS, frequency synthesizer; FC, frequency counter; FG, function generator.

[61] with customized code for data acquisition and management [62, 63]. The vapor cell is a cylindrical Pyrex cell, 17 mm in diameter and 25 mm long, filled with a small amount of ^{87}Rb metal. An external buffer-gas reservoir, pressure gauge, and vacuum port permit convenient changes of the buffer-gas species and pressure. An air-heated, non-magnetic oven (O) holds the cell at constant temperature between 35–65°C. The temperature of the cell controlled the equilibrium number density of the vapor of ^{87}Rb atoms produced by the small amount of ^{87}Rb metal in the cell. Helmholtz coils (HC) cancel ambient fields and provide a static longitudinal field B of about 0.2 G. A Toptica DL 100 diode laser (DL) provides 795 nm D1 optical pumping light for ^{87}Rb. A Faraday rotator (FR) isolates the laser from back-reflected light. A pellicle (PE) skims off light for analysis with a wavemeter and a Fabry–Pérot interferometer (not shown). Polarizers (PO) ensure that the pumping light is linearly polarized. When included, a liquid crystal wave plate (LCW, Meadowlark Optics LVR-200-IR1) driven by a function generator (FG) provides about 30% intensity modulation of the pumping light at a rate of 2 Hz. A beam shaper (BS), a beam expander (BE), and an iris (I) ensure that the pumping light fills the cell uniformly. A rotatable neutral density filter (NDF) adjusts the pumping beam intensity. A lens (L) collects the transmitted pumping light onto a photodetector (PD). Microwaves from a frequency synthesizer (FS, Agilent Technologies E8257C) are transmitted towards the cell by a horn (H, Narda Microwave-East Standard Gain Horn 642) roughly 10 cm away to drive magnetic resonances. A frequency counter (FC, Agilent Technologies 53150A) referenced to a rubidium frequency standard (not shown, Stanford Research Systems FS725) measures the microwave frequency. The microwaves are frequency modulated at a rate of roughly 100–500 Hz with a modulation index of about 1. A lock-in amplifier (LA1, Stanford Research Systems SR830) with a 10–300 ms time constant provides an error signal for a proportional-integral-derivative (PID) controller (PID1,

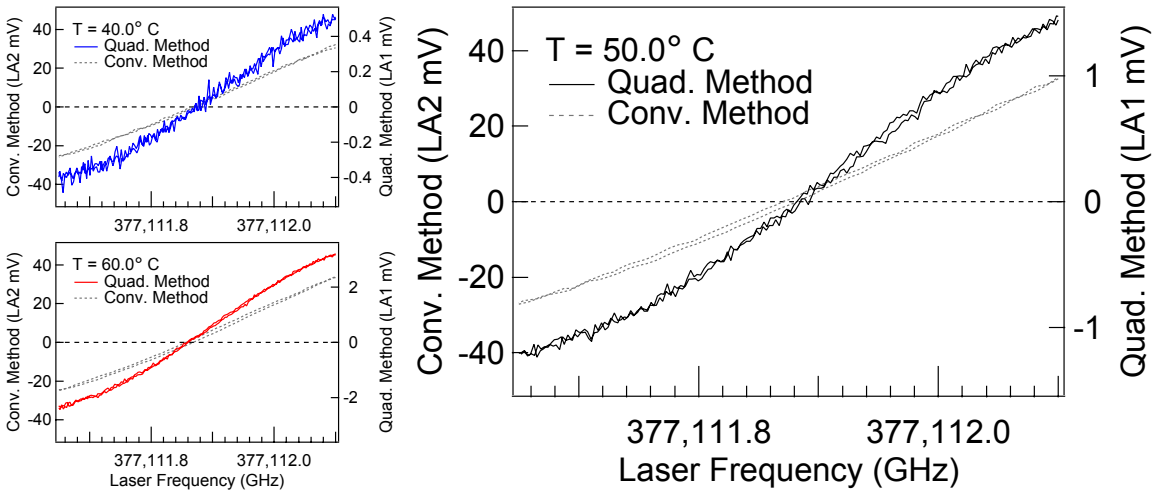

Figure 2.6: Comparison of laser frequency error signals illustrating that the quadrature method locks to the same frequency as the conventional method, which is a zero-shift frequency. The signal-to-noise ratio of the quadrature method improved at higher temperatures due to increased cell optical thickness.

Stanford Research Systems SIM960) to lock the microwave carrier frequency to the atomic resonance.

For implementation of the quadrature method (Fig. 2.5(a)), the quadrature channel of LA1 provides an error signal for a PID controller (PID2, Stanford Research Systems SIM960) to lock the laser to a zero-shift frequency. For implementation of the conventional method (Fig. 2.5(b)), a second lock-in amplifier (LA2, Stanford Research Systems SR530) provides the error signal for PID2 by detecting modulation in the first feedback loop control signal due to intensity modulation from the LCW. Feedback adjusts the laser frequency through a piezoactuator. As a quick test for light-shift suppression, we used the NDF filter to temporarily adjust the laser intensity by a factor of 2–4 to verify intensity-independence of the clock output.

To verify that the quadrature method locks the laser to a zero-shift frequency, we measured the error signals from both methods as a function of the laser frequency. Here, the cell was filled with 30.0 Torr of N_2 (at 50.0°C). The error signals for both methods were recorded separately with sweeps in both directions, using a wavemeter to record the laser frequency to a precision of 0.01 GHz. Fig. 2.6 shows the results

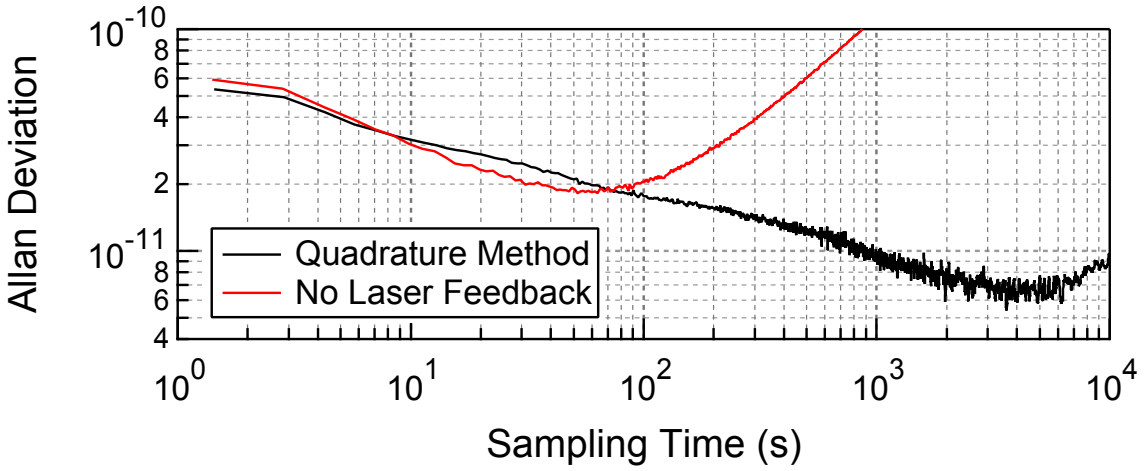

Figure 2.7: Comparison of clock frequency stability with and without the quadrature method of light-shift suppression.

at 40.0°C, 50.0°C, and 60.0°C, which demonstrate that both methods share the same zero-crossing frequency to within experimental error. Therefore both methods lock to the zero-shift frequency. The data also illustrate how higher temperatures improve the signal-to-noise ratio for the quadrature method, which results from increased cell optical thickness.

We measured the clock performance both with and without the quadrature method engaged. For these tests we used a 27.1 Torr buffer-gas mixture of N_2 and Ar at 52.6°C, manually optimized for zero-pressure shift as described in Chapter 5, since we were able to control temperature much better than pressure. Fig. 2.7 shows the Allan deviation for the data [64]. The clock stability is significantly improved with the quadrature method compared to a free-run system without laser feedback and light-shift suppression. Unfortunately, limitations in our setup prevented a comparison of the quadrature and the conventional methods. In the short-term, the measured stability was limited by the 1 Hz precision of the frequency counter. In the long-term, we think the measured stability was limited by fluctuations in the buffer-gas pressure due to our cell design, which is shown in Fig. 4.10 of Chapter 4.

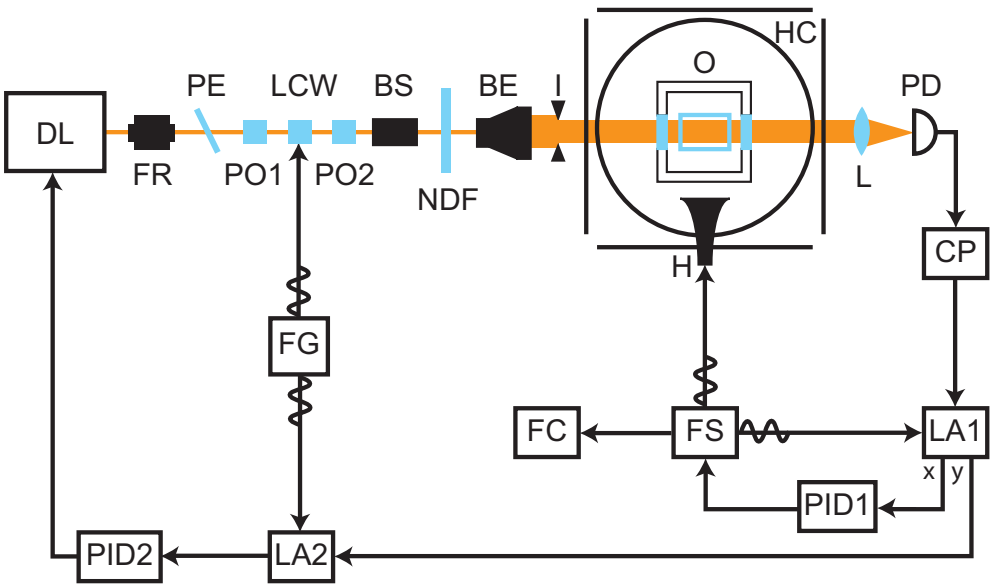

Figure 2.8: Alternate implementation of light-shift suppression method. DL, diode laser; FR, Faraday rotator; PE, pellicle; PO, polarizer; LCW, liquid crystal wave plate; BS, beam shaper; NDF, neutral density filter; BE, beam expander; I, iris; O, oven; H, horn; HC, Helmholtz coils; L, lens; PD, photodetector; CP, current preamplifier; LA, lock-in amplifier; PID, PID controller; FS, frequency synthesizer; FC, frequency counter; FG, function generator.

While for both methods the response speed of PID2 is limited below that of PID1, in principle this speed may be faster for the quadrature method than for the conventional due to the single-modulation scheme. The quadrature method may also be implemented with the configuration of Fig. 2.5(b) altered to use the quadrature channel of LA1 as the input to LA2, as sketched in Fig. 2.8. However, this version sacrifices the original simplicity, and in practice may mix error signals from both methods shown in Fig. 2.5.

2.4 Modeling

We modeled this phenomenon in two numerical simulations described below: two-level systems (2LSs) and damped linear harmonic oscillators (DLHOs). Both simulations combined an array representative of several regions in a cell with different light shifts

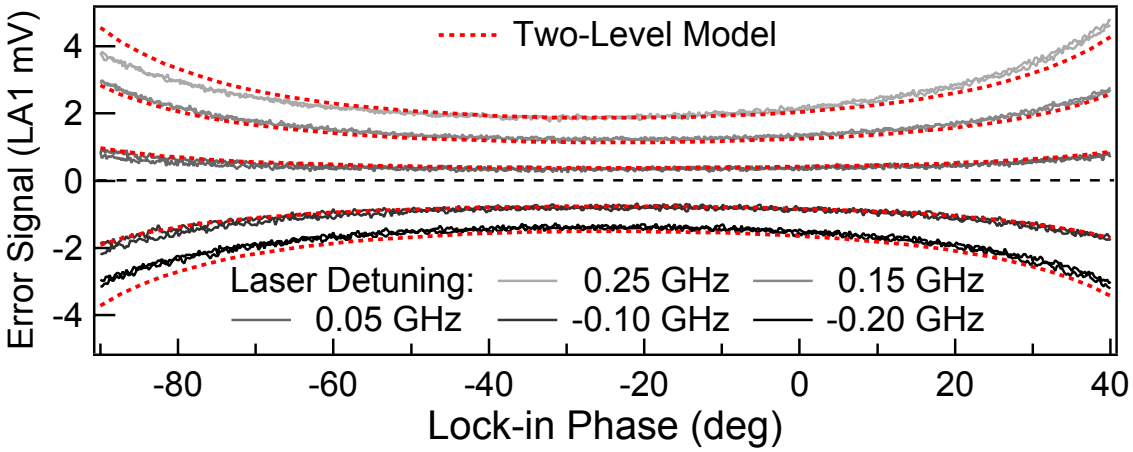

Figure 2.9: Quadrature channel error signals for experiment and modeling versus lock-in phase, with the local oscillator locked. The different curves denote different fixed laser detunings from the zero-shift frequency. The data are for 30.0 Torr N_2 at 50.0°C. See Section 2.4 for modeling detail.

and inhomogeneous broadening due to a light-intensity gradient. This is shown with the two-level simulation in Fig. 2.4. Both simulations agree qualitatively with experimental tests. In particular, both experiment and modeling show that the selection of lock-in phase is not critical for the quadrature error signal, as shown in Fig. 2.9, where the different curves represent different laser detuning from a zero-shift frequency. Additionally, both experiment and modeling reveal that the quadrature error signal changes sign with increased frequency modulation (FM) amplitude. Modeling also indicates that the quadrature error signal is affected by non-light-shift resonant frequency gradients in the cell, such as a temperature or magnetic-field gradient.

What follows are the details of these two simulations. Following the notation of Section 2.2.1, let $S(\omega)$ be the signal input to the lock-in for a fixed microwave carrier frequency ω. Lock-in detection at the FM rate ω_{m} and detector phase ϕ_0 gives the following lock-in channels

$$X(\omega) = \mathrm{Re}[S(\omega)e^{-i(\omega_{\mathrm{m}}t+\phi_0)}] = \mathrm{Re}[\widetilde{S}_1(\omega)e^{-i\phi_0}], \tag{2.46}$$

$$Y(\omega) = \mathrm{Im}[S(\omega)e^{-i(\omega_{\mathrm{m}}t+\phi_0)}] = \mathrm{Im}[\widetilde{S}_1(\omega)e^{-i\phi_0}], \tag{2.47}$$

where we have introduces the (complex-valued) first-harmonic component $\widetilde{S}_1(\omega)$ of $S(\omega)$. As we show below, we may write this component as

$$\widetilde{S}_1(\omega) = \sum_{n=0}^{\infty} J_n(m) J_{n+1}(m) C_n(\omega, \omega_{\mathrm{m}}), \tag{2.48}$$

where the J_n are Bessel functions of the first kind, and ω_{m} and m are the FM rate and index, respectively. The complex-valued coefficients $C_n(\omega, \omega_{\mathrm{m}})$ depend on the particular simulation and will be determined below.

The first-harmonic component $\widetilde{S}_1(\omega)$ is the error-signal amplitude measured by the lock-in, and its shape depends on the FM index m and rate ω_{m}. The index m determines the weight $J_n(m)J_{n+1}(m)$ of each n-th component $C_n(\omega, \omega_{\mathrm{m}})$, and the shapes of these components versus ω depends on the rate ω_{m}. For weak modulation, corresponding to an index $m \ll 1$, only the $n = 0$ term contributes. For slow modulation, corresponding to a rate ω_{m} much smaller than the microwave linewidth Γ, the shape of the component $C_0(\omega, \omega_{\mathrm{m}})$ versus ω is very much like the error signal sketched in Fig. 2.3(c). However, the phase of this and the other components are not constant with ω, and so the error signal cannot be adjusted into a single lock-in channel, as in Fig. 2.3(c), but will have projections in both the X and Y channels, as in Fig. 2.4. In practice, the error signal is optimized for an index $m \approx 1$, which maximizes the weight $J_0(m)J_1(m)$, and a rate ω_{m} a little less than half of the full-width-at-half-maximum (FWHM) Γ of the microwave line, $\omega_{\mathrm{m}} \lesssim \Gamma/2$. Larger values of the index m or rate ω_{m} lead to distortion of the error signal shape away from that desired for optimal feedback.

2.4.1 Damped linear harmonic oscillators

First, we derive the components $C_n(\omega, \omega_{\mathrm{m}})$ for the DHLO simulation. This model provides qualitatively similar error signals, and has a shorter derivation than the 2LS

model. It also shows that the quadrature error signal is not just an atomic clock phenomenon.

Consider a function $y(t)$ that describes the amplitude of a linear harmonic oscillator. Let $y(t)$ evolve according to

$$\frac{d^2y}{dt^2} + \Gamma\frac{dy}{dt} + \omega_0^2 y = F(t), \tag{2.49}$$

where ω_0 is a natural (undamped) resonant frequency, Γ is a damping coefficient, and $F(t)$ is a periodic driving force. For a single oscillator, corresponding to a single spatial region in our cell, the intensity $|y(t)|^2$ plays the role of our detected signal $S(\omega)$. The driving force $F(t)$ plays the role of the microwave magnetic field, which we take here to have unity amplitude.

We may write the time dependence of the microwave magnetic field as

$$F(t) = \cos[\omega t + \phi(t)], \tag{2.50}$$

where ω is the (angular) carrier frequency. For frequency modulation with rate ω_{m} and index m, we may choose to write the time-dependent phase as

$$\phi(t) = \int_{-\infty}^{t} \Delta\omega \cos(\omega_{\mathrm{m}} t')dt' = m\sin(\omega_{\mathrm{m}} t), \tag{2.51}$$

where $\Delta\omega = m\,\omega_{\mathrm{m}}$ is the modulation amplitude, and we chose $\phi(0) = 0$ such that $F(0) = 1$. Using the relation [65]

$$e^{im\sin(\omega t)} = \sum_{n=-\infty}^{\infty} J_n(m)e^{in\omega t}, \tag{2.52}$$

we may rewrite the function $F(t)$ as the sum

$$F(t) = \sum_{n=-\infty}^{\infty} J_n(m)\cos(\omega_n t) = \mathrm{Re}\sum_{n=-\infty}^{\infty} J_n(m)e^{i\omega_n t}, \tag{2.53}$$

where we introduced the shorthand

$$\omega_n = \omega + n\omega_{\mathrm{m}} \tag{2.54}$$

for the n-th sideband frequency. We see that FM leads to a superposition of continuous oscillations at the sideband frequencies ω_n in the function $F(t)$.

In the steady state, the amplitude $y(t)$ will be entirely due to the driving force $F(t)$. For a trial driving force

$$F_{\mathrm{trial}}(t) = e^{s_n t}, \tag{2.55}$$

we see by inspection that the inhomogenous (or particular) solution of (2.49) is

$$y_{\mathrm{trial}}(t) = H_1(s_n)e^{s_n t}, \tag{2.56}$$

where we introduced the function

$$H_1(s) = \frac{1}{\omega_0^2 + s^2 + s\Gamma}. \tag{2.57}$$

Since the driving force $F(t)$ of (2.53) is a sum of terms proportional to the trial force (2.55), we see that the steady-state solution of (2.49) for the $F(t)$ of (2.53) is

$$y(t) = \mathrm{Re}\sum_{n=-\infty}^{\infty} J_n(m)H_1(i\omega_n)e^{i\omega_n t}. \tag{2.58}$$

Before we continue, we note that the function $H_1(s)$ of (2.57) is known as a transfer function, and is equal to the ratio of the steady-state solution to the driving force in the Laplace domain [66]. This is clear if we introduce the Laplace transform $\mathcal{L}\{g(t)\}$ of an arbitrary function $g(t)$,

$$\mathcal{L}\{g(t)\} = \int_0^\infty e^{-st} g(t) dt. \tag{2.59}$$

Using integration by parts, the Laplace transform of (2.49) is the algebraic equation

$$\frac{\mathcal{L}\{y(t)\}}{H_1(s)} - \frac{dy(0)}{dt} - (s+\Gamma)y(0) = \mathcal{L}\{F(t)\}. \tag{2.60}$$

To obtain the steady-state solution, we can ignore the initial conditions $y(0)$ and $dy(0)/dt$, which lead to a transient, homogeneous solution that decays over time. We then see from (2.60) that the ratio of the steady-state solution to the driving force is the transfer function (2.57),

$$H_1(s) = \frac{\mathcal{L}\{y(t)\}}{\mathcal{L}\{F(t)\}}. \tag{2.61}$$

In the temporal domain, the steady-state solution $y(t)$ is given by an inverse Laplace transform,

$$y(t) = \mathcal{L}^{-1}\{H_1(s)\mathcal{L}\{F(t)\}\} = \frac{1}{2\pi i}\int_{\gamma-i\infty}^{\gamma+i\infty} e^{st} H_1(s)\mathcal{L}\{F(t)\} dt, \tag{2.62}$$

where γ is a real number that is greater than the real part of all singularities of the integrand [65]. A convenient property of the trial driving force $F_{\text{trial}}(t)$ of (2.55), which has the Laplace transform

$$\mathcal{L}\{F_{\text{trial}}(t)\} = \frac{1}{s - s_n}, \tag{2.63}$$

is that the transfer function is also equal to the ratio of the steady-state solution to the driving force in the time domain, as shown by (2.56). This is clear if we use (2.62) with (2.63) and Cauchy's residue theorem. Noting that the two residues from the transfer function (2.57) cancel, we recover the trial solution (2.56).

Using the steady-state solution (2.58) with the relation $\mathrm{Re}[z]^2 = |z|^2/2 + z^2 + (z^*)^2$, and neglecting terms with the frequencies $\pm 2\omega_\mathrm{m}$, the (real-valued) signal $S(\omega) = |y(t)|^2$ for a single oscillator is

$$\begin{aligned} S(\omega) &\approx \frac{1}{2}\left|\sum_{n=-\infty}^{\infty} J_n(m) H_1(i\omega_n) e^{i\omega_n t}\right|^2 \\ &= \frac{1}{2}\sum_{n=-\infty}^{\infty}\sum_{k=-\infty}^{\infty} J_n(m) H_1(i\omega_n) J_k(m) H_1^*(i\omega_k) e^{i(\omega_n-\omega_k)t}. \end{aligned} \tag{2.64}$$

The first-harmonic component $\widetilde{S}_1(\omega)$ oscillating at the FM rate ω_m comes from the nearest-neighbor terms with $|n-k| = 1$. Neglecting the other harmonics, we may write the (real-valued) first-harmonic signal as

$$S_1(\omega) = \mathrm{Re}\sum_{n=-\infty}^{\infty} J_n(m) J_{n+1}(m) H_1^*(i\omega_n) H_1(i\omega_{n+1}) e^{i\omega_\mathrm{m} t}. \tag{2.65}$$

The corresponding, complex-valued first-harmonic component $\widetilde{S}_1(\omega)$ that satisfies

$$S_1(\omega) = \mathrm{Re}\left[\widetilde{S}_1(\omega) e^{i\omega_\mathrm{m} t}\right] \tag{2.66}$$

and gives the same lock-in channels (2.46) and (2.47) as the real-valued $S_1(\omega)$ is

$$\widetilde{S}_1(\omega) = \sum_{n=-\infty}^{\infty} J_n(m) J_{n+1}(m) H_1^*(i\omega_n) H_1(i\omega_{n+1}). \tag{2.67}$$

Using the relation $J_{-n}(m) = (-1)^n J_n(m)$ [65], we find that the error-signal components of (2.48) are

$$C_n^{\mathrm{DLHO}}(\omega, \omega_{\mathrm{m}}) = H_1^*(i\omega_n)H_1(i\omega_{n+1}) - H_1(i\omega_{-n})H_1^*\left(\omega_{-(n+1)}\right). \tag{2.68}$$

These components are for a single oscillator, which represents a single spatial region of the cell. For typical FM parameters $m \approx 1$ and $\omega_{\mathrm{m}} \approx \Gamma/2$, and trial oscillator parameters $\omega_0 = 1$ and $\Gamma = 10^{-6}\omega_0$, these components give error signals very similar to those shown in Fig. 2.4. We note that the zero-crossings of the X and Y lock-in channels for a single DLHO will be slightly mismatched for low quality factors $Q = \omega_0/\Gamma$, by an amount on the order of $1/Q$, but that this is not the quadrature error signal phenomenon. This mismatch vanishes in the limit of high Q, or if the transfer function (2.57) is simplified with the "high-Q" approximation, $\omega_0^2 - \omega^2 + i\Gamma\omega \approx 2\omega_0[\omega_0 - \omega + i\Gamma/2]$.

To model the quadrature error signal, an array of several oscillators with amplitudes $y_k(t)$ must be used to represent spatial regions in the cell with different ω_0 and Γ from a spatial light-intensity gradient. The detected signal is then the intensity of the total amplitude, $S(\omega) = |\sum_k y_k(t)|^2$. However, in practice, similar results are obtained with the approximation $S(\omega) \approx \sum_k |y_k(t)|^2$, which conveniently allows the use of a superposition of the components (2.68).

2.4.2 Two-level systems

Now we derive the components $C_n(\omega, \omega_{\mathrm{m}})$ for the 2LS simulation. Here, we ignore all states except the two ground-state sublevels that form the 0–0 transition, which are highlighted by the kets $|1\rangle$ and $|2\rangle$ in Fig. 2.1. We assume a two-level Hamiltonian

$$H = E_1|1\rangle\langle 1| + E_2|2\rangle\langle 2| + V_{21}(t), \tag{2.69}$$

where $V_{21}(t)$ is a time-dependent perturbation from the microwaves. In the full ground-state spin Hamiltonian $H^{\{g\}}$ of (2.1), the oscillatory magnetic field $\mathbf{B}_{\mathrm{mw}}(t)$ from the microwaves leads to a magnetic-dipole interaction,

$$V(t) = -\boldsymbol{\mu} \cdot \mathbf{B}_{\mathrm{mw}}(t). \tag{2.70}$$

Let $|\mathbf{B}_{\mathrm{mw}}| = B_{\mathrm{mw}} F(t)$, where the function $F(t)$ describes the time dependence of the field and satisfies $F(0) = 1$. Using the results from the last section, we may write this function as

$$F(t) = \cos[\omega t + m \sin(\omega_{\mathrm{m}} t)] = \sum_{n=-\infty}^{\infty} J_n(m) \cos(\omega_n t), \tag{2.71}$$

where frequency modulation with rate ω_{m} and index m lead to a superposition of continuous oscillations at the sideband frequencies $\omega_n = \omega + n\omega_m$ of (2.54) about the microwave carrier ω. If we define the Rabi frequency

$$\Omega_{21} = -\langle 2|\boldsymbol{\mu}|1\rangle \cdot \mathbf{B}_{\mathrm{mw}}(0)/\hbar, \tag{2.72}$$

then we can write the two-level interaction $V_{21}(t)$ in (2.69) due to (2.70) as

$$V_{21}(t) = \hbar F(t)\{\Omega_{21}|2\rangle\langle 1| + \Omega_{21}^{*}|1\rangle\langle 2|\}. \tag{2.73}$$

To calculate the error signal, we will model the absorption by the vapor using a density matrix. In general, the density operator for an ensemble of N identical atoms with wave functions $|\psi_j\rangle$, where $j = 1, 2, \ldots, N$, is defined as

$$\rho = \frac{1}{N} \sum_{j=1}^{N} |\psi_j\rangle\langle\psi_j|. \tag{2.74}$$

If we express each wave function in terms of a given basis $|\mu\rangle$ as $|\psi_j\rangle = \sum_\mu c_j(\mu)|\mu\rangle$, then we may write the density operator as

$$\rho = \sum_{\mu\nu} \rho_{\mu\nu} |\mu\rangle\langle\nu|, \tag{2.75}$$

where the coefficients $\rho_{\mu\nu} = \langle\mu|\rho|\nu\rangle$ are the matrix elements of the operator ρ in the basis $|\mu\rangle$, and are equal to $\rho_{\mu\nu} = \sum_j c_j(\mu)c_j^*(\nu)/N$. The diagonal elements $\rho_{\mu\mu}$ are known as populations, and give the occupation probability for each state $|\mu\rangle$. The off-diagonal elements $\rho_{\mu\nu}$ with $\mu \neq \nu$ are known as coherences, and satisfy $\rho_{\mu\nu} = \rho_{\nu\mu}^*$. The density operator evolves as

$$\frac{d}{dt}\rho = \frac{1}{i\hbar}[H, \rho] - R(\rho), \tag{2.76}$$

where H is the Hamiltonian for the atomic evolution and $R(\rho)$ is a correction for optical pumping and relaxation (or damping) effects.

For our two-level system with the sublevels $|1\rangle$ and $|2\rangle$, the Hamiltonian H_{21} of (2.69), and the perturbation $V_{21}(t)$ of (2.73), the evolution of the density operator ρ according to (2.76) is equivalent to the evolution of the density-matrix elements $\rho_{\mu\nu}$ for a given spatial region in the cell according to the coupled system

$$\frac{d}{dt}\rho_{11} = \Upsilon_{11} - \Gamma_{11}\rho_{11} - 2\,\mathrm{Im}[\Omega_{21}F(t)\rho_{12}], \tag{2.77}$$

$$\rho_{21} = \rho_{12}^*, \tag{2.78}$$

$$\frac{d}{dt}\rho_{12} = (i\omega_{21} - \Gamma_{21})\rho_{12} - iF(t)(\Omega_{21}^*\rho_{22} - \Omega_{21}\rho_{11}), \tag{2.79}$$

$$\frac{d}{dt}\rho_{22} = \Upsilon_{22} - \Gamma_{22}\rho_{22} + 2\,\mathrm{Im}[\Omega_{21}F(t)\rho_{12}]. \tag{2.80}$$

Here, the Υ and Γ are replenishment and relaxation rates from $R(\rho)$, respectively, $\omega_{21} = (E_2 - E_1)/\hbar$ is the Bohr frequency for the 0–0 transition, and $\mathrm{Im}[z]$ denotes

the imaginary part of z. This system is valid locally at each spatial region in the cell. Without microwaves, $\Omega_{21} = 0$ and optical pumping produces the equilibrium populations $\rho_{\mu\mu} = \Upsilon_{\mu\mu}/\Gamma_{\mu\mu}$.

The attenuation of the pumping light at each point in the cell is proportional to the population difference $\rho_{22} - \rho_{11}$. To calculate this difference in the presence of microwaves, we must first solve for the coherence ρ_{12}. Neglecting the nuclear contribution to the moment $\boldsymbol{\mu}$ of (2.4) and assuming that the microwave field is aligned with the applied static field B along the Cartesian direction $\mathbf{z}$, which defines the quantization axis, the Rabi frequency becomes

$$\Omega_{21} = g_S \mu_B \langle 2|S_z|1\rangle B_{\mathrm{mw}}/\hbar. \tag{2.81}$$

From the spin-basis expansion (2.12), we see that the matrix element $\langle 2|S_z|1\rangle = \langle a\,0|S_z|b\,0\rangle$ is real valued. Therefore, the Rabi frequency Ω_{21} is real, or $\Omega_{21} = \Omega_{21}^*$, which simplifies the coupled system of equations (2.77)–(2.80).

Solving (2.79), we may write the coherence as

$$\rho_{12}(t) = -i \int_{-\infty}^{t} e^{(i\omega_{21} - \Gamma_{12})(t-t')} F(t') \Omega_{21} [\rho_{22}(t') - \rho_{11}(t')] dt'. \tag{2.82}$$

If we assume that the population difference $\rho_{22} - \rho_{11}$ is slowly varying, or that any oscillations induced in this difference lead only to a small correction, then we may approximate

$$\rho_{12}(t) \approx -i\Omega_{21}(\rho_{22} - \rho_{11}) \int_{-\infty}^{t} e^{(i\omega_{21} - \Gamma_{12})(t-t')} F(t') dt'. \tag{2.83}$$

Using the secular approximation, we assume that only the low-frequency terms of the product $e^{-i\omega_{21}t} F(t)$ are important to the evolution of the coherence, and that we may neglect the high-frequency components. For a microwave carrier ω tuned near the

0–0 frequency ω_{21}, this gives the approximate solution

$$\rho_{12}(t) \approx \frac{\Omega_{21}}{2}(\rho_{22} - \rho_{11}) \sum_{n=-\infty}^{\infty} J_n(m) H_2(i\omega_n) e^{i\omega_n t}, \tag{2.84}$$

where we introduced the function

$$H_2(s) = \frac{1}{\omega_{21} + is + i\Gamma_{21}}. \tag{2.85}$$

This function plays a similar role as the transfer function $H_1(s)$ of (2.57) obtained for the DLHO, and these two functions have the same form for $s = i\omega$ if $H_1(s)$ is simplified with the "high-Q" approximation, $\omega_0^2 - \omega^2 + i\Gamma\omega \approx 2\omega_0[\omega_0 - \omega + i\Gamma/2]$.

We can now solve for the population difference $D = \rho_{22} - \rho_{11}$. For simplicity, let $\Gamma_D = \Gamma_{11} = \Gamma_{22}$ and denote the steady-state difference without microwaves as $D_0 = \Upsilon_{22}/\Gamma_{22} - \Upsilon_{11}/\Gamma_{11}$. Subtracting (2.77) from (2.80), we find that D evolves as

$$\frac{d}{dt} D = \Gamma_D(D_0 - D) - \Gamma_{\rm mw}(t) D, \tag{2.86}$$

where the time-dependent relaxation rate from the microwaves is

$$\Gamma_{\rm mw}(t) = -4\,\mathrm{Im}[\Omega_{21} F(t) \rho_{12}]/D. \tag{2.87}$$

Using (2.84), (2.71), and the secular approximation, we may approximate this rate as

$$\Gamma_{\rm mw}(t) \approx -\Omega_{21}^2\,\mathrm{Im}\left[\sum_{n=-\infty}^{\infty} \sum_{k=-\infty}^{\infty} J_n(m) J_k(m) H_2(i\omega_n) e^{i(\omega_n - \omega_k)t}\right]. \tag{2.88}$$

Separating the rate (2.88) into constant and time-varying portions,

$$\Gamma_{\rm mw}(t) = \overline{\Gamma}_{\rm mw} + \widetilde{\Gamma}_{\rm mw}(t), \tag{2.89}$$

we may use (2.85) to find that the constant portion is

$$\overline{\Gamma}_{\rm mw} = \frac{\Gamma_{21}\Omega_{21}^2}{(\omega_{21}-\omega)^2+\Gamma_{21}^2} \sum_{n=-\infty}^{\infty} J_n^2(m). \tag{2.90}$$

For no modulation, $m = 0$, the sum on the right-hand side equals 1, since $J_n(0) = \delta_{n0}$. Keeping only the first-harmonic component, the time-dependent portion of (2.88) is

$$\widetilde{\Gamma}_{\rm mw}(t) \approx -\Omega_{21}^2 \,{\rm Im}\left[\sum_{n=-\infty}^{\infty} J_n(m)J_{n+1}(m)\left(H_2(i\omega_n)e^{-i\omega_{\rm m}t} + H_2(i\omega_{n+1})e^{i\omega_{\rm m}t}\right)\right]. \tag{2.91}$$

Note that for intermediate modulation ($m \gtrsim 1$) the constant (2.90) and time-dependent (2.91) portions of $\Gamma_{\rm mw}$ are comparable in magnitude.

Similarly, we may separate the population difference $D = \rho_{22} - \rho_{11}$ into constant and time-varying portions,

$$D = \overline{D} + \widetilde{D}(t). \tag{2.92}$$

Using (2.86) and (2.89), the constant portion is

$$\overline{D} = \frac{D_0\Gamma_D}{\Gamma_D + \overline{\Gamma}_{\rm mw}}. \tag{2.93}$$

Using (2.90), the relative change in the constant portion of the population difference due to the microwaves is

$$\frac{\overline{D}-D_0}{D_0} = \frac{-\overline{\Gamma}_{\rm mw}}{\Gamma_D+\overline{\Gamma}_{\rm mw}} = \frac{-(\Gamma_{21}/\Gamma_D)\Omega_{21}^2\sum_n J_n(m)^2}{(\omega_{21}-\omega)^2+\Gamma_{21}^2+(\Gamma_{21}/\Gamma_D)\Omega_{21}^2\sum_n J_n(m)^2}. \tag{2.94}$$

As a function of microwave carrier ω, we see that the population difference due to the microwaves is a Lorentzian dip about resonance, as sketched in Fig. 2.3(b) and observed in practice. We also see that the rate Γ_{21} plays the role of a half-width-at-half-maximum (HWHM) for the microwave line. Typically, the density of alkali-metal

atoms in the cell is adjusted so that the optical absorption attenuates the light passing through the cell by roughly a factor of $1/e$. In comparison, the additional relative attenuation, (2.94) above, of this light due to microwave absorption is typically about 1% for clocks that use lasers.

Assuming that any oscillation induced in the population difference D is small, we can approximate the evolution of the time-dependent portion $\widetilde{D}(t)$ from (2.86) as

$$\frac{d}{dt}\widetilde{D} = -[\Gamma_D + \Gamma_{\rm mw}(t)]\widetilde{D} - \widetilde{\Gamma}_{\rm mw}(t)\overline{D} \approx -\widetilde{\Gamma}_{\rm mw}(t)\overline{D}. \tag{2.95}$$

Since the microwave absorption (2.94) is typically small, we can further approximate $\overline{D} \approx D_0$ in (2.95),

$$\frac{d}{dt}\widetilde{D} \approx -\widetilde{\Gamma}_{\rm mw}(t)D_0. \tag{2.96}$$

If we write the first-harmonic component (2.91) as

$$\widetilde{\Gamma}_{\rm mw}(t) = -\operatorname{Im}\left[\widetilde{S}_1(\omega)e^{i\omega_{\rm m}t}\right], \tag{2.97}$$

then the solution of (2.96) including only the first-harmonic modulation is

$$\widetilde{D}(t) = \frac{D_0}{\omega_{\rm m}}\operatorname{Re}\left[\widetilde{S}_1(\omega)e^{i\omega_{\rm m}t}\right]. \tag{2.98}$$

The attenuation of the pumping light intensity is proportional to D, and so from (2.98) we see that the (real-valued) lock-in signal is

$$S_1(\omega) \propto \operatorname{Re}\left[\widetilde{S}_1(\omega)e^{i\omega_{\rm m}t}\right]. \tag{2.99}$$

Combining (2.91), (2.97), and (2.99), the complex-valued signal $\widetilde{S}_1(\omega)$ of (2.48) has the error-signal components

$$C_n^{\mathrm{2LS}}(\omega, \omega_{\mathrm{m}}) \propto H_2(i\omega_{n+1}) - H_2(i\omega_{-n}) - H_2^*(i\omega_n) + H_2^*\left(i\omega_{-(n+1)}\right). \tag{2.100}$$

Just as with the DLHO result (2.68), these error-signal components are for a single spatial region in the cell. For typical modulation parameters $m \approx 1$ and $\omega_{\mathrm{m}} \approx \Gamma/2$, where the microwave full-width $\Gamma = 2\Gamma_{21}$, and trial atomic parameters $\omega_{21} \approx 10^9$ and $\Gamma_{12} \approx 10^3$, these components give error signals like those shown in Fig. 2.4.

To model the quadrature error signal in Figs. 2.4 and 2.9, an array of ten solutions representing different spatial regions in the cell were combined to obtain the total lock-in signal. To simulate the quadrature error signal in Fig. 2.4, the values of ω_{21} and of Γ_{21} were adjusted to vary uniformly by a total of 20% over the whole array. To simulate the signals in Fig. 2.9, the size of the total variation in ω_{21} over the cell was chosen to be proportional to the laser-frequency detuning from the zero-shift frequency. The only free parameters were a lock-in phase offset and an overall vertical-scaling coefficient for all of the quadrature error signals, which were adjusted to match the theory curves with the experimental curves in the figure.

2.5 Summary and discussion

We have demonstrated a simple method to suppress the light shift in optical pumping systems, which can be readily applied to existing atomic clocks with few additional components. The method uses only frequency modulation of a radio frequency or microwave source in order to simultaneously lock the source to an atomic resonance and lock the pumping light to suppress the light shift. In contrast, conventional stabilization of both sources requires two individual modulation schemes, adding complexity. This technique also works for clocks based on coherent population trapping (CPT),

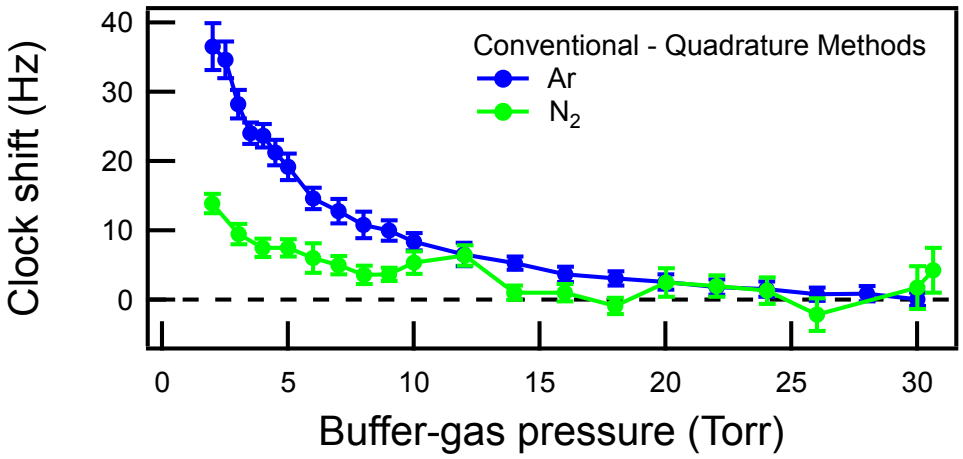

Figure 2.10: Clock frequency difference between the quadrature and conventional light-shift suppression methods at low buffer-gas pressures. The data are for ^{87}Rb in either N_2 at 50.0° C and $B = 0.2$ G, or Ar at 40.0° C and $B = 1.0$ G.

as demonstrated by Boudot *et al.* [67] with a Cs-Ne CPT clock. In principle, this technique can also work with many other optical pumping systems that experience light shifts.

Although the quadrature method performs well, as shown in Fig. 2.7, we have observed a noticeable difference between the clock frequencies for the quadrature and the conventional methods when the buffer-gas pressure is less than about 20 Torr.

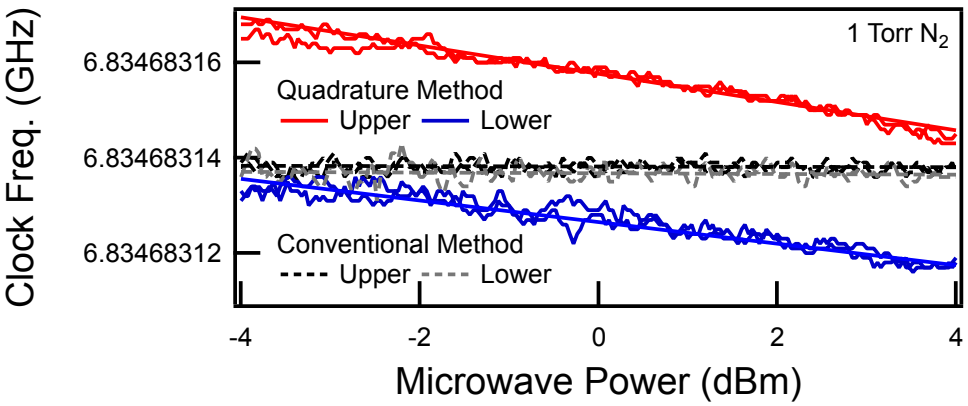

Figure 2.11: Dependence of the clock frequency at low pressure on the applied microwave power and the choice of zero-shift frequency, either near the upper or lower hyperfine manifold. The data are for ^{87}Rb in 1 Torr of N_2 at 50.0° C.

This difference can be up to a few tens of Hz for 2 Torr of Ar or N_2, as shown in Fig. 2.10. When there is a difference, the clock frequency using the quadrature method shows a dependence on the applied microwave power and the choice of hyperfine multiplet for optical pumping, as shown in Fig. 2.11. The conventional method does not show such dependence. While these discrepancies may be partly due to the poor signal-to-noise ratio of the quadrature error signal at very low buffer-gas pressures, detailed understanding requires further investigation.

Chapter 3

Estimation of the hyperfine-shift potential from the pressure shift

3.1 Introduction

During a collision with a chemically inert atom or molecule, the hyperfine coupling $A\,\mathbf{I}\cdot\mathbf{S}$ of (2.1), between the nuclear spin $\mathbf{I}$ and electronic spin $\mathbf{S}$ of a ground-state alkali-metal atom, is perturbed by the isotropic hyperfine-shift interaction [21]

$$H_{\rm hfs} = \delta A\,\mathbf{I}\cdot\mathbf{S}, \tag{3.1}$$

in addition to smaller anisotropic interactions, such as the electric quadrupole and non-contact magnetic-dipole interactions. The shift parameter $\delta A = \delta A(R)$ is a potential that depends on the internuclear separation R of the colliding pair. Because of the interaction (3.1), the microwave resonant frequencies ν of alkali-metal atoms in cells with buffer gas, which have long been used in atomic frequency standards (or clocks) and magnetometers, are not the same as the free-atom frequencies ν_0, but instead are shifted by an amount that depends on the pressure and composition of the buffer gas and on the temperature T [11]. Known as the pressure shift, the mean

frequency shift $\delta\nu = \nu - \nu_0$ due to binary collisions of a dilute alkali-metal vapor with a buffer gas is given by the isotope-independent statistical average

$$\frac{\delta\nu}{\nu_0} = 4\pi N \int_0^\infty \left(\frac{\delta A(R)}{A}\right) e^{-V(R)/kT} R^2 dR, \tag{3.2}$$

where N is the buffer-gas number density, $V(R)$ is an interaction (or interatomic) potential for the colliding alkali-buffer pair, and k is the Boltzmann constant [68, 69]. The smaller anisotropic interactions average to zero in the mean shift (3.2) [70].

Despite much theoretical and experimental attention, not much is known yet about the potential $\delta A(R)$, especially at small separations R. Theoretical calculation of $\delta A(R)$ is difficult even for H [71, 72], and for the heavy alkali metals is a hard, if not unsolved, problem [73]. (For early work, see the references listed in Happer [19].) In contrast, much more is known about the other quantities in (3.2): The fractional shift $\delta\nu/\nu_0$ has been measured very precisely for certain alkali-buffer pairs, in part because of its importance to practical atomic clocks, and estimates exist for $V(R)$ that have been inferred from theory or experiment. While this knowledge is not enough to invert (3.2) in order to uniquely determine $\delta A(R)$, here we show that (3.2) still yields a surprising amount of information about $\delta A(R)$. For a typical $V(R)$ with a potential well, the change of the pressure shift with temperature depends strongly on the shape of $\delta A(R)$ near the well. We demonstrate how to use experimental data for the pressure shift to estimate simple trial forms of $\delta A(R)$ for Na, K, and Rb in He, Ne, or Ar gas. The results provide an estimate for the shape of $\delta A(R)$ about a potential well in $V(R)$, which agree well with theoretical and experimental results in the few cases where they are available. Additionally, to aid these estimates, we first derive an improved estimate of the large-R asymptote of the ratio $\delta A(R)/V(R)$.

Before we begin, we first provide some background on the pressure shift in vapor-cell clocks and a derivation of the average (3.2).

3.1.1 Pressure shifts

In general, the pressure shift refers to the frequency shift of an atomic resonance due to collisions with other atoms or molecules, for example, from a chemically inert buffer gas. The same collisions that produce shifts also tend to broaden the atomic resonance lines [74]. Most atomic clocks suffer pressure shifts from buffer gases, so we review features of the pressure shift important to this and later chapters here.

For conventional vapor-cell clocks, the phrase "pressure shift" specifically refers to the differential shift of the 0–0 hyperfine transition from collisions with the buffer gas [11, 16]. Sometimes this shift is referred to as the hyperfine pressure shift, to differentiate it from the pressure shifts of the optical transitions important to optical pumping. Fig. 3.1 is a sketch of the pressure shift of the 0–0 transition of ^{133}Cs for several different buffer gases, as measured by Arditi and Carver [29, 30]. As the curves show, the frequency shift is very nearly linear with the buffer-gas pressure. The slope depends on the particular buffer gas, and also on the temperature, as sketched in Fig. 3.2. Commercial vapor-cell clocks typically use mixtures of buffer gases, such as N_2 and Ar, which are optimized to reduce any change in the pressure shift with temperature. This has the advantage of improving the short-term stability against temperature fluctuation, but the consequence that there is still a significant net pressure shift. This net pressure shift is the main reason why vapor-cell clocks are secondary standards, which require calibration to correct for the initial inaccuracy and the long-term drift from this shift [11, 15, 16], as we discuss in Section 5.1.1.

The pressure shift of the 0–0 transition is almost entirely due to the hyperfine-shift interaction (3.1) [21]. From Section 2.1.1, we may write the 0–0 frequency as

$$\nu_{00} = A(I + 1/2)/h, \tag{3.3}$$

where the magnetic-dipole coupling coefficient A of (2.3) is proportional to the probability density $|\psi(0)|^2$ for the alkali-metal valence electron to be located at the alkali-metal nucleus. During a collision, the perturbing buffer-gas atom or molecule changes this density $|\psi(0)|^2$. When the alkali-metal atom is immersed in a gas, the net effect of collisions is an average perturbation $\langle \delta A \rangle$ to the coupling coefficient A, and a corresponding shift of the 0–0 frequency away from the free-atom value (3.3),

$$\delta\nu_{00} = \langle \delta A \rangle (I + 1/2)/h. \tag{3.4}$$

In vapor-cell clocks, this shift is mostly due to independent binary collisions. We can write the average perturbation as $\langle \delta A \rangle = \langle \delta A \rangle_1 \tau_\mathrm{b}/T_\mathrm{b}$, where $\langle \delta A \rangle_1$ is the average perturbation during a single binary collision of mean duration τ_b (≈ 1 ps) [19]. Since the rate $1/T_\mathrm{b}$ of binary collisions is proportional to the buffer-gas pressure p, we see

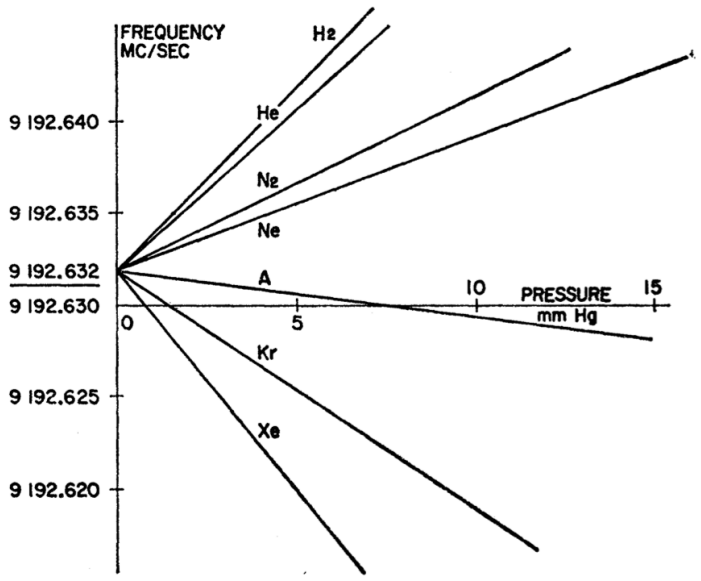

Figure 3.1: Measured pressure shift of the 0–0 transition frequency of ^{133}Cs in H_2, He, N_2, Ne, Ar, Kr, or Xe buffer gas at 30° C from Arditi and Carver [29, 30]. Each curve is the 0–0 frequency in MHz as a function of the buffer-gas pressure (10 mm Hg = 1 Torr). As the curves show, collisions with the buffer gas lead to a mostly linear shift of the 0–0 frequency, with a slope that depends on the particular buffer gas (and temperature). Reprinted figure with permission from [30]. Copyright 1961 by the American Physical Society.

that the overall shift (3.4) is also proportional to the pressure p. We can estimate this rate from spatial diffusion to be $1/T_{\rm b} = v^3/(3D)$. For a characteristic mean velocity $v \approx 3 \times 10^4$ cm/s, diffusion coefficient $D \approx 0.1 \times (760 \text{ Torr}/p)$ cm^2/s, and pressure $p \approx 10$ Torr, this gives $1/T_{\rm b} \approx 1320$ s^{-1} [21].

The pressure shift is positive for some gases and negative for others, as sketched in Fig. 3.1. This dependence on the particular gas can be qualitatively understood as follows. At large separations the attractive van der Waals forces between the atoms dominate, and the interaction potential $V(R)$ is negative. This attraction tends to decrease the probability density $|\psi(0)|^2$ by pulling the valence electron away from the nucleus, leading to a negative frequency shift. However, at smaller separations the repulsive exchange forces between the atoms dominate, and the interaction potential $V(R)$ is positive. This repulsion tends to increase $|\psi(0)|^2$ by concentrating the valence electron at the nucleus, leading to a positive frequency shift. Averaging over collisions, these long- and short-range effects compete to produce the average perturbation $\langle \delta A \rangle$ and the overall shift (3.4), which can be of either sign. For the lighter gases such as He and Ne, the exchange forces tend to dominate, leading to a positive shift. For the heavier gases such as Kr and Xe, which are more polarizable, the van der Waals forces tend to dominate, leading to a negative shift. For the intermediate gas Ar these effects almost cancel, leaving to a relatively small negative shift. However, the exact dependence of the shift with internuclear separation R is described by the hyperfine-shift potential $\delta A = \delta A(R)$, which is the subject of this chapter. While this potential comes from the same interactions that produce the interaction potential $V(R)$, much less is known about the precise shape of $\delta A(R)$ than of $V(R)$.

As expression (3.2) shows, the pressure shift $\delta\nu = \nu - \nu_0$ for a particular hyperfine frequency ν is the combined result of both $\delta A(R)$ and $V(R)$. The expression (3.2) has a remarkably simple form, which we may derive as follows. Pressure shifts, unlike collisional broadenings, are an equilibrium phenonena that can be calculated rather

simply with statistical mechanics. Instead of averaging over all possible collisions (e.g., Appendix A of Camparo [73]), we can average over all possible configurations of the buffer gas about an alkali-metal atom for a given temperature T. Consider a single alkali-metal atom in a volume Ω filled with a buffer gas of number density N. We assume that the buffer gas is dilute enough that the alkali-metal atom is perturbed by at most one buffer-gas atom or molecule at any given time. The probability for a buffer-gas particle to be at the position $\mathbf{R}$ relative to the alkali-metal atom is then

$$dP = \frac{1}{Z} e^{-V(R)/kT} d^3\mathbf{R}, \tag{3.5}$$

where $e^{-V(R)/kT}$ is a Boltzmann factor and Z is the canonical partition function. Since the interatomic potential $V(R)$ differs significantly from zero only within a small radius R, roughly on the order of 100 Å, the partition function is almost exactly equal to the volume,

$$Z = \int_\Omega e^{-V(R)/kT} d^3\mathbf{R} \approx \Omega. \tag{3.6}$$

The average value $\langle \delta A \rangle$ of the perturbation is then given by a statistical average over the potential $\delta A(R)$ using the probability (3.5) and normalization (3.6),

$$\langle \delta A \rangle = N\Omega \int \delta A(R) dP = 4\pi N \int_0^\infty \delta A(R) e^{-V(R)/kT} R^2 dR, \tag{3.7}$$

where we multiplied by the number of particles $N\Omega$ to account for the whole buffer gas. From (3.3) and (3.4), we see that the relative shift $\delta\nu/\nu_0 = \langle \delta A \rangle / A$, and so the expression (3.2) follows directly from (3.7). Finally, we note that since the ratio $\delta A(R)/A$ is equal to a fractional change in the density $|\psi(0)|^2$, the ratio $\delta A(R)/A$ and the fractional shift $\delta\nu/\nu_0$ of (3.2) are very nearly independent of the particular choice of isotope for a given alkali-metal atom.

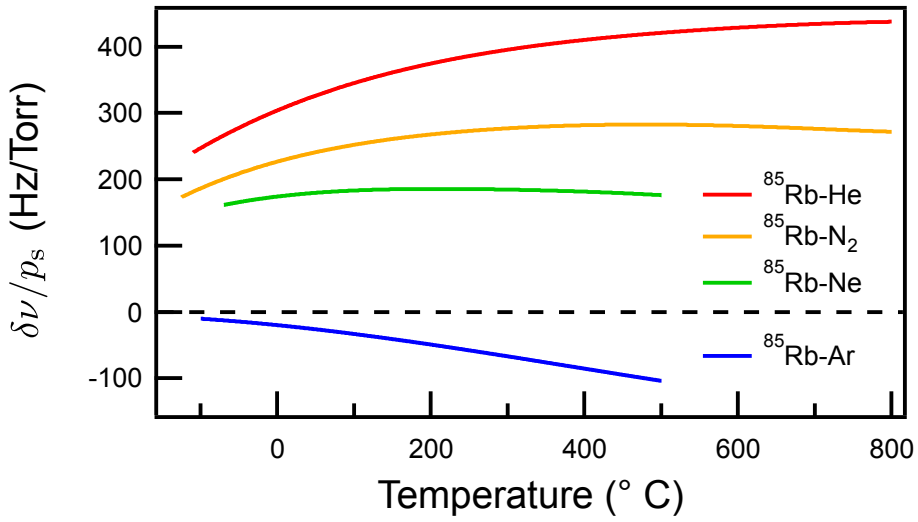

Figure 3.2: Pressure shift of ^{85}Rb versus temperature for a sealed cell with a constant number density N of He, Ne, N_2, or Ar buffer gas. Each curve is the shift $\delta\nu/p_s$ of (3.29) using the measured coefficients of Bean and Lambert [75], where p_s is the buffer-gas pressure of the cell when it was sealed at a temperature $T_s = 300$ K. As the curves show, the shift is a nonlinear function of temperature, which depends on the particular buffer gas. The shifts for ^{23}Na and ^{39}K, also measured by Bean and Lambert [75], have very similar behavior with temperature.

As sketched in Fig. 3.2, the pressure shift depends on temperature in a nonlinear fashion. In Section 3.3, we use this dependence to estimate the shape of the potential $\delta A(R)$. To understand why the pressure shift is sensitive to the shape of $\delta A(R)$ at relatively small R, we note that nearly all the change with temperature of the Boltzmann factor $e^{-V(R)/kT}$ in the statistical average (3.2) occurs at R near the potential well and the region where the potential $V(R)$ initially becomes repulsive. At larger R, the Boltzmann factor quickly asymptotes to 1, and at smaller R, it quickly decays to zero.

The pressure shift may also depend on the buffer-gas pressure in a nonlinear fashion, for example, if the pressure is high enough that three-body collisions or deviation from the ideal-gas equation of state are significant [76, 77, 78, 79]. However, these effects are typically negligible in vapor-cell clocks, which normally use buffer-gas pressures of a few Torr or tens of Torr. Instead, for vapor-cell clocks there may be a

significant nonlinear (and linear) contribution to the pressure shift from short-lived van der Waals molecules, which is discussed in Chapter 4.

3.2 Estimation of the large-R asymptote of $\delta A(R)$

In this section, we derive an improved estimate of the ratio $\delta A(R)/V(R)$ of the hyperfine-shift and interaction potentials at large internuclear separations R, which we will use in Section 3.3. Retardation effects [80] should be negligible in the range of R important to the shift (3.2), so the following large-R asymptotic forms of the interaction potential,

$$V(R) \approx \frac{C_6}{R^6}, \tag{3.8}$$

and of the hyperfine-shift potential,

$$\frac{\delta A(R)}{A} \approx \frac{A_6}{R^6}, \tag{3.9}$$

should be good approximations. We derive below a relation between the coefficient A_6 in (3.9) and the van der Waals dispersion coefficient C_6 in (3.8),

$$A_6 \approx \frac{2}{E_\mathrm{a}} C_6, \tag{3.10}$$

where the characteristic energy E_a depends only on the particular alkali-metal atom. Previous work has produced expressions similar to (3.10), usually of the form

$$A_6 \approx \left(\frac{2}{E_\mathrm{a}} + \frac{1}{E_\mathrm{a} + I_\mathrm{b}} \right) C_6, \tag{3.11}$$

where I_b is an ionization energy for the perturbing buffer-gas atom or molecule. The additional term in (3.11) not present in (3.10) is a small correction, typically 5–10%,

Table 3.1: Characteristic energies E_a (eV) for Na, K, Rb, and Cs in the relation (3.10). The values of E_A were numerically estimated using the expression (3.20). Previously suggested values for E_a are included for comparison: $\overline{E}_e$ from Vanier and Audoin [11] and the ionization energy E_∞ [83] from Herman and Margenau [81].

Alkali metal:	Na	K	Rb	Cs
E_a (this work):	6.574	5.311	5.056	4.586
Vanier and Audoin $\overline{E}_e$ [11]:	3.62	2.98	2.88	2.66
Ionization energy E_∞ [83]:	5.14	4.34	4.18	3.89

and is negligible compared to the disagreement between the very different values provided for the energy E_a: Vanier and Audoin [11] estimated E_a as an average of optical (D1 and D2) transition and ionization energies, while Herman and Margenau [81] estimated E_a as an ionization energy. As shown in Table 3.1, these values for E_a differ by roughly a factor of 2. Here we provide an unambiguous derivation of E_a in (3.10), similar in approach to Adrian [82] for H, which we use to numerically estimate the values of E_a in Table 3.1 for Na, K, Rb, and Cs. These values allow for an improved estimation of the large-R asymptote (3.9) of $\delta A(R)$ for a given value of C_6 using the expression (3.10).

Consider an alkali-metal atom at position $\mathbf{r}_\mathrm{a}$ and a buffer-gas atom (or molecule) at position $\mathbf{r}_\mathrm{b} = \mathbf{r}_\mathrm{a} + \mathbf{R}$, both of which are in their ground states. For large enough $R = |\mathbf{R}|$ and ignoring retardation [80], the leading-order interaction U responsible for $V(R)$ is the dispersive van der Waals interaction between an induced electric-dipole moment $\mathbf{p}_\mathrm{b}$ of the buffer-gas atom and the electric field $\mathbf{E}_\mathrm{a}$ from the instantaneous dipole moment $\mathbf{p}_\mathrm{a}$ of the alkali-metal valence electron,

$$U = -\frac{1}{2}\mathbf{p}_\mathrm{b} \cdot \mathbf{E}_\mathrm{a}(\mathbf{r}_\mathrm{b}), \tag{3.12}$$

where the factor of $1/2$ accounts for $\mathbf{p}_\mathrm{b}$ being induced. We assume that the buffer-gas atom is fully described by an electric-dipole polarizability α, such that $\mathbf{p}_\mathrm{b} = \alpha \mathbf{E}_\mathrm{a}(\mathbf{r}_\mathrm{b})$.

The moment $\mathbf{p}_\mathrm{a} = -|e|\mathbf{r}_\mathrm{e}$, where e is the charge and $\mathbf{r}_\mathrm{e}$ is the position relative to $\mathbf{r}_\mathrm{a}$ of the alkali-metal valence electron. The field $\mathbf{E}_\mathrm{a} = \mathbf{p}_\mathrm{a} \cdot (3\mathbf{nn} - \mathbb{1})/R^3$, where $\mathbf{n} = \mathbf{R}/R$ and $\mathbb{1}$ is the identity dyadic tensor, so we may write

$$U = -\frac{\alpha e^2(r_\mathrm{e}^2 + 3z_\mathrm{e}^2)}{2R^6}, \tag{3.13}$$

where $r_\mathrm{e} = |\mathbf{r}_\mathrm{e}|$ and $z_\mathrm{e} = \mathbf{r}_\mathrm{e} \cdot \mathbf{n}$. Following Adrian [82], we treat both U and the contact hyperfine interaction of (2.2),

$$H_\mathrm{hf} = \frac{8\pi}{3} g_S \mu_B \frac{\mu_I}{I} \delta(\mathbf{r}_\mathrm{e})\, \mathbf{I} \cdot \mathbf{S}, \tag{3.14}$$

as perturbations to the alkali-metal atom. Let $|n\rangle$ denote the S-state wave function for an unperturbed alkali-metal valence electron with principle quantum number n and energy E_n, and let $|g\rangle$ denote the ground S-state with energy E_g and $n = g = 3$, 4, 5, and 6 for Na, K, Rb, and Cs, respectively. Each S-state $|n\rangle$ has a magnetic-dipole coupling coefficient

$$A_n = \frac{8\pi}{3} g_S \mu_B \frac{\mu_I}{I} |\psi_n(0)|^2, \tag{3.15}$$

with $A_g = A$ of (2.1) and where $|\psi_n(0)|^2$ is the valence-electron probability density at the nucleus. Please note that the A_6 of (3.10) is not to be confused with a magnetic-dipole coupling coefficient A_n of (3.15). Then the first-order perturbation to the ground-state energy E_g is

$$\delta E_{g,1} = \langle g|U + H_\mathrm{hf}|g\rangle = \frac{C_6}{R^6} + A\langle \mathbf{I} \cdot \mathbf{S}\rangle, \tag{3.16}$$

where

$$C_6 = -\alpha e^2 \langle r_{\rm e}^2 \rangle, \tag{3.17}$$

which is the Unsöld form for C_6 [74]. Here and subsequently in this section, angle brackets denote ground-state expectation values.

The leading-order hyperfine-shift interaction (3.1) comes from the terms in the second-order perturbation $\delta E_{g,2}$ that are linear in both U and $H_{\rm hf}$. Because the interaction (3.14) only has non-zero matrix elements between S-states, we may write these terms as

$$\delta E'_{g,2} = 2\ {\rm Re} \sum_{n>g} \frac{\langle g|U|n\rangle\langle n|H_{\rm hf}|g\rangle}{E_g - E_n}. \tag{3.18}$$

Using (3.16) with (3.18), the resulting large-R form (3.9) is

$$\frac{\delta A(R)}{A} = \frac{\delta E'_{g,2}}{A\langle \mathbf{I}\cdot\mathbf{S}\rangle}, \tag{3.19}$$

and using (3.17) and (3.15), we find that the characteristic energy in (3.10) is

$$\frac{1}{E_{\rm a}} = \frac{1}{\langle r_{\rm e}^2\rangle} \sum_{n>g} \frac{\langle g|r_{\rm e}^2|n\rangle \sqrt{|A_n/A_g|}}{E_g - E_n}. \tag{3.20}$$

We numerically estimated the values of $E_{\rm a}$ in Table 3.1 using this expression, as described below.

Following Oreto *et al.* [70], and using Eqs. 5.13(1), 8.4.3(10), and 8.5.1(2) from Varshalovich *et al.* [54], we write the wave function for the S-state $|n\rangle$ as

$$\psi_{n,m}(\mathbf{r}_{\rm e},\sigma) = \frac{P_{n0}(r_{\rm e})}{2\sqrt{\pi}\, r_{\rm e}} \delta_{\sigma m}, \tag{3.21}$$

where m is the azimuthal quantum number, the electronic spin variable $\sigma = \pm 1/2$, and $P_{n0}(r)$ is the (real) radial wave function. Then the remaining matrix elements in (3.20) simplify to radial integrals,

$$\langle g|r_{\rm e}^2|n\rangle = \int_0^\infty P_{g0}(r_{\rm e})P_{n0}(r_{\rm e})r_{\rm e}^2 dr_{\rm e}. \tag{3.22}$$

For the ground-state functions $P_{g0}(r_{\rm e})$ and expectations $\langle r_{\rm e}^2\rangle$, we used the tabulated Roothaan-Hartree-Fock (RHF) wave functions and values of Bunge *et al.* [84] for Na, K, and Rb, and of McLean and McLean [85] (Triple Zeta form) for Cs. For the excited-state functions $P_{n0}(r_{\rm e})$ we used Coulomb-approximation (CA) wave functions, since the operator r^2 contributes mostly away from the nucleus, near which these functions are least accurate. Following Oreto *et al.* [70], the CA functions are given by the asymptotic series

$$P_{n0}(r_{\rm e}) = \sum_{q=0}^{p} c_q e^{-r_{\rm e}/n^*} r_{\rm e}^{n^*-q}, \tag{3.23}$$

where the effective quantum number

$$n^* = \sqrt{\frac{R_\infty}{E_\infty - E_n}}, \tag{3.24}$$

R_∞ is the Rydberg constant, and E_∞ is the ionization energy of the alkali-metal atom. Up to overall normalization, the coefficients c_q are given by the recurrence relation

$$c_q = \frac{n^*(n^*-q)(n^*-q+1)}{2q} c_{q-1}. \tag{3.25}$$

We chose the upper limit p of the series (3.23) to get the best convergence at $r_{\rm e} =$ 1 Bohr (≈ 0.53 Å), and normalized the CA functions such that

$$\int_{0.1}^{\infty} P_{n0}(r_{\rm e})^2 dr_{\rm e} = 1, \tag{3.26}$$

where the lower bound is 0.1 Bohr. To match the RHF convention, we chose the sign of the CA functions so that the nuclear value of the unapproximated functions $P'_{n0}(0)$ are positive, using the relation

$$\frac{P'_{n0}(0)}{|P'_{n0}(0)|} = (-1)^{n+g} \lim_{r_{\rm e}\to\infty} \frac{P_{n0}(r_{\rm e})}{|P_{n0}(r_{\rm e})|}, \tag{3.27}$$

which lead to negative values for all the elements (3.22). One consequence of using RHF functions for the ground state and CA functions for the excited states is that the combined set of radial functions is not perfectly orthogonal. That is, the numerical integrals

$$\int_{0.1}^{\infty} P_{g0}(r_{\rm e}) P_{n0}(r_{\rm e}) dr_{\rm e} \tag{3.28}$$

are not exactly zero for $n \neq g$, but are, for example, between 0.02–0.13 for the worst case of $n = g+1$. However, the orthogonality quickly improves with n, as the accuracy of the CA functions improves with n. This small error is not expected to contribute much to $E_{\rm a}$, since it is due to the inaccuracy of the CA functions near the nucleus, where the operator $r_{\rm e}^2$ in (3.22) contributes least.

For the physical parameters in (3.20), we used measured values where available, and extrapolated otherwise. We used the values of A_n from Arimondo *et al.* [53] for ^{23}Na, ^{39}K, ^{87}Rb, and ^{133}Cs, as well as additional values for ^{133}Cs from Sansonetti [86]. Though the parameters A_n are isotope dependent, the ratio A_n/A_g is very nearly

isotope independent [53]. For the energies E_∞ and E_n we used the values from the NIST Spectra Database [83].

In general, the parameters A_n are the least available. We extrapolated the A_n to higher n using a linear fit to a plot of $\ln(A_n)$ vs $\ln(n^*)$, which is very nearly a straight line with a slope of almost exactly -3, in agreement with semiempirical formulas for A_n [53]. To extrapolate n^* and E_n we used a linear fit to a plot of n^* vs n, which is very nearly a straight line, in agreement with semiempirical formulas using a quantum defect [21]. We explicitly calculated the matrix elements (3.22) up to $n = 35$. We optimized the limit p for $P_{n0}(r_\mathrm{e})$ where E_n is available, and extrapolated p to higher n by noticing that p is very nearly equal to n at large n, up to a constant offset. We extrapolated the matrix elements (3.22) to higher n using a linear fit to the large-n^* asymptote of a plot of $\ln(-\langle g|r_\mathrm{e}^2|n\rangle)$ vs $\ln(n^*)$, in the region $n = 30$–35, which gave intercepts and slopes close to 3.5 and -1.5, respectively, for each alkali-metal atom. Such a dependence is expected since, as n increases, the CA functions $P_{n0}(r_\mathrm{e})$ converge to the same shape over the important range of r_e, up to normalization.

Using the values and approximations described above, we extrapolated the sum (3.20) to $n = 100$, a value large enough to approximate including all n. The sums converged quickly, with the highest terms contributing at least 1% being $n = 15$, 15, 17, and 18 for Na, K, Rb, and Cs, respectively. The extrapolation for $n > 35$ contributed roughly -6%, -3%, -2%, and -1% for Na, K, Rb, and Cs, respectively. As Table 3.1 shows, the improved values of E_a are significantly larger than those of previous work. These values allow for an improved estimation of the large-R asymptote (3.9) of $\delta A(R)$ for a given value of the van der Waals dispersion coefficient C_6 using the expression (3.10).

Table 3.2: Parameters for the measured pressure shift δ_ν/p_s of (3.29): polynomial degree D, temperature range (° C), and fit coefficients c_n (Hz Torr^{-1} °C^{-n}) measured by Bean and Lambert [75]. The sealing pressure p_s in (3.29) corresponds to a sealing temperature $T_s = 300$ K, and the expansion variable in (3.29) is $\delta T = (T - 0°\text{C})/10^3$. Fig. 3.2 is a sketch of these shifts for ^{85}Rb.

Metal	Gas	D	Range (° C)	c_0	c_1	c_2	c_3	c_4
^{23}Na	He	4	50–800	103.562	217.478	-267.284	213.028	-79.5682
^{23}Na	Ne	4	85–850	65.4070	110.205	-191.787	151.680	-50.3432
^{23}Na	Ar	3	100–700	-1.16738	50.2190	-109.832	51.5151	–
^{39}K	He	4	-100–800	41.9861	70.8683	-105.084	88.0880	-33.4209
^{39}K	Ne	4	-65–750	23.7893	24.4247	-74.1786	84.1616	-38.4843
^{39}K	Ar	4	-80–750	-1.93265	-7.37039	-57.9824	93.3986	-53.4416
^{85}Rb	He	4	-110–800	304.358	483.871	-779.542	692.833	-266.542
^{85}Rb	Ne	4	-70–50	174.398	138.574	-562.524	927.353	-680.600
^{85}Rb	Ar	3	-100–500	-19.6621	-116.826	-180.190	155.223	–

3.3 Estimation of the shape of $\delta A(R)$

In this section, we demonstrate how to use experimental data for the temperature-dependence of the pressure shift to estimate simple trial forms of $\delta A(R)$ for Na, K, and Rb in He, Ne, or Ar gas. Experimental knowledge of the pressure shift is usually summarized by a polynomial fit to the shift over a range of temperatures,

$$\left(\frac{\delta\nu}{p_s}\right)_{\text{exp}} \approx \sum_{m=0}^{D} c_m(\delta T)^m = c_0 + c_1\delta T + \ldots + c_D(\delta T)^D, \tag{3.29}$$

where the c_m are non-zero fit coefficients and δT is the change in temperature away from some reference. For a sealed cell with fixed N, $p_s = NkT_s$ is the buffer-gas pressure at the sealing temperature T_s. For certain alkali–buffer pairs, Bean and Lambert [75] provide fit coefficients c_m for measurements over wide temperature ranges of hundreds of degrees C, with $\delta T = (T - 0°\text{C})/10^3$, $T_s = 300$ K, and typical polynomial degree $D = 4$. Table 3.2 lists these parameters for ^{23}Na, ^{39}K, and ^{85}Rb in He, Ne, or Ar, and Fig. 3.2 is a sketch of these shifts (3.29) versus temperature for ^{85}Rb.

Table 3.3: Parameters for the interaction potential $V(R)$ of (3.30): well depth $\epsilon_{\rm m}$ (meV) and location $R_{\rm m}$ (Å) from Patil [87].

Metal	Na	Na	Na	K	K	K	Rb	Rb	Rb
Gas	He	Ne	Ar	He	Ne	Ar	He	Ne	Ar
$\epsilon_{\rm m}$ (meV)	0.149	1.007	5.551	0.121	0.762	5.252	0.122	0.890	4.980
$R_{\rm m}$ (Å)	6.41	5.29	5.01	7.18	5.40	5.34	7.33	5.70	5.31

Many different models exist for the interaction potentials $V(R)$ of ground-state alkali-metal–noble-gas pairs. For simplicity, we use a 6-12 Lennard–Jones form,

$$V(R) = \epsilon_{\rm m} \left(\frac{1}{r^{12}} - \frac{2}{r^6} \right), \text{ where } r = \frac{R}{R_{\rm m}} \tag{3.30}$$

is a dimensionless separation and $\epsilon_{\rm m}$ is the positive depth of a potential well minimum located at $R = R_{\rm m}$. Patil [87] gives a convenient summary of experimental or theoretical estimates for $\epsilon_{\rm m}$ and $R_{\rm m}$, which are listed in Table 3.3. Since the shift (3.2) is the combined result of both $\delta A(R)$ and $V(R)$, this choice of $V(R)$ will affect the results inferred for $\delta A(R)$. However, since we cannot uniquely determine $\delta A(R)$ from the shift (3.2), there is no real advantage to using a more realistic potential, such as from Buck and Pauli [88] or Pascale and Vandeplanque [89].

For the hyperfine-shift potential $\delta A(R)$, there are no standard models. Instead, we use an educated guess for the isotope-independent ratio,

$$\frac{\delta A(R)}{A} = \sum_{n=6,8,\ldots}^{P} \frac{a_n}{r^n} = \frac{a_6}{r^6} + \frac{a_8}{r^8} + \ldots + \frac{a_P}{r^P}, \tag{3.31}$$

where the maximal power P for $r = R/R_{\rm m}$ is chosen to truncate the series. Similar models with even powers of $1/R$ have been suggested before [68, 71, 73, 90]. Since both $\delta A(R)$ and $V(R)$ are due to the same interactions, the form of $\delta A(R)$ is likely similar to that of $V(R)$. The model (3.31) resembles the typical van der Waals

dispersion terms (e.g., C_6/R^6) in interaction potentials and the typical even-power terms in Lennard–Jones potentials.

Using the results of Section 3.2, we may determine the leading coefficient a_6 as follows. Comparing the model (3.31) with the asymptotic expression (3.9) and using the relation (3.10), we see that the leading coefficient is related to the van der Waals dispersion coefficient C_6 as

$$a_6 = \frac{A_6}{R_{\mathrm{m}}^6} \approx \frac{2C_6}{E_{\mathrm{a}} R_{\mathrm{m}}^6}. \tag{3.32}$$

Table 3.1 gives numerically estimated values for the characteristic energy E_{a} from Section 3.2, which depends only on the particular alkali-metal atom. For simplicity, we use the values

$$C_6 = -2\epsilon_{\mathrm{m}} R_m^6 \tag{3.33}$$

from the potential (3.30), which, using the parameters from Patil [87], are in reasonable agreement with the bounds of Standard and Certain [91]. As with choosing a model for $V(R)$, there is no real advantage to using more realistic values of C_6 for our purpose. Combining (3.32) and (3.33), the leading coefficient a_6 in the model (3.31) is then

$$a_6 \approx -4\frac{\epsilon_{\mathrm{m}}}{E_{\mathrm{a}}} < 0, \tag{3.34}$$

where the parameter ϵ_{m} is from Patil [87] and the energy E_{a} is from Table 3.1. Values of a_6 using (3.34) are given in Table 3.4.

With the exception of the leading coefficient a_6, which we determine above, the dimensionless parameters a_n in the model (3.31) for the hyperfine-shift potential are unknown. We now describe how to estimate these remaining parameters a_n, for $n \neq 6$,

from a measurement of the temperature dependence of the pressure shift, summarized by (3.29). Using the expression (3.2) with the interaction potential (3.30) and the model (3.31), we can calculate a theoretical pressure shift for a given set of parameters a_n. By inspection, we see that each coefficient a_n in the model (3.31) contributes independently in the expression (3.2), so we can write this theoretical shift as

$$\left(\frac{\delta\nu}{p_\mathrm{s}}\right)_\mathrm{th} = \frac{\nu_0}{kT_\mathrm{s}} \sum_{n=6,8,\ldots}^{P} a_n F_n(T), \tag{3.35}$$

where $T_\mathrm{s} = p_\mathrm{s}/(Nk)$ is the sealing temperature from the measurement, ν_0 is the measured free-atom frequency, and the functions

$$F_n(T) = 4\pi R_\mathrm{m}^n \int_0^\infty e^{-V(R)/kT} R^{2-n} dR \tag{3.36}$$

are independent of the parameters a_n. Examples of these functions for ^{85}Rb in Ar are sketched in Fig. 3.3. However, to compare this theoretical shift to the measured shift, we would like to summarize (3.35) using the same polynomial form as the fit

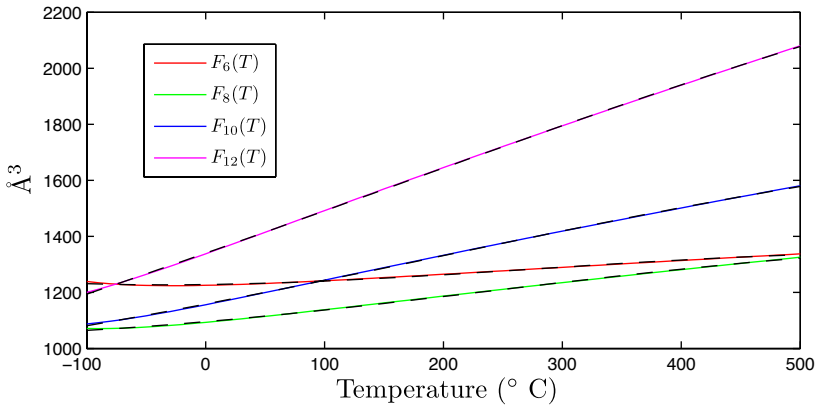

Figure 3.3: Example functions $F_n(T)$ of (3.36) for ^{85}Rb in Ar. The dashed lines are polynomial fits of the form (3.38).

(3.29) of the measurement,

$$\left(\frac{\delta\nu}{p_{\mathrm{s}}}\right)_{\mathrm{th}} \approx \sum_{m=0}^{D} d_m(\delta T)^m. \tag{3.37}$$

To relate the coefficients d_m in (3.37) to the unknown parameters a_n in (3.35), we could perform a linear least-squares fit of the theoretical shift (3.35) with the fit function (3.37) over the same temperature range used for the fit of the measurement. This is inconvenient, however, since the fit would have to be repeated to determine the new fit coefficients d_m for each choice of the parameters a_n. Instead, we note that in an overdetermined, linear least-squares fit of the theoretical shift (3.35) with the fit function (3.37), each term in the sum (3.35) contributes independently to the fit coefficients d_m in (3.37). As a result, if we instead perform a linear least-squares fit of each function $F_n(T)$ of (3.36) with a fit function of the same form as (3.37),

$$F_n(T) \approx \sum_{m=0}^{D} f_{mn}(\delta T)^m, \tag{3.38}$$

over the same temperature range as used for the measurements, then we may substitute the fit result (3.38) into the theoretical shift (3.35) to produce the fit result (3.37), which gives the relation

$$d_m = \sum_{n=6,8,\ldots}^{P} B_{mn}a_n, \text{ where } B_{mn} = \frac{\nu_0}{kT_{\mathrm{s}}} f_{mn}. \tag{3.39}$$

We now have the theoretical shift (3.35) expressed in the convenient form (3.37), with the fit coefficients d_m given by (3.39) in terms of the unknown parameters a_n in the model (3.31).

Comparing (3.37) with (3.29), we see that the theoretical shift (3.35) would reproduce the measured shift (3.29) if the two fitted polynomials match, or

$$\left(\frac{\delta\nu}{p_{\rm s}}\right)_{\rm th} = \left(\frac{\delta\nu}{p_{\rm s}}\right)_{\rm exp} \longleftrightarrow \; d_m = c_m. \tag{3.40}$$

Combining (3.39) and (3.40), we see that we can estimate $\delta A(R)$, a continuous function of R, by solving the linear system

$$c_m = \sum_{n=6,8,\ldots}^{P} B_{mn} a_n \tag{3.41}$$

for the unknown parameters a_n in the model (3.31). However, since we have already determined the leading parameter a_6, it will be convenient to simplify the system (3.41) by removing a_6 and its contributions to the c_m. If we write the set of unknown model parameters a_n as the vector

$$a = [a_8, a_{10}, \ldots, a_P], \tag{3.42}$$

where we have excluded a_6, and we write the measured coefficients c_m as the vector

$$c = [c_0, c_0, \ldots, c_D] - a_6[B_{06}, B_{16}, \ldots, B_{D6}], \tag{3.43}$$

where again we have removed the contribution from a_6, then we may rewrite (3.41) as the matrix equation

$$c = Ba, \tag{3.44}$$

where B is a $(D+1)$ by $(P/2-3)$ matrix with elements B_{mn} defined by (3.41). Therefore, we may estimate $\delta A(R)$, a continuous function of R, by solving the linear system (3.44) for the unknown model coefficients a_n in (3.42).

Unfortunately, we do not know what maximal power P to choose for the series (3.31). One choice is the smallest P that allows a solution of the system (3.44), which is typically $P = 2(D + 4)$, corresponding to a square matrix B that gives a unique solution. However, there is no reason to truncate the series (3.31) so short. For all other choices of P, the linear system (3.44) is underdetermined, since the matrix B has many more columns than rows. Thus, we cannot invert (3.44) to uniquely determine a and $\delta A(R)$. However, we can still solve the system (3.44) with pseudoinversion techniques. Since these solutions are not unique, we generate trial forms for $\delta A(R)$ by picking the solutions that are, in a sense, the simplest solutions, for which the vector a of (3.42) is minimized in one of three ways:

(i) the least-squares solution with $\|a\|_2 = \sum_n a_n^2$ minimized,

(ii) the compressive-sensing solution with $\|a\|_1 = \sum_n |a_n|$ minimized, and

(iii) the sparse solution with $\|a\|_0$ (the number of nonzero elements of a) minimized.

The least-squares solution (i) corresponds to a Moore–Penrose pseudoinverse [92, 93]. These solutions may be conveniently generated in MATLAB [94] with the function pinv(), the package l_1-MAGIC [95], and the function mldivision(), respectively. Except for the case where B is a square matrix, the minimizations (i)–(iii) usually give three different solutions. Minimization (ii) was only successful for some cases, while minimizations (i) and (iii) worked for all cases attempted.

We estimated trial forms for the potentials $\delta A(R)$ of Na, K, and Rb in He, Ne, or Ar gas for multiple values of P, using the T_s and measured coefficients c_m for ^{23}Na, ^{39}K, and ^{85}Rb from Bean and Lambert [75] (Table 3.2), the corresponding values of ν_0 from Arimondo *et al.* [53] (summarized in Section 2.1.1), the parameters ϵ_m and R_m from Patil [87] (Table 3.3), and the values for a_6 determined by (3.34). Remarkably, though the trial forms depend on the choice of P and minimization, (i)–(iii), their qualitative shapes are relatively consistent about the potential well

and initial repulsive region of $V(R)$. These shapes are also relatively insensitive to artificial changes to the coefficient a_6 by factors of 2. To demonstrate this stability, Fig. 3.4 shows a comparison of particular trials forms for the alkali-buffer pairs Na-He and Rb-Ar. Panel (a) is representative of all the pairs with He or Ne gas. Though the trial form changes quantitatively as P varies from 16 to 40, and with minimization (i) or (iii), the qualitative shape for $r \gtrsim 0.55$ is relatively unchanged. Panel (b) is representative of all pairs with Ar gas, which have a more complicated shape. Except for the outlier of $P = 14$, the qualitative shape of the trial form for $r \gtrsim 0.8$ is relatively unchanged for $P = 16$–40 and with minimization (i)–(iii). For Na-Ar, the smallest-P

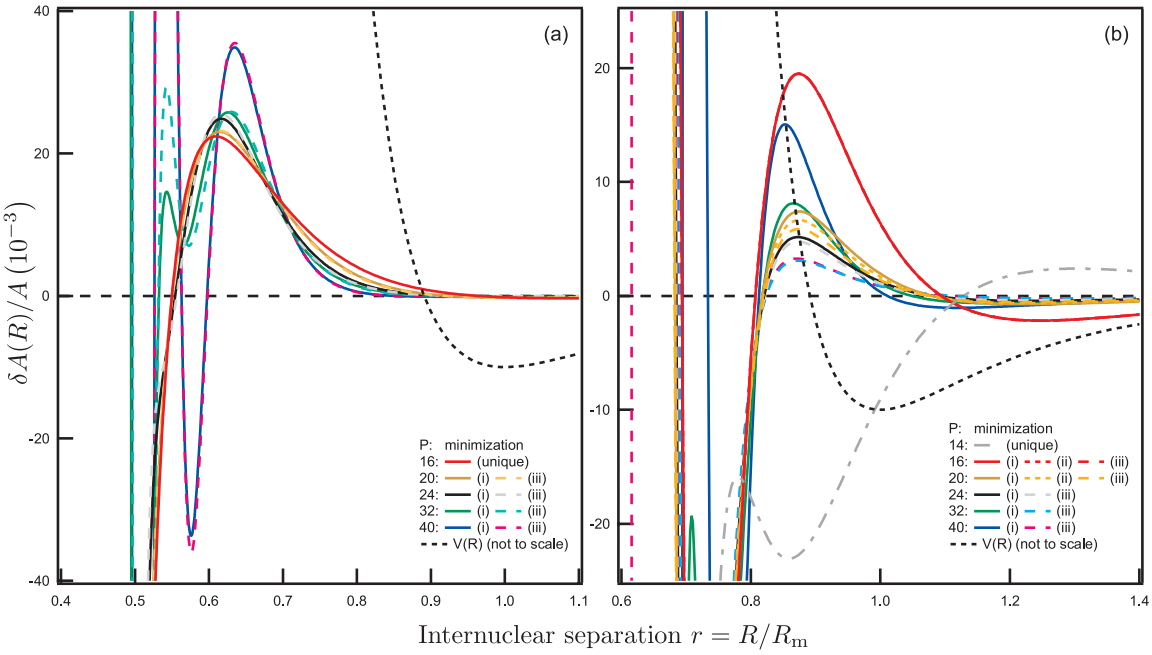

Figure 3.4: Consistency of trial forms of $\delta A(R)$ with different P and minimization (i)–(iii). (a) Na-He, which is representative of all pairs with He or Ne. (b) Rb-Ar, which is representative of all pairs with Ar. Except for the outlier of $P = 14$ with Rb-Ar, the qualitative shapes are relatively insensitive to the choice of P and of minimization, for $r \gtrsim 0.55$ for Na-He and $r \gtrsim 0.8$ for Rb-Ar. The solutions for the same P but different minimizations (i)–(iii) are usually very similar; for example, the three $P = 16$ Rb-Ar solutions are visually indistinguishable. The solutions usually evolve smoothly as P is varied. Solutions for (ii) are shown where successful.

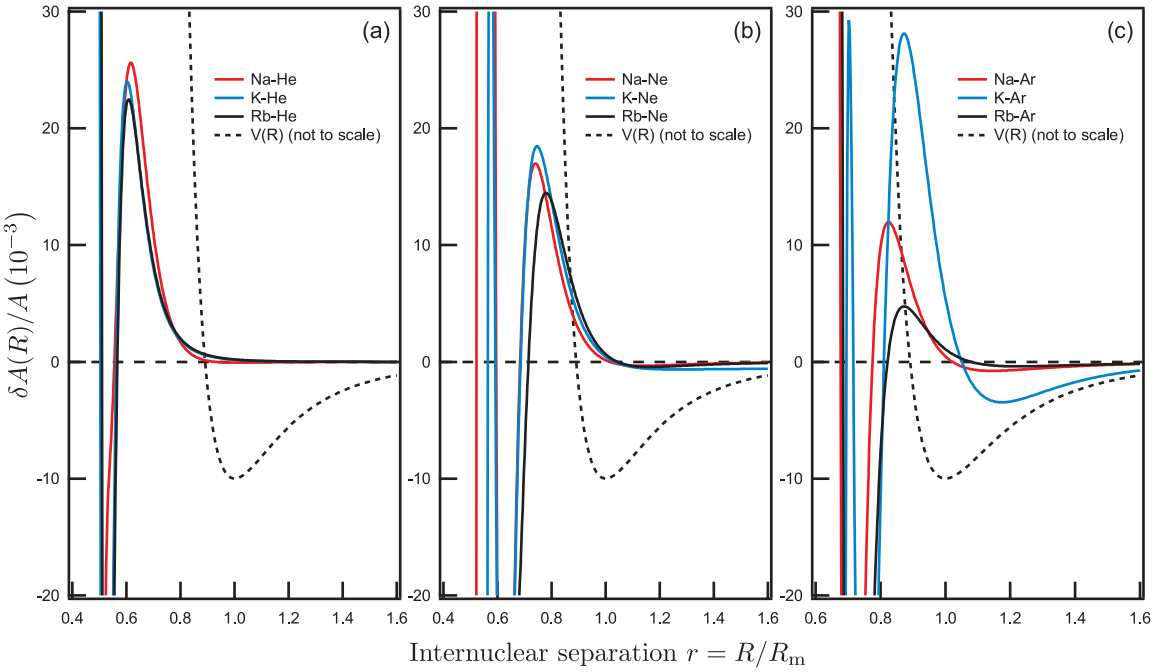

Figure 3.5: Representative trial forms of $\delta A(R)$ with the parameters of Table 3.4. The trial forms are grouped according to buffer gas, since the shapes are qualitatively similar for the same gas. Interaction potentials $V(R)$ are included for reference, and are not to scale.

solution is not an outlier, and has the same shape as the other solutions. For the pair K-Ar, however, the solutions for P =16–22 seem to be outliers.

Representative solutions with $P = 24$ and minimization (iii) are shown in Fig. 3.5, and given by the parameters in Table 3.4. We chose the maximal power $P = 24$ since it gives similar results for the different minimizations (i)–(iii), and works for the worst-case pair K-Ar. Remarkably, the qualitative shapes of these agree well with the theoretical calculations for Na-He, K-He, and Rb-He by Oreto *et al.* [70], with the experimental results for K-Ar of Freeman *et al.* [96, 97], and with the experimental results for Rb-Ar of Gong *et al.* [39]. We do not expect the qualitative shapes of these solutions to be reliable further inward than $r \sim 0.55$, 0.60, and 0.75 for panels (a), (b), and (c) of Fig. 3.5, respectively.

All of the shapes in Fig. 3.5 demonstrate that, though $\delta A(R)$ and $V(R)$ arise from the same interactions, they do not in general have the same shape. Thus, the

Table 3.4: Parameters for the trial forms of $\delta A(R)$ shown in Fig. 3.5. Arranged by buffer gas, each row gives the leading coefficient a_6 of (3.34), and the nonzero parameters a_n (dimensionless) for the model (3.31) obtained by solving (3.44) with maximal power $P = 24$ and sparse minimization (iii). The notation "xE-y" is shorthand for $x \times 10^{-y}$.

Metal	Gas	a_6	a_8	a_{10}	a_{12}	a_{14}	a_{16}	a_{18}	a_{20}	a_{22}	a_{24}
Na	He	-9.072E-5	–	–	–	-1.722E-4	–	4.642E-4	-3.581E-4	9.674E-5	-8.905E-6
K	He	-9.115E-5	2.545E-4	–	–	–	–	3.019E-6	-9.751E-6	-2.111E-6	6.660E-7
Rb	He	-9.644E-5	2.841E-4	–	–	–	–	2.722E-5	-5.909E-6	-3.856E-6	9.177E-7
Na	Ne	-6.131E-4	-1.304E-3	–	–	3.229E-3	–	-1.368E-3	–	2.483E-4	-4.481E-5
K	Ne	-5.740E-4	-1.215E-3	–	–	3.642E-3	–	-1.684E-3	–	3.409E-4	-6.598E-5
Rb	Ne	-7.036E-4	-2.657E-3	–	–	7.285E-3	–	-4.093E-3	–	1.059E-3	-2.349E-4
Na	Ar	-3.380E-3	7.228E-4	–	–	–	5.997E-3	–	-3.291E-3	–	4.285E-4
K	Ar	-3.956E-3	-2.349E-2	–	–	–	1.155E-1	–	-1.891E-1	1.328E-1	-2.625E-2
Rb	Ar	-3.937E-3	3.391E-3	–	–	–	4.073E-3	–	-2.868E-3	–	4.297E-4

potential $\delta A(R)$ should not be expected to have a minimum at roughly the same location as that of $V(R)$, which had been suggested by Camparo [73]. The shapes of the pairs with Ar demonstrate that, in addition to a zero-crossing near the minimum of $V(R)$, which was inferred for K-Ar by Freeman *et al.* [97] and suggested for Rb-Ar by Gong *et al.* [39], the temperature dependence of the shift (3.2) predicts that there must be another zero-crossing in the region where the potential $V(R)$ begins to be repulsive as R decreases. This predicted zero-crossing explains the discrepancy in the calculation of the pressure shift by Freeman *et al.* [97] with an experimentally inferred $\delta A(R)$, which was previously attributed to the small anisotropic interactions that may be important in molecular-beam experiments, but which average out in the shift (3.2).

3.4 Summary and discussion

In summary, we have provided an improved estimate of the large-R asymptote of the ratio $\delta A(R)/V(R)$ for Na, K, Rb, and Cs, and have demonstrated how to use measurements of the pressure shift to estimate simple trial forms for the potential $\delta A(R)$ in the hyperfine-shift interaction (3.1) of Na, K, and Rb in He, Ne, or Ar gas. Though these trial forms are not unique, they still yield a surprising amount of information about the shapes of $\delta A(R)$ about a potential well in the interaction potential $V(R)$, which agree with the few available theoretical and experimental results. We hope this work encourages renewed study of the poorly known potentials $\delta A(R)$, which, for example, are important to the study of the shifting and broadening of hyperfine resonances in vapor-cell atomic clocks [70, 73], to the study of spin interactions in alkali-metal–noble-gas van der Waals molecules [39, 31], such as in the next chapter, and are anticipated to aid the formation of ultracold molecules such as RbSr [98].

Chapter 4

Pressure shifts from van der Waals molecules

4.1 Introduction

The microwave resonant frequencies ν of a dilute vapor of alkali-metal atoms in a chemically inert buffer gas are shifted away from the free-atom frequencies ν_0 by collisions. As described in the previous chapter, this pressure shift, $\nu - \nu_0$, is very nearly linear with the buffer-gas pressure, and depends on the buffer-gas composition and temperature. Most of this shift is due to binary collisions between the alkali-metal atoms and the buffer gas. However, recent precision measurements by Gong *et al.* [39, 40] discovered that the pressure shift may have a nonlinear dependence on the buffer-gas pressure, which is presumably due to the short-lived van der Waals molecules that are known to form between certain pairs of alkali-metal and noble-gas atoms [37, 38]. The frequency shifts, $\nu - \nu_0$, can be measured very precisely, and are one of the few measurable phenomena that can provide information about spin interactions in van der Waals molecules, which are of considerable current interest [99, 100].

Here we present surprising results from precision measurements of the shifts of the 0–0 resonant frequencies ν of ^{87}Rb, ^{85}Rb, and ^{133}Cs atoms in He, Ne, N_2, Ar, Kr, and, in particular, Xe gas [31, 32, 33, 34, 35, 36]. We show that the nonlinear shifts for Xe are opposite in sign to the shifts for Ar and Kr, even though all three have negative linear shifts. The Xe data show striking discrepancies with the previous theory for nonlinear shifts [39, 40], which assumes that the shift is entirely due to the hyperfine-shift interaction,

$$H_{\rm hfs} = \delta A\, \mathbf{I} \cdot \mathbf{S}, \tag{4.1}$$

which was the subject of Chapter 3. We show that most of this discrepancy is eliminated by accounting for the spin-rotation interaction [41, 42],

$$H_{\rm sr} = \gamma\, \mathbf{N} \cdot \mathbf{S}, \tag{4.2}$$

between the rotational angular momentum $\mathbf{N}$ of a molecule and the electronic spin $\mathbf{S}$, in addition to the hyperfine-shift interaction (4.1) in van der Waals molecules. The spin-rotation interaction (4.2) leads to significant spin relaxation of optically pumped alkali-metal atoms, which is often referred to as S-damping [21]. Like the hyperfine-shift potential $\delta A = \delta A(R)$ in (4.1), the isotope-independent parameter $\gamma = \gamma(R)$ in (4.2) depends on the internuclear separation R of a colliding pair. However, much more is known about $\gamma(R)$ than $\delta A(R)$ [42, 101, 102].

Before we begin, we first provide some background on alkali-metal–noble-gas van der Waals molecules.

4.1.1 Van der Waals molecules

A van der Waals molecule is a weakly bound complex of at least two atoms or molecules that are held together by polarization forces instead of chemical bonds

[103, 104]. For example, while the noble gases do not react chemically with the alkali metals, they may still form alkali-metal–noble-gas van der Waals molecules. The importance of these molecules to the spin relaxation of optically pumped alkali-metal atoms in Ar, Kr, and Xe was discovered almost forty years ago by Bouchiat *et al.* [37, 38, 105, 106]. Van der Waals molecules also play an important role in the polarization of ^{129}Xe by spin-exchange optical pumping [99].

Consider a dilute vapor of Rb atoms immersed in a Xe gas at a pressure of several Torr. Besides binary (two-body, simple, or sudden) collisions, there will also be occasional three-body collisions. As sketched in Fig. 4.1, some of these three-body collisions may produce a van der Waals molecule, which lasts until another collision with the buffer gas breaks up the molecule. Though these sticking collisions are rare, the typical lifetime of a molecule ($\tau \approx 1$ ns) is much longer than that of a binary collision ($\tau_b \approx 1$ ps), so the effects of van der Waals molecules may still be significant.

We can estimate the number of van der Waals molecules in a typical vapor cell as follows. Let [Rb] denote the number density of Rb atoms, and let M be the number density of molecules, for example, [RbXe]. For low buffer-gas pressures, the density

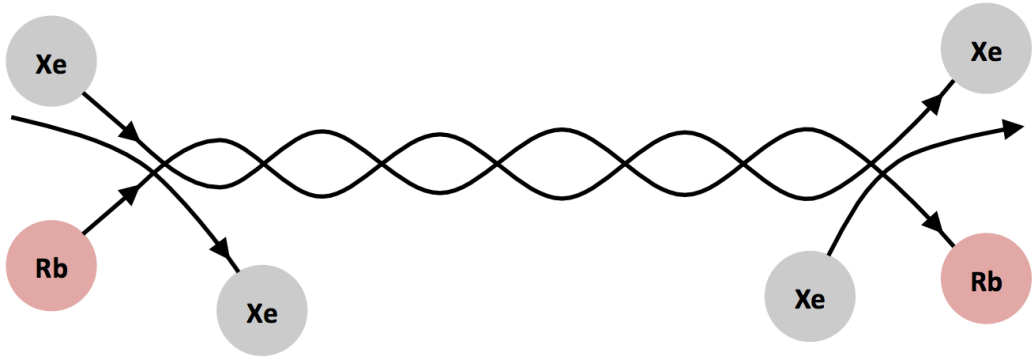

Figure 4.1: Sketch of the formation and breakup of a RbXe van der Waals molecule for Rb in Xe buffer gas. Starting on the left, a three-body collision, $\mathrm{Rb} + \mathrm{Xe} + \mathrm{Xe} \longrightarrow \mathrm{RbXe} + \mathrm{Xe}$, forms a RbXe molecule that is later broken up by another collision, $\mathrm{RbXe} + \mathrm{Xe} \longrightarrow \mathrm{Rb} + \mathrm{Xe} + \mathrm{Xe}$. In each collision, a second free Xe atom is required to carry away (or contribute) the excess energy needed to bind (or release) the molecule from a potential well in the Rb-Xe interaction potential.

Table 4.1: Characteristic parameters for Rb–noble-gas van der Waals molecules measured by Bouchiat *et al.* [38, 106] at room temperature (300 K): molecular formation rate $1/T$, molecular lifetime τ, root-mean-square (rms) value of the rotational angular momentum N^*, rms value of the spin-rotation interaction (4.2) coupling coefficient γ, and rms value of the characteristic magnetic field $H_1^* = \gamma N^*/(g_S \mu_B)$. The pressure-dependent parameters T and τ assume a pure Ar, Kr, or Xe gas of pressure p.

Molecule	Tp^2 (ms Torr^2)	τp (ns Torr)	N^*	γ/h (MHz)	H_1^* (G)
RbAr	16.1 ± 1.3	48.5 ± 1.9	30.5–33.3	0.105 ± 0.018	1.19 ± 0.05
RbKr	10.6 ± 0.5	56.9 ± 1.7	41.5	0.657 ± 0.018	9.59 ± 0.28
RbXe	4.29 ± 0.23	34–61	63.2–76.7	34–61	38.1 ± 1.6

M evolves as

$$\frac{dM}{dt} = \frac{1}{T}[\mathrm{Rb}] - \frac{1}{\tau}M, \tag{4.3}$$

where $1/T$ is the molecular formation rate per alkali-metal atom, and τ is a characteristic molecular lifetime. Table 4.1 gives experimental values for T and τ inferred by Bouchiat *et al.* [38, 106], along with other characteristic parameters for Rb–noble-gas molecules. As the table shows, the parameters T and τ depend on the buffer-gas pressure p, but the parameters Tp^2 and τp are independent of pressure. In terms of these pressure-independent parameters, the evolution (4.3) is

$$\frac{dM}{dt} = \frac{p^2}{(Tp^2)}[\mathrm{Rb}] - \frac{p}{(\tau p)}M. \tag{4.4}$$

We see that sticking collisions produce molecules at a rate proportional to p^2, and that collisions breakup the molecules at a rate proportional to p. The equilibrium density that satisfies $dM/dt = 0$ is

$$M = \frac{(\tau p)p}{(Tp^2)}[\mathrm{Rb}], \tag{4.5}$$

which is linear with the buffer-gas pressure. Using the parameters for RbXe in Table 4.1, the bound fraction $M/[\mathrm{Rb}] = [\mathrm{RbXe}]/[\mathrm{Rb}] \approx 1.1 \times 10^{-5} \times (p \text{ in Torr})$, which means that the fraction of Rb atoms bound in a RbXe molecule will vary from about 10^{-5} at 1 Torr to about 10^{-3} at 100 Torr of Xe gas. At a temperature of 40.0° C, the density $[\mathrm{Rb}] \approx 6 \times 10^{10}$ cm^{-3} [52]. For a typical vapor cell of volume $V \approx 7$ cm^3, the total number of Rb atoms is $[\mathrm{Rb}]V \approx 4 \times 10^{11}$, while the total number of RbXe molecules $[\mathrm{RbXe}]V \approx 5 \times 10^6 \times (p \text{ in Torr})$. Since conventional vapor-cell clocks typically use buffer-gas mixtures of mostly Ar with some N_2 [11, 16], they will contain a comparable number of RbAr molecules.

The heavy noble gases Ar, Kr, and Xe may form molecules with alkali-metal atoms in many (hundreds of) vibration-rotation states [107, 108]. As shown in Table 4.1, the characteristic values for the rotational angular momentum $N = |\mathbf{N}|$ of these molecules are quite large, so much so that the molecular states may often be approximated with a classical distribution [37, 109, 110]. In contrast, the lighter noble gas Ne may form molecules with only a few (tens of) vibration-rotation states, and He with even less, if any molecules are formed at all. In addition to bound vibration-rotation states, there are a smaller number of quasibound (or resonant diffusion) states that may also form in binary collisions and spontaneously breakup before the next collision. These additional quasibound processes are not expected to contribute significantly for Ar, Kr, or Xe [37], in part because many quasibound molecules should survive long enough to effectively behave as bound molecules in practice [107, 108]. There is some disagreement over the significance of quasibound molecules with He and Ne [111, 112, 113, 114, 115]. However, the precision measurements of Gong *et al.* [39] provide evidence against any significant formation of molecules with He, and this chapter provides evidence against any significant formation with Ne.

While bound in a van der Waals molecule, an alkali-metal atom evolves very much like a free alkali-metal atom, but with the same perturbing interactions that

are present in binary collisions. For example, besides the interactions (4.1) and (4.2), the interaction potentials that are responsible for the interatomic forces during a collision also strongly disturb the optical resonance lines of alkali-metal atoms in molecules [116]. Overall, this molecular structure is remarkably simple compared to more typical molecular structures, which are quite complicated in general [117].

While there was speculation about significant pressure shifts from van der Waals molecules [19, 105] shortly after the discovery of the importance of such molecules in vapor cells by Bouchiat *et al.* [37], it took almost four decades before these shifts were first measured [39]. Experimentally, the pressure shifts from van der Waals molecules are distinguishable from those of binary collisions because they depend on the buffer-gas pressure in a nonlinear manner, as we will see in this chapter. Interestingly, Bouchiat *et al.* [105] predicted that the spin-rotation interaction (4.2) should not contribute to any molecular shift of the 0–0 transition. Before we continue, we note that van der Waals molecules also contribute significantly to the linear pressure shift at high buffer-gas pressures. This is important, for example, when buffer gases are mixed, since the resulting linear pressure shift will depend on how the mixture affects the formation and breakup of any van der Waals molecules.

4.2 Hyperfine frequencies of ^{87}Rb and ^{133}Cs atoms in Xe gas

Gong *et al.* [39] showed that one would expect the pressure shifts from Xe to have a nonlinear dependence on the Xe pressure p because of the formation of van der Waals molecules in three-body collisions between two Xe atoms and a Rb atom, as sketched in Fig. 4.1. For a Rb atom bound in a RbXe molecule the precession of the nuclear spin $\mathbf{I}$ and the electronic spin $\mathbf{S}$ about each other is perturbed by the hyperfine-shift interaction (4.1), which acts until the molecule is broken up in a collision with another

Xe atom. The same interaction (4.1) acts impulsively when an alkali-metal atom has a binary collision with a buffer-gas atom or molecule. Following Gong *et al.* [39], we fit our measured 0–0 hyperfine frequencies ν to a theoretical function of pressure,

$$f_0 = \nu_0 + sp + \Delta_0^2\nu, \tag{4.6}$$

where the nonlinear shift is

$$\Delta_0^2\nu = -\left(\frac{1}{2\pi T}\right)\frac{\phi^3}{1+\phi^2}. \tag{4.7}$$

The theoretical function (4.6) is characterized by four parameters:

(i) the free-atom frequency ν_0, which varies daily by a few Hz because of drifts in the ambient magnetic field of our laboratory;

(ii) the "slope" s, which represents the linear shifts due to binary collisions and three-body collisions at high pressures [39];

(iii) the formation rate $1/T \propto p^2$ of molecules in three-body collisions; and

(iv) the differential phase shift $\phi = \delta A[I]\tau/(2\hbar) \propto 1/p$ of the atomic coherence after a mean bound-atom lifetime τ.

Here, $[I] = 2I + 1$ denotes the number of sublevels for a spin of quantum number I. Table 4.2 lists the values of these parameters reported by Gong *et al.* [39]. We will derive the fit function (4.7) in Section 4.5. Here, and subsequently in this chapter, it is to be understood that the values of coupling coefficients, such as δA, should be expectation values for van der Waals molecules.

In Fig. 4.2(a) we plot the measured shift

$$\delta\nu_1 = \nu - \nu_0 \tag{4.8}$$

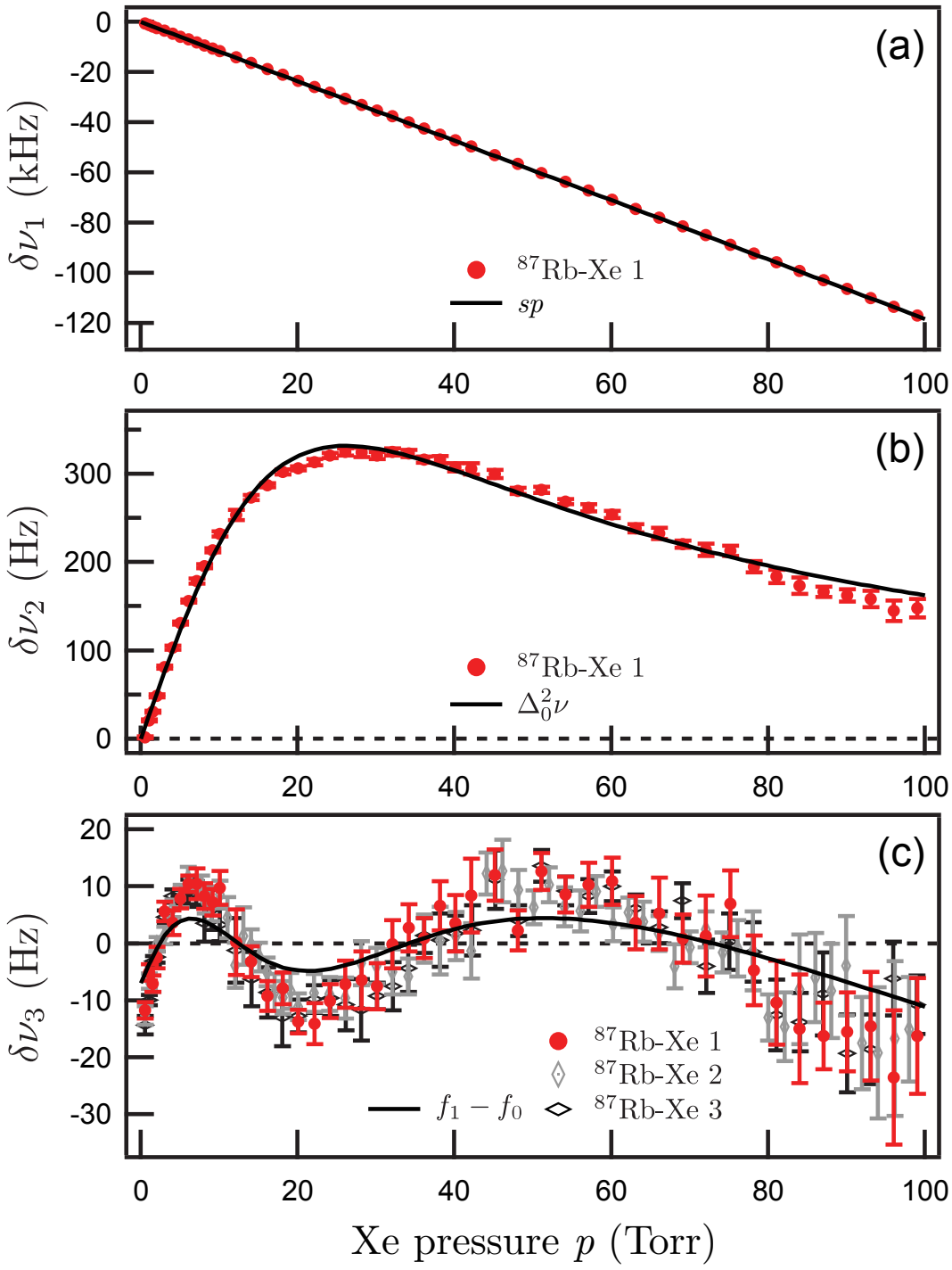

Figure 4.2: Measured 0–0 resonant frequencies ν of ^{87}Rb in Xe at 40.0° C and $B = 1$ G. (a) The shift $\delta\nu_1 = \nu - \nu_0$ from the free-atom frequency $\nu_0 \approx 6.834683$ GHz. The solid line is the linear, limiting shift sp at high pressures. (b) The nonlinear shift $\delta\nu_2 = \delta\nu_1 - sp$. The solid curve is the nonlinear shift $\Delta_0^2\nu$ of (4.7). (c) The fit residuals to (4.6), $\delta\nu_3 = \delta\nu_2 - \Delta_0^2\nu = \nu - f_0$. The solid curve is the difference, $f_1 - f_0$, of the best-fit theoretical curves, with and without the spin-rotation interaction (4.2). Three separate data sets demonstrate the repeatability of the measurements.

Table 4.2: Previous fit parameters for the pressure shifts of ^{87}Rb at 40°C and of ^{133}Cs at 35°C in different buffer gases from Gong *et al.* [39, 40]. These fit parameters might be influenced by a nonlinearity in pressure measurement, as discussed in Section 4.4.1.

Metal	Gas	Tp^2 (sec Torr^2)	ϕp (rad Torr)	s (Hz Torr^{-1})
^{87}Rb	Ar	0.094 ± 0.025	2.69 ± 0.22	-54.26
	Kr	1.287 ± 0.096	25 ± 2.13	-559.58
	He			714.3
	N_2			518.4
^{133}Cs	Ar	0.05 ± 0.01	3.90 ± 0.44	-194.3
	Kr	0.153 ± 0.015	14.82 ± 0.74	-1123
	He			1132.86
	N_2			824.6

of ^{87}Rb in Xe at 40.0°C. The free-atom frequency ν_0 was obtained by fitting the data to the model (4.6). The solid curve is sp, the linear part of (4.6). The apparent linearity of the shift $\delta\nu_1$ is deceptive, as shown in Fig. 4.2(b), where we plot

$$\delta\nu_2 = \delta\nu_1 - sp = \nu - \nu_0 - sp. \tag{4.9}$$

This reveals the highly nonlinear nature of the shift. The solid curve in Fig. 4.2(b) is the nonlinear shift $\Delta_0^2\nu$ of (4.6). Once more, the apparently good agreement between the measured $\delta\nu_2$ and the predicted $\Delta_0^2\nu$ is deceptive, as shown in Fig. 4.2(c), where we plot the fit residuals

$$\delta\nu_3 = \delta\nu_2 - \Delta_0^2\nu = \nu - f_0. \tag{4.10}$$

The residuals $\delta\nu_3$ have a striking, oscillatory behavior, which is the same for three independent sets of measurements. Similar residuals $\delta\nu_3$ are seen with ^{133}Cs in Xe, as shown in Fig. 4.3.

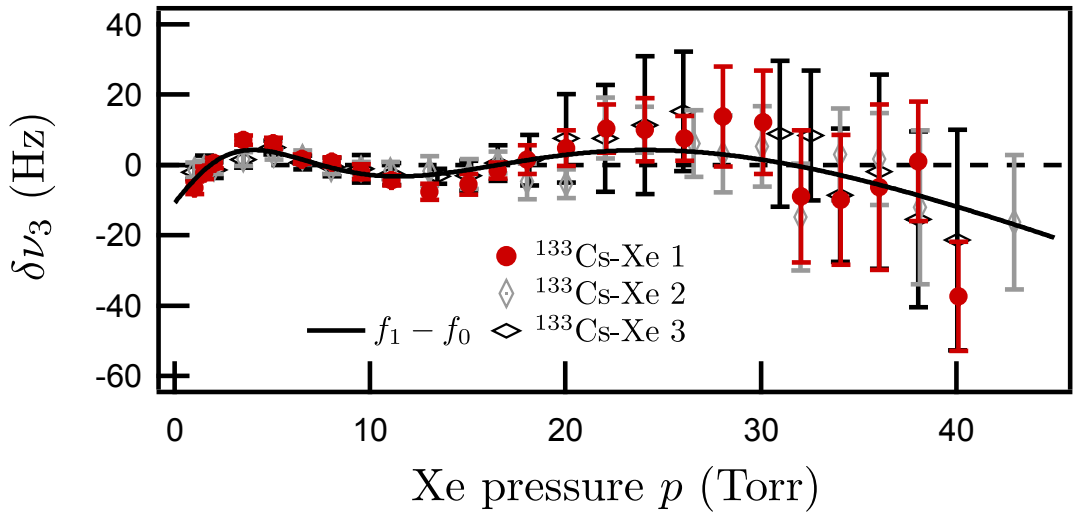

Figure 4.3: The fit residuals $\delta\nu_3$ to (4.6) for the measured 0–0 resonant frequencies ν of ^{133}Cs in Xe at 35.0° C and $B = 0.2$ G. As in Fig. 4.2(c), the solid curve is the difference, $f_1 - f_0$, of the best-fit theoretical curves, with and without the spin-rotation interaction (4.2), and three separate data sets demonstrate the repeatability of the measurements.

To derive the nonlinear shift (4.7), Gong *et al.* [39] assumed that van der Waals molecules form in a single vibration-rotation state in which the evolution of **I** and **S** is perturbed by the hyperfine-shift interaction (4.1). Two problems with this assumption are:

(i) the van der Waals molecules can form in many (hundreds of) vibration-rotation states [107, 108], each with different values of the shift parameter δA and of T and ϕ; and

(ii) the effects of spin interactions other than (4.1), such as the spin-rotation interaction (4.2), are ignored.

The interaction (4.2) is particularly large for RbXe or CsXe molecules, and is equivalent to a magnetic field, of roughly 38 G for RbXe, oriented along **N** [42, 38]. Both interactions (4.1) and (4.2) need to be included in an improved theory of nonlinear pressure shifts.

Here, we show that for ^{87}Rb or ^{133}Cs in Xe, most of the discrepancy between theory and experiment is eliminated by including the effects of the spin-rotation interaction (4.2) in a model that still has only one vibration-rotation state. The function (4.6) must be replaced by

$$f_1 = \nu_0 + sp + \Delta_1^2\nu, \tag{4.11}$$

where the nonlinear shift that includes the effects of both (4.1) and (4.2) is

$$\Delta_1^2\nu = -\left(\frac{1}{2\pi T}\right)\sum_{\sigma=-2I}^{2I}\frac{W_\sigma(1+r_1\sigma)^3\phi^3}{1+(1+r_1\sigma)^2\phi^2}. \tag{4.12}$$

The parameter $r_1 = 2\gamma N/(\delta A[I]^2)$ accounts for the spin-rotation interaction (4.2). We will discuss the meaning of the remaining symbols of (4.12) and its derivation below.

We refit our data to the revised function (4.11), where we constrained the new parameter r_1 by estimating

$$r_1\phi p = \frac{\gamma N\tau p}{[I]\hbar} \tag{4.13}$$

from measurements of $\langle\gamma N\rangle$ and $\langle\tau p\rangle$ for RbXe by Bouchiat *et al.* [38]. We do not show the fits of (4.11) corresponding to Fig. 4.2(a)–(b), since they look very similar to the fits of (4.6). However, as Table 4.3 shows, the fits to (4.11) give substantially different values for the parameters T and ϕ. In Fig. 4.2(c) the solid line is the difference, $f_1 - f_0$, between the two theoretical fit functions. The revised curve f_1 gives substantially smaller residuals, and displays the same oscillatory behavior with pressure. Similar results are seen with ^{133}Cs in Xe, as shown in Fig. 4.3. The remaining residuals are probably due to the distribution of vibration-rotation states of the van der Waals molecules, or the neglect of still-smaller spin interactions, such

Table 4.3: Fit parameters for the pressure shifts of ^{87}Rb at 40°C and $B = 1$ G and of ^{133}Cs at 35°C and $B = 0.2$ G. Uncertainties for the slopes s are typically $\pm 0.25\%$.

Metal	Gas	$r_1\phi p$ (rad Torr)	Tp^2 (sec Torr^2)	ϕp (rad Torr)	s (Hz Torr^{-1})
^{87}Rb	Xe	7.97	0.082 ± 0.010	-14.8 ± 1.5	-1184.0
	Xe	–	0.164 ± 0.013	-26.2 ± 1.2	-1183.7
	Ar	–	0.070 ± 0.012	2.21 ± 0.16	-53.71
	Kr	–	1.08 ± 0.31	12.5 ± 1.9	-558.1
	He				714.2
	Ne				387.3
	N_2				518.0
^{133}Cs	Xe	2.79	0.0185	-5.96	-2243.9
	Xe	–	0.059 ± 0.006	-15.8 ± 1.3	-2242.4
	He				1141.9
	Ne				579.9
	N_2				828.6

as the anisotropic hyperfine-shift interaction or the electric quadrupole interaction, which we explore in the next section.

To understand the origin of the formulas (4.7) and (4.12), which we will derive in Section 4.5, note that when a clock atom is captured in a van der Waals molecule, the microwave coherence frequency changes slightly. Gong *et al.* [39] ignored the spin-rotation interaction (4.2) and assumed that the coherence frequency was shifted by the amount $\delta\omega = \delta A[I]/(2\hbar)$, leading to the mean phase shift $\phi = \delta\omega\,\tau$. The form of the function (4.7) describes how a statistical ensemble of molecular lifetimes shifts the resonant frequency ν.

The generalization (4.12) is a superposition of functions with the same form as (4.7), each labeled by an integer σ, with a weight W_σ and with a mean phase shift $\phi \to (1 + r_1\sigma)\phi$. Assuming the Zeeman interaction $g_S\mu_B S_z B$ with an external magnetic field B is negligible compared to the spin-rotation interaction (4.2), the ground-state sublevels $|F\,m\rangle$ for a bound clock atom will be quantized with the azimuthal quantum number m along the rotational angular momentum $\mathbf{N}$. The total spin an-

gular momentum quantum number is $F = a = I + 1/2$ or $F = b = I - 1/2$. The interactions (4.1) and (4.2) shift the sublevel energies as shown in Fig. 4.4. We can write the shift in the Bohr frequency of a coherence between sublevels $|a\,m\rangle$ and $|b, \sigma - m\rangle$ as $\delta\omega_\sigma = (\delta E_{am} - \delta E_{b,\sigma-m})/\hbar = \delta A[I](1 + r_1\sigma)/(2\hbar)$. The weights account for the fraction of the unbound-atom coherence that evolves with the frequency shift $\delta\omega_\sigma$ in the molecule. Averaging over an isotropic distribution of quantization directions gives the weights as the sum of Clebsch-Gordan coefficients [54],

$$W_\sigma = \sum_{\mu k} \frac{(-1)^\sigma}{[k]} C^{k0}_{a0;a0} C^{k0}_{a,\mu;a,-\mu} C^{k0}_{b0;b0} C^{k0}_{b,\sigma-\mu;b,\mu-\sigma}. \tag{4.14}$$

For ^{87}Rb with $I = 3/2$, (4.14) becomes $[W_3, \ldots, W_{-3}] = [9, 9, 23, 23, 23, 9, 9]/105$. The weights W_σ for other alkali-metal atoms are given in Section 4.5.4. As we show later, the weights depend on the choice of the unbound-atom hyperfine coherence, and the nonlinear shifts (4.12) will be different for clocks that do not use the 0–0 transition, for example, "end-resonance" clocks [44] or lin‖lin clocks [55]. The weights satisfy $\sum_\sigma W_\sigma = 1$, so if we let $r_1 \longrightarrow 0$ in (4.12) we recover (4.7). We also recover

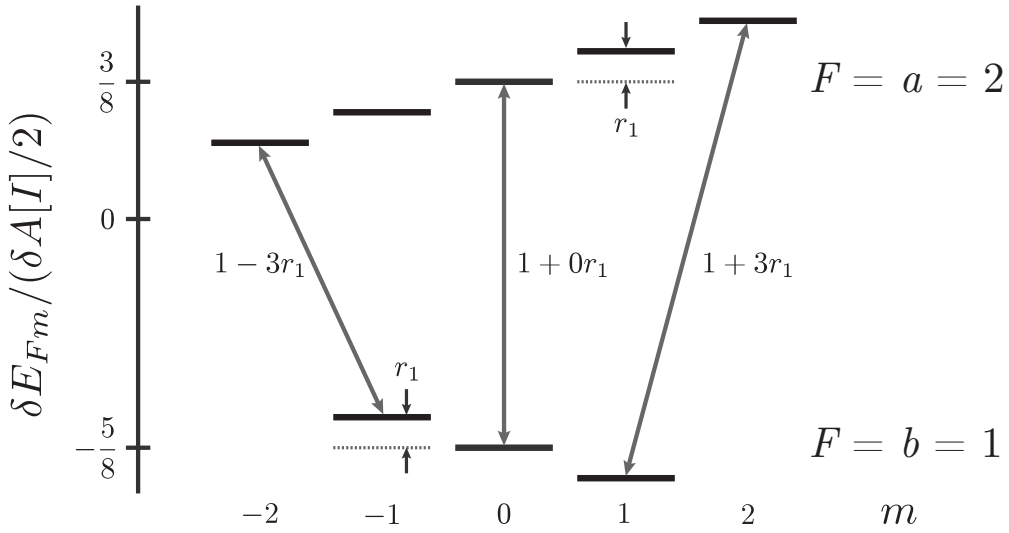

Figure 4.4: Energy shifts of the sublevels of a ^{87}Rb atom in a van der Waals molecule due to interactions (4.1) and (4.2). Representative perturbations $1 + r_1\sigma$ of the coherence frequencies are shown. The sublevels are quantized along **N**.

(4.7) in the limit that the spin-rotation interaction (4.2) is negligible compared to the interaction $g_S \mu_B S_z B$. Between the small-B and large-B limits, the nonlinear shifts from van der Waals molecules will depend on the applied field B. In all cases, the analysis leading to (4.12) predicts a molecular contribution $s_{\rm m} = \phi/(2\pi T p)$ to the slope s of (4.6) or (4.11) for the 0–0 transition.

Figs. 4.5 and 4.6 summarize our experimental measurements. As Fig. 4.6(a) shows, the nonlinear shifts in Xe are relatively large and opposite in sign compared to those in Ar and Kr. Table 4.3 lists the pressure-independent fit parameters for the data. The linear shifts s are consistent with previous work [39, 30, 75, 118]. For Xe, results are provided for both fit functions (4.6) and (4.11). For ^{133}Cs in Xe, we fit to f_1 of (4.11) with r_1 as a free parameter, since we were unable to estimate $r_1 \phi p$, as we did for ^{87}Rb, due to a lack of experimental data for $\langle \tau p \rangle$. Because of this, and the reduced pressure range, the fit returned unrealistic uncertainties, not shown in Table 4.3. For ^{87}Rb in Ar and Kr, we did not fit with f_1 of (4.11) since the effects of the applied field B may be important. Instead, we fit with the f_0 of (4.6) to provide improved

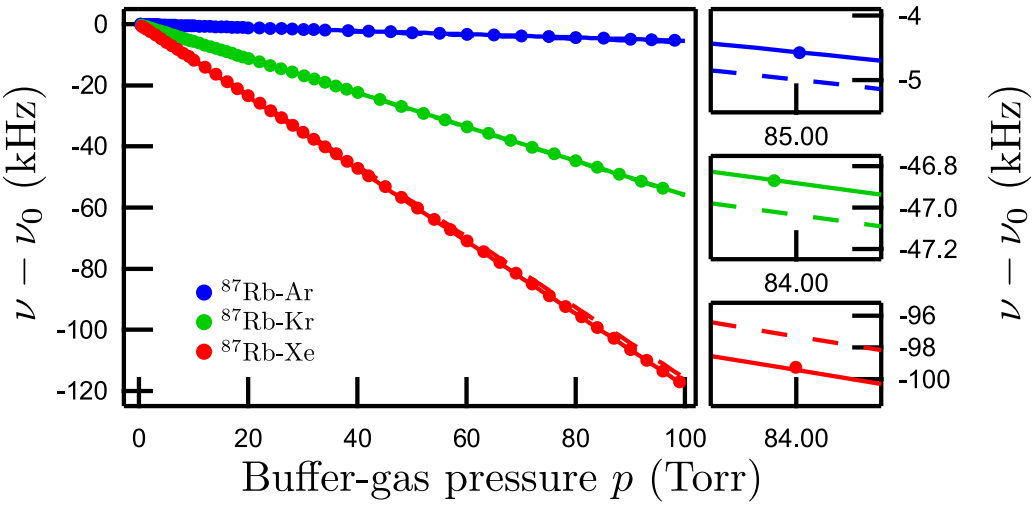

Figure 4.5: Measured 0–0 resonant frequencies ν of ^{87}Rb in Ar, Kr, or Xe at 40.0° C and $B = 1$ G, with zero-pressure frequency $\nu_0 \approx 6.834683$ GHz removed. Error bars are too small to display. Solid dots are the data, solid lines are the linear limiting shifts sp, and dashed lines are the binary shifts $s_{\rm b} p$, where $s_{\rm b} = s - s_{\rm m}$. Insets show that the limiting shift is above the binary shift for Ar and Kr, but below for Xe.

results over those of Gong *et al.* [39], given in Table 4.2. The new values for Tp^2 and ϕp agree, with the exception of ϕp for ^{87}Rb in Kr, which is roughly half the value of 25 ± 2.13 rad Torr reported by Gong *et al.* [39]. As a result, we suspect that the previous results may be biased by a nonlinearity in pressure measurement, as described in Section 4.4.1, which we corrected for in our independent measurements using (4.18).

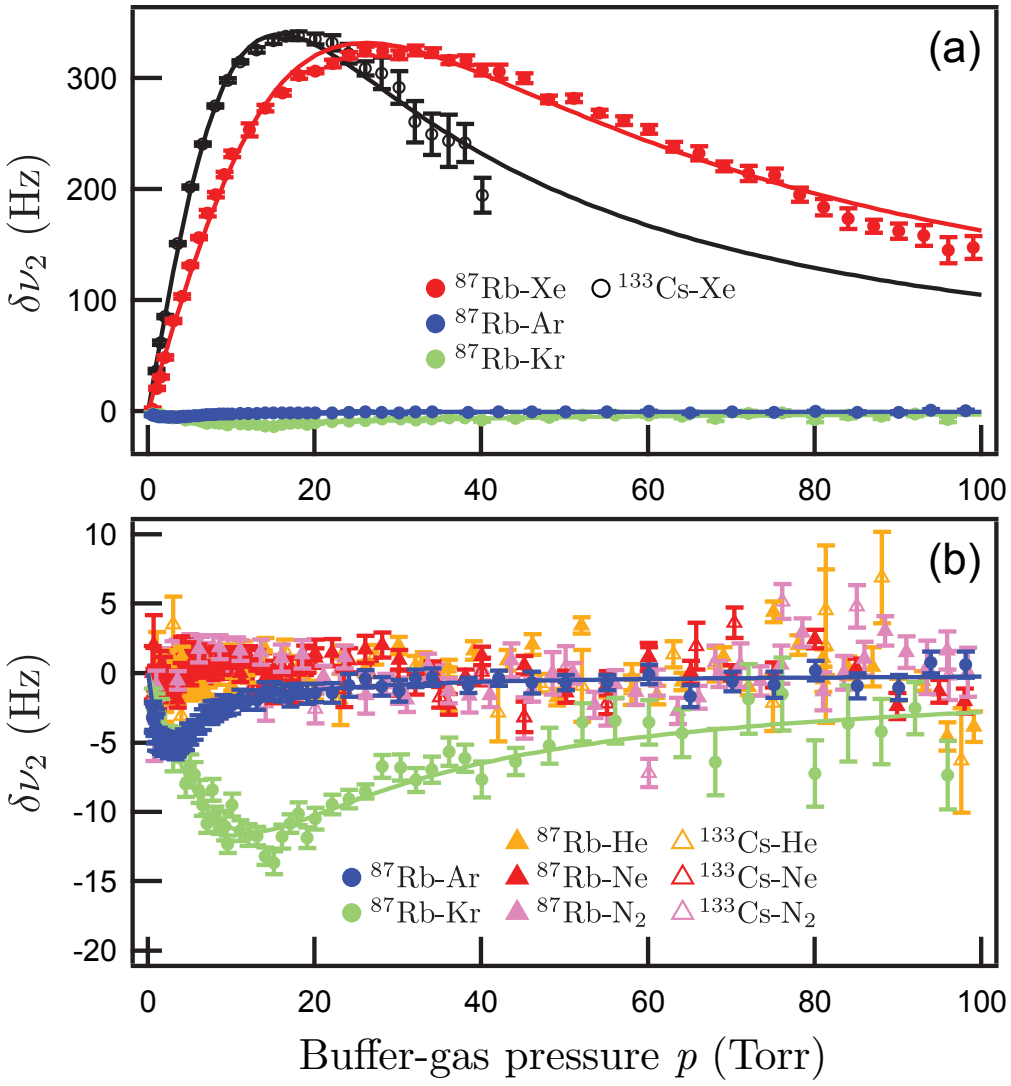

Figure 4.6: Summary of the nonlinear shifts $\delta\nu_2$ for ^{87}Rb at 40.0° C and $B = 1$ G and for ^{133}Cs at 35.0° C and $B = 0.2$ G. (a) ^{87}Rb and ^{133}Cs in Xe, with ^{87}Rb in Ar and Kr for comparison. (b) ^{87}Rb in Ar and Kr, and ^{87}Rb and ^{133}Cs in He, Ne, and N_2. The solid curves are the functions f_0 of (4.6) with parameters in Table 4.3.

The formation-rate parameters Tp^2 are larger than the corresponding values measured by Bouchiat *et al.* [38, 106], which are given in Table 4.1. As pointed out by Gong *et al.* [39], this is likely due to a cancellation of contributions from different vibration-rotation states of the van der Waals molecules. For Ar and Kr, where the signs of ϕ and s are opposite, the hyperfine-shift potential $\delta A = \delta A(R)$ must change sign as the internuclear separation R increases, as discussed in Chapter 3. A similar radial dependence for δA was measured for K in Ar [97]. For Xe, however, the signs of ϕ and s are the same, which suggests that $\delta A(R)$ may have a qualitatively different shape over the range of R important to van der Waals molecules.

4.3 Isotope comparison with ^{85}Rb and ^{87}Rb

To investigate the remaining discrepancy between the improved model (4.11) and the measured shifts with Xe in the last section, and to rigorously test this model, we repeated our measurements with ^{85}Rb, the other naturally abundant isotope of Rb, which has a different nuclear spin quantum number, $I = 5/2$, than ^{87}Rb, with $I = 3/2$. In this section, we report the preliminary results of this isotope comparison.

Fig. 4.7 summarizes our experimental measurements with ^{85}Rb. Table 4.4 lists the pressure-independent fit parameters for the data, and includes the fit parameters for ^{87}Rb of the last section for comparison. As Fig. 4.7(a) shows, and like before, the nonlinear shift in Xe is relatively large and opposite in sign compared to the nonlinear shifts in Ar and Kr, which are highlighted in Fig. 4.7(b). As before, we only fit the data with Ar and Kr with the f_0 of (4.6), which ignores the spin-rotation interaction (4.2), since the effects of the applied field might be important. However, varying the applied field B from 0.25–1 G for Kr and Xe did not change the fit parameters significantly. For Ar, we note that the peak of the nonlinearity occurs at a very low pressure, near the limit of our experimental range. The linear shifts s are consistent

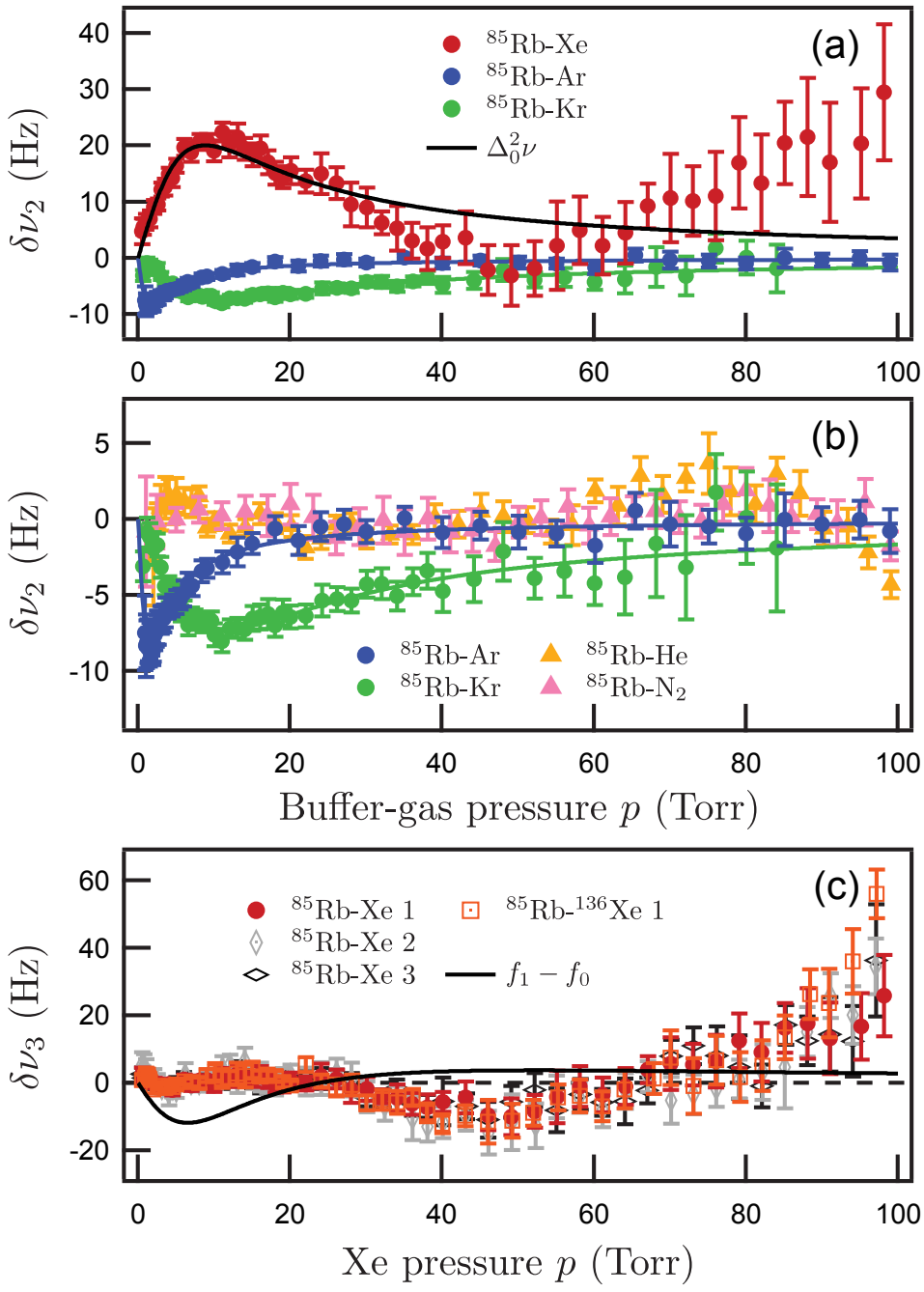

Figure 4.7: Summary of the nonlinear shifts $\delta\nu_2$ for ^{85}Rb at 40.0° C and $B = 1$ G. (a) ^{85}Rb in Xe, with ^{85}Rb in Ar and Kr for comparison. (b) ^{87}Rb in Ar, Kr, He, and N_2. The solid curves in (a) and (b) are the function f_0 of (4.6), with the nonlinear shift $\Delta_0^2\nu$ of (4.7), using the parameters in Table 4.4. (c) The fit residuals to (4.6), $\delta\nu_3 = \delta\nu_2 - \Delta_0^2\nu = \nu - f_0$, for ^{85}Rb in Xe and ^{136}Xe. The solid curve is the difference, $f_1 - f_0$, of the best-fit theoretical curves, with and without the spin-rotation interaction (4.2). Three separate data sets demonstrate the repeatability of the measurements in natural abundance Xe. The residuals are unchanged with isotopically enriched ^{136}Xe.

Table 4.4: Fit parameters for the pressure shifts of ^{85}Rb at 40°C and $B = 1$ G. Fit parameters from Table 4.3 for the pressure shifts of ^{87}Rb with the same conditions are included for comparison. Uncertainties for the slopes s are typically ±0.25%.

Metal	Gas	$r_1\phi p$ (rad Torr)	Tp^2 (sec Torr^2)	ϕp (rad Torr)	s (Hz Torr^{-1})
^{85}Rb	Xe	5.31	0.0022	−0.018	−517.9
	Xe	–	0.310 ± 0.075	-8.8 ± 1.1	−517.7
	Ar	–	0.0271 ± 0.0045	1.68 ± 0.14	−23.85
	Kr	–	1.50 ± 0.45	11.7 ± 2.0	−249.7
	He				316.8
	N_2				229.6
^{87}Rb	Xe	7.97	0.082 ± 0.010	-14.8 ± 1.5	−1184.0
	Xe	–	0.164 ± 0.013	-26.2 ± 1.2	−1183.7
	Ar	–	0.070 ± 0.012	2.21 ± 0.16	−53.71
	Kr	–	1.08 ± 0.31	12.5 ± 1.9	−558.1
	He				714.2
	Ne				387.3
	N_2				518.0

with previous work [39, 30, 75, 118], and the expected isotopic scaling, (s for ^{87}Rb)/(s for ^{85}Rb) $\propto$ (ν_{00} for ^{87}Rb)/(ν_{00} for ^{85}Rb) ≈ 2.2514. To the limits of our experimental accuracy, the shifts in He and N_2 were again linear.

As with ^{87}Rb, the nonlinear shift in Xe is not completely described by the fit function f_0 of (4.6), as shown in Fig. 4.7(c), where we plot the fit residuals $\delta\nu_3 = \nu - f_0$. The residuals $\delta\nu_3$ are the same for three independent sets of measurements. We refit our data to the function f_1 of (4.11), where again we estimated the parameter $r_1\phi p$ of (4.13) from measurements by Bouchiat *et al.* [38]. The weights W_σ of (4.14) for ^{85}Rb are listed in Section 4.5.4. This fit returned unrealistic uncertainties, which are not shown in Table 4.4. The solid curve in Fig. 4.7(c) shows the difference, $f_1 - f_0$, between the two theoretical fit functions. However, unlike the case for ^{87}Rb or ^{133}Cs in Xe, the revised function (4.11) does not give substantially smaller residuals. Instead, the difference $f_1 - f_0$ displays almost the opposite, oscillatory behavior with pressure

as the measured residuals $\delta\nu_3$. Fitting with r_1 as a free parameter does not improve the results much.

Following the previous section, this disagreement between theory and experiment is most likely due to the neglect of either

(i) the vibration-rotation state distribution for the molecules, which might be different for the two Rb isotopes because of their slightly different mass, or

(ii) the effects of additional spin interactions other than (4.1) and (4.2) in the molecules, for example, with any nuclear spin of the buffer gas.

Compared to natural-abundance Ar and Kr, which are mostly free of nuclear spin, natural-abundance Xe is composed of roughly 26% ^{129}Xe, with $I = 1/2$, and 21% ^{131}Xe, with $I = 3/2$. Therefore, an interaction with the nuclear spin in Xe gas is one candidate to explain this discrepancy.

To explore both (i) and (ii) above, we took advantage of the existence of the multiple naturally abundant isotopes of Xe, by measuring the nonlinear shift of ^{85}Rb in an 83% isotopically enriched ^{136}Xe gas (Isotec/Sigma–Aldrich 602213). Since the relative change in mass between ^{136}Xe and natural-abundance Xe is almost equal to that between ^{87}Rb and ^{85}Rb, this measurement is a test of (i). In addition, the enriched ^{136}Xe gas contained only 0.05% ^{129}Xe and 0.39% ^{131}Xe (by atom), and so is almost free of nuclear spin. As a result, this measurement is also a test of (ii) for any interactions with the nuclear spin of the buffer gas. As Fig. 4.7(c) shows, the results are the same for the enriched ^{136}Xe gas as for natural-abundance Xe gas. Therefore, we expect that the remaining disagreement between theory and experiment is most likely due to the neglect of additional spin interactions other than (4.1) and (4.2), but not with the nuclear spin of the buffer gas.

During this study, we discovered an empirical fit function,

$$f_{\rm q} = \nu_0 + sp + \Delta^2_{\rm q}\nu, \tag{4.15}$$

which is able to summarize the measured shift of ^{87}Rb in Xe without any significant fit residuals,

$$\delta\nu_{\rm q} = \delta\nu_2 - \Delta^2_{\rm q}\nu = \nu - f_{\rm q}, \tag{4.16}$$

as shown in Fig. 4.8. Here, the nonlinear shift is the function

$$\Delta^2_{\rm q}\nu = -\left(\frac{1}{2\pi(Tp^2)}\right)\frac{(\phi p)^3 p}{(p+p_0)^2+(\phi p)^2}. \tag{4.17}$$

As we show in Section 4.5.3, this fit function may be interpreted as the theoretical shift for a single quasibound state, instead of a single bound vibration-rotation state, which considers only the hyperfine-shift interaction (4.1). The additional parameter $p_{\rm q}$ characterizes the effects of two-body formation and spontaneous dissociation. Fig. 4.8

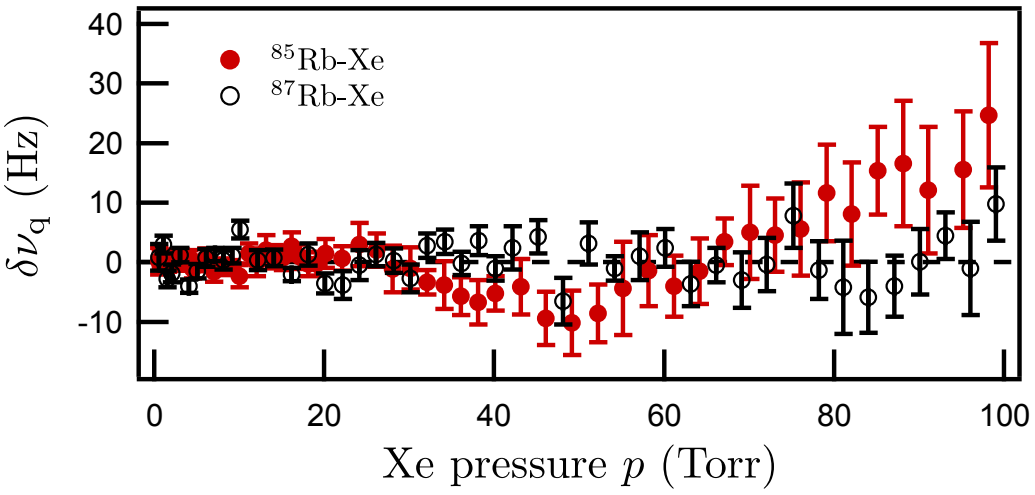

Figure 4.8: Fit residuals $\delta\nu_{\rm q} = \nu - f_{\rm q}$ for the pressure shifts of ^{87}Rb and ^{85}Rb in Xe with the empirical, quasibound state fit function $f_{\rm q}$ of (4.15). Fit parameters are given in Table 4.5.

Table 4.5: Fit parameters for the pressure shifts of ^{87}Rb and ^{85}Rb in Xe at 40°C and $B = 1$ G with the empirical, quasibound state model $f_{\rm q}$ of (4.15), and nonlinear shift $\Delta_{\rm q}^2\nu$ of (4.17). Uncertainties for the slopes s are typically $\pm 0.25\%$.

Metal	Gas	Tp^2 (sec Torr^2)	ϕp (rad Torr)	$p_{\rm q}$ (Torr)	s (Hz Torr^{-1})
^{87}Rb	Xe	0.063 ± 0.016	-25.0 ± 1.3	20.5 ± 3.4	-1184.8
^{85}Rb	Xe	0.472 ± 0.076	-7.7 ± 1.3	-4.81 ± 1.1	-517.7

is a plot of the fit residuals $\delta\nu_{\rm q}$ for ^{87}Rb and ^{85}Rb in Xe, with the fit parameters given in Table 4.5. As the figure shows, the quasibound fit function $f_{\rm q}$ of (4.15) is not able to summarize the measurements with ^{85}Rb in Xe any better than the other fit functions, f_0 or f_1, but instead displays oscillatory fit residuals similar to those in Fig. 4.7(c).

Finally, we note that there is a significant nonlinearity in our measurement of the buffer-gas pressure. As we describe in Section 4.4.1, we correct for this nonlinearity in our measurements. This error is characterized by the parameter α in (4.18), and could account for the fit residuals $\delta\nu_3$ shown in Fig. 4.7(c) if we had underestimated the value of α by at least a factor of 2. However, given our estimated uncertainty for the value of α in (4.21), which was determined from the measurements with He and N_2, we do not think this is a likely explanation.

4.4 Experiment

We measured the ground-state 0–0 hyperfine resonant frequencies ν of ^{87}Rb, ^{85}Rb, and ^{133}Cs in pure buffer gases with two laser-pumped, vapor-cell clock systems that closely follow the design of Gong *et al.* [39, 40]. The Rb system used most of the same equipment described in Section 2.3. Both systems are based on two feedback loops: one to lock the carrier frequency of frequency-modulated microwaves to the 0–0 transition, and another to lock the optical frequency of the pumping light to

produce no light shift of the 0–0 transition. For the second feedback loop, we used the intensity-modulation method described in Chapter 2, which for convenience is sketched again in Fig. 4.9.

The ^{87}Rb, ^{85}Rb, and ^{133}Cs vapor cells are cylindrical Pyrex cells, 17 mm in diameter and about 25, 19, or 13 mm long, respectively, and are filled with a small excess of ^{87}Rb, ^{85}Rb, or ^{133}Cs metal, respectively. Each cell has an external buffer-gas reservoir, pressure gauge, and vacuum port as shown in Fig. 4.10, which permit convenient changes of the buffer-gas species and pressure. Before every experiment, we used the vacuum port and a turbomolecular pump to empty the cell and to zero the pressure gauge. During an experiment, we waited roughly 1 minute for the cell to equilibrate after each incremental increase of the buffer gas pressure, before making a measurement. Except for the source of isotopically enriched ^{136}Xe gas, which was

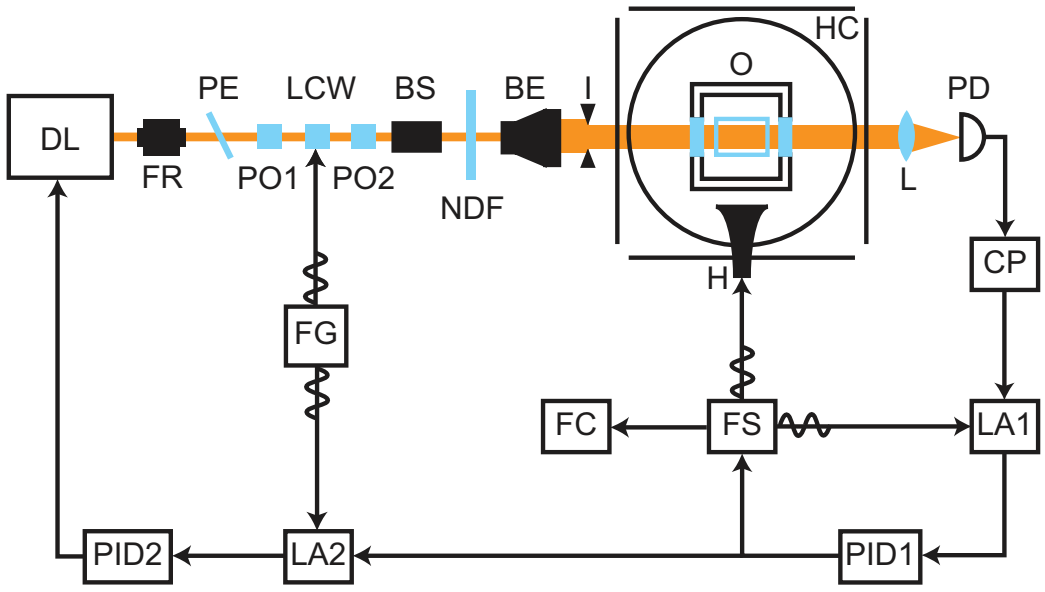

Figure 4.9: Experimental setup for the measurement of nonlinear pressure shifts. DL, diode laser; FR, Faraday rotator; PE, pellicle; PO, polarizer; LCW, liquid crystal wave plate; BS, beam shaper; NDF, neutral density filter; BE, beam expander; I, iris; O, oven; H, horn; HC, Helmholtz coils; L, lens; PD, photodetector; CP, current preamplifier; LA, lock-in amplifier; PID, PID controller; FS, frequency synthesizer; FC, frequency counter; FG, function generator.

only guaranteed to have a chemical purity above 99.8%, the source for each buffer gas was of scientific or research grade chemical purity (99.995% or better).

An air-heated, non-magnetic oven (O) holds the cylindrical glass vapor cell at a constant temperature of 40.0° C for Rb and 35.0° C for Cs. Helmholtz coils (HC) cancel ambient magnetic fields and provide a static longitudinal field B of 1.0 G for Rb and 0.2 G for Cs. A Toptica DL 100 diode laser (DL) provides 795 nm D1 optical pumping light for Rb and 895 nm D1 light for Cs. A Faraday rotator (FR) isolates the laser from back-reflected light. A pellicle (PE) skims off light for analysis with a wavemeter and a Fabry–Perót interferometer (not shown). Polarizers (PO) ensure that the pumping light is linearly polarized. A liquid crystal wave plate (LCW) driven by a function generator (FG) provides about 30% intensity modulation of the

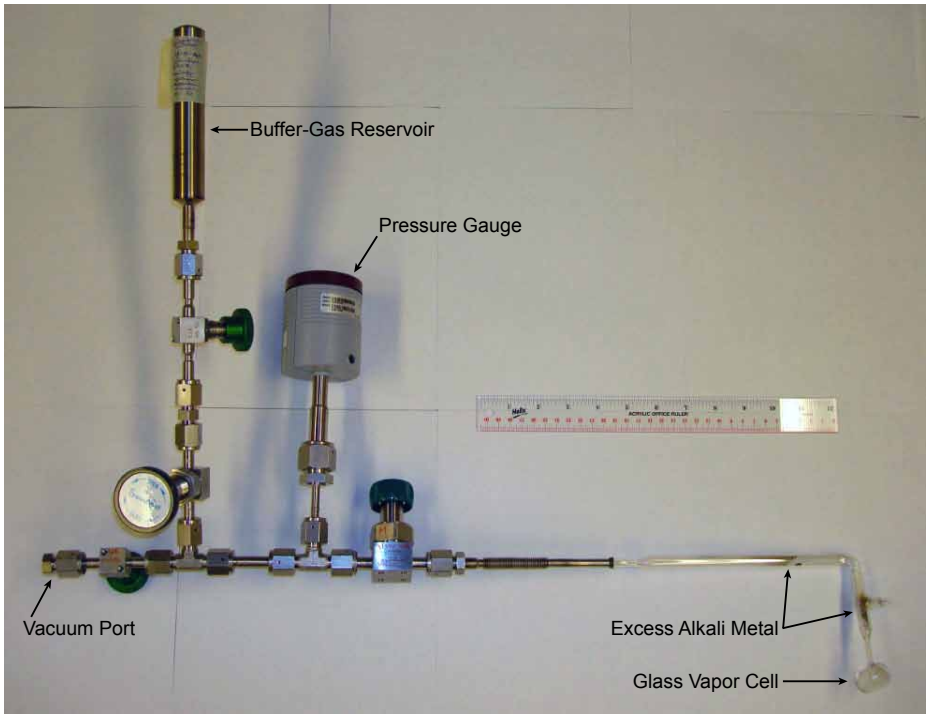

Figure 4.10: ^{87}Rb vapor cell with external pressure gauge, buffer-gas reservoir, and vacuum port to conveniently change the buffer-gas species and pressure. The glass cell is Pyrex, and the metal manifold is mostly stainless steel. The vacuum connections are VCR fittings with copper or stainless steel gaskets. The ^{85}Rb vapor cell is almost identical. Pictures of the ^{133}Cs cell are available as Figs. 4.2 and 4.3 in Ref. [34].

pumping light at a rate of 2 Hz. A beam shaper (BS), a beam expander (BE), and an iris (I) ensure that the pumping light fills the cell uniformly. A rotatable neutral density filter (NDF) adjusts the pumping light intensity. A lens (L) collects the transmitted pumping light onto a photodetector (PD).

Microwaves from a frequency synthesizer (FS) are transmitted towards the cell by a horn (H, Narda Microwave-East Standard Gain Horn 642 for ^{87}Rb, 644S for ^{85}Rb, and 640 for ^{133}Cs) roughly 10 cm away to drive magnetic resonances. For the ^{85}Rb measurements, we used a high-power amplifier (Mini-Circuits ZHL-16W-43+) before the horn to obtain enough signal at high Xe pressures. A frequency counter (FC) with 1 Hz precision, referenced to a rubidium frequency standard (not shown), sampled the locked carrier to provide ν. We estimated the uncertainty with the sample standard deviation, which increased with the 0–0 linewidth at higher pressures. For the Rb system, the microwaves are frequency modulated internally by the FS at a rate between 0.2–9.0 kHz, depending on the buffer gas and pressure, and a modulation index of about 1. For the Cs system, the microwaves are frequency modulated at a rate of roughly 255 Hz by modulating an external 10 MHz quartz oscillator (Stanford Research Systems SC10) used as an external reference for the FS [34]. This implementation limited the Xe pressure range and led to increased carrier noise for the Cs measurements.

A lock-in amplifier (LA1) with a 10-300 ms time constant provides an error signal for a proportional-integral-derivative (PID) controller (PID1) to lock the microwave carrier frequency to the clock transition. A second lock-in amplifier (LA2) with a time constant of roughly 1-3 s provides an error signal for another PID controller (PID2) to lock the laser to a zero-shift optical frequency using a piezoactuator. As a quick test for light-shift suppression, we use the NDF filter to temporarily adjust the laser intensity by a factor of 2–4 to verify the intensity independence of the clock output. As a final check for light-shift suppression, we compared the results

of measurements that used each of the two different zero-shift optical frequencies, as described in Chapter 2, for all choices of buffer gas with ^{87}Rb and ^{85}Rb.

4.4.1 Correction for nonlinearity in pressure measurement

The interactions (4.1) and (4.2) are so large for RbXe molecules that we needed substantially higher gas pressures than those used by Gong *et al.* [39] to approach the high-pressure, linear regime. As Fig. 4.2(b) shows, even at 100 Torr, much of the nonlinear shift is still present. Several improvements were needed to precisely measure nonlinear shifts of a few Hz on top of background, linear shifts of up to 120 kHz at high pressures. For example, we found that stabilization of the temperature gradient along the section of the vapor cell that exits the oven was critical to reduce the additional clock noise and drift that are produced by temperature-induced changes of the cell volume at higher pressures. The most important improvement was the removal of nonlinearity in pressure measurement, which we describe below.

We measured the pressure p with capacitance manometers (MKS Instruments Baratron) to a precision of roughly ± 0.002 Torr and an accuracy of about $\pm 0.25\%$. We found that the true pressure p has a slight quadratic dependence on the pressure p_{g} measured by these gauges. We estimated the true pressure for our data with the empirical formula,

$$p = r(\alpha)(p_{\mathrm{g}} + \alpha\, p_{\mathrm{g}}^2), \tag{4.18}$$

where the coefficient α describes the curvature and the coefficient $r(\alpha) \approx 1$ minimizes the small linear bias of (4.18). We determined $r(\alpha)$ by minimizing the least-squares linear bias $\int (p - p_{\mathrm{g}})^2 dp_{\mathrm{g}}$ over a 0–100 Torr gauge range, which gives

$$r(\alpha) = \frac{1 + 75\alpha}{1 + 150\alpha + 6000\alpha^2}. \tag{4.19}$$

Using the measured pressures p_g, He, Ne, and N_2 appear to have nonlinear shifts, as demonstrated in Fig. 4.11. However, using the same empirically determined value of α with (4.18) eliminates these nonlinearities. We determined the values of α from measurements with He, Ne, and N_2, for which the effects of van der Waals molecules, if present at all, appear below our experimental accuracy. The results are:

$$^{87}\text{Rb gauge: } \alpha = (-3.40 \pm 0.22) \times 10^{-5} \text{ Torr}^{-1}, \tag{4.20}$$

$$^{85}\text{Rb gauge: } \alpha = (-1.71 \pm 0.52) \times 10^{-5} \text{ Torr}^{-1}, \tag{4.21}$$

$$^{133}\text{Cs gauge: } \alpha = (-1.71 \pm 0.46) \times 10^{-5} \text{ Torr}^{-1}. \tag{4.22}$$

These values of α appear to have been stable over the course of our measurements. Concern over the influence of fluctuations in the room temperature lead to the construction of a temperature-controlled enclosure for the^{85}Rb gauge. However, manual variation of the enclosure temperature showed that small changes in temperature had a negligible effect on the value of α, compared to the uncertainties listed above. Additionally, we found that a gauge controller initially used in the Cs system imparted

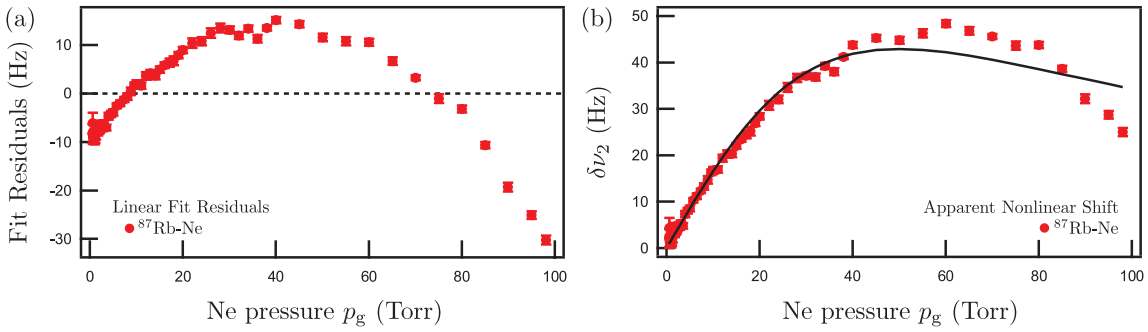

Figure 4.11: Demonstration of a quadratic nonlinearity in pressure measurement with ^{87}Rb in Ne at 40.0° C and $B = 1$ G. (a) Residuals after fitting ν versus the gauge pressure p_g with a straight line, $\nu_0 + sp_g$, which show a quadratic dependence with p_g. (b) The apparent nonlinear shift $\delta\nu_2$ after fitting ν with the fit function f_0 of (4.6) using p_g instead of p. The black curve is the f_0 of (4.6) estimated by this fit, which is due to the pressure gauge nonlinearity. For comparison, Fig. 4.6 shows $\delta\nu_2$ after fitting ν versus the estimated pressure p from (4.18), which agree with a straight line.

a several-Hz jump near 4 Torr, which disappeared after replacing the controller. Finally, we note that the uncertainties reported for the fit parameters in this chapter include numerical estimates of the contributions from the 0.25% gauge inaccuracy and the uncertainty in the value of α.

We observed anomalous frequency shifts in some measurements at very low pressures, below about 1 Torr, with gases other than Xe. These shifts were most noticeable with the Cs system, where they could be as large as -25 Hz at 0.7 Torr for He, Ne, or N_2. The shifts were less reproducible in the Rb system, where they were typically less than 5 Hz at 0.5 Torr for ^{87}Rb in Ar, Kr, Ne, or N_2, but were not observed in He. Except for ^{87}Rb in Ar, where they were of either sign, these shifts were negative. We observed similar shifts with ^{85}Rb. The origin of these anomalous shifts seems to be a systematic effect, perhaps associated with the very poor signal-to-noise ratios at very low pressures. Further investigation is needed to identify their cause.

Finally, we note that we were unable to detect any pressure difference between the heated and unheated portions of the vapor cell due to thermal transpiration [119, 120, 121, 122, 123, 124], which we investigated by measuring the pressure p and frequency ν while varying the spatial temperature gradient along the ^{87}Rb vapor cell, using very low pressures of He buffer gas.

4.5 Modeling

To derive the fit functions used to analyze the nonlinear pressure shifts in Sections 4.2 and 4.3, we will model the effects of van der Waals molecules using a density matrix, which was introduced in Section 2.4.2. We begin with a general treatment before obtaining the specific fit functions.

In the time between collisions, a free alkali-metal atom evolves under the influence of the common ground-state spin Hamiltonian $H^{\{g\}}$ of (2.1),

$$H^{\{g\}} = A\,\mathbf{I}\cdot\mathbf{S} - \boldsymbol{\mu}\cdot\mathbf{B}. \tag{4.23}$$

As before, we assume that a static applied field $B = |\mathbf{B}|$ is oriented along the Cartesian unit vector $\mathbf{z}$. During the time spent in a molecule, the alkali-metal atom evolves under the influence of a perturbed Hamiltonian,

$$\overline{H} = H^{\{g\}} + H_{\rm m}, \tag{4.24}$$

where $H_{\rm m}$ is the contribution from the molecule, to be discussed below. The sublevel energies E_μ and $E_{\bar\mu}$ of free and bound atoms, respectively, and the corresponding spin eigenvectors $|\mu\rangle$ and $|\bar\mu\rangle$ are given by

$$H^{\{g\}}|\mu\rangle = E_\mu|\mu\rangle \quad \text{and} \quad \overline{H}|\bar\mu\rangle = E_{\bar\mu}|\bar\mu\rangle. \tag{4.25}$$

These spin eigenvectors are complete,

$$\sum_\mu |\mu\rangle\langle\mu| = \sum_{\bar\mu} |\bar\mu\rangle\langle\bar\mu| = 1, \tag{4.26}$$

and orthonormal

$$\langle\mu|\nu\rangle = \delta_{\mu\nu} \quad \text{and} \quad \langle\bar\mu|\bar\nu\rangle = \delta_{\bar\mu\bar\nu}. \tag{4.27}$$

If we assume that sticking collisions occur at a characteristic rate $1/T$, then the density operator $\rho = \rho(t)$ for ground-state alkali-metal atoms will evolve according to

$$\frac{\partial}{\partial t}\rho = -\frac{i}{\hbar}\left[H^{\{g\}},\rho\right] + \frac{1}{T}\left\langle S\rho S^\dagger - \rho\right\rangle, \tag{4.28}$$

where for simplicity we ignore the effects of optical pumping and binary collisions. Here, the first term on the right describes the free-atom evolution according to the $H^{\{g\}}$ of (4.23). Following Chapter 10 of Ref. [21], the second term describes the bound-atom evolution with a scattering matrix (or S-matrix) S, which is the unitary operator that evolves a free-atom wave function $|\psi\rangle$ into the perturbed wave function $|\psi'\rangle$ of a free atom that has just undergone a collisional perturbation,

$$|\psi'\rangle = S|\psi\rangle. \tag{4.29}$$

For a particular van der Waals molecule with lifetime τ, we may use (4.23) and (4.24) to write the S-matrix (4.29) as

$$S = e^{-i\overline{H}\tau/\hbar} e^{iH^{\{g\}}\tau/\hbar}. \tag{4.30}$$

However, van der Waals molecules may exist in many different vibration-rotation states, each with different formation rates and lifetimes. To account for this variation, the angle brackets in (4.28) denote a statistical average over all sticking collisions and resulting molecular states.

Consider a hyperfine transition between the two different ground-state sublevels $|\alpha\rangle$ and $|\beta\rangle$. Following Section 2.1.1, we may write these sublevels in the low-field basis $|F\,m\rangle$ as

$$|\alpha\rangle = |a\,\alpha\rangle \quad \text{and} \quad |\beta\rangle = |b\,\beta\rangle, \tag{4.31}$$

where the total spin angular momentum quantum numbers are $F = a = I + 1/2$ and $F = b = I - 1/2$ for the upper and lower hyperfine manifolds, respectively. From

(4.28), the coherence $\rho_{\alpha\beta} = \langle\alpha|\rho|\beta\rangle$ for this "α–β" transition will evolve according to

$$\frac{\partial}{\partial t}\rho_{\alpha\beta} = -i\omega_{\alpha\beta}\rho_{\alpha\beta} + \frac{1}{T}\left\langle \sum_{\mu\nu}\langle\alpha|S|\mu\rangle\rho_{\mu\nu}\langle\nu|S^{\dagger}|\beta\rangle - \rho_{\alpha\beta}\right\rangle, \tag{4.32}$$

where the free-atom Bohr frequency $\omega_{\alpha\beta} = (E_\alpha - E_\beta)/\hbar$.

In an ideal experiment, the measured hyperfine frequency ν for the α–β transition is equal to the precession frequency of the coherence $\rho_{\alpha\beta}$. Without any collisions, $1/T \longrightarrow 0$, the measured value of ν would be the zero-pressure frequency

$$\nu_0 = \frac{\omega_{\alpha\beta}}{2\pi}, \tag{4.33}$$

which for the 0–0 transition is given by (2.20). With collisions, the measured value of ν will be shifted by an amount

$$\Delta\nu = \nu - \nu_0 = \frac{\Delta\omega}{2\pi}. \tag{4.34}$$

This is clear if we collect the terms for each density-matrix component $\rho_{\mu\nu} = \langle\mu|\rho|\nu\rangle$ on the right hand side of (4.32), and write

$$\frac{\partial}{\partial t}\rho_{\alpha\beta} = -[i(\omega_{\alpha\beta} + \Delta\omega) + \Delta\gamma]\rho_{\alpha\beta} + \frac{1}{T}\sum_{\mu\neq\alpha,\nu\neq\beta}\left\langle S_{\alpha\mu}S^{\dagger}_{\nu\beta}\right\rangle\rho_{\mu\nu}, \tag{4.35}$$

where $\Delta\omega$ is the same frequency shift as (4.34). Here, we introduced the notation

$$S_{\mu\nu} = \langle\mu|S|\nu\rangle \tag{4.36}$$

for the components of the S-matrix S in Schrödinger space. With this notation, we may write the frequency shift $\Delta\omega$ and damping rate $\Delta\gamma$ due to molecules in the

evolution (4.35) as

$$\Delta\omega = 2\pi\Delta\nu = -\frac{1}{T}\,\mathrm{Im}\left\langle S_{\alpha\alpha}S_{\beta\beta}^{\dagger}\right\rangle, \text{ and} \tag{4.37}$$

$$\Delta\gamma = \frac{1}{T}\,\mathrm{Re}\left\langle 1 - S_{\alpha\alpha}S_{\beta\beta}^{\dagger}\right\rangle. \tag{4.38}$$

Once again, the angle brackets denote the same statistical average as in (4.28). In this form, we see that the shift and damping are determined by how sticking collisions preserve the states $|\alpha\rangle$ and $|\beta\rangle$, as described by the diagonal S-matrix components $S_{\alpha\alpha}$ and $S_{\beta\beta}^{\dagger}$, or alternatively, by how molecules preserve the coherence $\rho_{\alpha\beta}$, as described by the product $S_{\alpha\alpha}S_{\beta\beta}^{\dagger}$. Note that if we had considered a population ($\alpha = \beta$) instead of a coherence ($\alpha \neq \beta$), then the shift and damping would be zero since the S-matrix is unitary, $S^{\dagger} = S^{-1}$.

In addition to the frequency shift (4.37) and damping rate (4.38), the sticking collisions also introduce couplings with the other density-matrix components in (4.35). To understand the effects of these couplings, it is useful to transform the density operator $\rho = \rho(t)$ into the interaction picture,

$$\widetilde{\rho} = e^{iH^{\{g\}}t/\hbar}\,\rho\,e^{-iH^{\{g\}}t/\hbar}, \tag{4.39}$$

where the transformed operator $\widetilde{\rho}$ has the components $\widetilde{\rho}_{\mu\nu} = \langle\mu|\,\widetilde{\rho}\,|\nu\rangle = e^{i\omega_{\mu\nu}t}\rho_{\mu\nu}$. In this picture, the evolution (4.35) becomes

$$\frac{\partial}{\partial t}\widetilde{\rho}_{\alpha\beta} = -(i\Delta\omega + \Delta\gamma)\widetilde{\rho}_{\alpha\beta} + \frac{1}{T}\sum_{\mu\neq\alpha,\nu\neq\beta} e^{i(\omega_{\alpha\beta}-\omega_{\mu\nu})t}\left\langle S_{\alpha\mu}S_{\nu\beta}^{\dagger}\right\rangle\widetilde{\rho}_{\mu\nu}. \tag{4.40}$$

Comparing with (4.35), we see that the interaction picture conveniently removes the oscillation of the density-matrix components at their respective Bohr frequencies. Instead, each coupling with a different component in (4.40) now oscillates at the difference of the two respective Bohr frequencies. At minimum, these Bohr frequencies

will be separated by a Zeeman transition, which for a typical applied field B is on the order of 1 MHz. In the secular approximation we expect the interaction-picture components $\widetilde{\rho}_{\mu\nu}$ to evolve slowly in time, so we see from (4.40) that the couplings between the different components should be negligible.

4.5.1 Molecular vibration-rotation states

Before we determine the nonlinear pressure shift $\Delta^2\nu$ from the frequency shift $\Delta\omega$ of (4.37), we first need to consider the statistical average denoted by angle brackets. In equilibrium, molecules will exist in many different vibration-rotation states, which we can characterize with the label v, the rotational quantum number N_v, and the statistical weight $g_v = [N_v] = 2N_v + 1$. For example, consider the case of RbXe molecules, such as described in Section 4.1.1. The total number density of molecules, [RbXe], will be the sum of the densities for each state v,

$$[\mathrm{RbXe}] = \sum_v [\mathrm{RbXe}]_v. \tag{4.41}$$

Each state v will have a different characteristic lifetime τ_v and formation rate $1/T_v$. In equilibrium, the formation and breakup of molecules in each state must balance,

$$\frac{1}{T_v}[\mathrm{Rb}] = \frac{1}{\tau_v}[\mathrm{RbXe}]_v. \tag{4.42}$$

As a result, we see that the fraction of Rb atoms bound in a molecule of state v is

$$f_v = \frac{[\mathrm{RbXe}]_v}{[\mathrm{Rb}]} = \frac{\tau_v}{T_v}. \tag{4.43}$$

Comparing (4.42) with (4.3), we also see that the characteristic rate $1/T$ of sticking collisions introduced in (4.28) is the sum

$$\frac{1}{T} = \sum_v \frac{1}{T_v}. \tag{4.44}$$

We expect the lifetimes τ of molecules in a given vibration-rotation state v to follow an exponential distribution with mean τ_v and probability density $P_v(\tau) = e^{-\tau/\tau_v}/\tau_v$. At minimum, we need to average over this distribution. For a particular molecule with lifetime τ, we may use (4.36) with (4.30), (4.26), and (4.25) to write the quantity

$$S_{\alpha\alpha} S^\dagger_{\beta\beta} = \sum_{\bar{\mu}\bar{\nu}} e^{i(\omega_{\alpha\beta} - \omega_{\bar{\mu}\bar{\nu}})\tau} |\langle\alpha|\bar{\mu}\rangle\langle\bar{\nu}|\beta\rangle|^2, \tag{4.45}$$

where the bound-atom Bohr frequencies $\omega_{\bar{\mu}\bar{\nu}} = (E_{\bar{\mu}} - E_{\bar{\nu}})/\hbar$. Averaging (4.45) over the distribution of lifetimes for the state v gives

$$\left\langle S_{\alpha\alpha} S^\dagger_{\beta\beta} \right\rangle_{\tau_v} = \int_0^\infty S_{\alpha\alpha} S^\dagger_{\beta\beta} P_v(\tau) d\tau = \sum_{\bar{\mu}\bar{\nu}} \frac{|\langle\alpha|\bar{\mu}\rangle\langle\bar{\nu}|\beta\rangle|^2}{1 + i(\omega_{\bar{\mu}\bar{\nu}} - \omega_{\alpha\beta})\tau_v}. \tag{4.46}$$

Using this average with (4.43) and (4.44), we can write the frequency shift (4.37) and damping rate (4.38) as the sums over vibration-rotation states

$$\Delta\omega = \sum_v f_v \left\langle \sum_{\bar{\mu}\bar{\nu}} \frac{|\langle\alpha|\bar{\mu}\rangle\langle\bar{\nu}|\beta\rangle|^2 (\omega_{\bar{\mu}\bar{\nu}} - \omega_{\alpha\beta})}{1 + (\omega_{\bar{\mu}\bar{\nu}} - \omega_{\alpha\beta})^2 \tau_v^2} \right\rangle_v, \text{ and} \tag{4.47}$$

$$\Delta\gamma = \sum_v f_v \left\langle \sum_{\bar{\mu}\bar{\nu}} \frac{|\langle\alpha|\bar{\mu}\rangle\langle\bar{\nu}|\beta\rangle|^2 (\omega_{\bar{\mu}\bar{\nu}} - \omega_{\alpha\beta})^2 \tau_v}{1 + (\omega_{\bar{\mu}\bar{\nu}} - \omega_{\alpha\beta})^2 \tau_v^2} \right\rangle_v. \tag{4.48}$$

Here, the angle brackets $\langle\,\rangle_v$ denote an expectation value for a given vibration-rotation state v. To simplify (4.48), we used completeness (4.26) to write $1 = \sum_{\bar{\mu}\bar{\nu}} |\langle\alpha|\bar{\mu}\rangle\langle\bar{\nu}|\beta\rangle|^2$.

We can now determine the (temporal) nonlinear shift $\Delta^2\nu$ from the (angular) frequency shift $\Delta\omega$ of (4.47). In the limit of high buffer-gas pressures, $p \longrightarrow \infty$, the molecular lifetimes $\tau_v \longrightarrow 0$. Noting that the bound fractions $f_v = \tau_v/T_v \propto p$, we see that the shift $\Delta\omega$ becomes proportional to the pressure in this limit. If we define the limiting slope

$$s_{\rm m} = \lim_{p\to\infty} \frac{\Delta\omega}{2\pi p} = -\lim_{p\to\infty} \frac{1}{2\pi T p} \,{\rm Im}\left\langle S_{\alpha\alpha} S^{\dagger}_{\beta\beta} \right\rangle , \tag{4.49}$$

then we may define the nonlinear pressure shift to be

$$\Delta^2\nu = \Delta\nu - s_{\rm m} p = -\frac{1}{2\pi T}\,{\rm Im}\left\{ \left\langle S_{\alpha\alpha} S^{\dagger}_{\beta\beta} \right\rangle - p \lim_{p\to\infty} \frac{1}{p} \left\langle S_{\alpha\alpha} S^{\dagger}_{\beta\beta} \right\rangle \right\} . \tag{4.50}$$

Using (4.47), the limiting slope (4.49) is

$$\begin{aligned} s_{\rm m} &= \frac{1}{2\pi p} \sum_v f_v \left\langle \sum_{\bar\mu\bar\nu} |\langle\alpha|\bar\mu\rangle\langle\bar\nu|\beta\rangle|^2 (\omega_{\bar\mu\bar\nu} - \omega_{\alpha\beta}) \right\rangle_v \\ &= \frac{1}{hp} \sum_v f_v \big\langle\, \langle\alpha|H_{\rm m}|\alpha\rangle - \langle\beta|H_{\rm m}|\beta\rangle \,\big\rangle_v , \end{aligned} \tag{4.51}$$

where we used (4.24)–(4.26) in the last step, and the nonlinear shift (4.50) is

$$\Delta^2\nu = -\frac{1}{2\pi} \sum_v f_v \left\langle \sum_{\bar\mu\bar\nu} \frac{|\langle\alpha|\bar\mu\rangle\langle\bar\nu|\beta\rangle|^2 (\omega_{\bar\mu\bar\nu} - \omega_{\alpha\beta})^3 \tau_v^2}{1 + (\omega_{\bar\mu\bar\nu} - \omega_{\alpha\beta})^2 \tau_v^2} \right\rangle_v . \tag{4.52}$$

This nonlinear shift is more convenient for analysis than the total frequency shift $\Delta\omega$ since it has a finite area when graphed versus pressure, and since it is more easily distinguishable from the linear pressure shift due to binary collisions.

It is important to note that the nonlinear shift $\Delta^2\nu$ is not a direct frequency shift from van der Waals molecules. The actual frequency shift from the molecules is $\Delta\nu = \Delta\omega/(2\pi)$. Instead, the nonlinear shift $\Delta^2\nu$ is only the apparent nonlinearity of the pressure shift from the molecules, due to the gradual "turning on" of the linear,

limiting molecular shift $s_{\rm m}p$ in $\Delta\nu$ with increasing pressure p. This distinction is clear if we examine the nonlinear shift $\Delta^2\nu$ in the limit of low buffer-gas pressures, $p \longrightarrow 0$, where the lifetimes $\tau_v \longrightarrow \infty$. From (4.52) and (4.51), we see that

$$\lim_{p\to 0} \Delta^2\nu = -s_{\rm m}p. \tag{4.53}$$

However, we know that molecules do not contribute any shift in this limit, since there are so few molecules, $f_v \longrightarrow 0$, and since the molecules formed last so long that their contributions wash out. This is clear from inspecting the actual shift (4.47), where we see that

$$\lim_{p\to 0} \Delta\omega \propto p^3. \tag{4.54}$$

The distinction is also clear in the high-pressure limit, where the molecules produce the shift $\Delta\nu \longrightarrow s_{\rm m}p$, but where the nonlinear shift $\Delta^2\nu \longrightarrow 0$ by construction. Relatedly, we note that the maximum size of the nonlinear shift $\Delta^2\nu$ may increase as the result of either a larger limiting slope $s_{\rm m}$, a more gradual "turning on" of the slope $s_{\rm m}$ with increasing buffer-gas pressure p, or both.

Unfortunately, we do not have enough information to accurately model the effects of the distribution of molecular vibration-rotation states, even though the rotational angular momentum $\mathbf{N}$ of the molecules is usually large enough that this distribution may be modeled classically [37, 109, 110]. The main difficulty is the lack of information about the poorly known interaction potentials, such as the $V(R)$ of Chapter 3, and the poorly known interaction coefficients from the molecular contribution $H_{\rm m}$ of (4.24). In particular, not much is known yet about the potential $\delta A = \delta A(R)$ in the hyperfine-shift interaction (4.1), which was the subject of Chapter 3. Although much more is known about the shape of the potential $\gamma = \gamma(R)$ in the spin-rotation interaction

(4.2) than $\delta A(R)$, the resulting coefficients are still poorly known since they are very sensitive to the shape of the interaction potentials [42, 101, 102].

Fortunately, the frequency shift from van der Waals molecules may be modeled quite well by assuming that there is only a single vibration-rotation state. In this case, we may let $\tau_v \longrightarrow \tau$ and $T_v \longrightarrow T$. The shift (4.47) and damping (4.48) become

$$\Delta\omega = \frac{1}{T}\left\langle \sum_{\bar{\mu}\bar{\nu}} \frac{|\langle\alpha|\bar{\mu}\rangle\langle\bar{\nu}|\beta\rangle|^2(\omega_{\bar{\mu}\bar{\nu}} - \omega_{\alpha\beta})\tau}{1 + (\omega_{\bar{\mu}\bar{\nu}} - \omega_{\alpha\beta})^2\tau^2} \right\rangle, \text{ and} \tag{4.55}$$

$$\Delta\gamma = \frac{1}{T}\left\langle \sum_{\bar{\mu}\bar{\nu}} \frac{|\langle\alpha|\bar{\mu}\rangle\langle\bar{\nu}|\beta\rangle|^2(\omega_{\bar{\mu}\bar{\nu}} - \omega_{\alpha\beta})^2\tau^2}{1 + (\omega_{\bar{\mu}\bar{\nu}} - \omega_{\alpha\beta})^2\tau^2} \right\rangle, \tag{4.56}$$

and the limiting slope (4.51) and nonlinear shift (4.52) become

$$\begin{aligned} s_{\mathrm{m}} &= \frac{1}{2\pi T p}\left\langle \sum_{\bar{\mu}\bar{\nu}} |\langle\alpha|\bar{\mu}\rangle\langle\bar{\nu}|\beta\rangle|^2(\omega_{\bar{\mu}\bar{\nu}} - \omega_{\alpha\beta})\tau \right\rangle \\ &= \frac{\tau}{hTp}\big\langle\, \langle\alpha|H_{\mathrm{m}}|\alpha\rangle - \langle\beta|H_{\mathrm{m}}|\beta\rangle \,\big\rangle, \text{ and} \end{aligned} \tag{4.57}$$

$$\Delta^2\nu = -\frac{1}{2\pi T}\left\langle \sum_{\bar{\mu}\bar{\nu}} \frac{|\langle\alpha|\bar{\mu}\rangle\langle\bar{\nu}|\beta\rangle|^2(\omega_{\bar{\mu}\bar{\nu}} - \omega_{\alpha\beta})^3\tau^3}{1 + (\omega_{\bar{\mu}\bar{\nu}} - \omega_{\alpha\beta})^2\tau^2} \right\rangle. \tag{4.58}$$

For these expressions, the angle brackets denote an expectation value for the hypothetical single vibration-rotation state.

In the next sections we derive specific fit functions for the nonlinear shift, after first specifying the molecular contribution H_{m} to the bound-atom Hamiltonian $\overline{H}$ of (4.24). Before we begin, we note that we do not expect light shifts from the pumping light to be significant in the molecules. As mentioned in Section 4.1.1, the optical transitions are strongly perturbed in the molecule, so the pumping light will be effectively far off-resonance. From Section 2.1.3, we see that any AC Stark shifts should be common mode and thus cancel for the differential shifts of hyperfine transitions. Additionally, for the typical pumping light intensities in vapor-cell clocks, we do not expect the light to significantly affect the molecular dynamics [58].

4.5.2 Single state with hyperfine-shift interaction

Here, we derive the previous model $\Delta_0^2\nu$ of (4.7) from Gong *et al.* [39, 40, 34]. We assume a single bound vibration-rotation state, and that the molecular contribution $H_{\rm m}$ of (4.24) is only due to the hyperfine-shift interaction (4.1),

$$H_{\rm m} \approx H_{\rm hfs} = \delta A\, \mathbf{I}\cdot\mathbf{S}. \tag{4.59}$$

In this case, the quantization axis is the same for free and bound alkali-metal atoms, and we may take the free and bound spin eigenvectors to be the same, $|\mu\rangle = |\bar{\mu}\rangle$. As a result, only the term with $\bar{\mu} = \bar{\alpha}$ and $\bar{\nu} = \bar{\beta}$ contributes in the sum (4.58). If we define the phase shift

$$\phi = \langle \omega_{\bar{\alpha}\bar{\beta}} - \omega_{\alpha\beta}\rangle \tau, \tag{4.60}$$

then we may write the nonlinear shift (4.58) as

$$\Delta^2\nu \approx \Delta_0^2\nu = -\left(\frac{1}{2\pi T}\right)\frac{\phi^3}{1+\phi^2}, \tag{4.61}$$

which is the same form as the fit function $\Delta_0^2\nu$ of (4.7). Similarly, we see from (4.57) that we may write the limiting slope (4.57) as

$$s_{\rm m} = \frac{\phi}{2\pi T p}. \tag{4.62}$$

For the low-field basis $|\mu\rangle = |F\, m\rangle$ of Section 2.1.1, the bound-atom Bohr frequencies are then

$$\omega_{\bar{\mu}\bar{\nu}} = \omega_{\mu\nu} + \frac{\delta A[I]}{2\hbar}, \tag{4.63}$$

so the phase shift (4.60) is

$$\phi = \frac{\delta A[I]\tau}{2\hbar}, \tag{4.64}$$

as given in Section 4.2. Here, as stated earlier in the chapter, it is understood that δA is really an expectation value, $\langle \delta A \rangle$, of the potential $\delta A = \delta A(R)$ of Chapter 3. Since the phase shift (4.64) is independent of the choice of hyperfine transition, we see that the nonlinear shift (4.61) and limiting slope (4.62) are too.

The explicit dependence of the nonlinear shift on the buffer-gas pressure p is clear if we use the pressure-independent parameters Tp^2 and ϕp to write (4.61) as

$$\Delta_0^2\nu = -\left(\frac{1}{2\pi(Tp^2)}\right)\frac{(\phi p)^3 p}{p^2 + (\phi p)^2}. \tag{4.65}$$

Similarly, we see that the limiting slope (4.62) is independent of pressure,

$$s_{\rm m} = \frac{(\phi p)}{2\pi(Tp^2)}. \tag{4.66}$$

We note that the shift (4.61) is maximized when $p = |\phi p|$, or $|\phi| = 1$, where it has the value $\Delta_0^2\nu|_{\phi\to 1} = -\mathrm{sgn}(\phi)/(4\pi T)$.

4.5.3 Single quasibound state with hyperfine-shift interaction

Here, we derive the model $\Delta_{\rm q}^2\nu$ of (4.17). The derivation of this model is identical to that of the last section, with the exception that we now assume that the molecules form in a single quasibound state instead of a bound vibration-rotation state.

As mentioned in Section 4.1.1, a quasibound state may also form in two-body collisions, and breakup by spontaneous dissociation. We can account for these extra

processes by making the substitutions

$$\frac{1}{T} \quad \longrightarrow \quad \frac{1}{T_{\rm q}} = \frac{1}{T}\left(1 + \frac{p_{\rm q}}{p}\right) = \frac{1}{(Tp^2)}(p^2 + p_{\rm q}p), \text{ and} \tag{4.67}$$

$$\frac{1}{\tau} \quad \longrightarrow \quad \frac{1}{\tau_{\rm q}} = \frac{1}{\tau}\left(1 + \frac{p_{\rm q}}{p}\right) = \frac{1}{(\tau p)}(p + p_{\rm q}). \tag{4.68}$$

Here, the additional parameter $p_{\rm q}$ is a characteristic pressure at which the bound and quasibound contributions are equal in both the molecular formation rate or the breakup rate. As constructed, the quasibound formation rate $1/T_{\rm q}$ and lifetime $\tau_{\rm q}$ still satisfy the equilibrium constraint that the formation and breakup of molecules must balance, as in (4.42).

Making the substitutions (4.67) and (4.68) in (4.61), the nonlinear shift becomes

$$\Delta^2\nu \approx \Delta^2_{\rm q}\nu = -\left(\frac{1}{2\pi(Tp^2)}\right)\frac{(\phi p)^3 p}{(p + p_{\rm q})^2 + (\phi p)^2}, \tag{4.69}$$

which is the same as the fit function $\Delta^2_{\rm q}\nu$ of (4.17). Here, the phase shift ϕ is still defined by (4.64). For $p_{\rm q} = 0$, we recover the previous single-bound-state model, $\Delta^2_{\rm q}\nu \longrightarrow \Delta^2_0\nu$ of (4.61). For all values of $p_{\rm q}$, the limiting slope $s_{\rm m}$ is unchanged from the previous result (4.62).

4.5.4 Single state with hyperfine-shift and spin-rotation interactions

Here, we derive the improved model $\Delta^2_1\nu$ of (4.12) from Section 4.2 and its generalizations. We assume a single bound vibration-rotation state, and that the molecular contribution $H_{\rm m}$ of (4.24) includes both the hyperfine-shift interaction (4.1) and the spin-rotation interaction (4.2),

$$H_{\rm m} \approx H_{\rm hfs} + H_{\rm sr} = \delta A\, \mathbf{I}\cdot\mathbf{S} + \gamma\, \mathbf{N}\cdot\mathbf{S}. \tag{4.70}$$

To a good approximation, the spin-rotation interaction is equivalent to an interaction with a static magnetic field,

$$\gamma\,\mathbf{N}\cdot\mathbf{S} \approx -\boldsymbol{\mu}\cdot\mathbf{B}_1, \tag{4.71}$$

where $\boldsymbol{\mu}$ is the total atomic dipole moment (2.4), and the effective magnetic field is

$$\mathbf{B}_1 = \frac{\gamma\mathbf{N}}{g_S\mu_B} = B_1(\mathbf{x}\sin\theta\cos\chi + \mathbf{y}\sin\theta\sin\chi + \mathbf{z}\cos\theta). \tag{4.72}$$

The effective field $\mathbf{B}_1$ is oriented along the direction of the rotational angular momentum $\mathbf{N}$ of a given molecule, which we take to have a colatitude angle θ and azimuthal angle χ. In a statistical average over sticking collisions and molecules, we expect the direction of the momenta $\mathbf{N}$ to follow an isotropic distribution with no preferred direction. Tables 4.1 and 4.6 list characteristic values of B_1 measured by Bouchiat *et al.* [38, 106], which are isotope independent and often denoted as H_1^*.

With this approximation, the bound-atom Hamiltonian (4.24) becomes

$$\overline{H} = (A+\delta A)\,\mathbf{I}\cdot\mathbf{S} - \boldsymbol{\mu}\cdot\overline{\mathbf{B}}, \tag{4.73}$$

where now the total effective field in the molecule is the sum

$$\overline{\mathbf{B}} = \mathbf{B}_0 + \mathbf{B}_1 = \overline{B}(\mathbf{x}\sin\psi\cos\chi + \mathbf{y}\sin\psi\sin\chi + \mathbf{z}\cos\psi). \tag{4.74}$$

Here, we changed the notation of the applied external field, previously denoted $\mathbf{B}$, to

$$\mathbf{B}_0 = B_0\mathbf{z}, \tag{4.75}$$

to avoid potential confusion with $\overline{\mathbf{B}}$. The magnitude of the molecular field (4.74) is

$$\overline{B} = \sqrt{B_0^2 + B_1^2 + 2B_0 B_1 \cos\theta}, \tag{4.76}$$

and the colatitude angle ψ in (4.74) is

$$\psi = \sin^{-1}\left(\frac{B_1}{\overline{B}}\sin\theta\right). \tag{4.77}$$

Because of the spin-rotation interaction (4.2), the quantization axis for bound alkali-metal atoms, which is defined by the molecular field $\overline{\mathbf{B}}$ of (4.74), will in general be different than that for free atoms, which is defined by the applied field $\mathbf{B}_0$ of (4.75). We can account for this difference by introducing a unitary rotation operator,

$$R = e^{-i\chi F_z} e^{-i\psi F_y}, \tag{4.78}$$

to change between the two quantization axes. Using the rotation operator (4.78), we can write the molecular Hamiltonian (4.73) as

$$\overline{H} = R\,\overline{H}_r R^\dagger, \tag{4.79}$$

where the reference Hamiltonian in the rotated frame is

$$\overline{H}_r = (A + \delta A)\,\mathbf{I}\cdot\mathbf{S} - \mu_z \overline{B}, \tag{4.80}$$

and where $\mu_z = \boldsymbol{\mu}\cdot\mathbf{z}$ is the projection of $\boldsymbol{\mu}$ along the z axis. To verify this result, we note that the dot product $\mathbf{I}\cdot\mathbf{S}$ is a scalar under simultaneous rotations of $\mathbf{I}$ and $\mathbf{S}$,

$$R(A + \delta A)\,\mathbf{I}\cdot\mathbf{S}R^\dagger = (A + \delta A)\,\mathbf{I}\cdot\mathbf{S}, \tag{4.81}$$

and that the Zeeman interaction satisfies

$$\begin{aligned} -R\,\mu_z\overline{B}R^\dagger &= -e^{-i\chi F_z}e^{-i\psi F_y}\mu_z e^{i\psi F_y}e^{i\chi F_z}B \\ &= -e^{-i\chi F_z}(\mu_z\cos\psi+\mu_x\sin\psi)e^{i\chi F_z}B \\ &= -(\mu_x\sin\psi\cos\chi+\mu_y\sin\psi\sin\chi+\mu_z\cos\psi)B \\ &= -\boldsymbol{\mu}\cdot\overline{\mathbf{B}}, \end{aligned} \tag{4.82}$$

where we used (4.74) in the last step. Using (4.25) with (4.79), we see the spin eigenstates of the reference Hamiltonian are rotated spin eigenstates of the molecular Hamiltonian,

$$\overline{H}_r R^\dagger|\bar{\mu}\rangle = E_{\bar{\mu}}R^\dagger|\bar{\mu}\rangle. \tag{4.83}$$

We expect the molecular field $\overline{\mathbf{B}}$ of (4.74) to be sufficiently small that we may still write the spin eigenstates of the reference Hamiltonian $\overline{H}_r$ of (4.80) in the low-field basis $|F\,m\rangle$ of Section 2.1.1,

$$\overline{H}_r|F\,m\rangle = E_{Fm}|F\,m\rangle. \tag{4.84}$$

Here, it should be a good approximation to keep only the first-order Zeeman interaction in the energies E_{Fm}. Again, the total spin angular momentum quantum numbers are $F=a=I+1/2$ and $F=b=I-1/2$ for the upper and lower hyperfine manifolds, respectively.

For what follows, it will be convenient to return to the averaged quantity $\langle S_{\alpha\alpha}S^\dagger_{\beta\beta}\rangle_\tau$ of (4.46). Considering (4.84) and (4.83), and using Eqs. 1.4.5(31) and 4.1(1) of the book *Quantum Theory of Angular Momentum* [54], which we will refer to subsequently as Varshalovich, we see that the only terms in the sum (4.46) that contribute to the

frequency shift satisfy

$$|\bar{\mu}\rangle = R|a\,\mu\rangle \quad \text{and} \quad |\bar{\nu}\rangle = R|b\,\nu\rangle. \tag{4.85}$$

Following (2.19), the bound-atom Bohr frequencies in (4.46) are

$$\omega_{\bar{\mu}\bar{\nu}} \approx \frac{(A+\delta A)[I]}{2\hbar} + \frac{g_S\mu_B\overline{B}}{\hbar[I]}(\mu+\nu), \tag{4.86}$$

and the free-atom Bohr frequencies are

$$\omega_{\alpha\beta} \approx \frac{A[I]}{2\hbar} + \frac{g_S\mu_B B_0}{\hbar[I]}(\alpha+\beta). \tag{4.87}$$

If we introduce the parameter

$$r = r(\cos\theta) = \frac{2g_S\mu_B\overline{B}}{\delta A[I]^2} = \sqrt{r_0^2 + r_1^2 + 2r_0r_1\cos\theta}, \tag{4.88}$$

where we used (4.76) to define the components

$$r_0 = \frac{2g_S\mu_B B_0}{\delta A[I]^2} \quad \text{and} \quad r_1 = \frac{2g_S\mu_B B_1}{\delta A[I]^2}, \tag{4.89}$$

which correspond to the applied magnetic field and the effective spin-rotation field, respectively, then we may use (4.86)–(4.89) write the Bohr frequency differences in (4.46) as

$$(\omega_{\bar{\mu}\bar{\nu}} - \omega_{\alpha\beta})\tau \approx [1 + r(\mu+\nu) - r_0(\alpha+\beta)]\phi. \tag{4.90}$$

Table 4.6: Estimates of the parameters $r_1\phi p$ and $r_0\phi p$ for Rb–noble-gas van der Waals molecules using the characteristic values $\langle B_1\rangle = \langle\gamma N\rangle/(g_S\mu_B) = H_1^*$ measured by Bouchiat *et al.* [38, 106] at room temperature (300 K). These values assume either a pure Ar, Kr, or Xe buffer gas. The values of $r_0\phi p$ depend on the applied field B_0, and are estimates for $B_0 = 1$ G.

Molecule	$\langle B_1\rangle = H_1^*$ (G)	$r_1\phi p$ (rad Torr)	$r_0\phi p$ (rad Torr) for $B_0 = 1$ G
^{87}RbAr	1.19 ± 0.05	0.254	0.213
^{87}RbKr	9.59 ± 0.28	2.40	0.250
^{87}RbXe	38.1 ± 1.6	7.97	0.209
^{85}RbAr	1.19 ± 0.05	0.169	0.142
^{85}RbKr	9.59 ± 0.28	1.60	0.167
^{85}RbXe	38.1 ± 1.6	5.31	0.142

Here, ϕ is the same phase shift from the previous sections, as defined by (4.64). Finally, we may write the quantity $\langle S_{\alpha\alpha}S_{\beta\beta}^\dagger\rangle_\tau$ of (4.46) as the sum

$$\left\langle S_{\alpha\alpha}S_{\beta\beta}^\dagger\right\rangle_\tau \approx \sum_{\mu\nu}\frac{|\langle a\,\alpha|R|a\,\mu\rangle\langle b\,\nu|R^\dagger|b\,\beta\rangle|^2}{1+i[1+r(\mu+\nu)-r_0(\alpha+\beta)]\phi}, \tag{4.91}$$

where we used (4.31).

Before we continue, we note that the combined pressure-independent parameters $r_0\phi p$ and $r_1\phi p$ are conveniently independent of δA, unlike the separate parameters ϕ of (4.64) or r_0 and r_1 of (4.89). We may estimate these parameters from measurements of $\langle B_1\rangle$, $\langle\gamma N\rangle$, and $\langle\tau p\rangle$ by Bouchiat *et al.* [38, 106] as

$$\langle r_1\phi p\rangle = \frac{\langle\gamma N\rangle\langle\tau p\rangle}{\hbar[I]} = \frac{g_s\mu_B\langle B_1\rangle\langle\tau p\rangle}{\hbar[I]}, \quad \text{and} \quad \langle r_0\phi p\rangle = \frac{g_s\mu_B B_0\langle\tau p\rangle}{\hbar[I]}, \tag{4.92}$$

which give the values listed in Table 4.6. Note that these values assume a pure, single-component buffer gas. We used the estimates of $r_1\phi p$ with Xe in Sections 4.2 and 4.3 as constraints during fits to measurements.

The quantity (4.91) has already been averaged over an exponential distribution of molecular lifetimes with mean value τ. However, to determine the frequency shift, we also need to perform an average over an isotropic distribution of directions for the momenta $\mathbf{N}$, or equivalently, for the effective field $\mathbf{B}_1$ of (4.72). Averaging (4.91) over all directions for $\mathbf{B}_1$ gives

$$\begin{aligned}\left\langle S_{\alpha\alpha}S^{\dagger}_{\beta\beta}\right\rangle_{\tau,\mathbf{N}} &= \frac{1}{4\pi}\int_0^{2\pi} d\chi \int_0^{\pi} \sin\theta d\theta \left\langle S_{\alpha\alpha}S^{\dagger}_{\beta\beta}\right\rangle_{\tau} \\ &\approx \frac{1}{2}\sum_{\sigma}\int_0^{\pi} \sin\theta d\theta \, \frac{f_{\sigma}^{\alpha\beta}(\cos\psi)}{1+i[1+r\sigma-r_0(\alpha+\beta)]\phi},\end{aligned} \tag{4.93}$$

where we introduced the index $\sigma = \mu + \nu$, which can take the values $-2I, 1-2I, \ldots, 2I-1, 2I$, and the angular functions

$$\begin{aligned}f_{\sigma}^{\alpha\beta}(\cos\psi) &= \frac{1}{2\pi}\sum_{\mu}\int_0^{2\pi} d\chi \, |\langle a\,\alpha|R|a\,\mu\rangle\langle b,\sigma-\mu|R^{\dagger}|b\,\beta\rangle|^2 \\ &= \frac{1}{2\pi}\sum_{\mu}\int_0^{2\pi} d\chi \, |D^{a}_{\alpha\mu}(\chi,\psi,0)D^{b}_{\sigma-\mu,\beta}(\chi,\psi,0)|^2 \\ &= \sum_{\mu}|d^{a}_{\alpha\mu}(\psi)d^{b}_{\sigma-\mu,\beta}(\psi)|^2,\end{aligned} \tag{4.94}$$

which depend on the colatitude angle θ through the relation (4.77). To go from the first to the second line, which uses Wigner D–functions, we used (4.78) and Eqs. 1.4.5(31) and 4.1(1) of Varshalovich [54]. To go from the second to the third line, which uses Wigner d–functions, we used Eq. 4.3(1) of Varshalovich [54]. The angular functions (4.94) sum to unity:

$$\begin{aligned}\sum_{\sigma} f_{\sigma}^{\alpha\beta}(\cos\psi) &= \frac{1}{2\pi}\sum_{\sigma\mu}\int_0^{2\pi} d\chi \, |\langle a\,\alpha|R|a\,\mu\rangle\langle b,\sigma-\mu|R^{\dagger}|b\,\beta\rangle|^2 \\ &= \frac{1}{2\pi}\sum_{\bar{\mu}\bar{\nu}}\int_0^{2\pi} d\chi \, |\langle\alpha|\bar{\mu}\rangle\langle\bar{\nu}|\beta\rangle|^2 \\ &= 1\end{aligned} \tag{4.95}$$

Here, we used the identities (4.31) and (4.85) to go from the first to the second line, and completeness (4.26) to go from the second to the third.

Before we further analyze the functions $f_\sigma^{\alpha\beta}(\cos\psi)$, we can use the result (4.93) to write the molecular frequency shift (4.37) of the α–β hyperfine transition as

$$\Delta\omega \approx \frac{1}{2T}\sum_\sigma \int_0^\pi \sin\theta d\theta \, \frac{f_\sigma^{\alpha\beta}(\cos\psi)[1+r\sigma-r_0(\alpha+\beta)]\phi}{1+[1+r\sigma-r_0(\alpha+\beta)]^2\phi^2}. \tag{4.96}$$

Noting that $\phi \propto \tau \propto 1/p$, we see that the linear, limiting slope (4.49) is

$$s_{\mathrm{m}} \approx \frac{\phi}{4\pi T p}\sum_\sigma \int_0^\pi \sin\theta d\theta \, f_\sigma^{\alpha\beta}(\cos\psi)[1+r\sigma-r_0(\alpha+\beta)], \tag{4.97}$$

and the nonlinear shift (4.50) is

$$\Delta^2\nu \approx -\frac{1}{2T}\sum_\sigma \int_0^\pi \sin\theta d\theta \, \frac{f_\sigma^{\alpha\beta}(\cos\psi)[1+r\sigma-r_0(\alpha+\beta)]^3\phi^3}{1+[1+r\sigma-r_0(\alpha+\beta)]^2\phi^2}. \tag{4.98}$$

In all three quantities above, both the angular functions $f_\sigma^{\alpha\beta}(\cos\psi)$ of (4.94) and the angular parameter $r = r(\cos\theta)$ of (4.88) depend on the colatitude angle θ.

To verify these results, we note that in the limit of a large applied field, $B_0 \gg B_1$, we expect to recover the relatively simple results of Section 4.5.2, since the quantization axis would then be defined by the direction of $\mathbf{B}_0$. In this limit, we see from (4.77) and (4.76) that $\cos\psi \longrightarrow 1$, and from (4.88) and (4.89) that $r \longrightarrow r_0$. Using Eq. 4.16(2) of Varshalovich [54], we find that the angular functions $f_\sigma^{\alpha\beta}(\cos\psi)$ of (4.94) become a Kronecker delta function,

$$f_\sigma^{\alpha\beta}(1) = \delta_{\sigma,\alpha+\beta}. \tag{4.99}$$

Together, we see that in this high-field limit, the nonlinear shift (4.98) and the limiting slope (4.97) simplify to the previous results (4.61) and (4.62), respectively. Alterna-

tively, we would recover the same results in the limit of a negligible spin-rotation interaction (4.2) compared to the hyperfine-shift interaction (4.1), $r_1 \longrightarrow 0$.

By inspection, we see that the nonlinear shift (4.98) and the limiting slope (4.97) depend on the choice of hyperfine transition. For the particular case of the 0–0 (or clock) transition, with $\alpha = \beta = 0$, we can further reduce the angular functions $f_\sigma^{\alpha\beta}(\cos\psi)$ of (4.94) as follows:

$$\begin{aligned} f_\sigma^{00}(\cos\psi) &= \frac{1}{2\pi}\sum_\mu \int_0^{2\pi} d\chi \, |D^a_{0\mu}(\chi,\psi,0) D^b_{\sigma-\mu,0}(\chi,\psi,0)|^2 \\ &= \frac{8\pi}{[a][b]}\sum_\mu \int_0^{2\pi} d\chi \, |Y_{a\mu}(\psi,\chi) Y_{b,\sigma-\mu}(\psi,\chi)|^2 \\ &= \sum_\mu \frac{(a-\mu)!(b-\sigma+\mu)!}{(a+\mu)!(b+\sigma-\mu)!} |P_a^\mu(\cos\psi) P_b^{\sigma-\mu}(\cos\psi)|^2. \end{aligned} \tag{4.100}$$

To go from the first to the second line, which uses spherical harmonics, we used Eq. 4.17(1) of Varshalovich [54], and from the second to the third line, which uses associated Legendre polynomials, we used Eq. 5.2(1). Using the identities $P_n^{-m}(x) = (-1)^m (l-m)! P_n^m(x)/(l+m)!$ and $P_n^m(-x) = (-1)^{n+m} P_n^m(x)$ [65], one can show that this particular function is even in both arguments,

$$f_{-\sigma}^{00}(x) = f_\sigma^{00}(x) \quad \text{and} \quad f_\sigma^{00}(-x) = f_\sigma^{00}(x). \tag{4.101}$$

The final expression on the third line of (4.100) is relatively straightforward to evaluate numerically, for example, with the function legendre() in MATLAB [94].

For the improved model $\Delta_1^2\nu$ of (4.12) from Section 4.2, we considered the limit of a negligible applied field, $B_0 \ll B_1$. In this low-field limit, we see from (4.88) and (4.89) that the parameter $r \longrightarrow r_1$, and that the quantity (4.93) simplifies to

$$\lim_{B_0 \ll B_1} \left\langle S_{\alpha\alpha} S^\dagger_{\beta\beta} \right\rangle_{\tau,\mathbf{N}} \approx \sum_\sigma \frac{W_\sigma^{\alpha\beta}}{1 + i[1 + r_1\sigma - r_0(\alpha+\beta)]\phi}, \tag{4.102}$$

where we introduced the weight coefficients

$$W_\sigma^{\alpha\beta} = \frac{1}{2}\int_0^\pi \sin\theta d\theta\, f_\sigma^{\alpha\beta}(\cos\psi). \tag{4.103}$$

Using the result (4.102), we may write the low-field molecular frequency shift (4.37) of the α–β hyperfine transition as

$$\Delta\omega \approx \frac{1}{T}\sum_\sigma \frac{W_\sigma^{\alpha\beta}[1 + r_1\sigma - r_0(\alpha+\beta)]\phi}{1 + [1 + r_1\sigma - r_0(\alpha+\beta)]^2\phi^2}. \tag{4.104}$$

In this low-field limit, the linear, limiting slope (4.97) simplifies to

$$s_{\rm m} \approx \frac{1}{2\pi T p}\sum_\sigma W_\sigma^{\alpha\beta}[1 + r_1\sigma - r_0(\alpha+\beta)]\phi, \tag{4.105}$$

and the nonlinear shift (4.98) simplifies to

$$\Delta^2\nu \approx -\frac{1}{2\pi T}\sum_\sigma \frac{W_\sigma^{\alpha\beta}[1 + r_1\sigma - r_0(\alpha+\beta)]^3\phi^3}{1 + [1 + r_1\sigma - r_0(\alpha+\beta)]^2\phi^2}. \tag{4.106}$$

We can write the low-field weights $W_\sigma^{\alpha\beta}$ of (4.103) in terms of Clebsch–Gordon coefficients as follows:

$$\begin{aligned}
W_\sigma^{\alpha\beta} &= \frac{1}{4\pi}\sum_\mu \int_0^{2\pi} d\chi \int_0^\pi \sin\theta d\theta\, |d^a_{\alpha\mu}(\theta) d^b_{\sigma-\mu,\beta}(\theta)|^2 \\
&= \frac{1}{8\pi^2}\sum_\mu \int d\Omega\, D^a_{\alpha\mu} D^{a*}_{\alpha\mu} D^b_{\sigma-\mu,\beta} D^{b*}_{\sigma-\mu,\beta} \\
&= \frac{(-1)^{\sigma+\alpha+\beta}}{8\pi^2}\sum_\mu \int d\Omega\, D^a_{\alpha\mu} D^a_{-\alpha,-\mu} D^b_{\sigma-\mu,\beta} D^b_{\mu-\sigma,-\beta} \\
&= \frac{(-1)^{\sigma+\alpha+\beta}}{8\pi^2}\sum_{\mu jk} C^{j0}_{a\alpha;a,-\alpha} C^{j0}_{a\mu;a,-\mu} C^{k0}_{b\beta;b,-\beta} C^{k0}_{b,\sigma-\mu;b,\mu-\sigma} \int d\Omega\, D^j_{00} D^k_{00} \\
&= (-1)^{\sigma+\alpha+\beta}\sum_{\mu k} \frac{1}{[k]} C^{k0}_{a\alpha;a,-\alpha} C^{k0}_{a\mu;a,-\mu} C^{k0}_{b\beta;b,-\beta} C^{k0}_{b,\sigma-\mu;b,\mu-\sigma}.
\end{aligned} \tag{4.107}$$

The first line is the definition (4.103) using (4.94), where we noted from (4.77) that $\psi \longrightarrow \theta$ in the low-field limit. To go from the first to the second line we used Eq. 4.3(1) of Varshalovich [54], and wrote the angular average in terms of Euler angles, $\int_0^{2\pi} d\chi \int_0^{\pi} \sin\theta d\theta \longrightarrow \int_0^{2\pi} d\alpha \int_0^{2\pi} d\chi \int_0^{\pi} \sin\theta d\theta/(2\pi) = \int d\Omega/(2\pi)$. To go from the second line to the third line we used Eqs. 4.4(2) and 4.4(3) of Varshalovich [54], from the third to the fourth, Eq. 4.6.1(1), and from the fourth to the fifth, the orthogonality relation Eq. 4.11.1(2). In simplifying the power of the pre-factor -1, we assumed that the nuclear spin I is half-integer, which is required for a 0–0 transition to exist, and which is the case for the most common alkali-metal isotopes, as shown in Section 2.1.1. The final expression on the fifth line of (4.107) may be evaluated numerically, for example, with the code available in Ref. [21].

By inspection, the weights $W_\sigma^{\alpha\beta}$ of (4.103) depend on the choice of hyperfine transition. From the symmetry properties of Clebsch–Gordon coefficients, Eq. 8.4.3(10) of Varshalovich [54], one can show that

$$W_{-\sigma}^{\alpha\beta} = W_\sigma^{\alpha\beta} \quad \text{and} \quad W_\sigma^{\alpha\beta} = W_\sigma^{-\alpha,-\beta}. \tag{4.108}$$

As a result, out of the $[a][b] = [I]^2 - 1 = 4I(I+1)$ possible hyperfine transitions, there are only $([a][b]+1)/2 = [I]^2/2$ unique sets of weights $W_\sigma^{\alpha\beta}$ versus σ. For example, for ^{87}Rb, which has 15 possible hyperfine transitions, there are 8 unique sets of $W_\sigma^{\alpha\beta}$. Regardless of the choice of hyperfine transition, the set of weighs (4.103) sum to unity,

$$\sum_\sigma W_\sigma^{\alpha\beta} = 1, \tag{4.109}$$

because the angular functions $f_\sigma^{\alpha\beta}(\cos\psi)$ sum to unity, as in (4.95). From (4.108) we see that

$$\sum_\sigma W_\sigma^{\alpha\beta}\sigma = 0. \tag{4.110}$$

Using this with (4.109), we can further simplify the linear, limiting slope (4.105) to

$$s_\mathrm{m} \approx \frac{[1 - r_0(\alpha+\beta)]\phi}{2\pi T p}. \tag{4.111}$$

For the particular case of the 0–0 transition in the low-field limit, $B_0 \ll B_1$, we recover the fit function $\Delta_1^2\nu$ of (4.12) for the nonlinear shift from (4.106),

$$\Delta^2\nu \approx \Delta_1^2\nu = -\left(\frac{1}{2\pi T}\right)\sum_{\sigma=-2I}^{2I}\frac{W_\sigma(1+r_1\sigma)^3\phi^3}{1+(1+r_1\sigma)^2\phi^2}, \tag{4.112}$$

the expression (4.14) for the weights W_σ from (4.107),

$$W_\sigma = W_\sigma^{00} = \sum_{\mu k}\frac{(-1)^\sigma}{[k]}C^{k0}_{a0;a0}C^{k0}_{a,\mu;a,-\mu}C^{k0}_{b0;b0}C^{k0}_{b,\sigma-\mu;b,\mu-\sigma}, \tag{4.113}$$

and the previous result (4.62) for the limiting slope s_m from (4.111). For the first few half-integer values of I, the weights (4.113) form the sets:

$$I = \frac{1}{2}\colon\ [W_1,\ldots,W_{-1}] = \frac{[1,1,1]}{3}, \tag{4.114}$$

$$(^{87}\mathrm{Rb})\ I = \frac{3}{2}\colon\ [W_3,\ldots,W_{-3}] = \frac{[9,9,23,23,23,9,9]}{105}, \tag{4.115}$$

$$(^{85}\mathrm{Rb})\ I = \frac{5}{2}\colon\ [W_5,\ldots,W_{-5}] = \frac{[50,50,94,94,193,193,193,94,94,50,50]}{1155}, \tag{4.116}$$

$$(^{133}\mathrm{Cs})\ I = \frac{7}{2}\colon\ [W_7,\ldots,W_{-7}] = \frac{[245,245,425,425,659,659,1231,1231,1231,659,659,425,425,245,245]}{9009}. \tag{4.117}$$

In summary, the effect of the spin-rotation interaction (4.2) is to split the frequency shift (4.98) into a discrete sum of frequency shifts indexed by σ. Physically, the discrete sum results from the spin-rotation interaction tilting the quantization axis for a bound alkali-metal atom, by introducing the effective magnetic field $\mathbf{B}_1$ of (4.72). In general, the frequency shift (4.98) from molecules will depend on the applied magnetic field B_0, and the choice of hyperfine transition. For a large enough applied field, $B_0 \gg B_1$, the spin-rotation interaction becomes negligible, and we recover the previous model of Section 4.5.2. For smaller applied fields, the spin-rotation interaction generally increases the size of the nonlinear shift $\Delta^2\nu$ compared to the previous model $\Delta_0^2\nu$ of Section 4.5.2, for the same values of the parameters ϕ and T.

For a small enough applied field, $B_0 \ll B_1$, we obtain the relatively simple expression (4.104) for the molecular frequency shift, which recovers the fit function $\Delta_1^2\nu$ of (4.12) for the particular case of the 0–0 transition. Here, averaging over all orientations for van der Waals molecules produced the weights W_σ of (4.113) for the discrete frequency shifts. Finally, we note that the oscillatory fit residuals $\delta\nu_3$ displayed in Fig. 4.2 may be though of as an interference pattern produced by the superposition of the different, discrete frequency shifts indexed by σ in the nonlinear shift $\Delta_1^2\nu$ of (4.12) as the molecular lifetime $\tau \propto 1/p$ varies.

4.6 Summary and discussion

In summary, we report relatively large nonlinear pressure shifts of ^{87}Rb, ^{85}Rb, and ^{133}Cs in Xe, which are opposite in sign to the nonlinear shifts with Ar and Kr. Discrepancies with the previous model (4.6) demonstrate the importance of the spin-rotation interaction (4.2) to nonlinear pressure shifts and to the status of vapor-cell clocks as secondary frequency standards. We provide an improved model (4.11) of the shifts for ^{87}Rb and ^{133}Cs in Xe, and report improved measurements of the nonlinear

shifts of ^{87}Rb in Ar and Kr. We provide the first measurement of these shifts of ^{85}Rb in Ar, Kr, and Xe, which suggest that the remaining discrepancy between theory and experiment is most likely due to still-smaller spin interactions in the molecules, other than the hyperfine-shift interaction (4.1) and the spin-rotation interaction (4.2), though not with the nuclear spin of the buffer gas. To the limit of our experimental accuracy, the shifts of Rb and Cs in He, Ne, and N_2 were linear with pressure. Further precision measurement of nonlinear shifts should give a better understanding of the detailed physics of van der Waals molecules.

Chapter 5

Prospects for pressure-shift suppression

5.1 Introduction

Vapor-cell clocks require a chemically inert buffer gas to prevent the clock atoms from diffusing too quickly to the cell walls, where collisions broaden the resonance lines and seriously degrade the clock performance. Unfortunately, as discussed in the last two chapters, the buffer gas introduces a pressure shift of the clock frequency. This pressure shift is the main reason why vapor-cell clocks are secondary, not primary frequency standards, and require calibration [11, 15, 16]. In this chapter, we consider the prospects for suppressing the pressure shift in vapor-cell clocks.

A simple technique to suppress the pressure shift is to use a mixture of buffer gases with opposing shifts that cancel. For example, a mixture of Ar and N_2, similar to that typically used in conventional clocks, can be adjusted to give no pressure shift. However, such zero-shift mixtures will only produce a zero pressure shift at a particular zero-shift temperature, which depends on the exact composition and pressure of the buffer gas. In the next section, we demonstrate a zero-shift mixture of Ar and N_2 for

a ^{87}Rb vapor-cell clock. We then propose a few possible implementations for feedback to adjust the cell temperature to suppress the pressure shift. One advantage of this feedback is that it can compensate for significant changes to the buffer gas, for example, from the accumulation of contaminant gas over time, or for the irreproducibility in filling cells. We simulate this by adding He as an intentional contaminant in the next section. Unfortunately, the pressure shifts from van der Waals molecules, as discussed in Chapter 4, can introduce a significant error in this approach to suppress the pressure shift. We model this error in Section 5.4 for conditions similar to those of the experimental demonstration in Section 5.2.

Before we begin, we first provide some background on the accuracy of conventional vapor-cell clocks.

5.1.1 Accuracy of conventional vapor-cell clocks

As mentioned in Section 3.1.1, conventional ^{87}Rb vapor-cell clocks typically use mixtures of buffer gases, such as N_2 and Ar, that are optimized to reduce any change in the pressure shift with temperature. These mixtures still produce a net pressure shift, which is on the order of 200 Hz per Torr of buffer gas [16]. In practice, the irreproducibility of filling vapor cells with buffer gas leads to a fractional inaccuracy of the clock frequency on the order of 10^{-9}, or roughly 7 Hz for the 0–0 frequency ν of ^{87}Rb [16]. After an initial calibration by the manufacturer, this inaccuracy is typically reduced to within 5×10^{-11}, or roughly 1/3 Hz for ν [125].

Unfortunately, conventional vapor-cell clocks drift during use, with a typical reduction in accuracy of 5×10^{-11} per month and 5×10^{-10} per year [125]. This long term drift is not yet completely understood [14, 16], though changes in the pressure shift, for example, due to the accumulation of contaminant gas [126], are known to contribute significantly in miniature clocks [127]. As a result, conventional vapor-cell clocks require repeated calibration to maintain their initial accuracy, for example, by

monitoring signals from the Global Positioning System. In contrast, typical commercial Cs beam clocks are accurate to within 10^{-12} without calibration, and so serve as working primary standards [125].

Ideally, one would like a vapor-cell clock that has a significantly reduced drift and does not require calibration to maintain its accuracy, like a Cs beam clock [128]. One way to do this might be to suppress the two dominant frequency shifts in these clocks, the light shift and the pressure shift. While there is an important second-order Zeeman shift of the 0–0 transition, it may be precisely controlled, as is done in primary standards. We discussed how to suppress the light shift in Chapter 2, and so this chapter describes how one might similarly suppress the pressure shift.

5.2 Experiment

To demonstrate the properties of a zero-shift buffer-gas mixture, we measured the 0–0 hyperfine frequency ν of ^{87}Rb using the experimental setup of Chapter 4. We sup-

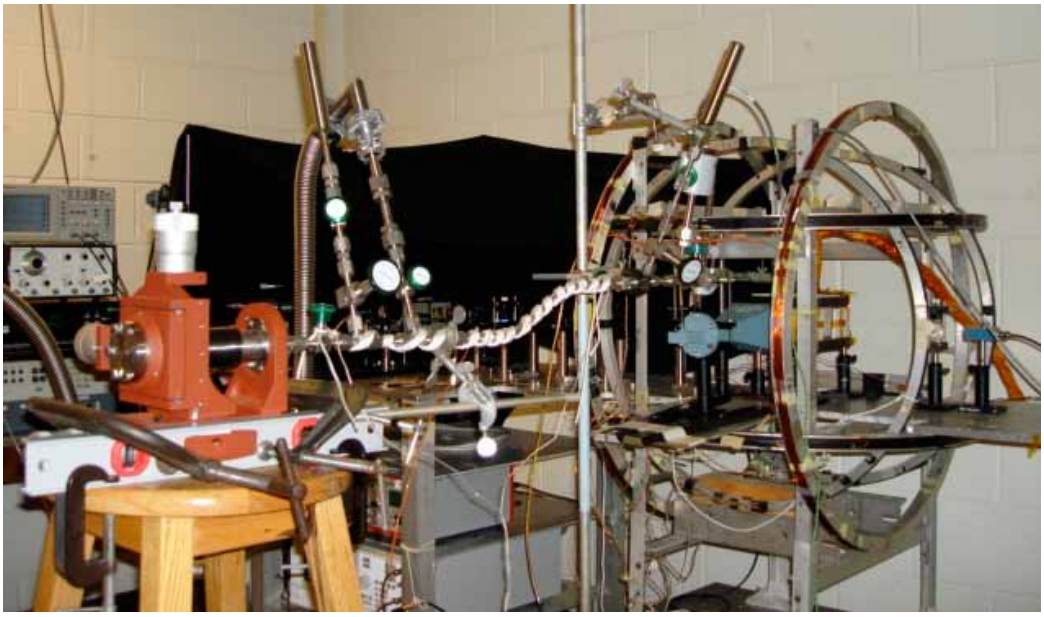

Figure 5.1: Experimental setup with adjustable vacuum bellows (left, on stool) attached to the ^{87}Rb vapor cell of Fig. 4.10 (right, inside Helmholtz coils). By adjusting the bellows, we could manually vary the buffer-gas pressure by roughly $\pm 13\%$.

pressed the light shift with the conventional, intensity-modulation method of Chapter 2. The applied magnetic field $B \approx 0.14$ G. To vary the buffer-gas pressure in a controlled manner, we modified the ^{87}Rb vapor cell of Chapter 4, shown in Fig. 4.10, by attaching a section of vacuum bellows (Huntington PM-275), as shown in Fig. 5.1.

Initially, we filled the vapor cell with a 30 Torr mixture of Ar and N_2 at 50.0° C. The ratio of partial pressures of Ar:N_2 was roughly 9.170:1. By manually adjusting the bellows, we could vary the buffer-gas pressure between 23–30 Torr. For a given bellows configuration, we measured the actual buffer-gas pressure with a capacitance manometer (MKS Instruments Baratron), and the 0–0 frequency ν with a frequency counter referenced to a rubidium frequency standard (Stanford Research Systems FS725).

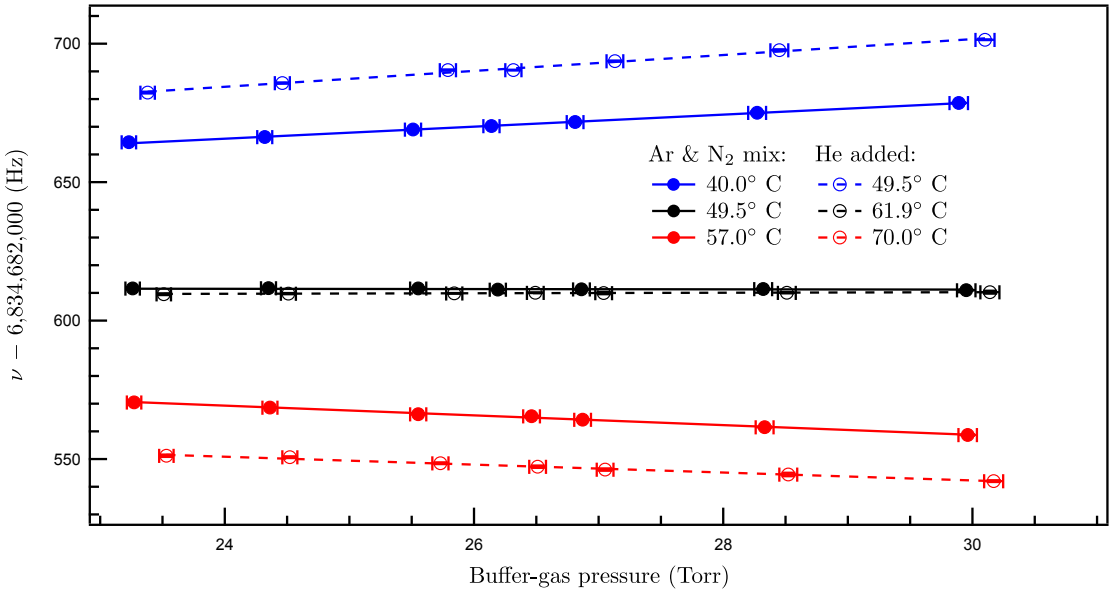

Figure 5.2: Demonstration of a zero-shift buffer-gas mixture for ^{87}Rb with applied field $B \approx 0.14$ G. Each point is a measurement of the clock frequency ν for a given buffer-gas pressure and oven temperature. The buffer-gas pressure was varied by adjusting the vacuum bellows shown in Fig. 5.1. The curves are straight line fits to the data for a given temperature. The solid points and curves are measurements with a 9.170:1 mixture of Ar and N_2. The open points and dashed curves are measurements after adding roughly 0.1 Torr of He to the mixture, which raised the zero-slope temperature by about 12° C.

Fig. 5.2 is a summary of measurements at three different oven temperatures. As the data show, when the temperature is increased from 40.0° C to 57.0° C, the change of the clock frequency ν with the buffer-gas pressure, or the slope in the figure, transitions from positive to negative. Therefore, there is an intermediate "zero-slope" temperature at which the clock frequency ν is independent of the buffer-gas pressure. For small deviations away from this zero-slope temperature, there will be a residual pressure dependence, or slope, whose sign and amplitude are proportional to the sign and amplitude of the temperature deviation. Therefore, this residual slope can be used as an error signal for feedback to servo the oven temperature to the zero-slope temperature. For buffer gases with linear pressure shifts, this zero-slope temperature is equivalent to a zero-shift temperature, at which there is no pressure shift.

By manually performing this feedback, we estimated the zero-slope temperature of the Ar and N_2 mixture to be nearly 49.5° C, as shown in Fig. 5.2. A linear fit to the data estimates a residual pressure dependence, or slope, of -0.052 ± 0.035 Hz Torr^{-1}, which could be reduced further by active feedback. An average of the data points at 49.5° C gives a zero-slope clock frequency $\nu \approx$ 6,834,682,611.5 ± 0.3 Hz.

Next, we simulated the effects of a contaminant gas by adding about 0.1 Torr of He to the cell, which increased the clock frequency ν by about 70 Hz. This quantity of contaminant gas is significantly larger than would be expected to accumulate during the working life of a vapor-cell clock. As shown in Fig. 5.2, the contaminant did not drastically alter the properties of the gas mixture. Instead, the net effect was to raise the zero-slope temperature by roughly 12° C. Performing manual feedback again, we estimated the zero-slope temperature of the Ar, N_2, and He mixture to be nearly 61.9° C. A linear fit to the data estimates a residual slope of 0.100 ± 0.014 Hz Torr^{-1}, which again could be further reduced by active feedback. An average of the data points at 61.9° C gives a zero-slope frequency $\nu \approx$ 6,834,682,610.0 ± 0.2 Hz.

The similarity of both zero-slope frequencies, from before and after adding He, suggests that these frequencies are very close to the zero-shift frequency. We chose the applied field $B \approx 0.14$ G so that this zero-shift frequency was close to the free-atom, zero-field frequency $\nu_{00} \approx 6,834,682,610.9$ Hz for ^{87}Rb, given in Chapter 2.1.1. It is important to note that we were only able to do this because of two sources of error:

(i) the long-term drift of the rubidium frequency standard used as a reference, and

(ii) a nonlinear pressure shift from RbAr van der Waals molecules.

Without these two errors, the inferred zero-shift frequency must be at least ~ 11.3 Hz above the free-atom, zero-field frequency ν_{00}, because of the quadratic Zeeman shift (≈ 575.15 Hz G^{-2} [52]). Instead, we see that these frequencies agree to within 1 Hz.

Most of this discrepancy is due to error (i), which offsets each measured frequency ν from its true value. We can estimate this offset from the manufacturer specifications for the rubidium frequency standard, which list an expected fractional drift below 5×10^{-10} per year [129]. A period of about 4.25 years elapsed between the latest calibration in April 2004 and the measurement in July 2008, so we should expect an offset between $\pm$ 14.5 Hz. Since the long-term drift of a conventional vapor-cell clock is mostly linear and cumulative with time [14], this error seems likely to account for most, if not all of the 11.3 Hz discrepancy.

We will estimate error (ii) in Section 5.4. In short, for zero-shift buffer-gas mixtures that can form van der Waals molecules with akali-metal atoms, such as RbAr, the zero-shift temperature may not equal the zero-slope temperature. As a result, there may be a significant pressure shift at the zero-slope temperature, even though the clock frequency is insensitive to small changes in the buffer-gas pressure.

Finally, we note that we repeated this process of manually suppressing the pressure shift with the same cell and bellows, but a new buffer-gas mixture in order to measure the clock performance data in Fig. 2.7 of Chapter 2.

5.3 Possible implementations

We now describe a few possible implementations of active feedback to servo the cell temperature to the zero-slope temperature, which are sketched in Fig. 5.3. In all implementations, it is assumed that the light shift is suppressed, for example, by a method described in Chapter 2.

The first implementation, sketched in Fig. 5.3(a), directly modulates the buffer-gas pressure in a sealed vapor cell [128]. A slow, isothermal modulation of the pressure will produce a resulting modulation of the clock frequency for temperatures other than the

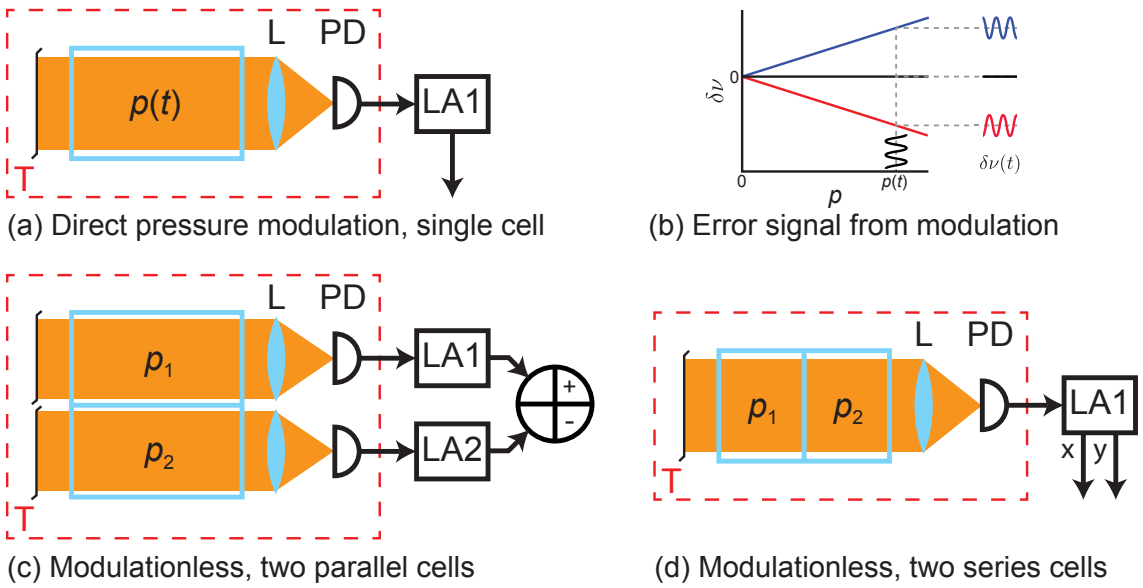

Figure 5.3: Possible implementations of pressure-shift suppression in a vapor-cell clock described in Section 5.3. (a) Direct modulation of the buffer-gas pressure in a single vapor cell. (b) The error signal from pressure modulation is due to the resulting modulation of the clock frequency for temperatures other than the zero-slope temperature. (c) Two vapor cells interrogated in parallel, without pressure modulation. (d) Two vapor cells interrogated in series, without pressure modulation. L, lens; PD, photodiode; LA, lock-in amplifier; T, oven temperature;

zero-slope temperature, as sketched in Fig. 5.3(b). An error signal may be produced by detecting this resulting clock-frequency modulation in the microwave feedback loop with a lock-in amplifier, just as in the conventional, intensity-modulation method of light-shift suppression described in Chapter 2. Feedback with this error signal will servo the cell temperature to the zero-slope temperature.

Possible means of producing such pressure modulation include using an actuated vacuum bellows, a separate chamber with a thermally cycled filament, a micro-electro-mechanical systems (MEMS) pump [130, 131], an electrowetted liquid-metal piston [132], or a nozzle-shaped acoustic rectifier [133] based on acoustic streaming [134, 135, 136, 137]. For example, a long glass stem could connect the cell to an external pressure modulator. We note that long glass stems have been used in high-performance vapor-cell clocks [138]. Unfortunately, none of these means seem particularly well suited for compact or miniature vapor-cell clocks.

Alternatively, to avoid the difficulty of pressure modulation, one could use two vapor cells (or one partitioned cell) with exactly the same buffer-gas mixture and temperature, but two slightly different buffer-gas pressures. Two such schemes are sketched in Fig. 5.3. In both, the error signal comes directly from the microwave feedback loop, as a result of the microwave frequency modulation, which is at a much faster rate than would be achievable with pressure modulation. We note that the use of two vapor cells is common in conventional, lamp-pumped vapor-cell clocks based on the "separated filter" approach [11], and that extra "clone" cells have been used in laser-pumped clocks to improve the short-term performance [16].

In Fig. 5.3(c), the two cells are interrogated in parallel. The pumping beam may be from the same source, or two different sources. The same microwaves probe both cells, either directly, for example, in a cavity, or indirectly through modulating the pumping light, as in coherent population trapping. Here, each cell produces its own error signal for the microwave carrier frequency. The sum of these two error signals

may be used to lock the microwave carrier frequency. The difference of the two then serves as an error signal to servo the temperature to a zero-slope temperature, at which both cells have the same microwave resonant frequency, the zero-slope frequency.

In Fig. 5.3(d), the two cells are interrogated in series by the same pumping beam. Here, the same lock-in amplifier provides the error signals for the microwave carrier frequency and the temperature, just as in the quadrature method of light-shift suppression described in Chapter 2. The same arguments in Section 2.2.1 apply here, where now the difference in resonant frequencies is due to the pressure shift, instead of the light shift. The microwave linewidths for the two cells will be different because of a difference in power broadening from the pumping light, and also in pressure broadening from the buffer gas.

While these two "proxy" modulation schemes avoid the difficulty of implementing pressure modulation, in the long-term, they might require a similarly difficult means of circulating gas between the two cells to maintain identical buffer-gas compositions. A two-cell design may also require a better control of spatial temperature gradients. In addition, too large of a pressure difference between the cells might require two separate pumping lasers to suppress the light shift for each cell independently, adding complexity.

Despite the implementation, the accuracy of pressure-shift suppression will greatly depend on the choice of buffer-gas mixture. This is because the most common buffer gases with negative pressure shifts — Ar, Kr, and Xe — all have nonlinear pressure shifts, as described in Chapter 4. These nonlinear shifts can lead to a residual pressure shift at the zero-slope temperature, as will be shown in the next section. Further precision measurement is required to find a negative-shifting gas with a sufficiently linear pressure shift. Possible candidates include molecular hydrocarbon gases, such as CH_4, which have been successfully used as buffer gases [11]. We note that Strumia *et al.* [139] have demonstrated how to reduce the temperature sensitivity of a zero-

shift buffer-gas mixture by using three or more components, for example, a mixture of He, N_2, and C_2H_6.

With a proper zero-shift buffer-gas mixture, each of the implementations shown in Fig. 5.3 would be able to correct for changes in the buffer-gas composition over time, for example, from He permeation or residual chemical reactions. They would also be insensitive to the irreproducibility of sealing vapor cells with a known buffer-gas pressure, as mentioned in Section 5.1.1. Finally, we note that depending on the desired degree of pressure-shift suppression, even smaller frequency shifts than the light shift may be important, such as the spin-exchange shift [16].

5.4 Modeling of error from van der Waals molecules

To demonstrate how a nonlinear pressure shift from van der Waals molecules may lead to an error in pressure-shift suppression, we will estimate this error for ^{87}Rb in the Ar and N_2 mixture demonstrated in Section 5.2. There, the vapor cell was initially filled to a pressure $p_{\text{fill}} = 30.0$ Torr at a temperature $T_{\text{fill}} = 50.0°$ C. Let p_{p} be the partial pressure at T_{fill} of the positive-shift gas N_2, and let p_{n} be the same for the negative-shift gas Ar, such that $p_{\text{fill}} = p_{\text{p}} + p_{\text{n}}$. We can then write the pressure shift for the sealed cell as the sum

$$\delta\nu = \nu - \nu_0 = s_{\text{p}}p_{\text{p}} + s_{\text{n}}p_{\text{n}} + \Delta^2\nu, \tag{5.1}$$

which depends on the actual cell temperature T. The first two terms are linear pressure shifts, and the third is a nonlinear pressure shift.

As discussed in Chapter 4, RbAr molecules contribute to both the linear shift $s_{\text{n}}p_{\text{n}}$ and the nonlinear shift $\Delta^2\nu$ in (5.1). Since the formation rate and lifetime of RbAr

molecules depend on the composition of the buffer gas, both of these contributions will too. For simplicity, we will ignore this composition dependence. Since the mixture is mostly Ar, we will overestimate the nonlinear shift to be the same as that of pure Ar,

$$\Delta^2\nu \approx -\left(\frac{1}{2\pi(Tp^2)}\right)\frac{(\phi p)^3 p_{\text{fill}}}{p_{\text{fill}}^2+(\phi p)^2}, \tag{5.2}$$

where the parameters (Tp^2) and (ϕp) are given in Table 4.3. In reality, the actual nonlinear shift is likely smaller, since the addition of N_2 should reduce the number of RbAr molecules. We will also ignore the weak dependence of the parameters (Tp^2) and (ϕp) on temperature [39, 140].

To model the linear pressure shifts, $s_{\text{p}}p_{\text{p}}$ and $s_{\text{n}}p_{\text{n}}$ in (5.1), we will use the measurements of Bean and Lambert [75]. Using (3.29) of Chapter 3, we may write each of the linear slopes, s_{p} and s_{n}, in the form

$$s = s(T) \approx 2.2514\left(\frac{T_{\text{s}}}{T_{\text{fill}}}\right)\sum_{n=0}^{D} c_n\,(\delta T)^n\,. \tag{5.3}$$

Here, the measured coefficients c_n are for ^{85}Rb in Ar or in N_2, the temperature $T_{\text{s}} = 0^\circ$ C, and the variable $\delta T = (T - 0^\circ\text{ C})/10^3$. The ratio of absolute temperatures $T_{\text{s}}/T_{\text{fill}}$ in Kelvin adjusts for the change in reference temperature, $T_{\text{s}} \longrightarrow T_{\text{fill}}$. The factor of 2.2514, which is approximately the ratio of the 0–0 frequencies of ^{87}Rb and ^{85}Rb, adjusts for the change in Rb isotope.

We numerically simulated active pressure-shift suppression in IGOR Pro [61] as follows. First, we determined the ratio of partial pressures p_{n}:p_{p} (or Ar:N_2) required to give a zero pressure shift, $\delta\nu = 0$, according to (5.1). For the initial conditions of $p_{\text{fill}} = 30.0$ Torr and $T_{\text{fill}} = 50.0^\circ$ C, this ratio is roughly 9.2974:1, which is close to the experimental value of 9.170:1 from Section 5.2. To simulate feedback with this mixture, we numerically determined the zero-slope temperature to be the temperature T where the pressure shift $\delta\nu$ of (5.1) is unchanged after an increase in p_{fill} by 0.1 Torr.

As shown in Fig. 5.4, the value of the shift (5.1) at this zero-shift temperature is not zero. Instead, this value is an estimate of the error in pressure-shift suppression due to the nonlinear shift $\Delta^2\nu$. To obtain a curve similar to those in Fig. 5.2, we repeated the simulated feedback for filling pressures over the range of 23–30 Torr, as used in Section 5.2. The residual slope in Fig. 5.4(a) is roughly 0.072 Hz Torr^{-1}, and not zero. The zero-slope temperature also depends slightly on the filling pressure, as shown in Fig. 5.4(b).

As Fig. 5.4 shows, a nonlinear shift from van der Waals molecules may lead to a difference between the zero-slope and zero-shift temperatures. In this case, none of the implementations of pressure-shift suppression described in Section 5.3 will completely suppress the pressure shift. For the Ar and N_2 mixture simulated here for ^{87}Rb, there will be a residual pressure shift of roughly -2 Hz, or an inaccuracy of 3×10^{-10}. This

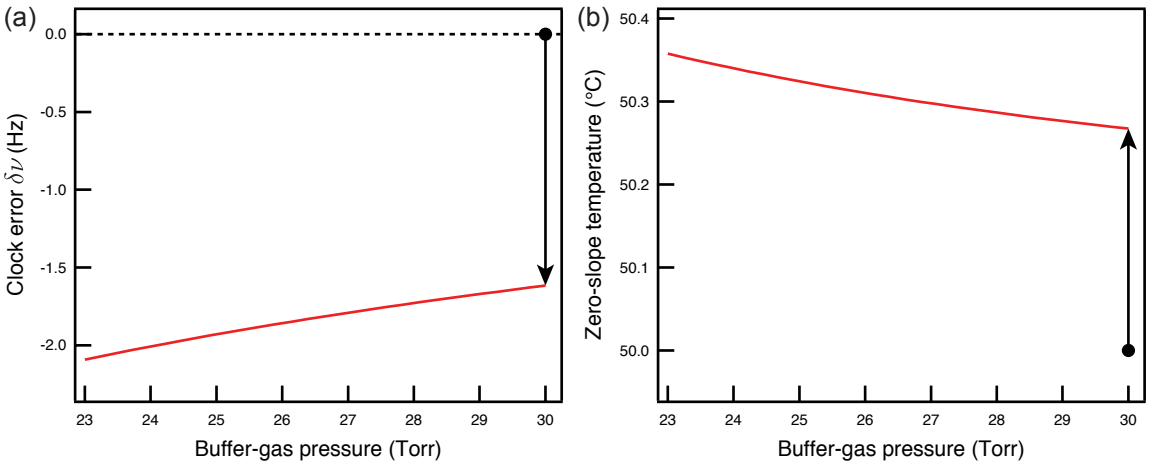

Figure 5.4: Numerical simulation of pressure-shift suppression error for ^{87}Rb in a mixture of Ar and N_2. The black dots represent the initial condition of a 9.2974:1 Ar:N_2 mixture adjusted to give zero pressure shift for a filling pressure of 30 Torr and temperature of 50.0° C. The arrows indicate how feedback would servo the temperature to the zero-slope temperature, by removing any dependence of the clock frequency on small changes in pressure. (a) At the locked, zero-slope temperature, there is a small clock error $\delta\nu = \nu - \nu_0$. (b) This error is due to a nonlinear pressure shift from RbAr van der Waals molecules, which make the zero-slope temperature slightly different from the zero-shift temperature of 50.0° C. The curves in both panels trace out how the clock error and zero-slope temperature change as the filling pressure (given for 50.0° C) is varied, for the same buffer-gas mixture.

error depends on the composition of the buffer gas and the filling pressure, and may be reduced with the proper choice of both. This error can only be eliminated by using a buffer gas that does not form van der Waals molecules with alkali-metal atoms.

5.5 Summary and discussion

In summary, we have proposed a simple technique to suppress the pressure shift in vapor-cell clocks. We demonstrated the properties of zero-shift buffer-gas mixtures, and proposed some possible implementations of this technique. Such suppression might be useful in the search for the mechanisms behind the long-term drift of vapor-cell clocks, and the study of smaller frequency shifts, such as the spin-exchange shift [16]. Unfortunately, we show that van der Waals molecules are expected to limit the accuracy of pressure-shift suppression. Further work is required to find a buffer gas with a negative pressure shift that does not form van der Waals molecules with alkali-metal atoms.

Even with the expected error from van der Waals molecules, it might be possible to construct a vapor-cell clock with pressure-shift suppression that serves as a working primary standard. In practice, this error might be predictable, reproducible, and stable enough, like the quadratic Zeeman shift, to maintain the typical desired accuracy of 5×10^{-11} without calibration. For example, the simulated pressure dependence of this error was 0.072 Hz Torr^{-1} in Section 5.4, which is over three orders of magnitude smaller than the typical pressure shift of 200 Hz Torr^{-1} in conventional clocks [16]. As a result, a vapor-cell clock with the simulated mixture would no longer require an initial calibration to account for the irreproducibility in filling vapor cells, which should be 10^{-12} or below. Active pressure-shift suppression should maintain this level of error, even against small changes to the buffer-gas composition over time. However,

there is still the possibility that additional, smaller frequency-shift mechanisms will produce enough drift to eventually require calibration.

Chapter 6

Integrating-sphere alkali-metal vapor cells

6.1 Introduction

Integrating spheres (or Ulbricht spheres) are optical cavities that use diffuse reflection to multi-pass light through an interior volume. Typically applied in radiometry and photometry, integrating spheres have previously been used to detect trace gases [141] and to cool and trap alkali-metal atoms [142, 143], for example, in a compact, cold cesium atomic clock [144, 145]. Here, we report on an investigation of the potential for integrating spheres to enhance the absorption of light in optically thin alkali-metal vapor cells [43].

Miniaturized vapor cells for atomic clocks and magnetometers have shortened optical path lengths. To compensate, miniature cells usually operate at higher temperatures to increase the density of alkali-metal atoms, which in turn leads to reduced performance from spin-exchange broadening of the microwave resonance lines [44] and to an increased power demand from heating the cell. Another way to enhance absorption is to pass light through the cell multiple times with a cavity, without increasing

the temperature or alkali-metal density. Integrating spheres are an attractive candidate since they are simple and robust optical cavities that do not require the precise alignment of specular-reflectance cavities with mirrors, which can misalign over time.

We demonstrate up to a roughly ten-fold enhancement of optical absorption, which seems to be limited by the effects of the glass cell required to contain the alkali-metal vapor. We were surprised to find that the most common diffuse-reflectance paint, sold for use in integrating spheres, is no longer a good diffuse reflector when applied to glass, and can lead to significant light-piping effects in a painted alkali-metal vapor cell. These effects could be important to the light-trapping enhancement of solar cells with diffuse reflectors [146, 147], and to other applications of integrating spheres that use internal glass bulbs [148, 149, 150, 151].

Before we begin, we first provide some background on integrating spheres.

6.1.1 Integrating spheres

An integrating sphere consists of a spherical cavity with diffusely reflecting walls and small ports for light entry and exit, as sketched in Fig. 6.1. Multiple diffuse reflections spread the input light into a uniform (unidirectional) irradiance E (W m^{-2}) over the entire inner sphere surface with area A (m^2). The enhancement of this irradiance due to reflections is described by a "sphere multiplier" M (dimensionless), which quantifies the effective number of "bounces" of light within the cavity. For a total input light power (or radiant flux) of P_0 (W), the inner surface irradiance is

$$E = M\left(\frac{P_0}{A}\right), \tag{6.1}$$

which we derive below. For commercial integrating spheres, the multiplier M is usually in the range of 10–30 [152].

Ideally, the inner wall of the sphere acts as a Lambertian surface, or an ideal diffuse reflector, and reflects light with an equal radiance L (W m^{-2} sr^{-1}) in all directions above the surface. Radiance is constant along any ray path, so a Lambertian surface can be thought of as reflecting light equally in all directions [153, 154]. This property is usually summarized by Lambert's cosine law, which states that the radiant intensity I (W sr^{-1}) of the reflected light obeys

$$I(\theta) = I(0)\cos(\theta), \tag{6.2}$$

where the colatitude angle θ is 0 for reflection normal to the surface and $\pi/2$ for reflection along the surface. To understand (6.2), note that $I(\theta) = L\,dA(\theta)$, and that the apparent surface area $dA(\theta)$ of the source area dA with unit normal vector $\hat{n}$ as seen by a reflection propagating along the unit vector $\hat{r}$ is $dA(\theta) = (\hat{r}\cdot\hat{n})dA = \cos(\theta)dA$.

A spherical geometry is convenient because a diffuse reflection from any point on the sphere contributes a uniform irradiance over the entire inner surface of the sphere. For example, consider the irradiance of the surface area dA_2 with unit normal $\hat{n}_2$ at the point $\mathbf{r}_2$ due to reflection from the point $\mathbf{r}_1$ on the surface with unit normal $\hat{n}_1$. If we write the chord $\mathbf{r}_{21} = \mathbf{r}_2 - \mathbf{r}_1$, then this irradiance is given by an inverse-square

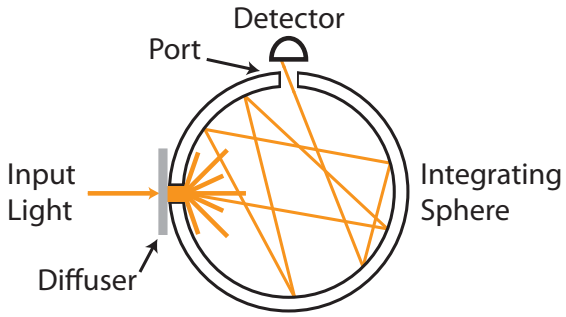

Figure 6.1: Sketch of the cross section of an integrating sphere with two ports. Light enters one port after first passing through an initial diffuser. Multi-passed light is sampled by a detector at an orthogonal port.

law,

$$E_{21} = \frac{(\mathbf{r}_{21} \cdot \hat{n}_2) I_1}{|\mathbf{r}_{21}|^3}, \tag{6.3}$$

where $I_1 = I_1(\theta)$ is the radiant intensity of a ray with solid angle $d\Omega_1$ originating from the point $\mathbf{r}_1$. For a sphere of diameter D, we have $\mathbf{r}_{21} \cdot \hat{n}_2 = \mathbf{r}_{21} \cdot \hat{n}_1 = |\mathbf{r}_{21}| \cos(\theta)$ and $|\mathbf{r}_{21}| = D \cos(\theta)$. If we write the total power reflected from the point $\mathbf{r}_1$ as

$$P_1 = \int I_1 d\Omega_1 = 2\pi I_1(0) \int_0^{\pi/2} \cos(\theta) \sin(\theta) d\theta = \pi I_1(0), \tag{6.4}$$

then using Lambert's cosine law (6.2), we find that the irradiance (6.3) is the total power divided by the surface area $A = \pi D^2$ of the sphere,

$$E_{21} = \frac{P_1}{A}, \tag{6.5}$$

which is independent of the location of $\mathbf{r}_2$. Since it will be important later, we note that average path length for all reflections from the point $\mathbf{r}_1$ is

$$\overline{L} = \frac{\int |\mathbf{r}_{21}| d\Omega_1}{\int d\Omega_1} = \frac{2\pi D \int_0^{\pi/2} \cos(\theta)^2 \sin(\theta) d\theta}{2\pi \int_0^{\pi/2} \cos(\theta) \sin(\theta) d\theta} = \frac{2}{3} D, \tag{6.6}$$

where $\overline{L}$ is not to be confused with a radiance L.

A Lambertian surface is described only by a reflectance ρ, also known as an albedo or hemispherical reflectance, which satisfies $0 < \rho < 1$. We can calculate the sphere multiplier M from this reflectivity ρ by summing over reflections as follows. Introducing light of total power P_0 into the sphere, let a fraction ρ_0 of this power survive a first reflection off the inner sphere surface. From (6.5) we see that a total power $P_1 = \rho_0 P_0$ from this first reflection will be spread uniformly over the inner sphere surface. Let h be the fraction of the surface area A that is covered by ports

Table 6.1: Example values of the sphere multiplier M of (6.9) as a function of the reflectivity ρ and port fraction h.

ρ	h							
	0%	1%	2%	3%	4%	5%	10%	20%
0.99	99.0	49.3	32.6	24.2	19.2	15.8	8.2	3.8
0.98	49.0	32.6	24.3	19.2	15.9	13.5	7.5	3.6
0.97	32.3	24.2	19.2	15.9	13.5	11.7	6.9	3.5
0.95	19.0	15.8	13.5	11.7	10.4	9.3	5.9	3.2
0.90	9.0	8.2	7.5	6.9	6.4	5.9	4.3	2.6
0.85	5.7	5.3	5.0	4.7	4.4	4.1	3.3	2.1
0.80	4.0	3.8	3.6	3.5	3.3	3.2	2.6	1.8

(or holes), and for simplicity, assume that all light incident on a port is lost. Then a second reflection will spread a total power $P_2 = \rho(1-h)P_1$ uniformly over the sphere surface. Likewise, each subsequent n-th reflection spreads a power $P_n = \rho(1-h)P_{n-1}$ over the sphere surface. The total surface irradiance is then the sum

$$E = \frac{1}{A}\sum_{n=1}^{\infty} P_n = \rho_0[1 + \rho(1-h) + \rho^2(1-h)^2 + \ldots]\left(\frac{P_0}{A}\right). \tag{6.7}$$

Comparing this with (6.1), we see that the sphere multiplier is

$$M = \frac{\rho_0}{1-\rho(1-h)}. \tag{6.8}$$

If we assume that the initial beam is perfectly diffused at entry, such as sketched in Fig. 6.1, then we may simplify (6.8) to

$$M = \frac{\overline{\rho}}{1-\overline{\rho}}, \tag{6.9}$$

where we have introduced an average reflectivity for the sphere wall,

$$\overline{\rho} = \rho(1-h). \tag{6.10}$$

Example values of M as a function of the reflectivity ρ and port fraction h are listed in Table 6.1. Typical parameters for commercial integrating spheres are $0.94 < \rho < 0.99$ and $0.02 < h < 0.05$ [152].

The multiple reflections inside an integrating sphere fill the interior with a nearly isotropic bath of diffuse light. One consequence is that the number of bounces, or the sphere multiplier M, is sensitive to the average reflectivity (6.10) for the entire sphere wall. In other words, the performance is very sensitive to all surface losses, such as the ports required for light input and output, since the entire inner surface is sampled by the diffuse light. In contrast, some specular-reflectance cavities may be adjusted to avoid lossy imperfections on mirror surfaces.

For additional information about integrating spheres and radiometric terminology, we recommend Whitehead and Mossman [153] and Ref. [152]. For additional information about diffusers and Lambertian surfaces, we recommend Carrascosa *et al.* [154] and Section 5.7 of Ref. [155].

6.2 Modeling absorption inside integrating spheres

In this section, we derive models for the effects of absorption in integrating spheres, and measures of performance that we will use to analyze the experiments in the next section. We will ignore the effects of the glass cell, which we return to in Section 6.4. At the end of this section, we discuss other important concerns for integrating-sphere alkali-metal vapor cells.

As sketched in Fig. 6.1, a detector gathering light at a port measures the irradiance E of (6.1), and thus the sphere multiplier M. Due to the multi-passing of the light, the detector signal is very sensitive to absorption in the interior volume of the sphere. Let the sphere interior be filled with a weak absorber described by an absorption coefficient α (m^{-1}). In general, the coefficient α will depend on the optical frequency

ω of the light, $\alpha = \alpha(\omega)$. However, for simplicity, we will let α denote the maximum value of $\alpha(\omega)$ that occurs as the frequency ω is swept across a resonance line.

If we assume that the maximum value α of the absorption coefficient $\alpha(\omega)$ is weak enough that $e^{-\alpha D} \approx 1 - \alpha D$, where D is the sphere diameter, then the light inside the integrating sphere may still be described by a sphere multiplier $M = M(\alpha)$. In this case, we may write the maximum optical contrast measured by a detector for light that is swept across an optical resonance as

$$\Delta(\alpha) = 1 - \frac{M(\alpha)}{M(0)}, \tag{6.11}$$

where $M(\alpha)$ is the sphere multiplier for light tuned on resonance ($\alpha(\omega) \to \alpha$), and $M(0)$ is the multiplier for light tuned off resonance ($\alpha(\omega) \to 0$). We can calculate the dependence of the sphere multiplier $M(\alpha)$ on the absorption coefficient α using the following two approaches.

6.2.1 Ray-tracing approach

The first method is a ray-tracing approach [141, 156, 157]. Due to diffuse reflection and spherical geometry, the light reflected by any point on the sphere wall deposits a uniform irradiance over the entire wall, as described in Section 6.1.1. Assuming a diffused initial beam, we will treat the introduction of the beam as a reflection. In this case, the sum (6.7) becomes

$$E \approx \left[\overline{\rho}(1 - \alpha\overline{L}) + \overline{\rho}^2(1 - \alpha\overline{L})^2 + \overline{\rho}^3(1 - \alpha\overline{L})^3 + \ldots\right] \frac{P_0}{A}, \tag{6.12}$$

where the average path length (6.6) is $\overline{L} = 2D/3$. Comparing this with (6.1), we see that the sphere multiplier is

$$M(\alpha) \approx \frac{\overline{\rho}(1-\alpha\overline{L})}{1-\overline{\rho}(1-\alpha\overline{L})}. \tag{6.13}$$

The maximum optical contrast (6.11) measured by a detector is then

$$\Delta(\alpha) \approx \frac{\alpha\overline{L}}{1-\overline{\rho}(1-\alpha\overline{L})}, \tag{6.14}$$

according to this ray-tracing approach.

6.2.2 Photon-gas approach

We will refer to the second method as the "photon-gas" approach [158]. In an ideal integrating sphere, the interior is filled with diffuse light much like monochromatic blackbody radiation. Instead of summing the total surface irradiance, we can calculate $M(\alpha)$ by balancing the optical power input P_0 with the power loss in the cavity,

$$P_0 = \underbrace{P_0(1-\rho_0)}_{\text{input loss}} + \underbrace{EA(1-\overline{\rho})}_{\text{wall loss}} + P_\alpha. \tag{6.15}$$

For simplicity, we describe the introductory loss with $(1-\rho_0)$, and we ignore absorption of the input beam in the sphere interior, which is a small correction.

To calculate the power loss P_α from absorption in the sphere interior, we will describe the diffuse light by a local radiant energy density w (W m^{-3}). For light propagating along the unit vector $\hat{r}$, absorption is described by the Beer-Lambert law

$$\nabla w = -\alpha\, w\, \hat{r}. \tag{6.16}$$

For a given point, we can calculate the power loss per unit volume p_α (W m^{-3}) by averaging over all rays of solid angle $d\Omega$ and direction $\hat{r}$ passing through the point,

$$p_\alpha = -\frac{dw}{dt} = -\frac{1}{4\pi}\int \nabla w \cdot (v_g \hat{r})\, d\Omega = \alpha\, v_g\, w, \tag{6.17}$$

where v_g is the group velocity of the light. Similarly, we can calculate the (unidirectional) irradiance E along the unit vector $\hat{n}$ for a given point as

$$E = \frac{1}{4\pi}\int (w\, v_g \hat{r}) \cdot \hat{n}\, d\Omega = \frac{w\, v_g}{2}\int_0^{\pi/2} \cos(\theta)\sin(\theta) d\theta = \frac{w\, v_g}{4}. \tag{6.18}$$

For weak absorption, the radiant density w is nearly constant throughout the sphere interior. In this case, both (6.17) and (6.18) are independent of position, and we can write the power loss P_α of (6.15) over the volume $V = \pi D^3/6$ of the sphere as

$$P_\alpha = p_\alpha V = (\alpha \overline{L}) E A, \tag{6.19}$$

where $\overline{L} = 4V/A = 2D/3$ is the average path length of (6.6). Note that if the absorber does not completely fill the sphere interior, then the effective path length in (6.19) would be less than $2D/3$.

Using (6.19) with (6.15), we find the sphere multiplier

$$M(\alpha) \approx \frac{\rho_0}{1 - \overline{\rho} + \alpha\overline{L}}. \tag{6.20}$$

The maximum optical contrast (6.11) measured by a detector is then

$$\Delta(\alpha) \approx \frac{\alpha\overline{L}}{1 - \overline{\rho} + \alpha\overline{L}}, \tag{6.21}$$

according to this photon-gas approach.

6.2.3 Measures of performance

Using the results of the two approaches above, we can define four measures to gauge the enhancement of optical absorption in an integrating sphere over the single-pass case. In an experiment, we can measure both the maximum multi-pass contrast $\Delta(\alpha)$ of (6.11) and an analogous maximum single-pass contrast $\Delta_1(\alpha)$ for comparison. From the Beer-Lambert law, we can write the maximum single-pass contrast along the sphere diameter D as

$$\Delta_1(\alpha; D) = 1 - e^{-\alpha D}. \tag{6.22}$$

While it is experimentally convenient to measure the single-pass absorption along the diameter D, it will be more convenient for analysis to use an estimate of the single-pass contrast along the average diffuse-reflectance length $\overline{L} = 2D/3$ of (6.6),

$$\Delta_1(\alpha; \overline{L}) = 1 - e^{2\ln[1-\Delta_1(\alpha;D)]/3} = 1 - e^{-\alpha\overline{L}}. \tag{6.23}$$

A first measure of performance is the ratio of contrasts

$$N_1 = \frac{\Delta(\alpha)}{\Delta_1(\alpha; \overline{L})}. \tag{6.24}$$

The is a convenient metric since for weak absorption it is very nearly equal to the sphere multiplier, $N_1 \approx M(\alpha)$, which is the traditional definition of a number of "bounces" in an integrating sphere. A second measure of performance is the ratio of effective path lengths

$$N_2 = \frac{\ln[1 - \Delta(\alpha)]}{\ln[1 - \Delta_1(\alpha; \overline{L})]}. \tag{6.25}$$

This is clear if we use the Beer-Lambert law to write the multi-pass contrast $\Delta(\alpha)$ as

$$\Delta(\alpha) = 1 - e^{-\alpha N_2 \overline{L}}, \tag{6.26}$$

which shows that the metric N_2 describes an effective path-length enhancement for multi-pass absorption compared to the single-pass contrast $\Delta_1(\alpha; \overline{L})$ of (6.23). As we will see, the two metrics N_1 and N_2 give similar results, though N_2 tends to be a more optimistic measure of performance. Both N_1 and N_2 decrease as the value of α increases.

Finally, we may estimate two performance limits from the measured contrasts. From the results of both models, (6.14) and (6.21), we see that the measure N_1 of (6.24) is limited below a maximum value,

$$N_1 \leq N_1^{\max} = \frac{1}{1 - \overline{\rho}}, \tag{6.27}$$

which depends only on the average reflectivity $\overline{\rho}$ of (6.10). We may estimate this limit for N_1 as follows. Assuming weak absorption, we may approximate

$$\alpha \overline{L} \approx \Delta_1(\alpha; \overline{L}). \tag{6.28}$$

Then from (6.14) and (6.21), we may estimate the maximum value of (6.27) to be

$$N_{1,\mathrm{rt}}^{\max} = \frac{1}{1 - \overline{\rho}} \approx \frac{1 - \Delta_1(\alpha; \overline{L})}{1/N_1 - \Delta_1(\alpha; \overline{L})} \text{ or} \tag{6.29}$$

$$N_{1,\mathrm{pg}}^{\max} = \frac{1}{1 - \overline{\rho}} \approx \frac{1}{1/N_1 - \Delta_1(\alpha; \overline{L})}, \tag{6.30}$$

for the ray-tracing ("rt") and photon-gas ("pg") approaches, respectively. As we will see, these two estimates for the maximum value of the measure N_1 of (6.24) give similar results for weak absorption.

6.2.4 Additional concerns for alkali-metal vapor cells

The analysis in this section has ignored several additional concerns that are important if alkali-metal vapor cells are used in integrating spheres, which we describe here.

First, we have assumed that a detector only measures the light multi-passed through the sphere interior. In practice, care must be taken to avoid any bias from the initial input of light. In traditional integrating spheres, this is usually done with internal baffles [152]. For alkali-metal vapor cells, this can be done by diffusing the input light before it enters the sphere, and recessing the detector to avoid a direct view of the input port.

Second, the glass bulb of the alkali-metal vapor cell may affect the performance. At minimum, the bulb will introduce additional absorption, due to both the glass itself and to imperfections from fabrication, such as dark discolorations. As we discuss in Section 6.4, the glass bulb may also introduce significant light-trapping and light-piping effects, as well as non-Lambertian behavior. In addition, the excess of alkali metal in the cell required to produce a vapor will introduce scattering and absorption. These effects may be reduced by confining this excess in a more desirable portion of the cell through selective heating and cooling.

Finally, for simplicity, we have assumed that the absorption of light by an alkali-metal vapor may be described by an absorption coefficient $\alpha(\omega)$ that is only a function of the optical frequency ω of the light. However, because of optical pumping, the absorption will also depend on the input light intensity and possibly its polarization. For our measurements, we can avoid this complication by using unpolarized input light with a sufficiently low power. We cannot avoid this complication in some applications, such as vapor-cell clocks, where the light must provide optical pumping to allow the absorption of microwaves, as described in Section 2.1.2. For example, this would lead to a reduced maximum optical contrast for microwave resonances, since there is optical absorption even when the microwaves are off resonance. In addition, if the

buffer gas does not provide enough quenching, the integrating sphere may lead to significant radiation trapping from the multi-passing of fluorescence [159].

6.3 Experiment

We performed two experiments with different alkali-metal vapor cells, a ^{85}Rb cell and a ^{133}Cs cell, as described below. For each cell, we measured the maximum single-pass optical contrast $\Delta_1(\alpha; D)$ of (6.22) and the maximum multi-pass optical contrast $\Delta(\alpha)$ of (6.11) for different values of the absorption coefficient α. Fig. 6.2 is a sketch of the setup for both experiments, as described below.

In the first experiment, we used a small Pyrex cell filled with an excess of ^{85}Rb and 60 Torr of N_2 buffer gas for quenching. As shown in Fig. 6.3(a), the cell was mostly a spherical bulb, with an outer diameter $D \approx 3.1$ cm, except for a stem with an outer diameter of roughly 9 mm at the bulb. We probed optical absorption of the D1 transition with weak, unpolarized 795 nm light from a diode laser (DL).

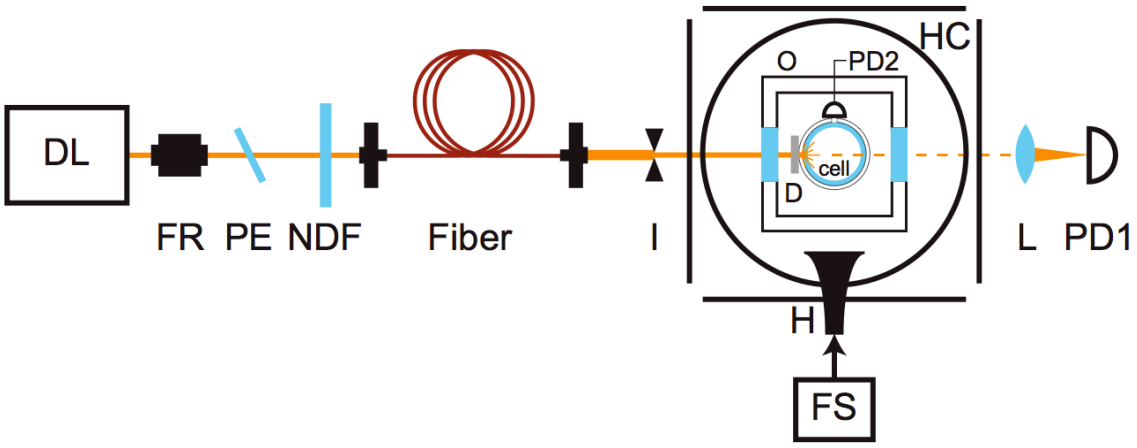

Figure 6.2: Experimental setup for measurements with integrating-sphere alkali-metal vapor cells. For the painted ^{133}Cs cell, a moveable diffuser (D) was used to switch between single-pass and multi-pass measurements in situ. DL, diode laser; FR, Faraday rotator; PE, pellicle; NDF, neutral density filter; I, iris; D, diffuser; O, oven; HC, Helmholtz coils; L, lens; PD1, single-pass photodetector; PD2, multi-pass photodetector; FS, frequency synthesizer; H, microwave horn;

Table 6.2: Measured optical contrasts for the ^{85}Rb vapor cell. The approximate values of the Rb number density were estimated from the oven temperature [52].

Temp. (° C)	Rb density (cm^{-3})	Single-pass contrast $\Delta_1(\alpha; D)$	$\Delta_1(\alpha; \overline{L})$	Multi-pass contrast $\Delta(\alpha)$ Spectralon	Paint
21.5	8.9×10^9	0.0410	0.0275	0.1930	0.2450
30.0	2.2×10^{10}	0.0961	0.0651	0.3672	0.4200
40.0	6.0×10^{10}	0.2220	0.1541	0.6017	0.5885
50.0	1.5×10^{11}	0.4167	0.3019	0.7480	0.7600

An air-heated, nonmagnetic oven (O) regulated the cell temperature, and thus the alkali-metal density and maximum absorption coefficient α. We initially measured the single-pass maximum contrast $\Delta_1(\alpha; D)$ for the D1 optical transition with a beam through the cell diameter, and estimated the contrast $\Delta_1(\alpha; \overline{L})$ using (6.23). We then measured the multi-pass contrast $\Delta(\alpha)$ in two configurations, described below. The results of these measurements are summarized in Table 6.2.

In the first configuration ("Spectralon"), we placed the cell inside a commercial integrating sphere (Ocean Optics FOIS-1) made of Labsphere Spectralon, which has a diffuse reflectivity $\rho \gtrsim 0.99$ for the near infrared [161]. This integrating sphere had

(a) ^{85}Rb vapor cell (b) ^{133}Cs vapor cell

Figure 6.3: Integrating-sphere alkali-metal vapor cells painted with Labsphere 6080 white reflectance coating [160]. (a) ^{85}Rb vapor cell with diameter $D \approx 3.1$ cm and port fraction $h \approx 0.02$–0.03. Roughly half the short cell stem is painted. (b) ^{133}Cs vapor cell with diameter $D \approx 2.0$ cm and port fraction $h \approx 0.05$–0.07. Most of the relatively large cell stem is unpainted, and instead is immersed in a white, thermally conductive grease during use.

Table 6.3: Performance measures for the ^{85}Rb vapor cell using the data of Table 6.2. The metrics N_1 and N_2 are actual performance, and the metrics $N_{1,rt}^{\max}$ and $N_{1,pg}^{\max}$ are estimates of the maximum possible value of N_1, as described in Section 6.2.3.

	Spectralon				Paint			
Temp. (° C)	N_1	N_2	$N_{1,rt}^{\max}$	$N_{1,pg}^{\max}$	N_1	N_2	$N_{1,\mathrm{rt}}^{\max}$	$N_{1,\mathrm{pg}}^{\max}$
21.5	7.02	7.69	8.46	8.70	8.91	10.08	11.48	11.80
30.0	5.64	6.79	8.33	8.91	6.45	8.09	10.39	11.12
40.0	3.90	5.50	8.29	9.80	3.82	5.31	7.85	9.28
50.0	2.48	3.84	6.86	9.83	2.52	3.97	7.32	10.49

a port fraction $h \approx 0.02$ and an inner diameter of roughly 3.8 cm. The cell did not completely fill the sphere interior, but was positioned to cover a port hole monitored by a photodetector (PD2). The light was introduced in a different port, and was diffused either by an external diffuser or by directing it to initially reflect off the sphere interior.

In the second configuration ("Paint"), we painted most of the cell with a commercial integrating-sphere paint, Labsphere 6080 white reflectance coating, which has a reflectivity $\rho \approx 0.975$ for the near infrared [160]. Fig. 6.3(a) shows the painted cell. We painted only half of the short cell stem, and we introduced two orthogonal port holes with diameters of roughly 3 mm. We estimate the port fraction $h \approx 0.02$–0.03 for the painted cell, which is mostly due to the stem.

Table 6.3 gives the calculated performance measures of Section 6.2.3 using the data in Table 6.2. The measures show an improvement in the optical contrast of up to roughly 9–10 with the painted cell, corresponding to around 9–10 "bounces" of light within the cell. This performance is close to the estimated maximum values, $N_{1,rt}^{\max}$ and $N_{1,pg}^{\max}$ from Section 6.2.3, so significantly better performance is not expected with this cell. The best results came with the painted-cell configuration, likely because the cell did not completely fill the Spectralon cavity in the external integrating-sphere configuration — see the comment after (6.19).

We also examined the microwave contrast for the painted-cell configuration, using Helmholtz coils (HCs), a microwave horn (H), and a frequency synthesizer (FS). Because of the difficulty in performing a quantitative comparison between the single-pass and multi-pass configurations, which are very sensitive to the optical and microwave powers, we do not report quantitative results. Instead, we note that the microwave contrast did show a similar enhancement from multi-passing. Additionally, we note that attempts to observe coherent population trapping by frequency modulating the light with a fiber-based electro-optic modulator were unsuccessful, likely because the diffuse reflection inside the cell made this modulation effectively incoherent.

For a second experiment, we chose to use ^{133}Cs to demonstrate how an integrating sphere might reduce the power budget of miniature vapor-cell devices: due to the higher vapor pressure of Cs than of Rb for the same temperature, we had to cool below room temperature to reach a weak absorption regime. Instead of cooling the entire cell, we cooled only the portion of the cell containing the excess of Cs metal, the stem, as sketched in Fig. 6.4. This method failed with several new cells that we fabricated, but functioned with one existing Pyrex cell filled with 20 Torr of a 4:1 mixture of Ar:N_2 buffer gas. As shown in Fig. 6.3(b), this cell has an unusual shape. The middle spherical bulb with outer diameter $D \approx 2.0$ cm is connected to

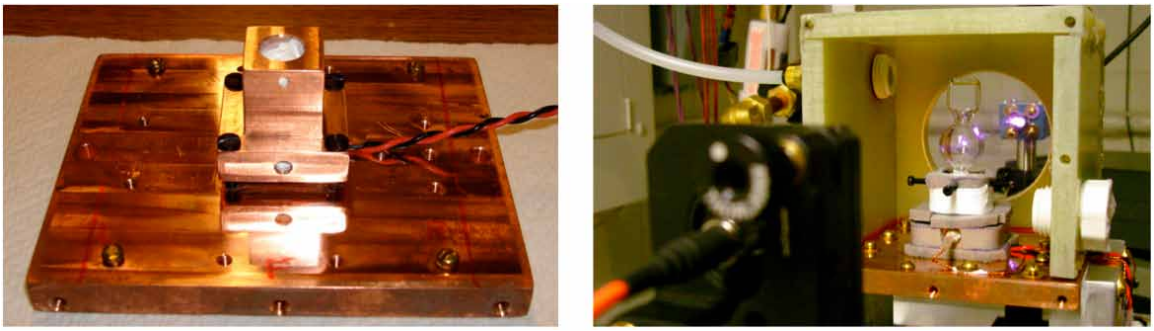

Figure 6.4: Stem-cooling setup for the ^{133}Cs cell. (Left) A copper cell holder is attached to a Peltier element on top of a copper base plate for heatsinking. (Right) The cell (unpainted) with its stem in the cell holder, during a preliminary single-pass measurement. The air-heated oven (green) is open for the picture.

Table 6.4: Measured optical contrast for the ^{133}Cs vapor cell. The approximate values of the Cs number density were estimated from the measured area of the optical absorption line shape [162, 21].

Stem temp. (° C)	Cs density (cm^{-3})	Single-pass contrast $\Delta_1(\alpha; D)$	Single-pass contrast $\Delta_1(\alpha; \overline{L})$	Multi-pass contrast $\Delta(\alpha)$
15.1	1.9×10^9	0.086 ± 0.02	0.0582	0.191 ± 0.02
		0.067 ± 0.02	0.0452	0.166 ± 0.02
15.1	3.9×10^9	0.146 ± 0.02	0.0999	0.322 ± 0.05
		0.122 ± 0.02	0.0831	0.303 ± 0.05
10.0	5.6×10^9	0.173 ± 0.02	0.1189	0.360 ± 0.02
		0.140 ± 0.02	0.0956	0.304 ± 0.02

an upper "pancake" extension, with outer diameter of roughly 6 mm at the bulb, and a relatively long cell stem with outer diameter of roughly 7 mm at the bulb. We painted most of the cell with Labsphere 6080, including the pancake region, as shown in Fig. 6.3(b). Most of the exposed portion of the stem was immersed in a white, thermally conductive grease during use, which reduced the optical loss from the stem.

While the stem-cooling method worked, it proved unreliable for precise control of the alkali-metal vapor density, due to the eventual migration of alkali metal out of the stem, which could be temporarily reversed by baking with the oven (O) while cooling the stem. As a result, we used 3 port holes, of roughly 3 mm diameter each, and a moveable diffuser (D) to switch between single-pass and multi-pass measurements in situ with the painted cell, as sketched in Fig. 6.2. We estimate the port fraction $h \approx$ 0.05–0.07, which assumes some attenuation of the loss from the pancake and stem portions of the cell by the paint and thermal grease, respectively.

We probed optical absorption of the D2 transition with weak, unpolarized 895 nm light from a diode laser (DL). For ^{133}Cs, the D2 transition is split into two peaks by the ground-state hyperfine structure, so we report two values, corresponding to these two resolved peaks, for each alkali-metal density in Table 6.4. The calculated performance

Table 6.5: Performance measures for the ^{133}Cs vapor cell using the data of Table 6.4. The metrics N_1 and N_2 are actual performance, and the metrics $N_{1,rt}^{\max}$ and $N_{1,pg}^{\max}$ are estimates of the maximum possible value of N_1, as described in Section 6.2.3.

Stem temp. (° C)	Cs tensity (cm^{-3})	N_1	N_2	$N_{1,\mathrm{rt}}^{\max}$	$N_{1,\mathrm{pg}}^{\max}$
15.1	1.9×10^9	3.28	3.54	3.82	4.06
		3.67	3.93	4.21	4.41
15.1	3.9×10^9	3.22	3.69	4.28	4.76
		3.65	4.16	4.80	5.23
10.0	5.6×10^9	3.03	3.52	4.17	4.73
		3.18	3.60	4.13	4.57
average	–	–	–	4.24	4.63

measures of Section 6.2.3 are summarized in Table 6.5. Compared to the ^{85}Rb cell, the ^{133}Cs cell performed poorly. The improvement in the optical contrast was less than a factor of 4. Repainting the cell did not change the results. The estimated maximum performance was similar, so significantly better performance is not expected with this cell. Surprisingly, these performance values were much worse than expected, even given the unusual shape of the cell, and prohibited further quantitative study. One possible explanation is that the undesirable effects of the glass are enhanced for the smaller ^{133}Cs cell because of the relatively thicker walls, which we estimate to be roughly 1 mm thick, and the relatively large pancake and stem portions. We explore the effects of the glass in the next section.

6.4 Modeling of glass effects

Attempts to understand the poor performance of the ^{133}Cs cell with a Monte Carlo simulation of photon trajectories in MATLAB [94] pointed out the importance of the glass cell, which we ignored in the modeling of Section 6.2. Here, we first provide some simple demonstrations of a few important properties of the reflection inside glass off

of a flat interface with Labsphere 6080. We then consider how to model the effects of the glass in integrating-sphere alkali-metal vapor cells.

Fig. 6.5 shows a flat interface between Pyrex glass and Labsphere 6080 that is illuminated by a collimated green laser beam. Fig. 6.5(Left) displays multiple rings due to the total internal reflection off of the upper, parallel glass-air interface, which demonstrate that Labsphere 6080 reflects the laser light in a diffuse-like manner inside the glass. As a result, we should expect some light-trapping and light-piping effects inside the glass bulb of our cells, which we will model with a photon-gas approach in Section 6.4.1.

However, Fig. 6.5(Right) shows that, in addition to diffuse-like reflection, there is still a specular reflection from the 6080-glass interface. This non-Lambertian behavior is not present for a typical Labsphere 6080 surface in air, perhaps due to surface roughness. In addition, Fig. 6.6 demonstrates that a flat 6080-glass interface undergoes a gradual transition towards total internal reflection with an increasing angle of incidence. In contrast, a Lambertian surface should appear "white" at all angles of incidence, with a constant brightness by eye (for the same illumination), and give no

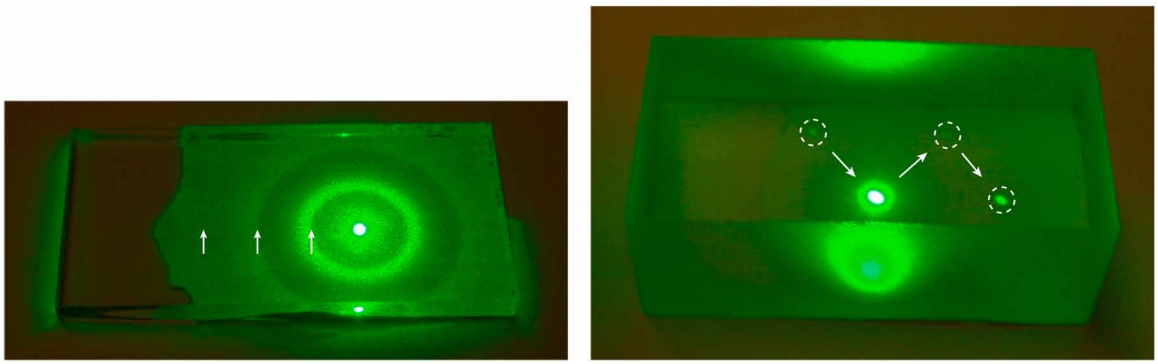

Figure 6.5: Reflection of a green laser pointer inside Pyrex glass, off of a rear interface with Labsphere 6080 paint. (Left) Multiple rings from total internal reflection at the front Pyrex-air interface. The Pyrex block is 1" × 2" in size and 0.125" thick, with polished sides. The ring radii are multiples of roughly 6 mm. (Right) Specular reflection of a tilted laser beam off the rear Pyrex-6080 interface. The Pyrex block is 1" × 2" in size and 0.75" thick, with ground sides.

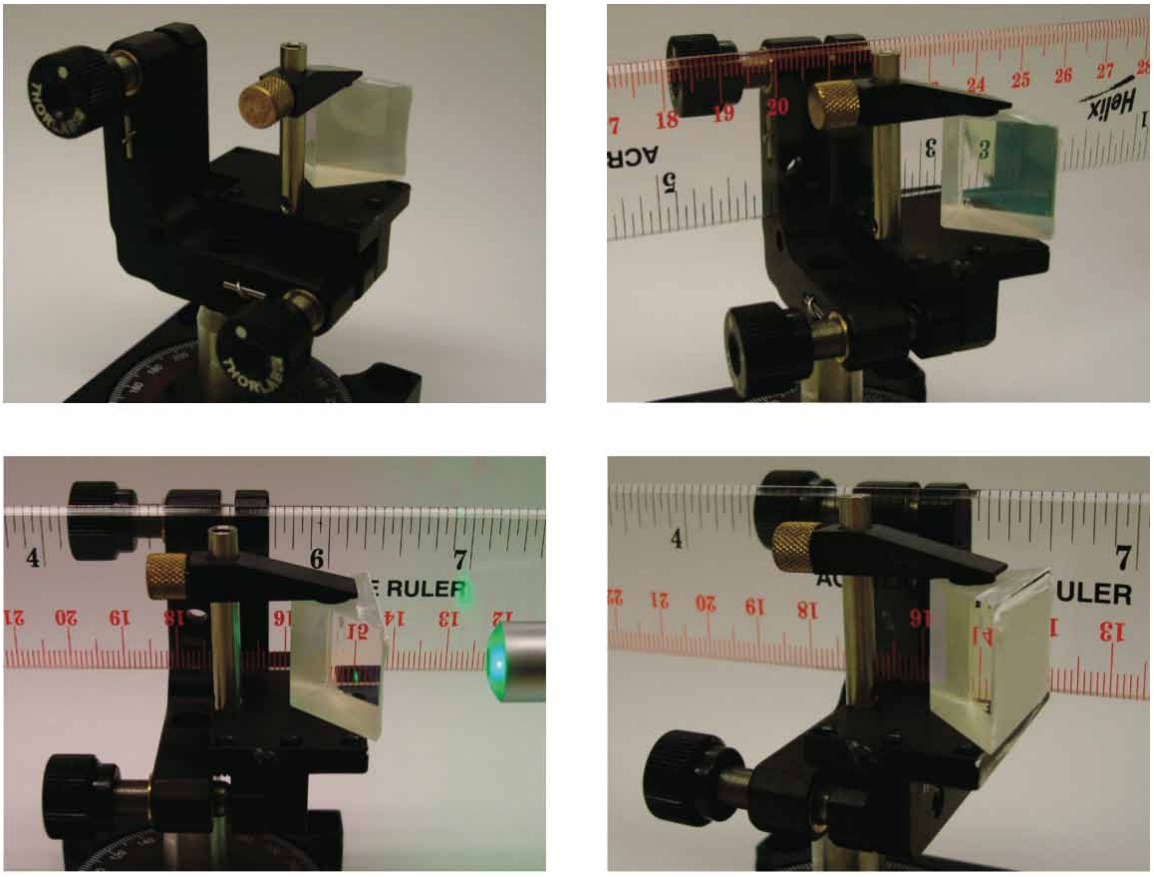

Figure 6.6: Gradual transition to total internal reflection for the hypotenuse of an N-BK7 right-angle prism (Thorlabs PS908L-B) painted with Labsphere 6080. Illumination with a green laser beam in the third panel demonstrates frustration of the total internal reflection when viewed with an angle of incidence of roughly 45° with an external prism face, which corresponds to an angle of incidence with the painted hypotenuse of roughly 73° inside the prism.

specular reflection. External illumination with a green laser pointer shows that this total internal reflection is frustrated [163], because of the optical contact with the Labsphere 6080 [164]. Therefore, we cannot assume that Labsphere 6080 is nearly Lambertian when it is applied to glass, so we consider how to model the 6080-glass interface in Section 6.4.2.

6.4.1 Light trapping and light piping

In this section, we consider the painted-cell configuration sketched in Fig. 6.7. For simplicity, we assume that the paint-glass interface is still Lambertian, with a diffuse reflectivity ρ_g for reflection inside the glass. We will ignore absorption by the bulk glass, and approximate the inner and outer glass surface areas of the integrating sphere, in the absence of a stem, to have approximately the same surface area A. Following the photon-gas approach [158] of Section 6.2.2, we can model the effects of the glass by balancing the power input and loss,

$$P_0 = \underbrace{P_0(1-\rho_0)}_{\text{input loss}} + \underbrace{E_g A(1-h)(1-\rho_g)}_{\text{paint loss}} + \underbrace{P_h}_{\text{port loss}} + \underbrace{E_c A(\alpha \overline{L})}_{\text{cell absorption}}. \tag{6.31}$$

Here, ρ_0 describes the loss during the introduction of the light, E_g is the (unidirectional) irradiance inside the glass, E_c is the (unidirectional) irradiance inside the sphere interior (or cell), h is the port fraction, and P_h is the loss from the ports.

To calculate the multi-pass contrast $\Delta(\alpha)$, we first need to relate the irradiance E_g inside the glass to the irradiance E_c inside the cell. We can do this by writing the radiant energy density w of an equilibrium photon gas as an integral over the photon energy ϵ with a density of states $g(\epsilon)$ and a probability distribution (or occupation

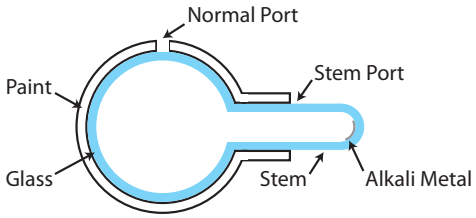

Figure 6.7: Sketch of the cross section of an integrating-sphere alkali-metal vapor cell with Labsphere 6080 paint. The glass required to contain the alkali-metal vapor may lead to significant light-trapping and light-piping effects, reducing the performance of the cell as an integrating sphere.

function) $f(\epsilon)$,

$$w = \int \epsilon f(\epsilon) g(\epsilon) d\epsilon. \tag{6.32}$$

For blackbody radiation, $f(\epsilon)$ would be the Planck distribution. For an integrating sphere, $f(\epsilon)$ is determined by both the spectrum of the input light, for example, narrowband laser light, and any extinction (absorption and scattering) inside the sphere. For weak absorption, the distribution $f(\epsilon)$ should be nearly the same in both the glass and the cell.

However, the density of states $g(\epsilon)$ depends on the refractive index n of the local medium. For photons with energy $\epsilon = \hbar\omega$, wavenumber $k = n\,\omega/c$, and group velocity $v_{\mathrm{g}} = d\omega/dk = c/n$, where c is the speed of light in vacuum, we can calculate the density of states by summing over modes in k-space:

$$\begin{aligned} g(\epsilon)d\epsilon &= \frac{(2 \text{ polarizations per mode})(\text{surface area of } k\text{-sphere})}{(\text{unit volume per mode in } k\text{-space})} \left(\frac{dk}{d\omega}\right)\left(\frac{d\omega}{d\epsilon}\right) d\epsilon \\ &= \frac{(2)(4\pi k^2)}{(2\pi)^3}\left(\frac{1}{v_{\mathrm{g}}}\right)\left(\frac{1}{\hbar}\right) d\epsilon = \frac{n^3\omega^2}{\pi^2\hbar c^3} d\epsilon. \end{aligned} \tag{6.33}$$

Using (6.33) with (6.32), we see that the equilibrium radiant energy density

$$w \propto n^3. \tag{6.34}$$

For simplicity, let the refractive index for the cell interior $n \longrightarrow 1$, and let n_{g} denote the refractive index of the cell glass. Using (6.34), (6.18), and $v_{\mathrm{g}} = c/n$, we obtain the relation

$$E_{\mathrm{g}} = n_{\mathrm{g}}^2\, E_{\mathrm{c}} \tag{6.35}$$

between the equilibrium irradiances in the glass and the cell interior [158].

Next, we need to determine the port loss P_h in (6.31). From Fig. 6.7, we see that for integrating-sphere alkali-metal vapor cells, there are at least two different types of ports, "normal" ports and "stem" ports. A normal port is simply a hole in the paint, which exposes part of the outer surface of the glass bulb to the surrounding air, which we take to have an index $n = 1$. However, a "stem" port is a tube-like extension of the glass bulb, away from its spherical shape. We may treat both types of ports in a simple manner if we approximate the light as still being an equilibrium photon gas as it exits a port. Let h_i be the fractional area for the i-th port, such that the total port fraction $h = \sum_i h_i$. For each port, let p_i be a reflectivity that describes how much of E_g is reflected back by the port. For example, if p_i were equal to ρ_g, then the i-th port would be indistinguishable from the rest of the painted wall. Then we can write the port loss in (6.31) as

$$P_h = E_\mathrm{g} A \sum_i (1 - p_i) h_i. \tag{6.36}$$

We can determine the port reflectivities p_i as follows. Let f_i be the fractional area of the cross section of a port that is composed of glass, taken just exterior to the sphere. For normal ports, $f_i = 0$ since the hole in the paint is filled with air. Here, the reflectivity would be $p_i \approx (1 - E_\mathrm{a}/E_\mathrm{g})$, where E_a is an (unidirectional) irradiance in the air just exterior to the sphere. From the derivation of (6.35), we see that $E_\mathrm{a} \approx E_\mathrm{c}$. However, for a port that resembles a glass rod attached to the cell, $f_i = 1$. Here, the reflectivity would be $p_i = 0$, since there is no physical interface between different media to reflect the light. For a typical stem port that resembles a glass tube, such as in Fig. 6.7, we would have an intermediate value, $0 < f_i < 1$. Combining these cases, the port reflectivity for arbitrary f_i is

$$p_i \approx (1 - f_i)(1 - E_\mathrm{c}/E_\mathrm{g}) = (1 - f_i)(1 - 1/n_\mathrm{g}^2), \tag{6.37}$$

where we used the relation (6.35).

Using (6.35), (6.36), and (6.37), the power balance (6.31) becomes

$$P_0 = P_0 A(1-\rho_0) + E_c A[n_g^2(1-\widetilde{\rho}_g) + \alpha\overline{L}], \tag{6.38}$$

where we introduced an average reflectivity inside the glass,

$$\widetilde{\rho}_g = \rho_g(1-h) + \sum_i p_i h_i. \tag{6.39}$$

Using (6.38) with (6.1), we find the sphere multiplier for the irradiance E_c is

$$M(\alpha) \approx \frac{\rho_0}{n_g^2(1-\widetilde{\rho}_g) + \alpha\overline{L}}. \tag{6.40}$$

The maximum optical contrast (6.11) measured by a detector is then

$$\Delta(\alpha) \approx \frac{\alpha\overline{L}}{n_g^2(1-\widetilde{\rho}_g) + \alpha\overline{L}}, \tag{6.41}$$

according to this photon-gas approach with the glass effects described above.

While the expression (6.41) for the contrast $\Delta(\alpha)$ is similar to the previous photon-gas expression (6.21), it exhibits two new and important effects because of the glass. The first effect is "light trapping." Since the refractive index $n_g > 1$ for glass, with a typical value $n_g \approx 1.47$ for Pyrex, the effect of n_g is to enhance the wall loss in (6.41) for a given value of $\widetilde{\rho}_g$. This effect is due to the dependence (6.34) of the radiant energy density w of an equilibrium photon gas on the local refractive index n, which leads to a stronger radiant energy density w in the glass bulb than in the cell interior. This effect is analogous to the concentration of static electric fields by dielectrics, such as glass, inside capacitors. Such light trapping has been used to increase the

performance of solar cells with diffusers [146]. A similar effect occurs with reflective powders immersed in liquid [165].

The second effect is "light piping" out of ports with glass attachments, such as a stem port. This effect is due to the dependence of the average reflectivity $\widetilde{\rho}_{\mathrm{g}}$ of (6.39) on the glass fractions f_i in the port reflectivity p_i of (6.37). For normal ports with $f_i = 0$, the port loss P_h does not change with n_{g}. This is because any light trapping is counterbalanced by the port reflectivity p_i, which is clear if we use (6.35) and (6.37) to write the port loss P_h of (6.36) as

$$P_h = E_{\mathrm{c}} A \sum_i \left[1 + f_i(n_{\mathrm{g}}^2 - 1)\right] h_i. \tag{6.42}$$

Here, we see that there would be no dependence on n_{g} for the i-th port loss if $f_i = 0$. However, for stem ports with non-negligible glass fractions, $f_i > 0$, we see that the light trapping in the glass bulb leads to an enhanced light-piping loss through any glass extensions attached to the port.

This analysis suggests that the relatively poor performance of the ^{133}Cs cell compared to the ^{85}Rb cell might be explained by an enhanced light-piping loss due to the relatively thicker glass and the unusual cell shape, in particular, the relatively large pancake and stem portions of the cell. Light trapping likely played an similar role in both of the painted integrating-sphere alkali-metal vapor cells. This section, however, has assumed that the Labsphere 6080 is nearly Lambertian when applied to glass. From Fig. 6.6 in the previous section, we know that this is probably not a good approximation. In the next section we consider how to model the 6080-glass interface.

6.4.2 6080-glass interface

High-quality diffuse reflectors are usually assumed to be Lambertian, and modeled by only a single parameter, a diffuse reflectivity ρ. These materials seem to be almost exclusively characterized for reflection into air ($\rho = \rho_{\text{air}}$). There seems to be a lack of information about the properties of their reflection inside other media, such as glass or plastic. In this section, we consider a flat interface between glass and Labsphere 6080, which we suspect to be non-Lambertian. We begin with a description of Labsphere 6080, and end with a suggestion of a possible model for this interface.

Labsphere 6080 is a coating made of barium sulfate ($BaSO_4$) particles suspended in a polyvinyl alcohol (PVA) binder [160]. It is sold as a paint diluted in ethanol, and must be applied by airbrush. The optimal coating thickness is 0.5–0.6 mm. When properly applied, the diffuse reflectivity in air (ρ_{air}) is between 95–98% for wavelengths in the range of 300–1200 nm. The same "6080" coating has been sold by different manufacturers in the past: Kodak, Eastman, and Munsell before Labsphere. According to Grum and Luckey [166], who were employees at Eastman, the optimal particle diameter is roughly 0.3–3.0 μm, and the sizes of most particles in the Eastman white reflectance coating were between roughly 0.05–3.0 μm. The ratio of PVA:$BaSO_4$ in the paint is stated as 1:100 "by parts," which was chosen to optimize the tradeoff of reduced performance for enhanced mechanical strength from the PVA binder, which most likely does not fill the voids between the particles. The volume packing fraction probably depends on how the paint is applied. However, it should be close to the fraction for pressed barium sulfate powders, which has been measured to be roughly 52% [167]. For comparison, a body-centered cubic crystal has a volume packing fraction of roughly 68%, so the pressed powder and 6080 paint are very tightly packed, perhaps nearly as tight as possible while still retaining a random structure.

As described, Labsphere 6080 is a highly reflective, random (or turbid), and heterogeneous (or porous) media. Though the study of scattering by such materials has

a long history, research is still ongoing [168, 169]. In particular, Labsphere 6080 is very difficult to model for three reason:

(i) it is densely-packed (the barium sulfate particles touch),

(ii) it is a strong multiple-scatterer, and

(iii) the particle size is of the same order as the wavelengths of interest.

Unfortunately, the traditional models for Labsphere 6080 and pressed barium sulfate powder — Kubelka–Munk, photon-diffusion, and radiative-transfer models [170, 171, 172, 173, 174, 169, 154] — do not appear to predict how the reflectance properties should change with the target medium.

One potentially elegant way to model an interface with Labsphere 6080, or a similar diffuse material, such as Spectralon, might be to use a complex refractive index for the coating. This approach has been recently used with some highly turbid media, where a complex refractive index was inferred from the measurement of a gradual transition to total internal reflection using a prism, such as displayed in Fig. 6.6 [175]. In addition, Egan and Hilgeman [167] measured the real part of an effective refractive index for pressed barium sulfate powder in air to be $n \approx 1.415$ at 800 nm, which is surprisingly a little less than that of typical glass [167]. This measurement, together with Figs. 6.5 and 6.6, provide some support for this idea. Such knowledge would be important to the understanding of how high-quality diffuse reflectors work as coatings for internal reflection inside media other than air. In particular, it would be valuable for Labsphere 6080 since that it is one of the most widely used diffuse reflectance coatings [155]. For example, this information could be important to the light-trapping enhancement of solar cells [146, 147], and to other applications of integrating spheres that use internal glass bulbs [148, 149, 150, 151]. It might even be useful to standard integrating spheres, which can suffer from internal specular reflection [176, 177].

6.5 Summary and discussion

In summary, we investigated the use of integrating spheres to enhance optical absorption in optically thin alkali-metal vapor cells. With one vapor cell, we demonstrated an enhancement of up to roughly a factor of 10. However, difficulty with another vapor cell highlighted the important effects of the glass cell required to contain the alkali metal. An improved performance should be possible with optimized cell designs, since neither vapor cell was designed for use with integrating spheres. However, we do not anticipate a significantly improved performance, for example, above an enhancement of roughly 20, due to the nature of integrating spheres and the effects of the glass cell. Though integrating-sphere alkali-metal vapor cells may be used in vapor-cell clocks, their inapplicability with coherent population trapping makes them unattractive for miniature clocks.

Future work would benefit from an improved modeling of the interface between glass and Labsphere 6080. For example, we suggest that it might be possible to model high-quality diffuse reflectors, such as Labsphere 6080, with a complex refractive index, which is an approach that has been recently used with other highly turbid materials [175]. In practice, surface roughening of the glass bulb might be able to improve the Lambertian quality of the 6080-glass interface, which has been applied with the light-trapping enhancement of solar cells [146, 147] and other applications of integrating spheres that use internal glass bulbs [148, 149, 150, 151].

Bibliography

[1] James Jespersen and Jane Fitz-Randolph. *From Sundials to Atomic Clocks: Understanding Time and Frequency*. U.S. Department of Commerce, Washington, D.C., 1999. (National Institute of Standards and Technology, Monograph 155, 1999 Ed.). Available from: `http://tf.boulder.nist.gov/general/publications.htm`.

[2] C. Hackman and D. B. Sullivan. Resource letter: TFM-1: time and frequency measurement. *American Journal of Physics*, 63(4):306–317, 1995. `doi:10.1119/1.17961`.

[3] Sir William Thomson and Peter Guthrie Tait. *Treatise on Natural Philosophy*, volume 1. Cambridge University Press, Cambridge, 2nd edition, 1879.

[4] W. F. Snider. Lord Kelvin on atoms as fundamental natural standards (for base units). *IEEE Transactions on Instrumentation and Measurement*, 22(1):99, 1973. `doi:10.1109/TIM.1973.4314109`.

[5] I. I. Rabi, J. R. Zacharias, S. Millman, and P. Kusch. A new method of measuring nuclear magnetic moment. *Physical Review*, 53(4):318, 1938. `doi:10.1103/PhysRev.53.318`.

[6] The atomic clock: an atomic standard of frequency and time. *National Bureau of Standards Technical News Bulletin*, 33(2):17–24, 1949. Available from: `http://tf.boulder.nist.gov/general/publications.htm`.

[7] M. A. Lombardi, T. P. Heavner, and S. R. Jefferts. NIST primary frequency standards and the realization of the SI second. *Measure: The Journal of Measurement Science*, 2(4):74–89, 2007. Available from: `http://www.nist.gov/publication-portal.cfm`.

[8] T. Quinn. Fifty years of atomic time-keeping: 1955 to 2005. *Metrologia*, 42(3), 2005. `doi:10.1088/0026-1394/42/3/E01`.

[9] W. Markowitz, R. Glenn Hall, L. Essen, and J. V. L. Parry. Frequency of cesium in terms of ephemeris time. *Physical Review Letters*, 1(3):105–107, 1958. `doi:10.1103/PhysRevLett.1.105`.

[10] Resolution 1 of the *13th Conference Generale des Poids et Mesures (CGPM)*, 1967.

[11] Jacques Vanier and Claude Audoin. *The Quantum Physics of Atomic Frequency Standards*. A. Hilger, Bristol, 1989.

[12] S. A. Diddams, Th. Udem, J. C. Bergquist, E. A. Curtis, R. E. Drullinger, L. Hollberg, W. M. Itano, W. D. Lee, C. W. Oates, K. R. Vogel, and D. J. Wineland. An optical clock based on a single trapped $^{199}Hg^{+}$ ion. *Science*, 293(5531):825–828, 2001. doi:10.1126/science.1061171.

[13] M. Takamoto, F.-L. Hong, R. Higashi, and H. Katori. An optical lattice clock. *Nature*, 435(7040):321–324, 2005. doi:10.1038/nature03541.

[14] James Camparo. The rubidium atomic clock and basic research. *Physics Today*, 60(11):33–39, 2007. doi:10.1063/1.2812121.

[15] J. Vanier. Atomic clocks based on coherent population trapping: a review. *Applied Physics B*, 81(4):421–442, 2005. doi:10.1007/s00340-005-1905-3.

[16] J. Vanier and C. Mandache. The passive optically pumped Rb frequency standard: the laser approach. *Applied Physics B*, 87(4):565–593, 2007. doi:10.1007/s00340-007-2643-5.

[17] S. Knappe, V. Shah, P. D. D. Schwindt, L. Hollberg, J. Kitching, L.-A. Liew, and J. Moreland. A microfabricated atomic clock. *Applied Physics Letters*, 85(9):1460–1462, 2004. doi:10.1063/1.1787942.

[18] A. Kastler. Quelques suggestions concernant la production optique et la détection optique d'une inégalité de population des niveaux de quantifigation spatiale des atomes. Application à l'expérience de Stern et Gerlach et à la résonance magnétique. *Journal de Physique et Le Radium*, 11(6):255–265, 1950. doi:10.1051/jphysrad:01950001106025500.

[19] W. Happer. Optical pumping. *Reviews of Modern Physics*, 44(2):169–249, 1972. doi:10.1103/RevModPhys.44.169.

[20] G. W. Series. Thirty years of optical pumping. *Contemporary Physics*, 22(5):487–509, 1981. doi:10.1080/00107518108231547.

[21] William Happer, Yuan-Yu Jau, and Thad G. Walker. *Optically Pumped Atoms*. Wiley VCH, Weinheim, 2010. Computer codes in this book are freely available online at http://digital.library.wisc.edu/1793/35675.

[22] R. H. Dicke. The effect of collisions upon the doppler width of spectral lines. *Physical Review*, 89(2):472–473, 1953. doi:10.1103/PhysRev.89.472.

[23] P. L. Bender, E. C. Beaty, and A. R. Chi. Optical detection of narrow Rb^{87} hyperfine absorption lines. *Physical Review Letters*, 1(9):311–313, 1958. doi:10.1103/PhysRevLett.1.311.

[24] B. S. Mathur, H. Tang, and W. Happer. Light shifts in the alkali atoms. *Physical Review*, 171(1):11–19, 1968. doi:10.1103/PhysRev.171.11.

[25] B. H. McGuyer, Y.-Y. Jau, and W. Happer. Simple method of light-shift suppression in optical pumping systems. *Applied Physics Letters*, 94(25):251110, 2009. doi:10.1063/1.3158961.

[26] B. H. McGuyer, Y.-Y. Jau, and W. Happer. New method for light-shift elimination. In *IEEE International Frequency Control Symposium, 2009 Joint with the 22nd European Frequency and Time forum*, pages 1005–1008, April 2009. doi:10.1109/FREQ.2009.5168343.

[27] Bart McGuyer, Yuan-Yu Jau, and William Happer. New Method for Light Shift Elimination in Optical Pumping Systems. In *APS Division of Atomic, Molecular and Optical Physics Meeting Abstracts*, page 3001, May 2009. Available from: http://adsabs.harvard.edu/abs/2009APS..DMP.Q3001M.

[28] Bart H. McGuyer, Yuan-Yu Jau, and William Happer. Method for suppressing light shift in optical pumping systems. U.S. Patent 7,825,736, filed December 18, 2008, and issued November 2, 2010.

[29] M. Arditi and T. R. Carver. Frequency shift of the zero-field hyperfine splitting of Cs^{133} produced by various buffer gases. *Physical Review*, 112(2):449, 1958. doi:10.1103/PhysRev.112.449.

[30] M. Arditi and T. R. Carver. Pressure, light, and temperature shifts in optical detection of 0-0 hyperfine resonance of alkali metals. *Physical Review*, 124(3):800–809, 1961. doi:10.1103/PhysRev.124.800.

[31] B. H. McGuyer, T. Xia, Y.-Y. Jau, and W. Happer. Hyperfine frequencies of ^{87}Rb and ^{133}Cs atoms in Xe gas. *Physical Review A*, 84(3):030501(R), 2011. doi:10.1103/PhysRevA.84.030501.

[32] B. H. McGuyer, T. Xia, Y.-Y. Jau, and W. Happer. Nonlinear pressure shifts of alkali-metal atoms in xenon. In *2011 Joint Conference of the IEEE International Frequency Control Symposium and European Frequency and Time Forum (FCS)*, pages 1–5, May 2011. doi:10.1109/FCS.2011.5977737.

[33] Bart McGuyer, Tian Xia, Yuan-Yu Jau, and William Happer. Nonlinear pressure shifts of alkali-metal atoms in xenon. In *APS Division of Atomic, Molecular and Optical Physics Meeting Abstracts*, page 1007, June 2011. Available from: http://adsabs.harvard.edu/abs/2011APS..DMP.T1007M.

[34] Tian Xia. *Polarization and hyperfine transitions of metastable ^{129}Xe in discharge cells and pressure shift of Cs in Neon.* PhD thesis, Princeton University, January 2011.

[35] Tian Xia, Bart McGuyer, Yuan-Yu Jau, and William Happer. Positive nonlinear pressure shift of Cs in Ne. In *APS Division of Atomic, Molecular and Optical Physics Meeting Abstracts*, page K6003, March 2010. Available from: http://adsabs.harvard.edu/abs/2010APS..DMP.K6003X.

[36] Bart McGuyer, Yuan-Yu Jau, and William Happer. Nonlinear Pressure Shifts of Rubidium in Inert Gases. In *APS Division of Atomic, Molecular and Optical Physics Meeting Abstracts*, page 1057, May 2009. Available from: http://adsabs.harvard.edu/abs/2009APS..DMP.M1057M.

[37] C. C. Bouchiat, M. A. Bouchiat, and L. C. L. Pottier. Evidence for Rb-rare-gas molecules from the relaxation of polarized Rb atoms in a rare gas. Theory. *Physical Review*, 181(1):144–165, 1969. doi:10.1103/PhysRev.181.144.

[38] M. A. Bouchiat, J. Brossel, and L. C. Pottier. Evidence for Rb-rare-gas molecules from the relaxation of polarized Rb atoms in a rare gas. Experimental results. *Journal of Chemical Physics*, 56(7):3703–3714, 1972. doi:10.1063/1.1677750.

[39] F. Gong, Y.-Y. Jau, and W. Happer. Nonlinear pressure shifts of alkali-metal atoms in inert gases. *Physical Review Letters*, 100(23):233002, 2008. doi:10.1103/PhysRevLett.100.233002.

[40] Fei Gong. *New Physics And Technology For Spin-polarized Alkali-metal Atoms*. PhD thesis, Princeton University, August 2008.

[41] R. A. Bernheim. Spin relaxation in optical pumping. *Journal of Chemical Physics*, 36(1):135–140, 1962. doi:10.1063/1.1732283.

[42] Z. Wu, T. G. Walker, and W. Happer. Spin-rotation interaction of noble-gas alkali-metal atom pairs. *Physical Review Letters*, 54(17):1921–1924, 1985. doi:10.1103/PhysRevLett.54.1921.

[43] Bart McGuyer, Amit Ben-Kish, Yuan-Yu Jau, and William Happer. Integrating Sphere Alkali-Metal Vapor Cells. In *APS Division of Atomic, Molecular and Optical Physics Meeting Abstracts*, page 1176, March 2010. Available from: http://adsabs.harvard.edu/abs/2010APS..DMP.T1176M.

[44] Y.-Y. Jau, A. B. Post, N. N. Kuzma, A. M. Braun, M. V. Romalis, and W. Happer. Intense, narrow atomic-clock resonances. *Physical Review Letters*, 92(11):110801, 2004. doi:10.1103/PhysRevLett.92.110801.

[45] V. Shah, V. Gerginov, P. D. D. Schwindt, S. Knappe, L. Hollberg, and J. Kitching. Continuous light-shift correction in modulated coherent population trapping clocks. *Applied Physics Letters*, 89(15):151124, 2006. doi:10.1063/1.2360921.

[46] M. Arditi and J.-L. Picqué. Application of the light-shift effect to laser frequency stabilization with reference to microwave frequency standard. *Optics Communications*, 15(2):317–322, 1975. doi:10.1016/0030-4018(75)90313-2.

[47] M. Hashimoto and M. Ohtsu. Modulation transfer and optical Stark effect in a rubidium atomic clock pumped by a semiconductor laser. *Journal of the Optical Society of America B*, 6(10):1777–1789, 1989. doi:10.1364/JOSAB.6.001777.

[48] M. Hashimoto and M. Ohtsu. A novel method to compensate for the effect of light shift in a rubidium atomic clock pumped by a semiconductor laser. *IEEE Transactions on Instrumentation and Measurement*, 39(3):458–462, 1990. doi:10.1109/19.106272.

[49] Jinquan Deng. Light shift compensation in a Rb gas cell frequency standard with two-laser pumping. *IEEE Transactions on Ultrasonics, Ferroelectrics and Frequency Control*, 48(6):1657–1661, 2001. doi:10.1109/58.971718.

[50] C. Affolderbach, C. Andreeva, S. Cartaleva, T. Karaulanov, G. Mileti, and D. Slavov. Light-shift suppression in laser optically pumped vapour-cell atomic frequency standards. *Applied Physics B*, 80(7):841–848, 2005. doi:10.1007/s00340-005-1804-7.

[51] M. Zhu. Optical pumping method to reduce light shift in a vapor cell atomic frequency standard. In *IEEE International Frequency Control Symposium, 2007 Joint with the 21st European Frequency and Time Forum*, pages 1334–1338, May-June 2007. doi:10.1109/FREQ.2007.4319293.

[52] Daniel A. Steck. Alkali D Line Data [Online]. February 2012. Available from: http://george.ph.utexas.edu/~dsteck/alkalidata/.

[53] E. Arimondo, M. Inguscio, and P. Violino. Experimental determinations of the hyperfine structure in the alkali atoms. *Reviews of Modern Physics*, 49(1):31–75, 1977. doi:10.1103/RevModPhys.49.31.

[54] D. A. Varshalovich, A. N. Moskalev, and V. K. Khersonskii. *Quantum Theory of Angular Momentum*. World Scientific, Singapore, 1988.

[55] A. V. Taichenachev, V. I. Yudin, V. L. Velichansky, and S. A. Zibrov. On the unique possibility of significantly increasing the contrast of dark resonances on the D1 line of ^{87}Rb. *Journal of Experimental and Theoretical Physics Letters*, 82(7):398–403, 2005. doi:10.1134/1.2142864.

[56] Dimitry Budker, Derek F. Kimball, and David P. DeMille. *Atomic Physics: An Exploration through Problems and Solutions*. Oxford University Press, New York, 2nd edition, 2008.

[57] J. D. Kleykamp, A. J. Hachtel, D. G. Kane, M. D. Marshall, N. J. Souther, P. K. Harnish, and S. Bali. Measurement of sub-natural linewidth AC stark shifts in

cold atoms: An experiment for an advanced undergraduate laboratory. *American Journal of Physics*, 79(12):1211–1217, 2011. doi:10.1119/1.3633702.

[58] B. J. Sussman. Five ways to the nonresonant dynamic Stark effect. *American Journal of Physics*, 79(5):477–484, 2011. doi:10.1119/1.3553018.

[59] M. Haas, U. D. Jentschura, and C. H. Keitel. Comparison of classical and second quantized description of the dynamic stark shift. *American Journal of Physics*, 74(1):77–81, 2006. doi:10.1119/1.2140742.

[60] J. C. Camparo, R. P. Frueholz, and C. H. Volk. Inhomogeneous light shift in alkali-metal atoms. *Physical Review A*, 27(4):1914–1924, 1983. doi:10.1103/PhysRevA.27.1914.

[61] Computer code IGOR Pro 5 & 6, WaveMetrics, Inc., Portland, OR, 2012. Available from: http://www.wavemetrics.com.

[62] Bart H. McGuyer. Computer code DAQ Procedures. December 2011. Available from: http://www.igorexchange.com/project/DAQ_Procedures.

[63] Bart H. McGuyer. Computer code Expt Procedures. December 2011. Available from: http://www.igorexchange.com/project/Expt_Procedures.

[64] D. W. Allan. Time and frequency (time-domain) characterization, estimation, and prediction of precision clocks and oscillators. *IEEE Transactions on Ultrasonics, Ferroelectrics and Frequency Control*, 34(6):647–654, 1987. doi:10.1109/T-UFFC.1987.26997.

[65] George B. Arfken and Hans J. Weber. *Mathematical Methods for Physicists*. Harcourt, New York, 5th edition, 2001.

[66] Paul J. Nahin. *The Science of Radio*. Springer-Verlag, New York, 2nd edition, 2001.

[67] R. Boudot, P. Dziuban, M. Hasegawa, R. K. Chutani, S. Galliou, V. Giordano, and C. Gorecki. Coherent population trapping resonances in Cs–Ne vapor microcells for miniature clocks applications. *Journal of Applied Physics*, 109(1):014912, 2011. doi:10.1063/1.3530951.

[68] L. B. Robinson. Frequency shifts in the hyperfine spectra of alkalis caused by foreign gases. *Physical Review*, 117(5):1275–1280, 1960. doi:10.1103/PhysRev.117.1275.

[69] B. L. Bean and R. H. Lambert. Temperature dependence of hyperfine density shifts. III. ^{23}Na, ^{39}K, and ^{85}Rb in He, Ne, Ar, and N_2. *Physical Review A*, 12(4):1498–1502, 1975. doi:10.1103/PhysRevA.12.1498.

[70] P. J. Oreto, Y.-Y. Jau, A. B. Post, N. N. Kuzma, and W. Happer. Buffer-gas induced shift and broadening of hyperfine resonances in alkali-metal vapors. *Physical Review A*, 69(4):042716, 2004. doi:10.1103/PhysRevA.69.042716.

[71] B. K. Rao, D. Ikenberry, and T. P. Das. Hyperfine pressure shift and van der Waals interaction. IV. Hydrogen-rare-gas systems. *Physical Review A*, 2(4):1411–1421, 1970. doi:10.1103/PhysRevA.2.1411.

[72] S. Ray. Molecular theory of hyperfine pressure shifts in H caused by Ar and He buffers. *Physical Review A*, 12(5):2031–2043, 1975. doi:10.1103/PhysRevA.12.2031.

[73] J. C. Camparo. Semiempirical theory of carver rates in alkali/noble-gas systems. *Journal of Chemical Physics*, 126(24):244310, 2007. doi:10.1063/1.2743958.

[74] N. Allard and J. Kielkopf. The effect of neutral nonresonant collisions on atomic spectral lines. *Reviews of Modern Physics*, 54(4):1103–1182, 1982. doi:10.1103/RevModPhys.54.1103.

[75] B. L. Bean and R. H. Lambert. Temperature dependence of hyperfine density shifts. IV. ^{23}Na, ^{39}K, and ^{85}Rb in He, Ne, Ar, and N_2 at low temperatures. *Physical Review A*, 13(1):492–494, 1976. doi:10.1103/PhysRevA.13.492.

[76] E. S. Ensberg and G. zu Putlitz. Nonlinear hyperfine pressure shift by optical pumping with white light. *Physical Review Letters*, 22(25):1349–1351, 1969. doi:10.1103/PhysRevLett.22.1349.

[77] S. Ray and S. L. Kaufman. Theoretical interpretation of the quadratic hyperfine pressure shift. *Physical Review Letters*, 29(14):895–898, 1972. doi:10.1103/PhysRevLett.29.895.

[78] K. Dorenburg, H.-J. Glas, S. L. Kaufman, and G. zu Putlitz. Hyperfine shifts for cesium in argon at high density. *Zeitschrift für Physik*, 267(4):257–259, 1974. doi:10.1007/BF01669445.

[79] K. Dorenburg, M. Gladisch, and G. zu Putlitz. Hyperfine structure density shift coefficients for K, Rb and Cs at high buffer gas densities. *Zeitschrift für Physik A Hadrons and Nuclei*, 289(2):145–149, 1979. doi:10.1007/BF01435931.

[80] H. B. G. Casimir and D. Polder. The influence of retardation on the London-van der Waals forces. *Physical Review*, 73(4):360–372, 1948. doi:10.1103/PhysRev.73.360.

[81] R. Herman and H. Margenau. Frequency shifts in hyperfine splitting of alkalis: a correction. *Physical Review*, 122(4):1204–1206, 1961. doi:10.1103/PhysRev.122.1204.

[82] F. J. Adrian. Matrix effects on the electron spin resonance spectra of trapped hydrogen atoms. *Journal of Chemical Physics*, 32(4):972–981, 1960. doi:10.1063/1.1730906.

[83] Yu. Ralchenko, A. Kramida, J. Reader, and NIST ASD Team. *NIST Atomic Spectra Database* (version 4.1.0). National Institute of Standards and Technology, Gaithersburg, MD. (2011). Available from: `http://physics.nist.gov/asd`.

[84] C. F. Bunge, J. A. Barrientos, and A. V. Bunge. Roothaan-Hartree-Fock ground-state atomic wave functions: Slater-type orbital expansions and expectation values for $Z = 2-54$. *Atomic Data and Nuclear Data Tables*, 53(1):113–162, 1993. `doi:10.1006/adnd.1993.1003`.

[85] A. D. McLean and R. S. McLean. Roothaan-Hartree-Fock atomic wave functions: Slater basis-set expansions for $Z = 55 - 92$. *Atomic Data and Nuclear Data Tables*, 26(3–4):197–381, 1981. `doi:10.1016/0092-640X(81)90012-7`.

[86] J. E. Sansonetti. Wavelengths, transition probabilities, and energy levels for the spectra of cesium (Cs I – Cs LV). *Journal of Physical and Chemical Reference Data*, 38(4):761–923, 2009. `doi:10.1063/1.3132702`.

[87] S. H. Patil. Adiabatic potentials for alkali intert-gas systems in the ground-state. *Journal of Chemical Physics*, 94(12):8089–8095, 1991. `doi:10.1063/1.460091`.

[88] U. Buck and H. Pauly. Interferenzen bei atomaren stoßprozessen und ihre interpretation durch ein modifiziertes Lennard-Jones-potential. *Zeitschrift für Physik*, 208(4):390–417, 1968. `doi:10.1007/BF01382701`.

[89] J. Pascale and J. Vandeplanque. Excited molecular terms of the alkali-rare gas atom pairs. *Journal of Chemical Physics*, 60(6):2278–2289, 1974. `doi:10.1063/1.1681360`.

[90] W. G. Greenwood and K. T. Tang. Dipole, quadrupole, and octupole terms in the long-range hyperfine frequency shift for hydrogen in the presence of inert gases. *Journal of Chemical Physics*, 86(6):3539–3548, 1987. `doi:10.1063/1.451957`.

[91] J. M. Standard and P. R. Certain. Bounds to two- and three-body long-range interaction coefficients for S-state atoms. *Journal of Chemical Physics*, 83(6):3002–3008, 1985. `doi:10.1063/1.449203`.

[92] E. H. Moore. On the reciprocal of the general algebraic matrix. *Bulletin of the American Mathematical Society*, 26(9):394–395, 1920. `doi:10.1090/S0002-9904-1920-03322-7`.

[93] R. Penrose. A generalized inverse for matrices. *Mathematical Proceedings of the Cambridge Philosophical Society*, 51:406–413, 1955. `doi:10.1017/S0305004100030401`.

[94] Computer code MATLAB 2011A, Mathworks, Natick, MA, 2012. Available from: `http://www.mathworks.com/`.

[95] Emmanuel Candès and Justin Romberg. Computer code l_1-MAGIC. October 2005. Available from: http://users.ece.gatech.edu/~justin/l1magic/.

[96] R. R. Freeman, E. M. Mattison, D. E. Pritchard, and D. Kleppner. Alkali-metal hyperfine shift in the van der Waals molecule KAr. *Physical Review Letters*, 33(7):397–399, 1974. doi:10.1103/PhysRevLett.33.397.

[97] R. R. Freeman, D. E. Pritchard, and D. Kleppner. Argon-induced hyperfine frequency shift in potassium. *Physical Review A*, 13(2):907–909, 1976. doi:10.1103/PhysRevA.13.907.

[98] P. S. Żuchowski, J. Aldegunde, and J. M. Hutson. Ultracold RbSr molecules can be formed by magnetoassociation. *Physical Review Letters*, 105(15):153201, 2010. doi:10.1103/PhysRevLett.105.153201.

[99] T. G. Walker and W. Happer. Spin-exchange optical pumping of noble-gas nuclei. *Reviews of Modern Physics*, 69(2):629–642, 1997. doi:10.1103/RevModPhys.69.629.

[100] N. Brahms, T. V. Tscherbul, P. Zhang, J. Kłos, H. R. Sadeghpour, A. Dalgarno, J. M. Doyle, and T. G. Walker. Formation of van der Waals molecules in buffer-gas-cooled magnetic traps. *Physical Review Letters*, 105(3):033001, 2010. doi:10.1103/PhysRevLett.105.033001.

[101] W. E. Cooke and R. R. Freeman. Molecular-beam magnetic-resonance measurement of the spin-rotational interaction in RbKr. *Physical Review A*, 16(6):2211–2215, 1977. doi:10.1103/PhysRevA.16.2211.

[102] R. R. Freeman, E. M. Mattison, D. E. Pritchard, and D. Kleppner. The spin-rotation interaction in the van der Waals molecule KAr. *Journal of Chemical Physics*, 64(3):1194–1203, 1976. doi:10.1063/1.432318.

[103] B. L. Blaney and G. E. Ewing. Van Der Waals Molecules. *Annual Review of Physical Chemistry*, 27:553–584, 1976. doi:10.1146/annurev.pc.27.100176.003005.

[104] B. Brutschy and P. Hobza. van der Waals Molecules III: Introduction. *Chemical Reviews*, 100(11):3861–3862, 2001. doi:10.1021/cr990074x.

[105] C. C. Bouchiat and M. A. Bouchiat. Alkali-rare-gas van der Waals molecules and ground-state relaxation processes in optical pumping. *Physical Review A*, 2(4):1274–1285, 1970. doi:10.1103/PhysRevA.2.1274.

[106] M. A. Bouchiat, J. Brossel, P. Mora, and L. Pottier. Properties of rubidium-argon Van der Waals molecules from the relaxation of polarized Rb atoms. *Journal de Physique*, 36(11):1075–1077, 1975. doi:10.1051/jphys:0197500360110107500.

[107] R. Goldhor and D. Pritchard. Bound and quasibound states of alkali-rare gas molecules. *Journal of Chemical Physics*, 64(3):1189–1193, 1976. doi:10.1063/1.432317.

[108] R. Goldhor and D. Pritchard. Erratum: Bound and quasibound states of alkali-rare gas molecules. *Journal of Chemical Physics*, 67(12):5985, 1977. doi:10.1063/1.434783.

[109] S. R. Schaefer, G. D. Cates, T.-R. Chien, D. Gonatas, W. Happer, and T. G. Walker. Frequency shifts of the magnetic-resonance spectrum of mixtures of nuclear spin-polarized noble gases and vapors of spin-polarized alkali-metal atoms. *Physical Review A*, 39(11):5613–5623, 1989. doi:10.1103/PhysRevA.39.5613.

[110] T. G. Walker. Estimates of spin-exchange parameters for alkali-metal–noble-gas pairs. *Physical Review A*, 40(9):4959–4964, 1989. doi:10.1103/PhysRevA.40.4959.

[111] F. A. Franz and A. Sieradzan. Binary formation of NaNe quasibound molecules observed in spin relaxation of Na. *Physical Review A*, 29(3):1599–1601, 1984. doi:10.1103/PhysRevA.29.1599.

[112] W. Happer. Comment on "Binary formation of NaNe quasibound molecules observed in spin relaxation of Na". *Physical Review A*, 31(6):4020–4021, 1985. doi:10.1103/PhysRevA.31.4020.

[113] F. A. Franz and A. Sieradzan. Response to "Comment on 'Binary formation of NaNe quasibound molecules observed in spin relaxation in Na' ". *Physical Review A*, 31(6):4022, 1985. doi:10.1103/PhysRevA.31.4022.

[114] F. A. Franz and C. Volk. Spin relaxation in Rb-He and Rb-Ne via modification of the Rb hyperfine interaction in van der Waals molecules. *Physical Review A*, 18(2):599–605, 1978. doi:10.1103/PhysRevA.18.599.

[115] F. A. Franz and C. Volk. Detection and lifetime measurement of Rb-He quasibound molecules. *Physical Review Letters*, 35(25):1704–1708, 1975. doi:10.1103/PhysRevLett.35.1704.

[116] D. L. Drummond and A. Gallagher. Potentials and continuum spectra of Rb-noble gas molecules. *Journal of Chemical Physics*, 60(9):3426–3435, 1974. doi:10.1063/1.1681555.

[117] John M. Brown and Alan Carrington. *Rotational Spectroscopy of Diatomic Molecules*. Cambridge University Press, Cambridge, 2003.

[118] J. Vanier, R. Kunski, N. Cyr, J. Y. Savard, and M. Têtu. On hyperfine frequency shifts caused by buffer gasses: Application to the optically pumped passive rubidium frequency standard. *Journal of Applied Physics*, 53(8):5387–5391, 1982. doi:10.1063/1.331467.

[119] K. F. Poulter, M.-J. Rodgers, P. J. Nash, T. J. Thompson, and M. P. Perkin. Thermal transpiration correction in capacitance manometers. *Vacuum*, 33(6):311–316, 1983. doi:10.1016/0042-207X(83)90098-2.

[120] D. Alcaide. Corrections to "Thermal transpiration correction in capacitance manometers" paper, Poulter et al, *Vacuum*, 1982, p311 to 316. June 26, 2001. Courtesy of D. Jacobs at MKS Instruments, Inc. 2010.

[121] K. Iwata and Y. Kusumoto. Modification of Takaishi–Sensui formula for a diaphragm gauge system connected by an arbitrary length pipe. *Vacuum*, 84(5):729–733, 2009. doi:10.1016/j.vacuum.2009.03.035.

[122] J. Šetina. New approach to corrections for thermal transpiration effects in capacitance diaphragm gauges. *Metrologia*, 36(6):623–626, 1999. doi:10.1088/0026-1394/36/6/27.

[123] W. Jitschin and P. Röhl. Quantitative study of the thermal transpiration effect in vacuum gauges. *Journal of Vacuum Science & Technology A: Vacuum, Surfaces, and Films*, 5(3):372–375, 1987. doi:10.1116/1.574162.

[124] T. Takaishi and Y. Sensui. Thermal transpiration effect of hydrogen, rare gases and methane. *Transactions of the Faraday Society*, 59:2503–2514, 1963. doi:10.1039/TF9635902503.

[125] J. Levine. Invited review article: The statistical modeling of atomic clocks and the design of time scales. *Review of Scientific Instruments*, 83(2):021101, 2012. doi:10.1063/1.3681448.

[126] M. P. R. Thomsen, L. J. Stief, and R. J. Fallon. Study of the phenomena affecting the composition of rubidium vapor cells. In *22nd Annual Symposium on Frequency Control*, pages 559–572, 1968. doi:10.1109/FREQ.1968.199733.

[127] J. Kitching, S. Knappe, L. Liew, J. Moreland, P. D. D. Schwindt, V. Shah, V. Gerginov, and L. Hollberg. Microfabricated atomic frequency references. *Metrologia*, 42(3):S100–S104, 2005. doi:10.1088/0026-1394/42/3/S11.

[128] Timothy Davis, Sterling McBride, Alaun Braun, and William Happer. System and method for modulating pressure in an alkali-vapor cell. U.S. Patent 7,902,927, filed June 18, 2009, and issued March 8, 2011.

[129] Stanford Research Systems, Inc. FS725 – Benchtop rubidium frequency standard. 2012. Available from: http://www.thinksrs.com/downloads/PDFs/Catalog/FS725c.pdf.

[130] B. Wagner, H. J. Quenzer, S. Hoerschelmann, T. Lisec, and M. Juerss. Bistable microvalve with pneumatically coupled membranes. In *IEEE Ninth Annual International Workshop on Micro Electro Mechanical Systems: 'An Investigation of Micro Structures, Sensors, Actuators, Machines and Systems'*, pages 384–388, February 1996. doi:10.1109/MEMSYS.1996.494012.

[131] H. Kim, A. A. Astle, K. Najafi, L. P. Bernal, and P. D. Washabaugh. A fully integrated high-efficiency peristaltic 18-stage gas micropump with active microvalves. In *IEEE 20th International Conference on Micro Electro Mechanical Systems*, pages 131–134, January 2007. doi:10.1109/MEMSYS.2007.4433033.

[132] G. Beni and S. Hackwood. Electro-wetting displays. *Applied Physics Letters*, 38(4):207–209, 1981. doi:10.1063/1.92322.

[133] Robert R. Riesz. Acoustic device. U.S. Patent 2,062,478, filed September 28, 1935, and issued December 1, 1936.

[134] C. Eckart. Vortices and streams caused by sound waves. *Physical Review*, 73(1):68–76, 1948. doi:10.1103/PhysRev.73.68.

[135] U. Ingard and H. Ising. Acoustic nonlinearity of an orifice. *The Journal of the Acoustical Society of America*, 42(1):6–17, 1967. doi:10.1121/1.1910576.

[136] J. Lighthill. Acoustic streaming. *Journal of Sound and Vibration*, 61(3):391–418, 1978. doi:10.1016/0022-460X(78)90388-7.

[137] A. A. Aganin, V. B. Kuznetsov, E. V. Martynov, and E. T. Smirnova. An experimental and numerical study of acoustic flows near cavity resonators. *Journal of Applied Mechanics and Technical Physics*, 38(6):868–876, 1997. doi:10.1007/BF02467952.

[138] A. Godone, S. Micalizio, F. Levi, and C. Calosso. Microwave cavities for vapor cell frequency standards. *Review of Scientific Instruments*, 82(7):074703, 2011. doi:10.1063/1.3606641.

[139] F. Strumia, N. Beverini, A. Moretti, and G. Rovera. Optimization of the buffer gas mixture for optically pumped Cs frequency standards. In *30th Annual Symposium on Frequency Control.*, pages 468–472, 1976. doi:10.1109/FREQ.1976.201353.

[140] Daniel Karl Walter. *Optical probes of angular momentum and energy transport in spin-exchange optical pumping systems*. PhD thesis, Princeton University, October 2001.

[141] S. Tranchart, I. H. Bachir, and J.-L. Destombes. Sensitive trace gas detection with near-infrared laser diodes and an integrating sphere. *Applied Optics*, 35(36):7070–7074, 1996. doi:10.1364/AO.35.007070.

[142] H.-D. Cheng, W.-Z. Zhang, H.-Y. Ma, L. Liu, and Y.-Z. Wang. Laser cooling of rubidium atoms from background vapor in diffuse light. *Physical Review A*, 79(2):023407, 2009. doi:10.1103/PhysRevA.79.023407.

[143] W.-Z. Zhang, H.-D. Cheng, L. Liu, and Y.-Z. Wang. Observation of recoil-induced resonances and electromagnetically induced absorption of diffuse light by cold atoms. *Physical Review A*, 79(5):053804, 2009. doi:10.1103/PhysRevA.79.053804.

[144] C. Valentin, E. Guillot, C. Guillemot, P. Petit, and N. Dimarcq. Microwave interrogation of cesium atoms cooled in isotropic light. *IEEE Transactions on Instrumentation and Measurement*, 50(5):1224 –1228, 2001. doi:10.1109/19.963188.

[145] F. X. Esnault, S. Perrin, D. Holleville, S. Guerandel, N. Dimarcq, and J. Delporte. Reaching a few 10^{-13} $\tau^{-1/2}$ stability level with the compact cold atom clock HORACE. In *2008 IEEE International Frequency Control Symposium*, pages 381–385, May 2008. doi:10.1109/FREQ.2008.4623024.

[146] E. Yablonovitch. Statistical ray optics. *Journal of the Optical Society of America*, 72(7):899–907, 1982. doi:10.1364/JOSA.72.000899.

[147] M. A. Green. Lambertian light trapping in textured solar cells and light-emitting diodes: analytical solutions. *Progress in Photovoltaics: Research and Applications*, 10(4):235–241, 2002. doi:10.1002/pip.404.

[148] E. S. Fry, G. W. Kattawar, and R. M. Pope. Integrating cavity absorption meter. *Applied Optics*, 31(12):2055–2065, 1992. doi:10.1364/AO.31.002055.

[149] J. A. Musser, E. S. Fry, and D. J. Gray. Flow-through integrating cavity absorption meter: experimental results. *Applied Optics*, 48(19):3596–3602, 2009. doi:10.1364/AO.48.003596.

[150] T. Jávorfi, J. Erostyák, J. Gál, A. Buzády, L. Menczel, G. Garab, and K. R. Naqvi. Quantitative spectrophotometry using integrating cavities. *Journal of Photochemistry and Photobiology B: Biology*, 82(2):127–131, 2006. doi:10.1016/j.jphotobiol.2005.10.002.

[151] J. Erostyák, T. Jávorfi, A. Buzády, K. R. Naqvi, and G. Garab. Comparative study of integrating cavity absorption meters. *Journal of Biochemical and Biophysical Methods*, 69(1–2):189–196, 2006. doi:10.1016/j.jbbm.2006.03.010.

[152] Labsphere, Inc. A Guide to Integrating Sphere Theory and Applications. 2011. Available from: http://www.labsphere.com/technical/technical-guides.aspx.

[153] L. A. Whitehead and M. A. Mossman. Jack O'Lanterns and integrating spheres: Halloween physics. *American Journal of Physics*, 74(6):537–541, 2006. doi:10.1119/1.2190687.

[154] M. Carrascosa, F. Cussó, and F. Agulló-López. Lambert emitters: a simple Monte-Carlo approach to optical diffusers. *European Journal of Physics*, 6(3):183–187, 1985. doi:10.1088/0143-0807/6/3/011.

[155] Philip C. Hobbs. *Building Electro-Optical Systems: Making It All Work*. Wiley, Hoboken, 2nd edition, 2009.

[156] J. Hodgkinson, D. Masiyano, and R. P. Tatam. Using integrating spheres as absorption cells: path-length distribution and application of Beer's law. *Applied Optics*, 48(30):5748–5758, 2009. doi:10.1364/AO.48.005748.

[157] E. S. Fry, G. W. Kattawar, B. D. Strycker, and P.-W. Zhai. Equivalent path lengths in an integrating cavity: comment. *Applied Optics*, 49(4):575–577, 2010. doi:10.1364/AO.49.000575.

[158] P. Elterman. Integrating cavity spectroscopy. *Applied Optics*, 9(9):2140–2142, 1970. doi:10.1364/AO.9.002140.

[159] M. A. Rosenberry, J. P. Reyes, D. Tupa, and T. J. Gay. Radiation trapping in rubidium optical pumping at low buffer-gas pressures. *Physical Review A*, 75(2):023401, 2007. doi:10.1103/PhysRevA.75.023401.

[160] Labsphere, Inc. 6080 White Reflectance Coating, 2011. Available from: http://www.labsphere.com/technical/literature.aspx.

[161] Labsphere, Inc. Optical-Grade Spectralon Material, 2011. Available from: http://www.labsphere.com/technical/literature.aspx.

[162] J. Ma, A. Kishinevski, Y.-Y. Jau, C. Reuter, and W. Happer. Modification of glass cell walls by rubidium vapor. *Physical Review A*, 79(4):042905, 2009. doi:10.1103/PhysRevA.79.042905.

[163] S. Zhu, A. W. Yu, D. Hawley, and R. Roy. Frustrated total internal reflection: A demonstration and review. *American Journal of Physics*, 54(7):601–607, 1986. doi:10.1119/1.14514.

[164] M. C. James. Novel optical properties of a submerged light bulb. *American Journal of Physics*, 76(9):856–862, 2008. doi:10.1119/1.2955794.

[165] E. L. Simmons. Reflectance of a powdered sample immersed in a liquid. *Journal of Applied Physics*, 46(6):2804–2805, 1975. doi:10.1063/1.321923.

[166] F. Grum and G. W. Luckey. Optical sphere paint and a working standard of reflectance. *Applied Optics*, 7(11):2289–2294, 1968. doi:10.1364/AO.7.002289.

[167] W. G. Egan and T. Hilgeman. Anomalous refractive index of submicron-sized particulates. *Applied Optics*, 19(22):3724–3727, 1980. doi:10.1364/AO.19.003724.

[168] M. C. W. van Rossum and Th. M. Nieuwenhuizen. Multiple scattering of classical waves: microscopy, mesoscopy, and diffusion. *Reviews of Modern Physics*, 71(1):313–371, 1999. doi:10.1103/RevModPhys.71.313.

[169] Akira Ishimaru. *Wave Propagation and Scattering in Random Media*. Academic Press, New York, 1978.

[170] L. F. Gate. Comparison of the photon diffusion model and Kubelka-Munk equation with the exact solution of the radiative transport equation. *Applied Optics*, 13(2):236–238, 1974. doi:10.1364/AO.13.000236.

[171] Gustav Kortüm. *Reflectance Spectroscopy*. Springer-Verlag, Berlin, 1969.

[172] E. M. Patterson, C. E. Shelden, and B. H. Stockton. Kubelka-Munk optical properties of a barium sulfate white reflectance standard. *Applied Optics*, 16(3):729–732, 1977. doi:10.1364/AO.16.000729.

[173] G. H. Goedecke. Radiative transfer in closely packed media. *Journal of the Optical Society of America*, 67(10):1339–1348, 1977. doi:10.1364/JOSA.67.001339.

[174] L. B. Wolff. Diffuse-reflectance model for smooth dielectric surfaces. *Journal of the Optical Society of America A*, 11(11):2956–2968, 1994. doi:10.1364/JOSAA.11.002956.

[175] W. R. Calhoun, H. Maeta, A. Combs, L. M. Bali, and S. Bali. Measurement of the refractive index of highly turbid media. *Optics Letters*, 35(8):1224–1226, 2010. doi:10.1364/OL.35.001224.

[176] C. C. Habeger. Angular radiance variation in an integrating sphere. *Journal of the Optical Society of America A*, 11(7):2130–2136, 1994. doi:10.1364/JOSAA.11.002130.

[177] L. M. Hanssen. Effects of non-Lambertian surfaces on integrating sphere measurements. *Applied Optics*, 35(19):3597–3606, 1996. doi:10.1364/AO.35.003597.